Passive Microwave Devices and Biomedical Sensors: Applications and Perspectives

Mohammed El Gibari

HABILITATION À DIRIGER DES RECHERCHES
HDR

NANTES UNIVERSITE

Spécialité : Électronique

Par
Mohammed EL GIBARI

« Dispositifs hyperfréquences passifs et capteurs biomédicaux : applications et perspectives »

Soutenance prévue le 9 Juillet 2025 à l'UFR Sciences et Techniques de Nantes Université

Unité de recherche : Institut d'Electronique et des Technologies du numéRique (IETR)

Rapporteurs avant soutenance :

Anne-Laure BILLABERT	Professeur des Universités, ESYCOM, CNAM de Paris
Denis BARATAUD	Professeur des Universités, XLIM, Université de Limoges
Elhadj DOGHECHE	Professeur des Universités, IEMN, Université Polytechnique Hauts-de-France

Composition du Jury :

Examinateurs :

Florence RAZAN	Professeur des Universités, IETR, ENS de Rennes
Hichame MAANANE	Dr/HDR Systems Architect, THALES DMS France Élancourt
André PERENNOU	Professeur des Universités, LabSTICC, École nationale d'ingénieurs de Brest
Ahmed RHALLABI	Professeur des Universités, IMN, Nantes Université
HongWu LI	Professeur des Universités, IETR, Nantes Université

1 Curriculum Vitae

Nom patronymique : **El Gibari**

Prénom : **Mohammed**

Grade : **Maître de conférences, hors classe**

Section CNU : **63**

Établissement : **Nantes Université**

Laboratoire d'accueil : **Institut d'Électronique et des Technologies du numéRique (IETR), UMR CNRS 6164**

J'ai obtenu mon diplôme de doctorat le 22 octobre 2009 à l'Université de Nantes, puis j'ai été nommé ATER à l'UFR Sciences et Techniques de l'Université de Nantes le 1er septembre 2010. Après un an de post-doc à l'école polytechnique à l'Université de Nantes, j'ai été nommé MCF en septembre 2011 sur un poste de 63ème section au laboratoire IETR, site de l'UFR Sciences et Techniques de Nantes Université.

Mes activités de recherche portent sur deux thématiques majeures : les composants opto-hyperfréquence et en particulier les modulateurs et les convertisseurs analogiques numériques à base de polymères électro-optiques en couches mince et les capteurs biomédicaux pour la santé du futur. Depuis le début de ma carrière, j'ai participé à plusieurs projets et prestations de recherche dont 2 comme porteur et responsable scientifique. À savoir, le projet MODPOL (2008-2011) financé par l'ANR où j'ai travaillé sur l'étude et la réalisation d'un modulateur à base de polymère électro-optique. J'ai beaucoup contribué dans l'axe de la conception et l'optimisation de guide optique et hyperfréquence et également dans l'axe concernant la caractérisation optique, diélectrique et électro-optique des matériaux et des échantillons. Ensuite, j'étais co-responsable de l'axe 1 (conception de convertisseurs analogique-numérique) du projet ADC PolyNano (2013-2017), co-responsable de l'axe 3 (étude des rendements énergétiques) du projet N-air-J (2014-2018) financés par la Région des Pays de la Loire et responsable de l'axe 1 (conception de déflecteur électro-optique) du projet ADC Poly (2017-2022) financé dans le cadre de l'appel à projet ANR ASTRID. Par ailleurs, j'ai été porteur et responsable scientifique du projet Interdisciplinarité (2017-2020) Ingénierie-Santé intitulé "Capteurs de pression artérielle sans fil implantables de grande précision et autonomie" financé par l'Université de Nantes en 2 phases : La première phase (2017-2018 avec une enveloppe de 19 k€) a permis de démontrer la faisabilité du projet. Suite aux résultats très positifs obtenus lors de cette première phase, mon projet a été sélectionné pour poursuivre en deuxième phase (2018-2020) avec un financement d'une bourse de thèse et un budget de fonctionnement de 50 k€. En 2023-2024, j'étais responsable scientifique d'une prestation (24 k€) avec MBDA pour la réalisation d'une structure de filtrage haute fréquence.

Enfin, j'ai obtenu une PEDR de 2018-2022 et je suis auteur/co-auteur de 20 articles dans des journaux internationaux, un chapitre dans un ouvrage en anglais et plus de 60 communications dans des conférences internationales et nationales, et co-inventeur d'un brevet international.

Depuis juin 2019, j'assure la mission de responsable du Fablab au sein de l'UFR Sciences et Techniques. Par ailleurs, depuis septembre 2021, je suis en charge de l'organisation des manifestations scientifiques de l'école doctorale MathSTIC (rebaptisée MASTIC en septembre 2022), telles que les colloques et les journées des doctorants.

Au cours de l'année universitaire 2023-2024, j'ai pris la responsabilité du Master 1 EEA en remplacement temporaire de la responsable en congé maternité. J'ai également coordonné le concours national et régional « Faites de la Science », organisé sous l'égide de la Conférence des Doyens et Directeurs des UFR Scientifiques (CDUS).

Actuellement, en plus de mes fonctions au Fablab et à l'école doctorale, je suis responsable de la Licence 2 SPI-EEA à l'UFR Sciences et Techniques et continue d'assurer la coordination régionale du concours « Faites de la Science » et également membre du conseil de gestion (depuis 2024) et membre du conseil scientifique de l'UFR Sciences et Techniques de Nantes Université (depuis 2020).

2 Encadrement doctoral et scientifique

2.1 Thèse de doctorat (9)

M. Hadjloum (2013-2016), "Conversion analogique-numérique de signaux hyperfréquences à base de polymères électro-optiques", H. W. Li (40 %), **M. El Gibari (50 %)** et A. Daryoush (10 %). Publications communes : **7** articles dans des revues internationales avec comité de lecture, **11** conférences avec actes dans un congrès international et **4** conférences dans un congrès national Devenir du docteur : Ingénieur Solution Matériel à Thales
D. Palessonga (2013-2017), "Mise en forme et caractérisation de matériaux polymères en vue de la réalisation de composants opto-hyperfréquences à haute performance", H. W. Li (40 %), B. Guiffard (30 %) et **M. El Gibari (30 %)**. Publications communes : **1** article dans une revue internationale avec comité de lecture, **2** conférences avec actes dans un congrès international et **2** conférences dans un congrès national Devenir du docteur : Enseignant chercheur à l'ESME Sudria
T. Sghaier (2016-2019), "Polymères électroactifs pour dispositifs antennaires innovants", B. Guiffard (50 %) et **M. El Gibari (50 %)**. Publications communes : **2** articles dans des revues internationales avec comité de lecture, **2** conférences avec actes dans un congrès international et **1** conférence dans un congrès national Devenir du docteur : Ingénieur de recherche en CDI à MCPP France à Tiffauges
P. –V. Dugué (2017-2021), "Etude et réalisation d'un déflecteur électro-optique en optique intégrée à base de matériaux polymères", H. W. Li (30 %), J. –P. Vilcot (40 %) et **M. El Gibari (30 %)**. Publications communes : **1** article dans une revue internationale avec comité de lecture, **3** conférences avec actes dans un congrès international et **4** conférences dans un congrès national Devenir du docteur : Ingénieur de recherche en CDI à MBDA Missile Systems à Selles-Saint-Denis
S. Mbacke (2018-2022), "Etude et réalisation d'un déflecteur électro-optique en optique intégrée à base de matériaux polymères", H. W. Li (40 %), **M. El Gibari (30 %)** et B. Lauzier (30%). Publications communes : **1** article dans une revue internationale avec comité de lecture et **3** conférences avec actes dans un congrès international Devenir du docteur : Ingénieur de recherche en CDI à EPSILON - ALCEN Group à Toulouse

Z. Jradi (2018-2022), " Nanocomposites à propriétés électro-optiques pour composants opto-hyperfréquences à haute performance", H. W. Li (30 %), **M. El Gibari (30 %)** et O. Chauvet (40%). Publications communes : **2** conférences avec actes dans un congrès international Devenir du docteur : Ingénieur à STMicroelectronics à Rousset
S. Adrar (2019-2022), "Semelle piézoélectrique connectée pour applications médicales", R. Séveno (50 %), **M. El Gibari (50 %)** Publications communes : **1** article dans une revue internationale avec comité de lecture et **2** conférences avec actes dans un congrès international Devenir du docteur : Ingénieur de recherche en CDI à Valeo en région Parisienne
A. Merainani (2023-…), "Modélisation d'une technologie transparente grillagée - Application à la conception d'antennes et de circuits radiofréquences", T. Razban (40 %), **M. El Gibari (30 %)** et Y. Mahé (30%) Publication commune : **1** conférence internationale avec acte à PIERS 2025
M. Belghiti (2024-…), (Thèse en co-tutelle avec l'UM6P Rabat au Maroc) "Conception et réalisation d'un capteur de gaz hyperfréquence à base d'oxydes de métaux déposés par procédé PVD", A. Rhallabi (50 %, IMN), **M. El Gibari (50 %**, IETR**)** et A. El Fallah Serghrouchni (pour l'UM6P) Publications communes : **3** conférences (1 en 2024 et 2 en 2025) avec actes dans un congrès international.

2.2 Master 2 (26)

Date	Nom	Nature	Durée
20-02-2012 au 20-07-2012	B. Benallal	Stage de fin d'étude	5 mois
08-09-2014 au 25-03-2015	P. –M. Bataille	Projet pédagogique	15 semaines (2 sem/mois)
07-09-2015 au 23-03-2016	O. Houssine et N. Jean Michel		
Mai à septembre 2016	M. Faye	Stage de fin d'étude	5 mois
05-09-2016 au 23-03-2017	C. Le Bleis et T. Ciceron	Projet pédagogique	15 semaines (2 sem/mois)
	A. Oggar et W. El Mazli		
	A. Abbes et N. Namir		
Avril à septembre 2017	C. Le Bleis	Stage de fin d'étude	5 mois
04-09-2017 au 23-03-2018	M. Ikhlef	Projet pédagogique	15 semaines (2 sem/mois)
10-09-2018 au 25-03-2019	S. Erguibi et A. Kharouai		
	M. Mghaith et A. Boussaidi		
16-09-2019 au 23-03-2020	R. Elolongue et T. Majd		
12-09-2022 au 17-03-2023	F-Z. El Faiz et M. El Boukhari		
18-09-2023 au 22-03-2024	R. Kaboré et K. V. Leubro		
	M. Habibou Issaka et M. A. Barhmi		
16-09-2024 au 28-03-2025	E. Sala		
	S. Tadil		
	S. Akherraz		

3 Responsabilités et participation à des projets scientifiques

a. Responsable scientifique d'un contrat de prestation avec MBDA (2023-2024, 24 k€) « étude et réalisation d'une solution de filtrage hyperfréquence » (confidentiel)

b. Porteur et responsable du projet de recherche Interdisciplinarité Ingénierie-Santé financé par l'Université de Nantes en deux phases (AAP Interdisciplinaires 2017-2021, 69 k€ et une bourse

de thèse), "Capteurs de pression artérielle sans fil implantables de grande précision et autonomie" en 2 phases :

- ✓ ***Phase 1*** (2017-2018, 19 k€) : démonstration de la faisabilité du projet.
- ✓ ***Phase 2*** : sélection du projet (2/15) pour un financement complémentaire incluant une bourse de thèse et un budget de fonctionnement de 50 k€, suite aux résultats très positifs obtenus lors de la première phase.

Résumé du projet :

Le projet vise à réaliser un capteur de pression artérielle implantable de grande précision et autonomie en corrigeant ses dérives thermiques d'une part et réduisant sa consommation moyenne d'autre part. Il allie la pluridisciplinarité (électronique, hyperfréquence, biologie et thermique) à l'approche multi-contraintes (précision, autonomie et compacité).

Cette étude répond au besoin important des sociétés pharmaceutiques et de leurs sous-traitants lors d'études précliniques de pharmacologie de sécurité ou de toxicologie sur les animaux. La méthodologie mise au point au cours du projet pourra s'appliquer à d'autres capteurs

Le consortium a regroupé 3 partenaires (IETR, l'institut du thorax et l'ESEO d'Angers).

c. Responsable de l'axe conception de composant, caractérisation de matériaux et de composants du projet ANR-ASTRID 2017 ADC Poly, "Déflecteur à base d'un guide optique à fuite en polymère en vue de la réalisation d'un convertisseur analogique-numérique tout-optique à plus de 40 Giga échantillons par seconde", financé (300 k€) par la DGA (2017-2022).

Résumé du projet :

Le projet consiste à démontrer la faisabilité d'une brique essentielle d'un convertisseur analogique numérique tout-optique compact permettant d'allier un taux d'échantillonnage à plus de 40 GSPS (GSPS pour Giga Samples Per Second) et une résolution de quantification de 6 bits. De tels ADCs à très grande fréquence d'échantillonnage sont indispensables à la fois pour des applications civiles et défense, les systèmes de guerre électronique dans le domaine de la défense et la communication large bande par satellite dans le domaine civil par exemple.

ADC Poly vise alors à réaliser un déflecteur électro-optique couplé à un collecteur en micro-optique qui assurent conjointement la fonction de quantification de cet ADC tout-optique. Ce composant opto-hyperfréquence innovant est centré sur l'utilisation d'un guide optique à fuite en optique intégrée fabriqué par les techniques de la microélectronique. Couplé in fine à un masque de codage, ADC Poly permettra de caractériser les fonctions de quantification de la structure d'ADC proposée. Des travaux de modélisation, fabrication et caractérisation sont alors attendus de manière à aboutir sur la conception, la réalisation technologique et la détermination des performances d'un

premier démonstrateur d'un tel composant.

Le consortium a regroupé 4 partenaires (IETR, IEMN, IMT Atlantique et Thales-TRT).

d. Co-responsable de l'axe (avec Pr Afshin Daryoush de Drexel University, USA) conception de convertisseurs analogique-numérique du projet ADC PolyNano, "Conversion analogique-numérique de signaux hyperfréquences à base de polymères électro-optiques dopés avec des nanoparticules", financé (200 k€) par la région des Pays de la Loire (2013-2017).

Résumé du projet :

Le projet a pour objectif de réaliser un convertisseur analogique-numérique optique capable d'atteindre une haute cadence d'échantillonnage, un nombre de bits élevé, et une faible consommation d'énergie. Pour ce faire, un déflecteur de faisceau optique, commandé par un signal hyperfréquence, sera utilisé. Afin d'optimiser les performances du dispositif, nous poursuivrons deux axes principaux. D'une part, nous chercherons à améliorer les propriétés fonctionnelles des polymères, telles que le coefficient électro-optique, la stabilité de l'effet électro-optique, ainsi que la compatibilité mécanique et thermique entre les matériaux du cœur et de la gaine. Pour y parvenir, ces polymères seront dopés avec des nanoparticules. D'autre part, nous travaillerons à la mise au point d'un laser impulsionnel picoseconde, émettant à une longueur d'onde proche de 1 µm, avec un taux de répétition supérieur à 1 GHz. Cette longueur d'onde est choisie car elle offre un bon compromis, permettant de réduire la gigue des impulsions, d'augmenter le nombre de bits et de diminuer la tension de commande, tout en minimisant l'absorption des polymères.

Le consortium a regroupé 4 partenaires (IETR, IMMM, IPR et Drexel University à Philadelphie).

e. Co-responsable de l'axe (avec Pr Lionel Petit du laboratoire LGEF à Lyon) étude des rendements énergétiques du projet N-air-J, "Récupération d'énergie propre par simple courant d'air à partir de micro-générateurs souples" (www.n-air-j.univ-nantes.fr) financé (236 k€) par la région des Pays de la Loire (2014-2018).

Résumé du projet :

Le projet vise à explorer la possibilité de récupérer de l'énergie propre en activant des couches minces piézoélectriques flexibles, d'une épaisseur de quelques micromètres, à l'aide d'un simple courant d'air. L'objectif est de concevoir des micro-générateurs électriques sous forme de films souples, capables de réagir au moindre flux d'air et facilement déployables. Ces micro-générateurs devront être économiques à réaliser et pourront être installés dans divers environnements, tels que des gaines d'aération, des véhicules en mouvement, ou toute structure extérieure exposée au vent. Au terme du projet, un prototype de micro-générateur devra être réalisé, avec des propriétés spécifiques répondant au cahier des charges nécessaires à sa possible industrialisation. Ce dispositif devra être

léger, très souple, simple de fabrication et à faible coût de production, avec une tenue mécanique, dans le temps, suffisante. De plus, le rapport gain énergétique/coût de fabrication, d'installation et d'entretien devra être suffisamment important pour valider son utilisation comme énergie alternative à grande échelle.

Le consortium a regroupé 3 partenaires (IETR, GeM et LGEF).

f. Membre du projet de recherche interdisciplinaire BioDREMV, "Biocapteurs pour la détection de molécules volatiles par résonance électromagnétique", financé (17 k€) par l'Université de Nantes (AAP Interdisciplinaires 2013-2015).

Résumé du projet :

Le projet se concentre sur le domaine des biocapteurs, spécifiquement pour la détection de molécules volatiles odorantes en utilisant des protéines de liaison à ces molécules (OBPs). Contrairement aux biocapteurs électro-acoustiques récents, qui opèrent dans la plage de 200-400 MHz, les partenaires proposent de démontrer le potentiel d'un nouveau type de biocapteur, fonctionnalisé avec des OBPs réceptrices sensibles développées dans l'Unité Fonctionnalité et Ingénierie des Protéines (UFIP). Ce biocapteur repose sur un principe de transduction basé sur la variation de la fréquence de résonance électromagnétique hyperfréquence du dispositif sensoriel. Dans cette première phase, l'objectif du projet est d'évaluer la faisabilité du dépôt de molécules d'OBP sur une antenne patch résonant autour de 10 GHz, ainsi que d'analyser l'influence de ce dépôt sur la fréquence de résonance.

Le consortium a regroupé deux laboratoires de l'Université de Nantes (IETR et UFIP).

g. Membre du projet ANR MODPOL (2008-2011, 300 k€) "Modulateurs à base de Polymères électro-optiques" avec une participation très active dans l'axe conception et caractérisation optique et hyperfréquence des matériaux et dispositifs réalisés.

Résumé du projet :

L'utilisation des polymères dans les dispositifs optiques devient de plus en plus prometteuse à mesure que ces matériaux évoluent, surtout en ce qui concerne leurs propriétés électro-optiques. Le projet MODPOL vise à tirer pleinement parti de ces propriétés en validant, à la fois en laboratoire et dans des applications industrielles, la conception de modulateurs optiques à faible tension de commande reposant sur la technologie des polymères. Les composants développés ciblent deux types d'applications, correspondant à deux architectures distinctes : la modulation haute fréquence (40 GHz et plus) avec un modulateur de type Mach-Zehnder, et les applications de radio sur fibre, pour lesquelles des structures résonantes sont développées. Le projet s'organise autour de trois axes

principaux, tous étroitement interconnectés. Le premier concerne les polymères électro-optiques eux-mêmes, leur optimisation, et la validation de leur utilisation potentielle dans les conditions opérationnelles visées. Deux structures chimiques différentes sont explorées, comparées, et leurs performances sont évaluées en fonction des applications de modulation envisagées afin de sélectionner le matériau le mieux adapté pour chaque application télécom. Le second axe porte sur l'identification et l'optimisation des différentes architectures de modulateurs développées dans le cadre du projet, en tenant compte des caractéristiques spécifiques des matériaux polymères. Enfin, le troisième volet est technologique et se concentre sur l'identification et l'optimisation des procédés de fabrication des composants, qui sont fortement influencés par la nature des polymères utilisés. Les composants fabriqués sont soumis à des tests exhaustifs, notamment en conditions réelles d'environnement télécom.

Le consortium a regroupé les partenaires suivants : IREENA (IETR aujourd'hui), IEMN, ENS-Lyon, IPCMS, PCAS, CEISAM, FOTON-CCLO, FT R&D et Thales-TRT.

4 Activités de recherche scientifiques

Les activités de recherche menées depuis mon recrutement portent sur les axes ci-dessous se déroulant dans le cadre des projets et thèses portés par l'IETR :

4.1 Composants opto-hyperfréquences sur polymères

L'étude et la réalisation des composants opto-hyperfréquence à base de polymère électro-optique en couches minces, en particulier les modulateurs et les convertisseurs analogique numérique. Dans cette thématique, j'ai fortement apporté dans les grandes lignes suivantes :

- Conception et optimisation des structures d'optique guidée.
- Conception et optimisation des guides à fuite délivrant une lumière dont le vecteur d'onde est modifié par l'effet électro-optique.
- Conception, optimisation des électrodes de commande large bande (> à 40 GHz).
- Réalisation et caractérisation des structures hyperfréquences, notamment des transitions entre différentes lignes de transmission, avec le système sous pointe (jusqu'à 40 GHz).
- Développement des modèles analytiques complets et fiables, qui tient compte à la fois des pertes optiques, hyperfréquences et de l'effet électro-optique. Ces modèles sont extrêmement importants pour pallier aux problèmes de simulation numérique nécessitant des ressources informatiques lourdes.

Synthèse de cette activité :

Dans le domaine des télécommunications et des hyperfréquences, la numérisation des signaux

est devenue une étape essentielle, étant donné que tous les signaux sont désormais traités numériquement. Ce processus offre l'avantage de réduire le nombre de composants analogiques, souvent coûteux et volumineux, tout en améliorant la flexibilité et les performances. Pour cela, des convertisseurs analogique-numérique (CAN) sont indispensables. Cependant, avec l'augmentation des débits d'information et des fréquences porteuses, les CAN électroniques atteignent leurs limites, plafonnant à 10^{11} échantillons par seconde et offrant un nombre de bits restreint. Les CAN basés sur des polymères électro-optiques pourraient surmonter ces limitations grâce à leur coefficient électro-optique élevé et à leur bonne adaptation des vitesses de phase des ondes optiques et hyperfréquences. Ces propriétés permettent la réalisation de CAN optiques, offrant une cadence d'échantillonnage élevée, un nombre de bits important et une faible consommation d'énergie. Cette approche est prometteuse, car, par exemple, ces polymères électro-optiques permettent de concevoir des modulateurs avec une bande passante supérieure à 100 GHz [1] et des modulateurs nécessitant une tension de commande inférieure à un volt [2].

L'architecture du CAN tout optique, illustrée dans la figure 1, se compose de trois étapes essentielles à la conversion : l'échantillonnage, réalisé par un laser à verrouillage de mode ; la quantification, assurée par un déflecteur électro-optique ; et la numérisation, effectuée par une matrice de photodiodes. Dans ce système, le faisceau optique est dévié proportionnellement au champ électrique appliqué sur le cœur du guide optique grâce à la tension appliquée entre les électrodes du déflecteur. Le faisceau dévié est ensuite collecté et mis en forme par un élément d'optique diffractif, qui permet d'illuminer une matrice de photodiodes. Le déflecteur transforme les variations de tension analogique présente entre ses électrodes en variations angulaires de la direction du faisceau sortant, et cet angle est ensuite traduit en information numérique par la matrice de photodiodes.

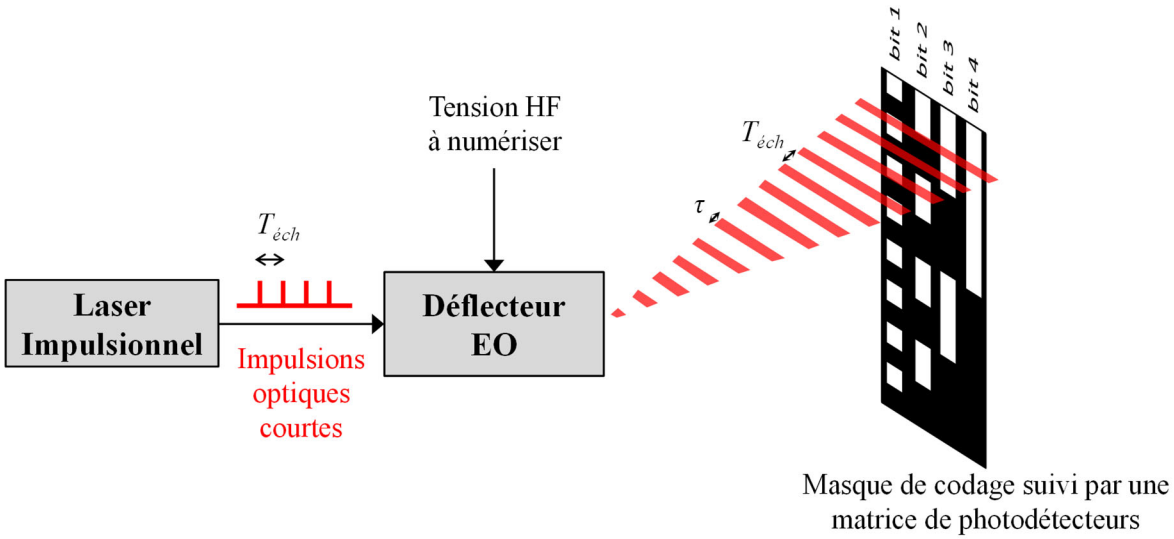

Figure 1 : Convertisseur Analogique Numérique tout-optique à base de déflecteur électro-optique

Ce déflecteur à base d'un guide d'onde à fuite est donc la brique indispensable d'un CAN tout-

optique. Il s'agit d'un déflecteur EO réalisé en optique intégrée à base de matériaux polymères auquel est couplé un collecteur en optique diffractive. Le rôle de ce composant opto-hyperfréquence est de convertir les variations d'un signal analogique en celles de la position spatiale d'impulsions laser sur une matrice de photodétecteurs.

La conception du déflecteur doit intégrer tous les facteurs influençant ses performances, afin de parvenir à une structure optimisée qui représente un compromis permettant d'atteindre les résultats escomptés. La première étape de cette conception consiste à définir un guide d'onde optique monomode. Ce choix impose la sélection d'un matériau polymère pour la gaine, chargé de confiner l'onde dans le cœur en polymère électro-optique. Une fois le guide monomode établi, l'épaisseur de la couche tampon supérieure doit être optimisée pour garantir une résolution élevée tout en assurant une puissance de fuite suffisante pour la détection. Les dimensions et la configuration des électrodes seront ensuite déterminées en fonction du taux de recouvrement entre les ondes optiques et hyperfréquences, ainsi que de l'adaptation de leurs vitesses de phase, ces facteurs ayant un impact significatif sur les pertes électriques et, par conséquent, sur la résolution du dispositif.

L'architecture du déflecteur EO a été proposée par l'équipe du Prof. A. Daryoush 2004 [3]. Suite à une collaboration avec le Prof Daryoush dans le cadre d'un projet régional, nous avons apporté des solutions innovantes et efficaces à de nombreux problèmes qui apparaissent quand on considère les propriétés réalistes des matériaux et les aspects pratiques du dispositif, tels l'atténuation du signal hyperfréquence lors de sa propagation, l'absorption du signal optique dans le guide optique ainsi que le croisement entre ce dernier et les électrodes de commande.

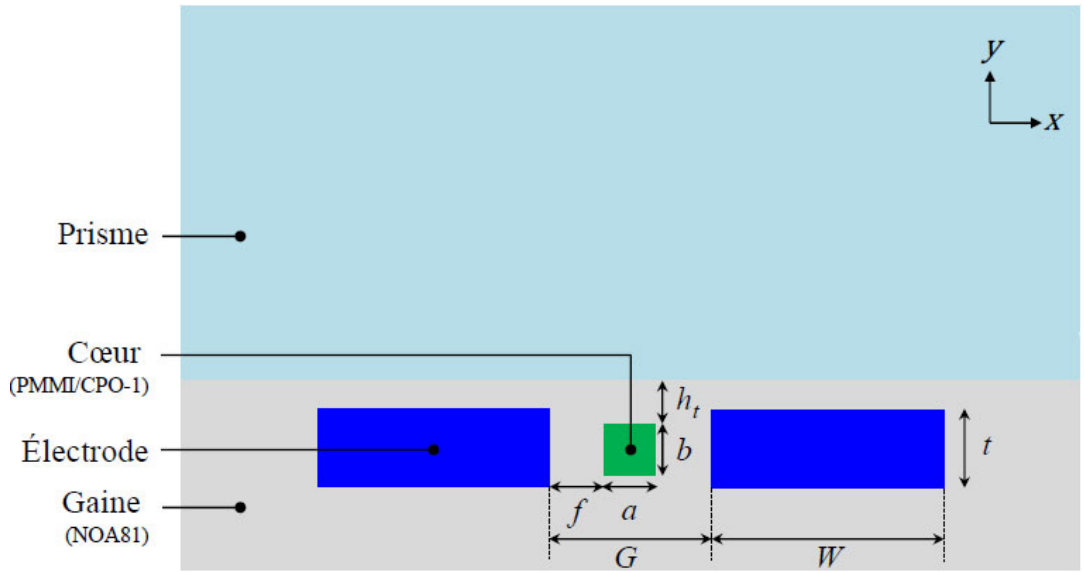

Figure 2: Vue en coupe du guide électro-optique à fuite

La figure 2 montre une section transversale du déflecteur EO. Il est composé d'un cœur en polymères EO entouré d'une gaine en polymère d'indice de réfraction inférieur à celui du cœur.

L'obtention du faisceau de fuite n'est possible qu'en utilisant un superstrat d'indice optique supérieur à celui du mode guidé de manière à convertir le faisceau "de fuite", qui est normalement évanescent dans une structure conventionnelle de guide (indice du superstrat inférieur à celui du cœur du guide), en un mode propagatif. Une couche tampon sépare le guide d'onde du prisme-superstrat, son indice de réfraction et son épaisseur sont ajustés pour permettre à une onde de fuite de passer du guide d'onde vers le prisme-superstrat. Cette couche est définie par un coefficient de fuite, qui mesure la quantité de puissance qui s'échappe du cœur vers le prisme. Des électrodes de commande sont placées de chaque côté du cœur électro-optique pour appliquer le signal hyperfréquence à numériser. Le déflecteur électro-optique possède une structure similaire à celle d'un modulateur de phase électro-optique, sauf que la couche supérieure (c'est-à-dire la couche tampon) est relativement mince et recouverte d'un prisme à indice élevé, ce qui permet la propagation d'un mode de fuite. Ainsi, la variation de l'indice de réfraction du cœur optique se traduit par un changement dans l'angle d'émergence du faisceau de fuite.

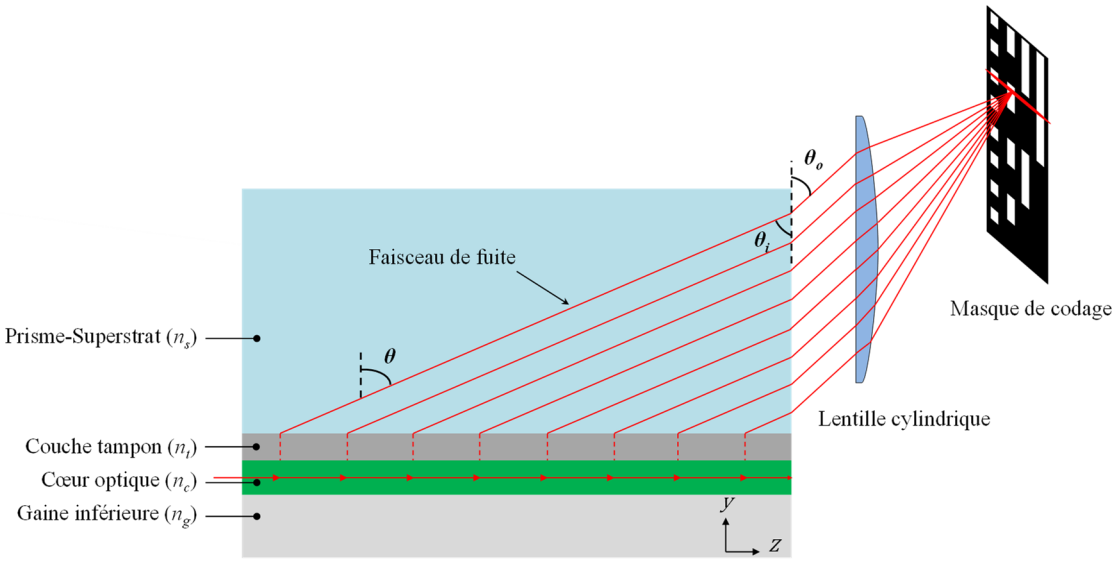

Figure 3: Coupe longitudinale du déflecteur à guide d'onde à fuite avec la lentille cylindrique et le masque de codage.

Pour des matériaux et une longueur d'interaction déterminés, la quantité de puissance de fuite qui passe du cœur optique vers le prisme est régulée par l'épaisseur de la couche tampon. Le faisceau optique de fuite passe dans le prisme avec un angle θ par rapport à la verticale (cf. Figure 3). Cet angle de fuite dépend de l'indice de réfraction effectif et de l'indice du prisme, par conséquent, une variation d'indice (effet Pockels) entraîne une variation de l'angle de fuite.

Une fois les matériaux sélectionnés, cette épaisseur de la couche tampon est donc un paramètre crucial pour l'optimisation du coefficient de fuite. La détermination de cette épaisseur doit permettre de satisfaire deux exigences : (i) maintenir une faible divergence verticale pour garantir une résolution élevée, ce qui nécessite une couche tampon relativement épaisse, et (ii) assurer une puissance de fuite

suffisamment élevée, requérant une couche tampon plus mince, de manière à ce que la puissance de l'onde de fuite soit bien supérieure au bruit. La figure 4 illustre la variation du coefficient de fuite en fonction de l'épaisseur de la couche tampon. Lorsque la couche tampon est épaisse, l'intensité de l'onde optique pénétrant dans le prisme diminue, ce qui entraîne une réduction du coefficient de fuite. Les cartographies du champ lumineux présentées sur la figure 5 démontrent clairement l'influence de l'épaisseur de la couche tampon sur la fuite de la lumière. Les épaisseurs très réduites, telles que 1,2 µm et 1,6 µm, ont été retenues pour visualiser distinctement l'onde de fuite et souligner l'impact de cette épaisseur sur le phénomène de fuite.

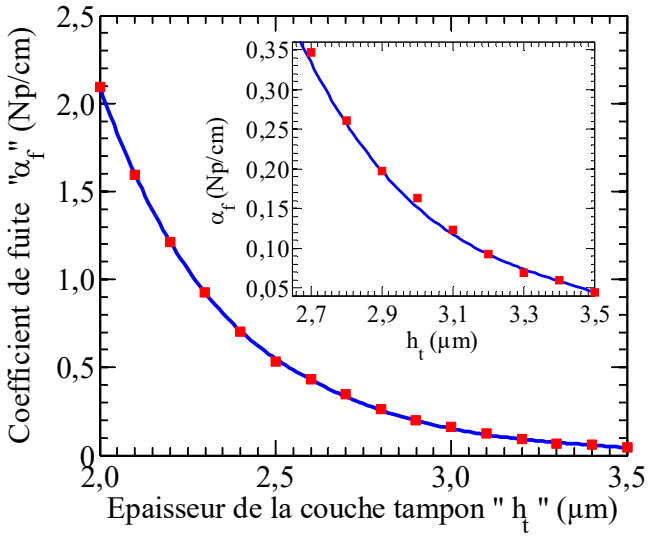

Figure 4: Coefficient de fuite α_f en fonction de l'épaisseur de la couche tampon.

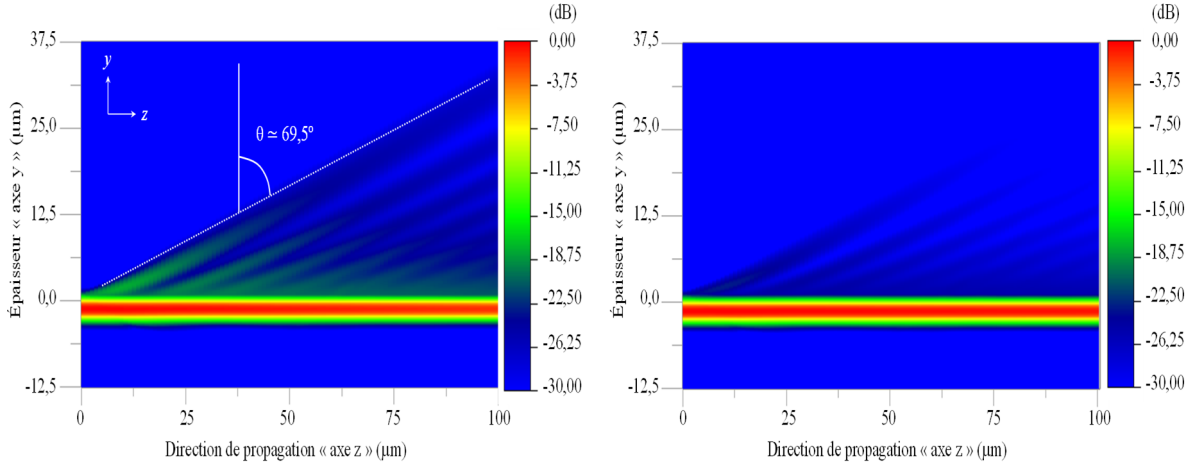

(a) *(b)*

Figure 5: Onde de fuite depuis le guide d'onde optique. a) ht = 1,2 µm ; b) ht = 1,6 µm.

Le taux de recouvrement entre l'onde lumineuse et l'onde hyperfréquence est lié à la distribution du champ électrique *E* dans le guide d'onde à fuite (cf. figure 6). Dans l'architecture du déflecteur

électro-optique proposée dans la thèse de doctorat de X. Hou [4], les électrodes de commande sont placées au-dessus de la couche tampon, donc dans un plan différent du cœur du guide, ce qui réduit considérablement le taux de recouvrement entre ondes optique et hyperfréquence, qui était effectivement plafonné à 40%. Nous y avons remédié en plaçant les électrodes de commande de part et d'autre du cœur du guide optique dans le même plan, nous avons pu ainsi porter le taux de recouvrement de 40% à 80%, ce qui permet de gagner un bit en résolution à toutes choses égales par ailleurs.

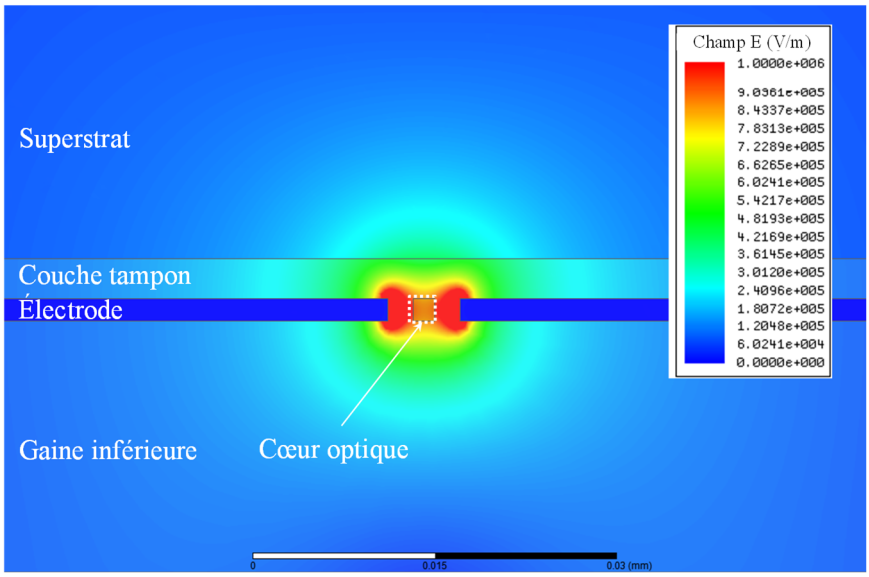

Figure 6 : Cartographie du champ E dans un déflecteur commandé par des électrodes CPS (CoPlanar Strips) dans le même plan que le cœur optique.

L'adaptation de vitesses de phase entre ondes lumineuse et hyperfréquence est un élément très important à prendre en considération, cela permet à chaque impulsion optique d'être « accompagnée », le long de sa propagation dans le guide, par le même champ E progressif afin de subir le même effet EO. Pour cette optimisation, le support mécanique du déflecteur, le wafer de silicium choisi pour sa planéité et sa rigidité mécanique, joue un rôle important. En effet, avec une épaisseur de gaine inférieure de quelques dizaines de µm du guide à fuite, non seulement les pertes diélectriques du silicium accentuent sérieusement l'atténuation du signal hyperfréquence, ce qui dégrade la résolution du déflecteur, mais en plus sa forte constante diélectrique (ε_r = 11,9) empêche d'obtenir une bonne adaptation de vitesses de propagation entre ondes lumineuse et hyperfréquence dans la structure. Un blindage métallique a été ainsi introduit pour écranter le wafer (cf. figure 7), ce qui a permis de rapprocher l'indice effectif n_{oe} du guide optique et la racine carrée de la constante diélectrique effective $\sqrt{\varepsilon_{HF}}$ pour optimiser la bande passante (ou fréquence maximale) selon la formule suivante :

$$f_{max} = \frac{2 \cdot c}{\pi \cdot |n_{oe} - \sqrt{\varepsilon_{HF}}| \cdot L}$$

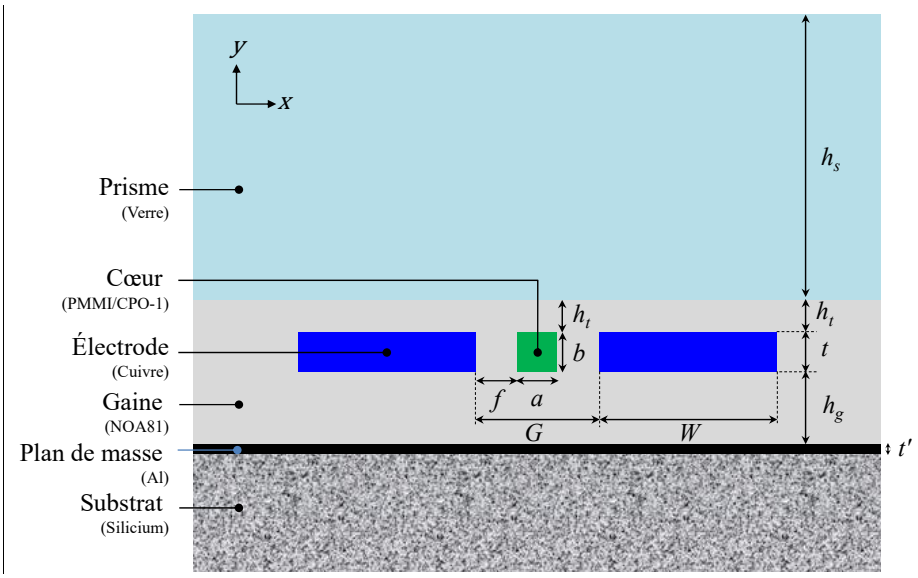

Figure 7 : Coupe transversale du déflecteur EO avec un plan de masse métallique pour écranter le wafer Si.

L'ajout de ce plan de masse transforme les électrodes initiales CPS en électrodes microruban couplée (CMS pour *Coupled MicroStrip*). Ce changement permet d'améliorer significativement la bande passante du déflecteur comme le montre la figure 8.

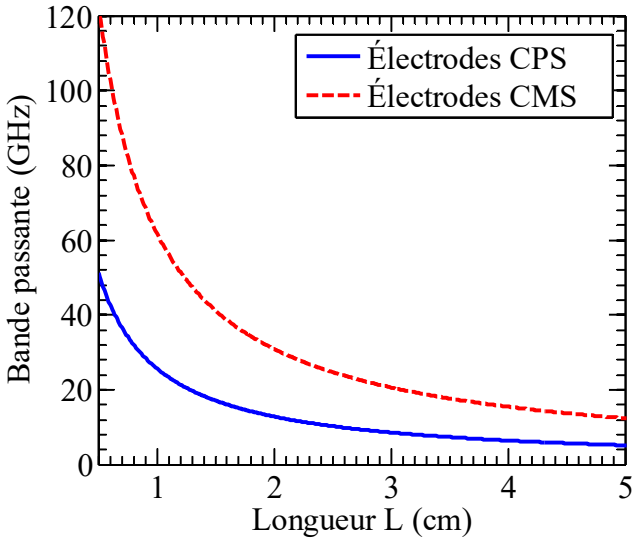

Figure 8 : Bande passante du déflecteur en fonction de sa longueur.

Une fois l'adaptation de vitesse de phase est optimisée, l'atténuation hyprefréquence est un facteur limitant la bande passante utile du déflecteur et dégrade par conséquent la résolution du converstisseur. Les principales sources d'atténuation du signal sont les pertes diélectriques des matériaux utilisés, les pertes métalliques par effet Joule et effet de peau, le rayonnement et les réflexions à l'entrée des électrodes de commande. En effet, Le signal hyperfréquence à numériser est appliqué entre les rubans de la ligne CMS de part et d'autre du cœur du guide à fuite pour modifier

l'indice de réfraction du cœur. À cause de l'atténuation inévitable de la ligne CMS, son amplitude décroît exponentiellement au cours de sa propagation. Le champ électrique décroît bien entendu suivant la même loi avec une ligne CMS à gap constant comme c'est classiquement le cas. Si le champ électrique E(z) responsable de l'effet Pockels varie avec z, l'indice effectif du mode guidé n_{oe} varie également avec z, l'angle de fuite varie aussi d'un point à l'autre, il s'ensuit un étalement angulaire du faisceau de fuite, donc une augmentation de sa divergence angulaire, d'où une baisse de la résolution pour une excursion donnée du faisceau de fuite, pouvant dépasser 1 bit. Pire, tant que ce problème d'atténuation hyperfréquence n'est pas réglé, on ne pourra pas augmenter la résolution en utilisant des polymères de coefficient électro-optique plus élevé. C'est clairement un point bloquant que nous avons réglé. En effet, Nous avons imaginé une méthode de compensation qui consiste à contrebalancer la diminution exponentielle de la tension par la réduction exponentielle du gap entre les rubans de la ligne CMS de l'entrée vers la sortie du guide (cf. figure 9). En effet, si le gap entre les rubans est réduit de la même manière que la tension est atténuée, il est possible de conserver un champ électrique d'amplitude constante au cours de la propagation du signal malgré son atténuation linéique. Cette technique de compensation de l'atténuation hyperfréquence permet de porter la résolution moyenne sur la bande de fréquence DC – 20 GHz de 2,7 bits à 3,4 bits avec un polymère de coefficient électro-optique de 70 V/m.

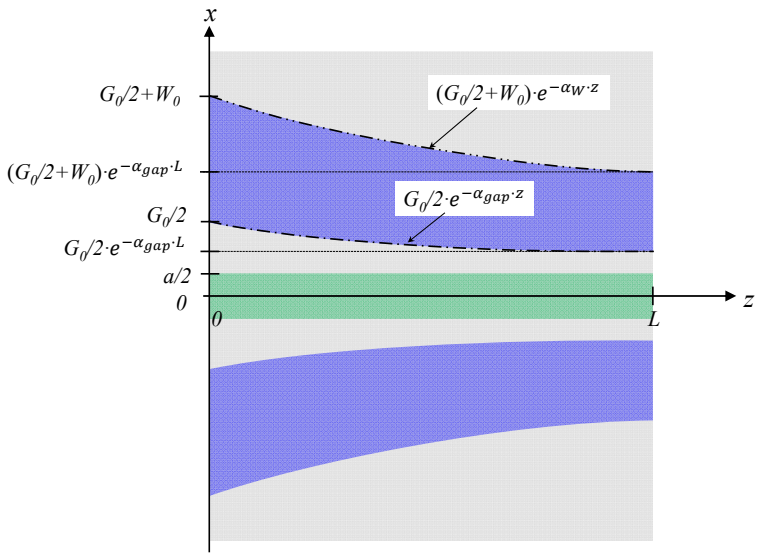

Figure 9 : Vue de dessus des électrodes CMS du déflecteur avec un gap décroissant exponentiellement selon z.

La figure 10 montre les résolutions de deux déflecteurs sur la plage de fréquence DC – 20 GHz, l'un commandé par une ligne CMS classique et l'autre par une ligne CMS à gap variable. Avec la ligne CMS à gap constant, la résolution maximale de 3,7 bits est atteinte en DC et la résolution minimale de 2,3 bits à 20 GHz. Avec la ligne CMS à gap variable, la même valeur maximale de 3,7 bits est obtenue à 2,9 GHz et une valeur minimale de 3 bits aux extrémités de la bande de fréquence, DC et 20 GHz. Ainsi, la variation de la résolution est réduite de moitié grâce à cette technique de

compensation, ce qui permet de diminuer globalement la dégradation de la résolution due aux pertes HF et d'obtenir une performance plus uniforme sur l'ensemble de la bande de fréquence.

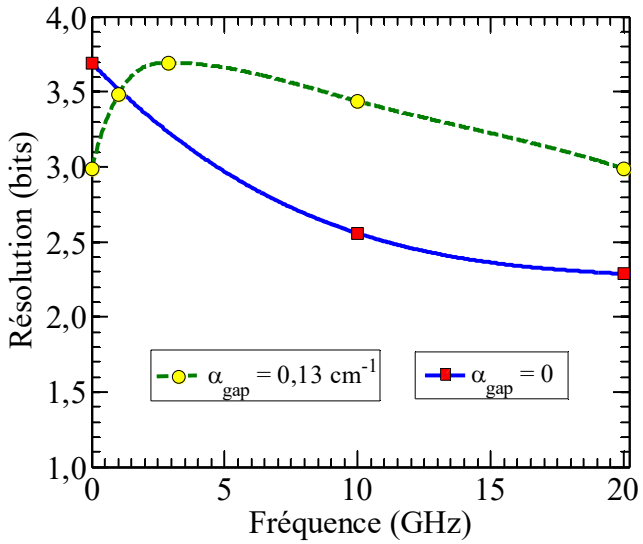

Figure 10 : La résolution en fonction de la fréquence (DC – 20 GHz) avec et sans compensation de l'atténuation du champ E.

Une des problématiques majeures des composants opto-hyperfréquence est l'optimisation des accès optique et hyperfréquence. Il faut un effort particulier pour rendre, d'une part, ces accès compatibles avec la géométrie du déflecteur et permettre aux ondes optique et hyperfréquence de se propager dans le même sens, et d'autre part, l'ensemble de la structure hyperfréquence doit avoir une large bande passante pour couvrir celle souhaitée pour le convertisseur. Or, dans la topologie retenue du déflecteur présentée précédemment, le cœur optique et le gap entre les rubans de l'électrode de commande de dimensions micrométriques sont situés dans le même plan horizontal que le cœur optique, ce qui oblige à séparer les accès optique et hyperfréquence, d'où guide optique en ligne droite et accès électrique perpendiculaire au guide (cf. figure 11). Cependant, couder les deux rubans de l'électrode CMS impliquerait inévitablement que l'un d'eux coupe le cœur du guide optique, ce qui est de toute évidence inacceptable. Pour éviter cette intersection entre ruban et guide optique, seul le ruban-signal est coudé pour le relier aux accès hyperfréquences. Nous utilisons alors le plan métallisé situé sur la face inférieure du dispositif comme l'électrode de masse. Cela nécessite d'une part, de mettre au même potentiel le plan métallisé avec les plots et rubans de masse en face "supérieure" et d'autre part, de réaliser des transitions de modes de propagation hyperfréquence entre l'accès coplanaire, l'interconnexion microruban et l'électrode de commande CMS. La mise au même potentiel des différents points de masse peut alors s'effectuer soit par des via-holes [5] soit par un couplage capacitif [6].

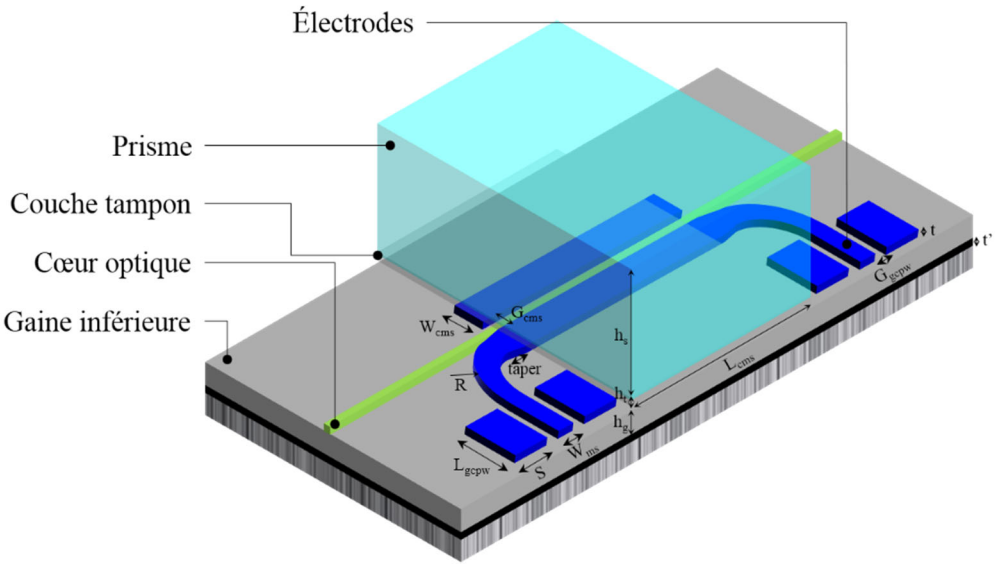

Figure 11 : Représentation en 3D du déflecteur EO avec une transition GCPW-CMS-GCPW pour l'application du signal HF.

La validation expérimentale de la transition GCPW-CMS-GCPW sur le polymère BCB, réalisée à l'aide d'un système sous pointes GSG (voir figure 12), a révélé un excellent accord entre les résultats de mesure et les simulations HFSS. Cette transition fonctionne comme un filtre passe-haut en raison du couplage capacitif entre les rubans de masse situés à la surface des sections GCPW et CMS, et le plan de masse inférieur pleine plaque. L'absence d'une connexion physique entre ces masses empêche la transmission des composantes de basse fréquence. Au cours de cette validation, une bande passante expérimentale supérieure à 40 GHz a été obtenue [7].

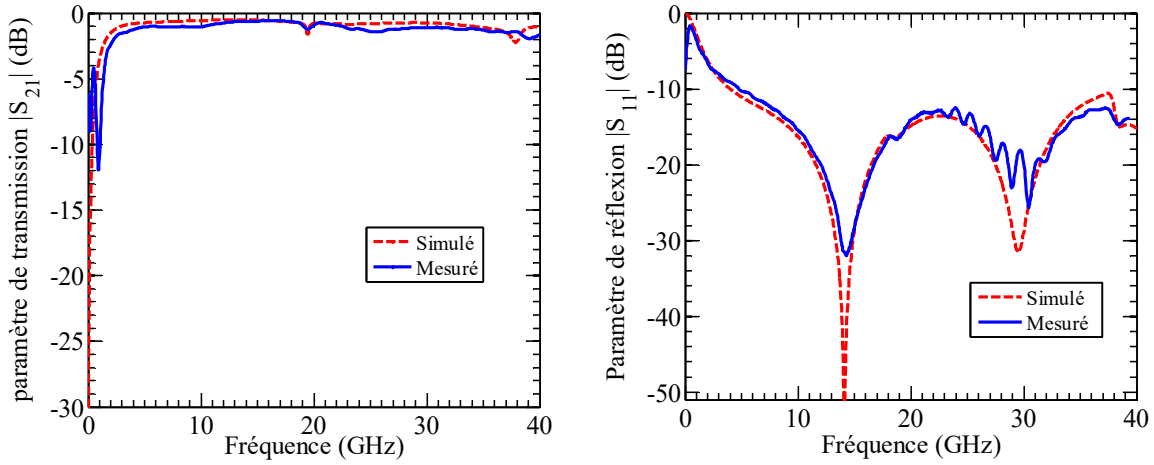

(a) *(b)*

Figure 12 : Paramètres-S mesurés et simulés de la transition GCPW-CMS-GCPW.

La transition GCPW-CMS-GCPW utilisée permet de ramener le signal de commande au déflecteur mais elle ne permet pas de réaliser l'opération d'orientation des chromophores par l'application d'une tension continue. Cette opération d'orientation est indispensable pour orienter tous les chromophores

dans la même direction du signal HF afin d'optimiser l'effet EO. Il faut alors adjoindre des contacts DC (courant continu) à la ligne CMS de commande large bande passante afin de pouvoir utiliser cette dernière pour cette opération d'orientation des chromophores. Issu des technologies utilisées en circuit intégré monolithique hyperfréquence, un filtre passe-bas du second ordre en éléments distribués est ajouté au niveau de la ligne CMS comme le montre la figure 13. Selon les mesures effectuées sur le circuit complet (contacts DC + filtres passe-bas + ligne CMS) réalisé sur le polymère NOA 81 la bande passante atteint la plage de 1,6 GHz à 20,6 GHz. En outre, la tension appliquée peut aller jusqu'à 1160 V avant la rupture d'un des rubans inductifs de 10 µm de large dans le filtre [8]. Comme le gap de la ligne CMS fait 10 µm, cela signifie que les rubans CMS permettent d'appliquer un champ de 116 V/µm, ce qui est largement suffisant pour l'opération d'orientation qui nécessite un champ entre 50 et 100 V/µm.

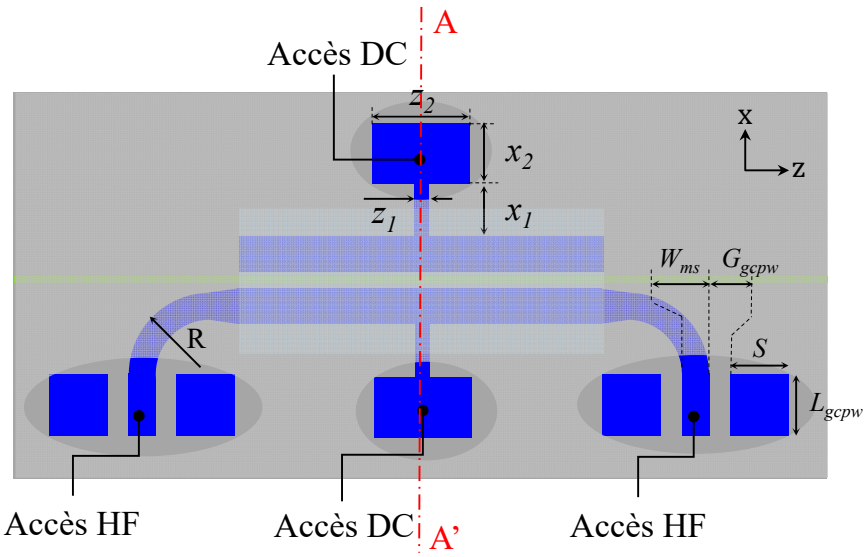

Figure 13 : Représentation schématique d'une vue de dessus d'un déflecteur EO alimenté par une transition GCPW-CMS-GCPW incluant le circuit d'orientation des chromophores.

La solution proposée pour isoler les électrodes de commande CMS des contacts DC est une innovation importante. En effet, elle permet de réaliser les électrodes d'orientation des chromophores et de commandes large bande simultanément, simplifiant en cela la réalisation. En outre, cela offre un moyen de régénérer l'orientation des chromophores pour éviter que leur relaxation dans le temps ne réduise les performances des composants à base de polymères.

Pour pouvoir utiliser le déflecteur avec des signaux hyperfréquences situées dans le domaine quasi-statique (quelques centaines de MHz), il est indispensable de d'intégrer les vias reliant les pads de masse coplanaire au plan de masse inférieur (cf. Figure 14). La réalisation des transitions sur polymère BCB a permis d'avoir des bandes passantes très intéressantes supérieures même à 110GHz [9]. Un schéma équivalent de ce type de transition hybride a même été optimisé sur ADS (cf. figure 15). L'intérêt de ce travail est de pouvoir

prédire à l'aide de ce schéma équivalent, quel peut être le comportement d'une transition avec via dans un environnement circuit plus complexe.

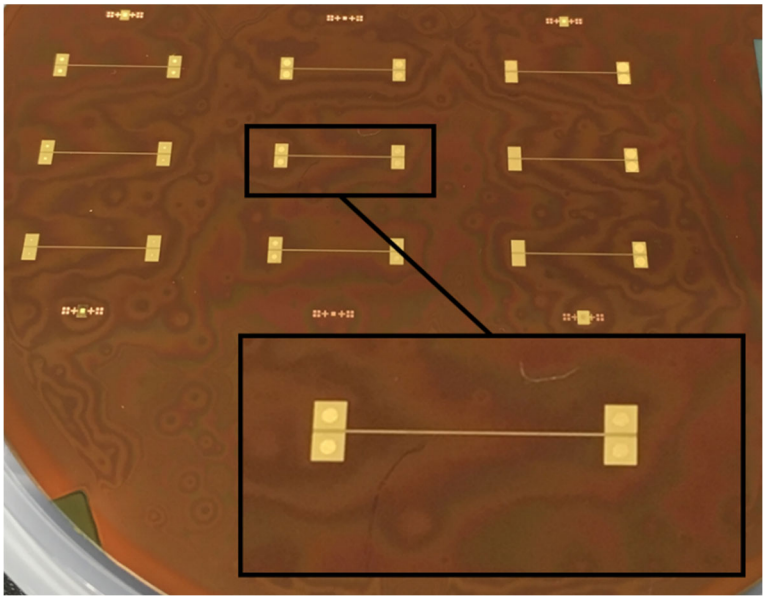

Figure 14 : Photo d'un wafer sur lequel ont été réalisées les transitions GCPW-MS-GCPW pour différents diamètres des vias.

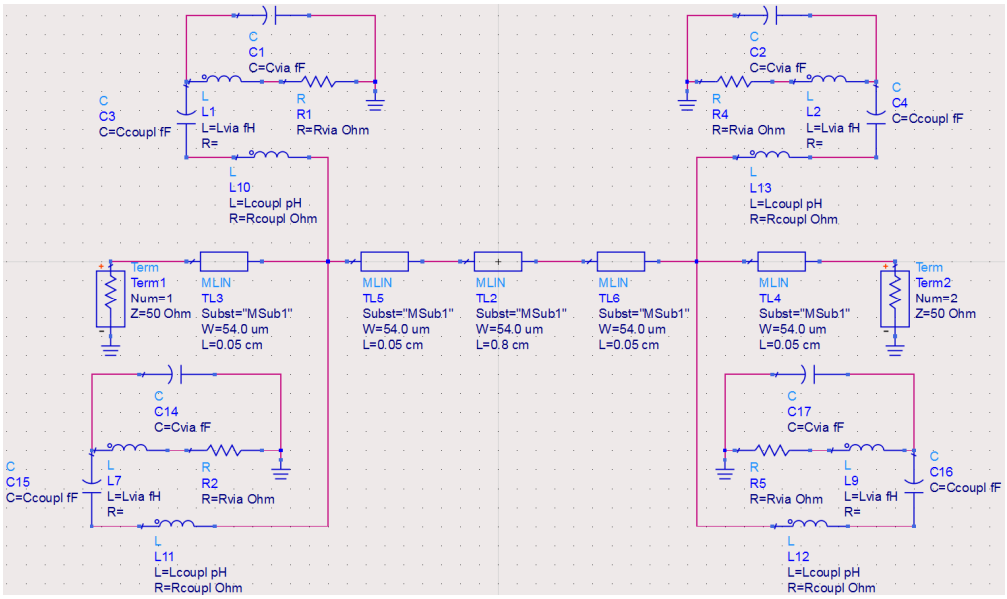

Figure 15 : Schéma équivalent d'une transition GCPW-MS-GCPW avec vias.

4.2 Étude de l'effet de l'incorporation de nanoparticules sur les propriétés de polymères électro-optiques pour les applications opto-hyperfréquence

La bande passante des composants opto-hyperfréquences sur polymères électro-optiques pourrait être considérablement augmentée, en accordant l'indice de réfraction avec la constante diélectrique à

l'aide de nanoparticules. De même l'ajout des nanoparticules pourrait contribuer à l'amélioration de la stabilité des polymères dans le temps. Dans ce contexte, je travaille sur la démonstration de l'influence de l'ajout des nanoparticules sur les propriétés optiques, électrique et électro-optique. Dans cette thématique, mon apport est concentré essentiellement sur les points suivants :

- Mesure de l'indice de réfraction et des pertes de propagation optique par spectroscopie M-lines à plusieurs longueurs d'onde (633 nm, 978 nm, 1307 nm et 1540 nm).
- Caractérisation et extraction des propriétés diélectriques des matériaux (ε_r et tanδ) sur une large bande passante (Jusqu'à 40 GHz) par plusieurs méthodes développées à l'IETR de Nantes (Ring résonateur, capacité Métal Isolant Métal (MIM), Algorithme Génétique).
- Optimisation de l'orientation des chromophores, responsable de l'effet électro-optique et étude de la stabilité de cet effet dans le temps en se basant sur les mesures de la seconde harmonique (SHG).
- Mise en place du banc d'injection électro-optique pour la caractérisation des démonstrateurs.
- Mise en place du banc de mesure du coefficient électro-optique par la méthode M-lines.

Synthèse de cette activité :

Les polymères électro-optiques sont des matériaux organiques particulièrement prometteurs pour la fabrication de composants opto-hyperfréquences de très haute performance. Ces matériaux sont constitués d'une matrice polymère et de chromophores. Ils offrent plusieurs avantages, notamment une bonne compatibilité des vitesses de phase entre les ondes optiques et hyperfréquences, permettant la fabrication de composants opto-hyperfréquences avec une large bande passante, dépassant les 100 GHz. En outre, leur fort coefficient électro-optique, atteignant jusqu'à 300 pm/V, permet de réduire la tension de commande à moins de 1 Volt.

Cependant, l'alignement des chromophores dans la matrice polymère est crucial pour obtenir un effet électro-optique macroscopique. Le principal inconvénient de ces polymères est la stabilité limitée de leur effet électro-optique au fil du temps. Après l'alignement, les chromophores peuvent subir un processus de relaxation, entraînant une désorientation et une perte progressive de l'effet électro-optique. De plus, l'agrégation des chromophores en configuration tête-bêche à des concentrations élevées limite la quantité de chromophores pouvant être ajoutée au polymère, empêchant ainsi l'optimisation de l'effet électro-optique. En raison de ces limitations, les modulateurs électro-optiques basés sur des matériaux organiques ne sont pas encore disponibles sur le marché.

Pour résoudre ces problèmes de stabilité, nous avons développé une nouvelle stratégie utilisant des nanocharges pour améliorer les propriétés optiques, hyperfréquences et électro-optiques du système hôte/invité, tel que le PMMA/DR1.

Les mesures des indices de réfraction par la méthode M-lines ont montré une augmentation de l'indice de réfraction quand les nanoparticules sont incorporées (cf. tableau 1). C'est un résultat très

intéressant puisqu'on arrive à un ajustement contrôlé de l'indice de réfraction dans un polymère électro-optique (nommé P) présentant de faibles pertes optiques et diélectriques, on peut alors obtenir un autre polymère électro-optique (nommé P') d'indice de réfraction différent. Les polymères électro-optiques P et P' pourront alors être utilisés comme matériaux de cœur et de gaines de guides optiques de faibles pertes, dont le cœur et les gaines sont électro-optiques, ce qui permet de bénéficier d'un effet électro-optique amélioré indépendant du taux de confinement.

Matériaux	1306,7 nm	1539,6 nm
PMMA	1,4816	1,4803
PMMA-DR1	1,5031	1,5011
PMMA-SIC (1%)	1,4852	1,4822
PMMA-SIC (2%)	1,4865	1,4838
PMMA-SIC (3%)	1,4888	1,4860
PMMA-DR1-SiC (1%)	1,5081	1,5035
PMMA-DR1-SiC (2%)	1,5116	1,5081

Tableau 1 : Exemple d'indice de réfraction des matériaux étudiés [10]

Un autre résultat intéressant est l'étude de l'effet de concentration en DR1 en mesurant le coefficient électro-optique de 3 films élaborés à partir des solutions contenantes respectivement 6,2%, 8,8 % et 12,4% de DR1 avant filtration. La Figure 16 montre l'évolution de la variation d'indice Δn en fonction de la tension de polarisation pour les trois films aux trois longueurs d'onde de mesure : 637 nm, 1308 nm et 1538 nm.

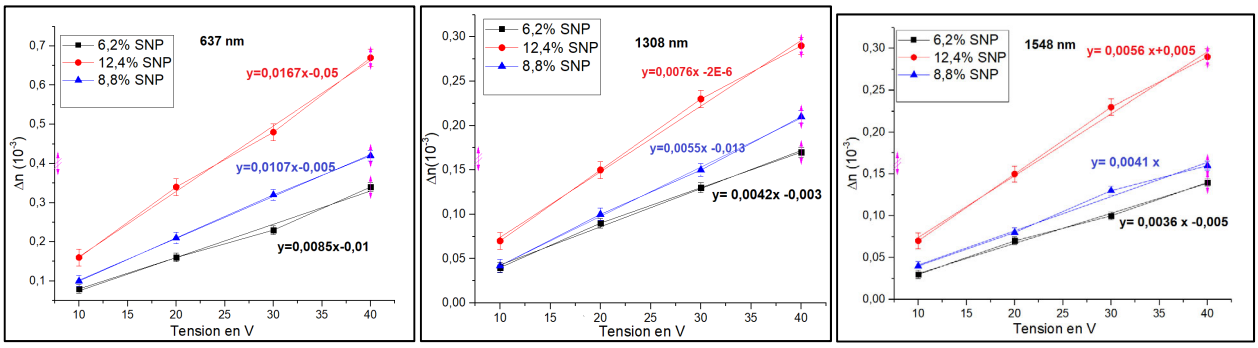

Figure 16 : Variation de Δn en fonction de la tension appliquée pour les 3 films avec une concentration de DR1 de 6,2, 8,8% et 12,4% aux trois longueurs d'onde 637, 1308 et 1548 nm.

Grace à cette variation linéaire de Δn (en accord avec l'effet Pockels), nous avons pu déterminer le coefficient électro-optique en fonction de la concentration du chromophore DR1. La figure 17 montre l'évolution du coefficient électro-optique r_{33} en fonction du pourcentage de DR1 et pour les trois longueurs d'onde. On constate bien une augmentation du coefficient r_{33} avec la quantité de DR1.

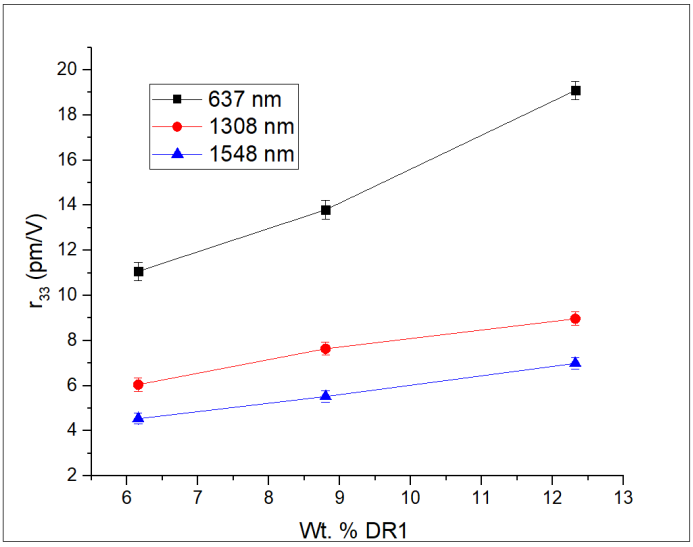

Figure 17 : Variation du coefficient électro-optique en fonction du pourcentage réel de DR1 dans les films aux trois longueurs d'onde 637, 1308 et 1548 nm.

Pour étudier le problème de la stabilité du polymère, nous avons accéléré la relaxation des chromophores en chauffant le film PMMA/DR1 (6,2%) (afin d'accroître la mobilité des chromophores) et nous avons extrait le coefficient r_{33} à la longueur d'onde de 637 nm (cf. Figure 18). Nous remarquons que le coefficient r_{33} diminue avec le temps. La dynamique de relaxation est donc assez lente avec une perte de 2 pm/V/heure.

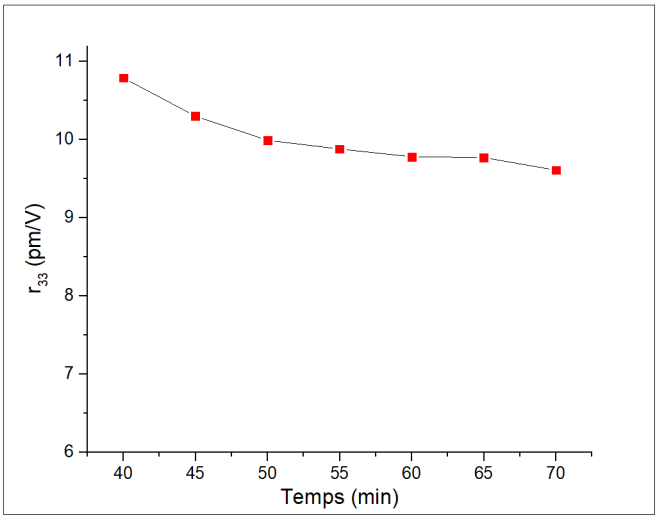

Figure 18 : Évolution du coefficient électro-optique r_{33} à 637 nm en fonction de temps après un chauffage de 40 min à 60°C pour un film de PMMA/DR1 (6,2%).

L'étude menée de l'ajout de nanoparticules de $BaTiO_3$ dans le système PMMA/DR1 a montré une variation assez importante du coefficient électro-optique r_{33} comme le montre le tableau ci-dessous. Quel que soit le pourcentage de DR1 dans le film, nous remarquons une augmentation significative du coefficient r_{33} après l'ajout des nanoparticules de BaTiO3 aux trois longueurs d'onde

étudiées. Par exemple, à 637 nm, après l'ajout de 1% des nanoparticules de BaTiO3, le coefficient électro-optique augmente de 5,07 pm/V, de 4,97 pm/V et de 2,91 pm/V pour des films contenant 6,2%, 8,8% et 12,4% de DR1 respectivement [11].

Référence	r_{33} (637 nm) en pm/V	r_{33} (1308nm) en pm/V	r_{33} (1548 nm) en pm/V
PMMA/6,2% DR1/1% $BaTiO_3$	**16,14**	**12,39**	**7,64**
PMMA/6,2% DR1/SNP	11,07	6,05	4,54
PMMA/8,8% DR1/1% $BaTiO_3$	**18,05**	**13,54**	**9,63**
PMMA/8,8% DR1/SNP	13,08	7,64	5,52
PMMA/12,4% DR1/1% $BaTiO_3$	**22,00**	**14,57**	**12,49**
PMMA/12,4% DR1/SNP	19,09	8,97	6,99

Tableau 2 : Valeurs du coefficient r_{33} des films PMMA/ DR1/BaTiO3 aux 3 longueurs d'ondes 637, 1308 et 1548 nm en fonction de taux de DR1 et de BaTiO3.

L'ajout des nanoparticules de BaTiO3 a également un effet significatif sur la stabilité de l'effet électro-optique, comme le montre la figure 19. La dynamique de relaxation est donc plus lente ici avec une perte de 0,62 pm/V/heure par rapport à la perte de 2 pm/V/heure sans nanoparticules (cf. figure 18). Ce résultat confirme, l'effet « stabilisateur » des nanoparticules BaTiO3 sur l'effet Pockels global, auquel contribuent les chromophores DR1 et les nanoparticules BaTiO3.

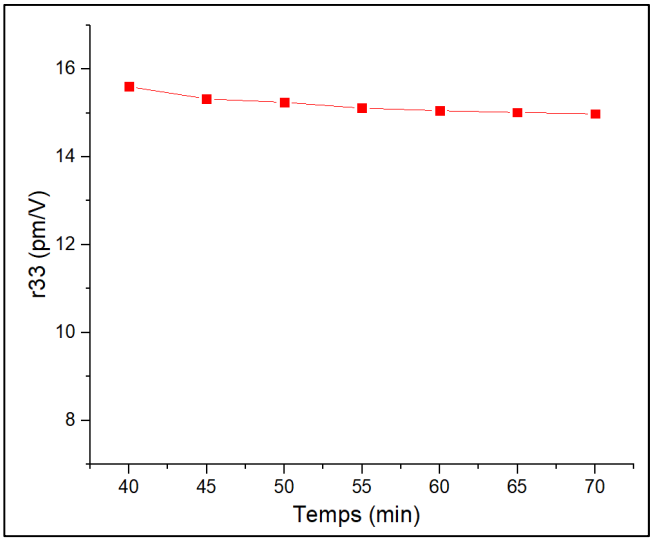

Figure 19 : Évolution du coefficient électro-optique r_{33} à 637 nm en fonction de temps après un chauffage de 40 min à 60°C pour un film de PMMA/6,2% DR1/1% BaTiO3.

La mesure de la permittivité relative est une propriété fondamentale pour la conception des composants opto-hyperfréquence en particulier pour optimiser la bande passante des composants. La Figure 20 montre l'évolution de la permittivité relative de films PMMA/12,4% DR1 et pour différents pourcentages des nanoparticules BaTiO3.

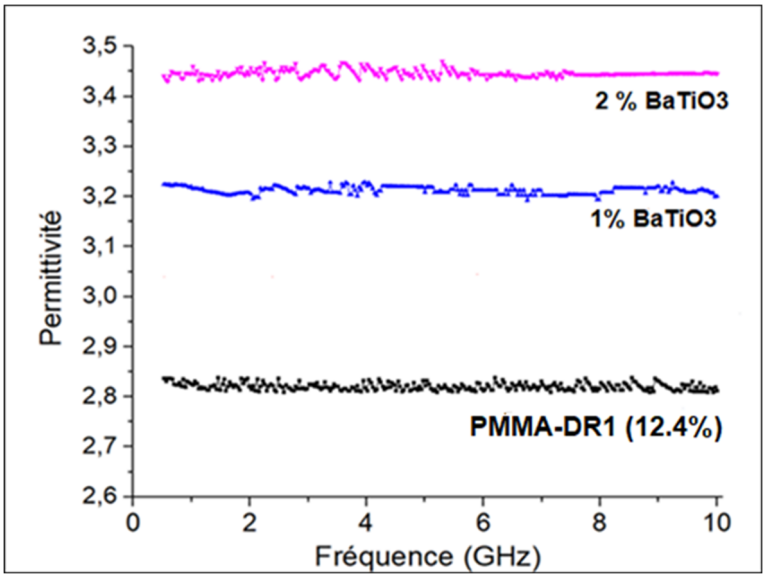

Figure 20 : Évolution de la permittivité relative mesurée en fonction de la fréquence après l'ajout de 1% et 2% de BaTiO3 dans un film de PMMA/12,4% DR1.

Contrairement à la variation de l'indice de réfraction quand on rajoute des nanoparticules, on constate que la permittivité augmente très significativement, même si on ne rajoute qu'une très faible fraction volumique de nanoparticules. Elle passe de 2,85 sans nanoparticule à 3,21 et 3,45 pour les taux de 1% et 2% en nanoparticules respectivement. Ceci s'explique par le fait que BaTiO3 est un matériau ferroélectrique qui présente une très forte permittivité relative selon l'orientation cristallographique et la mise en forme du matériau. Cette évolution notable de la permittivité quand on rajoute des nanoparticules, sans qu'augmente significativement l'indice est très intéressante pour l'optimisation de la bande passante d'un dispositif électro-optique.

L'augmentation de cette bande passante consiste en la réduction de la différence entre la racine carrée de la permittivité effective et l'indice de réfraction effectif. La figure 21 montre que l'utilisation du polymère EO chargé avec des nanoparticules de BaTiO3 permet de réduire cette différence. Le dopage optimal est d'environ 1% de nanoparticules de BaTiO3 dans le polymère hôte.

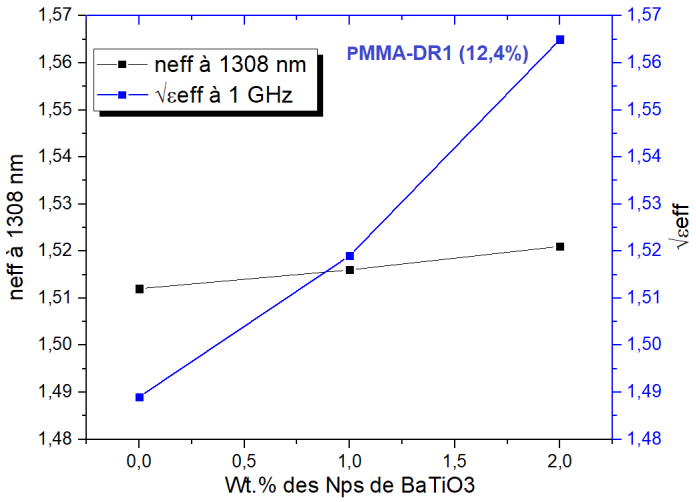

Figure 21 : Amélioration de l'adaptation de vitesse de phase en dopant des polymères EO avec des nanoparticules de BaTiO3.

4.3 Capteurs biomédicaux pour la santé du futur

Depuis 2017, je travaille sur des activités de recherche en lien avec la santé du futur. Mes actions se présentent essentiellement selon deux activités :

La première concerne le projet Interdisciplinarité Ingénierie-Santé (phase I : 2017- 2018 (19 k€)) puis phase II : 2018-2020 (50 k€) et une bourse de thèse dont je suis le coordinateur et responsable scientifique et qui vise l'étude et la compensation de la dérive thermique d'un capteur de pression artérielle sans fil implantables lors des études précliniques sur les animaux. Dans le cadre de cette activité de recherche, une thèse a été soutenue en mars 2022 et une seconde thèse a démarré en octobre 2022. Pour cette activité, j'ai apporté principalement dans les axes suivants :

- Mise en place des techniques de caractérisation des capteurs piézorésistifs pour la mesure de la pression.
- Étude de la dérive thermique des capteurs piézorésistifs en fonction de la température et la pression.
- Développement d'un modèle analytique permettant d'extraire les valeurs de chaque piézoresistances sans dégradation de la sonde.
- Développement d'un modèle de simulation original permettant de reproduire les caractéristiques de la sonde en fonction de la température et de la pression.
- Compensation de la dérive thermique avec des circuits analogiques à bas coût.
- Miniaturisation de dispositif en vue d'une implantation dans des animaux comme la souris.

Synthèse de cette activité :

Avec l'augmentation des maladies chroniques et en particulier les maladies cardio-vasculaires

ces dernières années, le développement de capteurs biomédicaux performants est devenu indispensable pour lutter contre ces maladies. Le capteur de pression artérielle est l'un des capteurs très recherché pour collecter des paramètres biologiques dans des conditions de vie normale et sur une longue période.

En effet, lors des études précliniques de pharmacologie, de sécurité ou de toxicologie sur les animaux, les sociétés pharmaceutiques ont besoin de connaître avec précision leur température, leur activité et leur pression artérielle. Ces capteurs doivent être implantés pour pouvoir effectuer des mesures in-vivo en continu sur des animaux libres de leur mouvement pendant plusieurs semaines. Cette implantation entraîne par conséquent de fortes contraintes, telles l'encombrement, le poids, la capacité du module de traitement des données et de transmission sans fil, l'autonomie énergétique de l'ensemble et la précision des mesures in-vivo soumises à la fluctuation de la température corporelle des animaux.

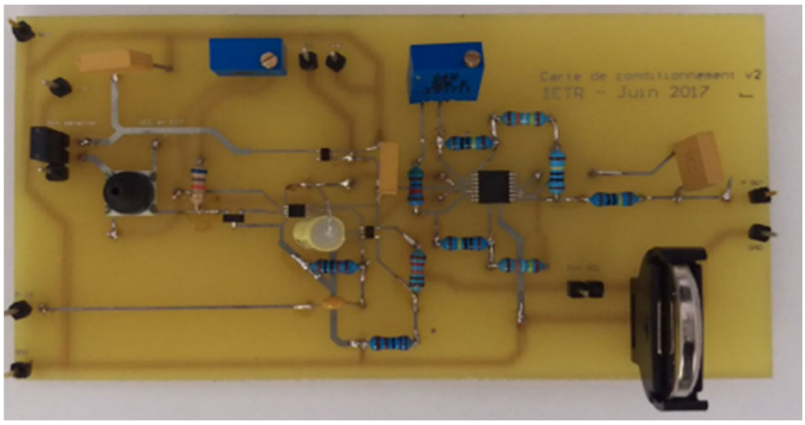

Figure 22 : Carte de conditionnement pour le test du capteur de pression réalisé à l'IETR avec la sonde NPB030 de Honeywell

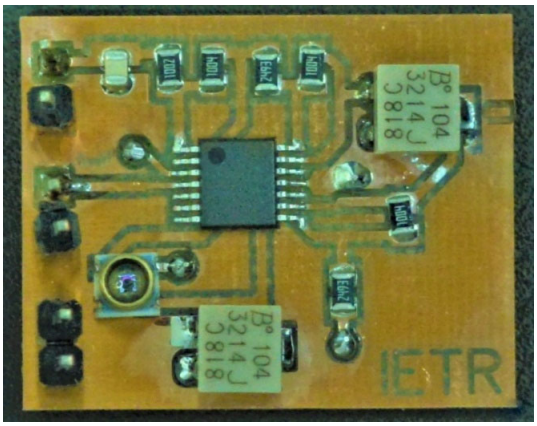

Figure 23 : Carte de conditionnement pour le test du capteur de pression miniaturisé réalisé à l'IETR avec la sonde HPSA 1100 [12]

La pression artérielle est l'un des paramètres le plus important mais aussi celui dont la mesure est la plus délicate car le point de mesure se situe dans une artère au contact du sang. Un des

problématiques majeurs de ces capteurs est la dérive aux variations de température trop importante comme le montre l'exemple de la figure 24. Ces études sont réalisées sur la sonde NPB030 de Honeywell (cf. figure 22) destinée pour les gros animaux (chat, chien…) et la sonde HPSA 1100 (cf. figure 23) pour les petits animaux (rat, souris...). Ces dérives sont liées à la variation de la température corporelle des animaux (de 1 °C à 2 °C pendant la journée) entrainant ainsi une dérive de plusieurs mmHg/°C et par conséquent des mesures de pressions instables dans le temps. La compensation analogique de cette dérive thermique est donc indispensable pour avoir des mesures précises et stables sur de longues périodes malgré des variations naturelles ou pathologiques de la température corporelle.

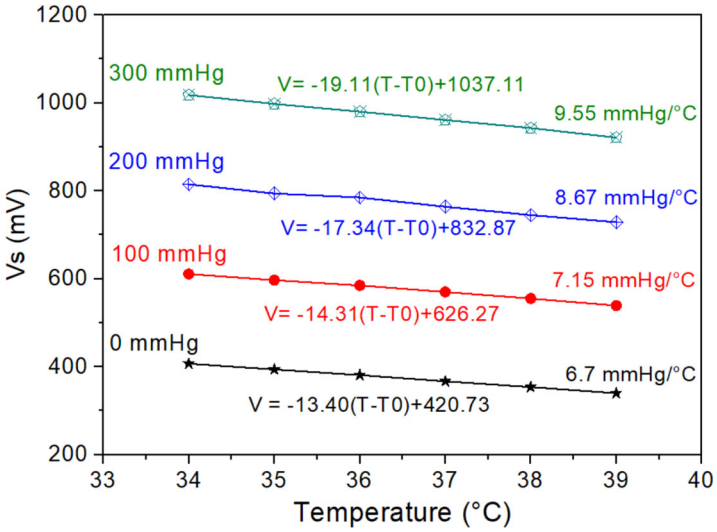

Figure 24: Tension de sortie du capteur montrant la dérive thermique en fonction de la pression

Pour atteindre une compensation efficace du capteur, une étude originale de l'extraction des valeurs des résistances de sondes piézorésistives a été réalisé puis implanté dans le logiciel de simulation Cadence/Pspice prenant en compte la variation de la sonde en fonction de la température et de la pression [12]. Ce travail nous a permis d'avoir un outil de simulation très fiable de capteurs piézorésistifs, permettant ainsi d'optimiser les circuits de compensation avant la réalisation, procurant un gain de temps très important et par conséquent le coût final du capteur.

Comme montré sur la figure 25, la correction de la dérive thermique est inévitable pour avoir des mesures stables et précises, l'avantage des techniques de compensation intégrées élimine le besoin d'un processus d'étalonnage coûteux et fastidieux pour chaque capteur à l'intérieur d'un lot fabriqué. Plusieurs circuits analogiques de compensation de la dérive thermique sont optimisés par simulation puis testés expérimentalement, nous présentons dans la figure 26, les résultats de mesures et simulations d'un exemple de circuit à base d'un transistor PNP.

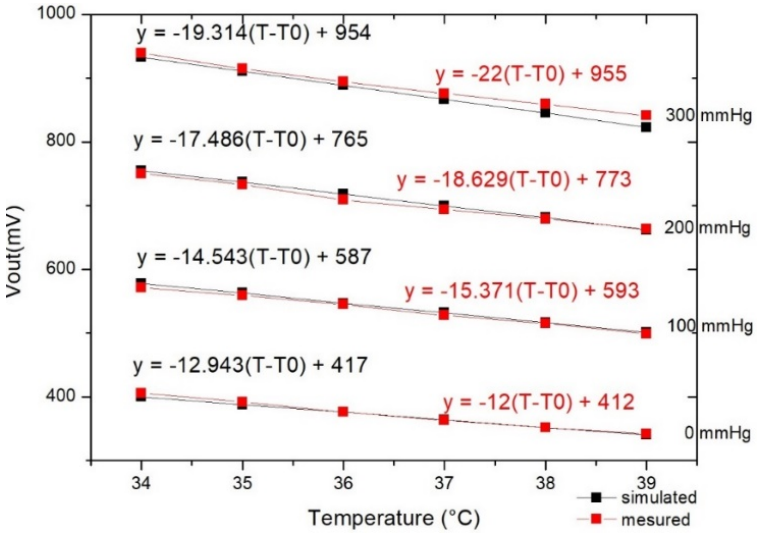

Figure 25: Résultats de mesures et simulations de la tension de sortie du capteur sans compensation

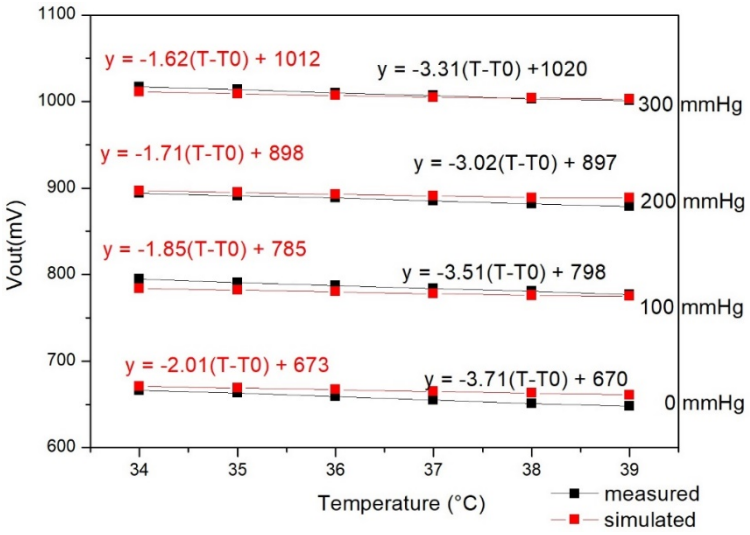

Figure 26 : Résultats de mesures et simulations de la tension de sortie du capteur compensé par un circuit analogique à base d'un transistor PNP

La seconde activité concerne l'étude et la réalisation des capteurs flexibles sur films minces piézoélectriques. Dans cette thématique, j'ai encadré une thèse (mon taux d'encadrement 50 %) qui vise l'étude et la réalisation d'une semelle connectée à base de capteurs piézoélectriques flexibles pour des applications médicales en lien avec un podologue à Nantes. Mon apport est essentiellement concentré sur les points suivants :

- Mise en place de circuit électronique autonome pour la caractérisation de la semelle connectée.
- Mise en place de la chaîne d'acquisition avec une transmission sans fil des données.
- Miniaturisation de dispositif complet pour l'intégration dans la chaussure.

Synthèse de cette activité :

L'étude de la marche représente un enjeu majeur dans le secteur médical, et ce, pour les différentes informations qu'elle peut fournir sur l'état de santé du patient. Plusieurs travaux de recherches sur les maladies chroniques ont montré qu'il existe une relation entre les troubles de la marche et l'apparition de certaines maladies ; les pieds creux par exemple sont d'origine neurologique et peuvent être des indicateurs de certaines maladies tels Parkinson et le diabète neuropathie, ils peuvent aussi provenir d'une blessure ou une fracture non traitée. Dans ce cadre, nous avons travaillé sur la réalisation d'un dispositif de suivi de la marche d'un patient afin de détecter précocement l'aggravation d'une maladie chronique telle que le diabète ou la Bronchopneumopathie Chronique Obstructive (BPCO) qui s'accompagnent de troubles de déambulation. L'originalité de ce travail réside à la fois dans l'approche de la conception du dispositif de suivi de la marche, car réalisée, d'une part, directement en concertation avec un médecin du CHU de Nantes et un podologue, puis d'autre part, dans la portabilité du dispositif qui devrait à terme permettre le suivi d'un patient à domicile.

Le système complet (cf. figure 27) réalisé représente une semelle connectée basée sur des capteurs piézoélectriques flexibles développés à l'IETR [13]. La propriété piézoélectrique de ces capteurs font qu'un signal électrique est engendré lors de l'application d'une contrainte mécanique. La récupération des signaux va se faire avec un système d'acquisition des données avec une transmission sans fil. Une étape de traitement et de conversion est nécessaire pour l'interprétation de l'information et l'affichage des données sur la plateforme développée dans le cadre de cette étude.

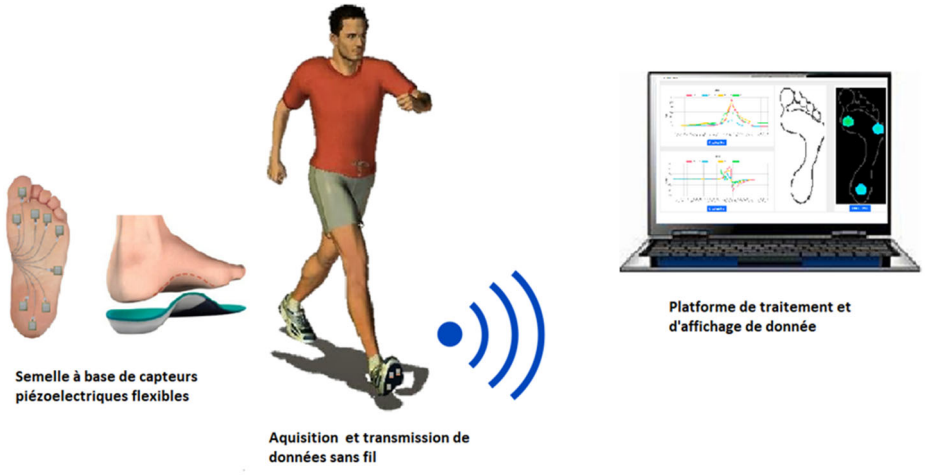

Figure 27 : Récapitulatifs du projet de réalisation de la semelle piézoélectrique connectée

La semelle connectée réalisée est montrée sur la figure 28, elle est branchée au système d'acquisition, constitué d'une carte de transmission ESP32, et de transmission de données pour envoyer les informations à la plateforme graphique web (cf. figure 29) correspondante en utilisant une transmission sans fil.

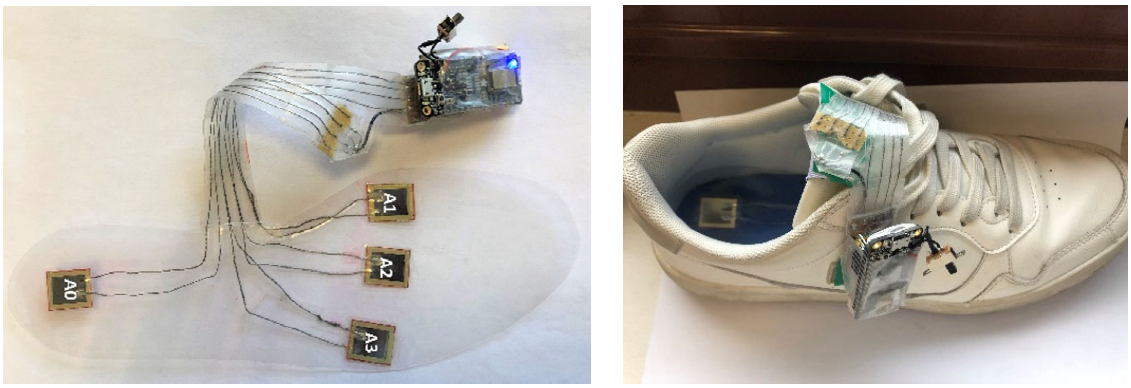

Figure 28 : Prototype de la semelle piézoélectrique connectée

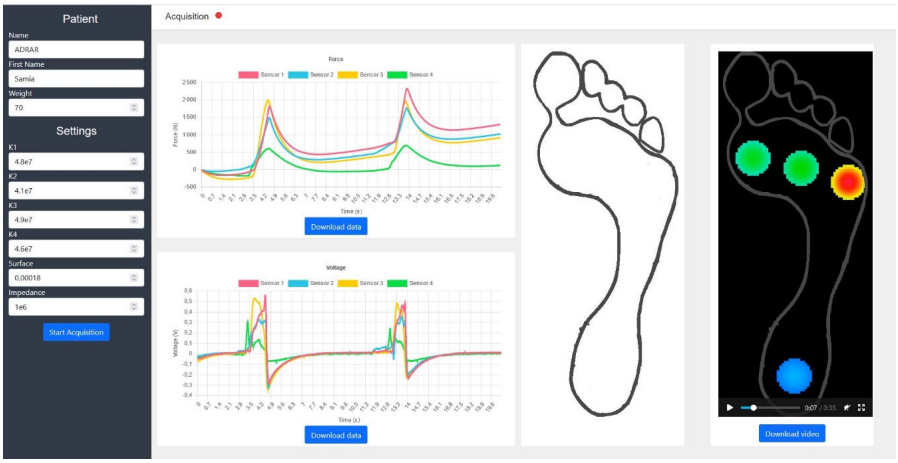

Figure 29 : Affichage des résultats sur la plateforme Web dévellopé à l'IETR

Les signaux à la sortie des capteurs permettent de tracer la courbe de la marche utilisée par les spécialistes de la santé pour détecter les anomalies. Cette courbe est obtenue après conversion des données en force, comme le montre la figure 30. Cette dernière figure, permet d'extraire la courbe qui représente le cycle de la marche, elle est obtenue à partir de l'extraction de la valeur maximale de la force enregistrée pour les quatre capteurs de la figure 31 à l'instant t.

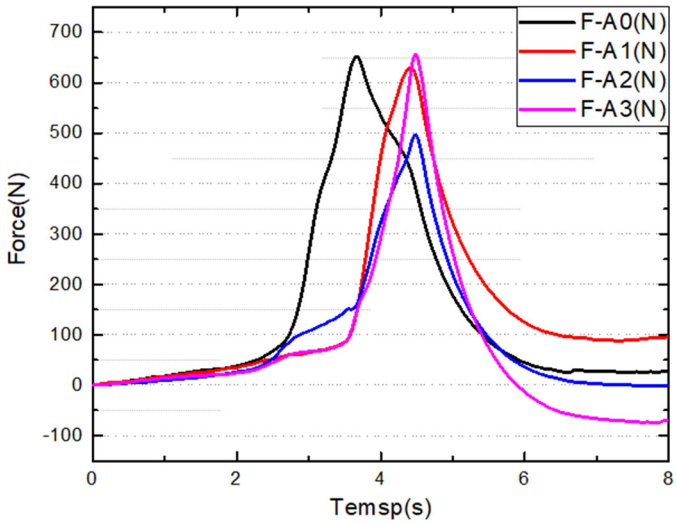

Figure 30 : Courbe de la marche illustrée en force en fonction de temps enregistrée par le système

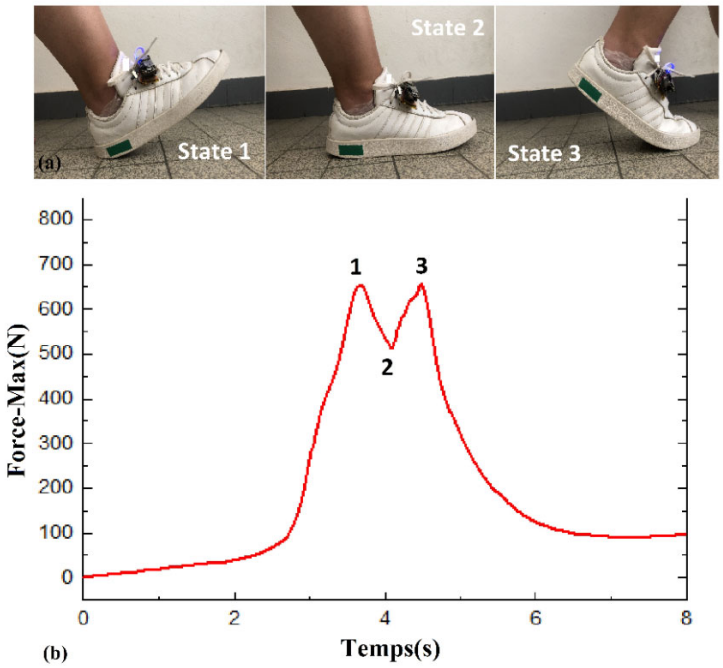

Figure 31 : Représentation : (a) des trois étapes d'une marche et (b) la courbe du cycle de marche correspondante

La courbe d'évolution du cycle de la marche représente la progression du pied dans les différentes phases de la progression du pas :

- Le premier état correspond au moment où le pied entre en contact avec le sol par le talon, la force de réaction est dans ce cas approximativement égale au poids du corps à vitesse normale et pendant cette phase le centre de gravité se situe derrière le talon.
- Le deuxième état, les pieds sont à plat sur la surface, la pression est alors dispersée dans tout le pied et le centre de gravité se déplace au centre du pied provoquant ainsi une petite baisse de force représentée par le M sur le graphique.
- Le dernier état, appelé aussi phase propulsive dans laquelle toute la pression est déplacée vers l'avant du pied remontant ainsi vers le poids initial de la personne et positionnement d'un nouveau centre de gravité.

Les tests et analyses effectués sur une personne ne présentant pas de troubles de marche ont permis au spécialiste d'identifier un modèle qui reconstitue le déroulement du cycle de marche. Ce modèle sert à comparer les différents cycles, à identifier les anomalies et à intervenir rapidement et plus efficacement.

4.4 Autre thématique en lien avec les hyperfréquences : Formulations et caractérisations des mélanges thermoplastiques souples comme substrats d'antennes

Dans le cadre d'une thèse Cifre avec l'entreprise MCCP France, j'ai encadré une thèse (mon taux d'encadrement : 50 %) qui portait sur la mise en place des mélanges thermoplastiques souples pour des applications antennaires. Dans ce cadre, j'ai apporté mon expertise dans le domaine des

hyperfréquences en particulier la caractérisation diélectrique, jusqu'à 40 GHz, des films flexibles obtenus de plusieurs mélanges thermoplastiques souples optimisés et réalisés dans le cadre de cette étude. La connaissance de ces propriétés diélectriques en haute fréquence est indispensable avant le design et la fabrication de l'antenne. La technique utilisée pour déterminer ces dernières est celle des anneaux résonateurs avec un guide d'onde coplanaire par le biais de la station sous pointes équipées des sondes coplanaires comme le montre la figure 32. L'extraction de la permittivité relative et la tangente de pertes du composite est faite à partir des mesures du coefficient de transmission S12 en fonction de la fréquence (cf. figure 32).

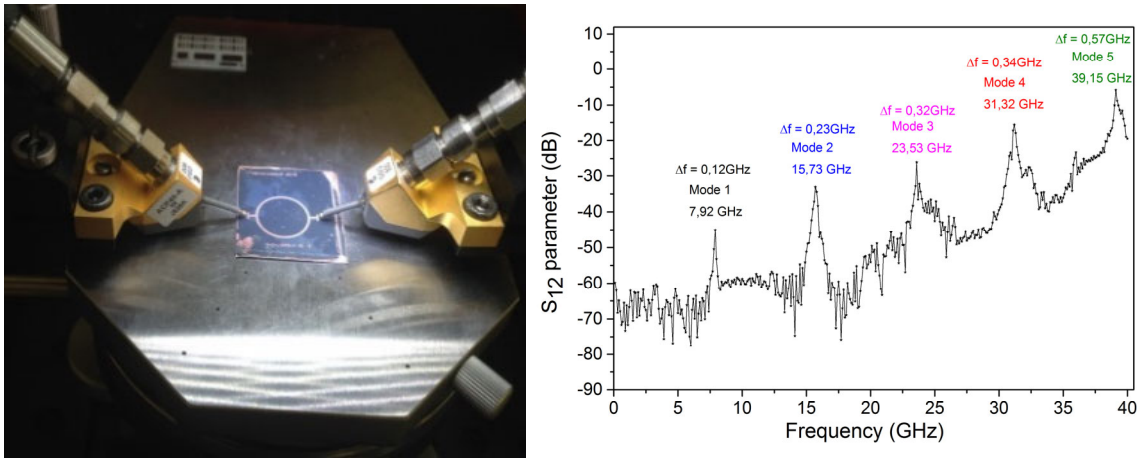

Figure 32 : Configuration de la mesure et résultat de la mesure du coefficient de transmission (S_{12}) obtenu par la méthode des anneaux résonateurs.

La figure 33 montre un exemple de résultat de caractérisation diélectrique de plusieurs formulations (le polyéthylène à haute densité (PEHD), le polyéthylène à basse densité (PEBD) et le polypropylène statique (r-PP)) testés dans le cadre de cette étude [14].

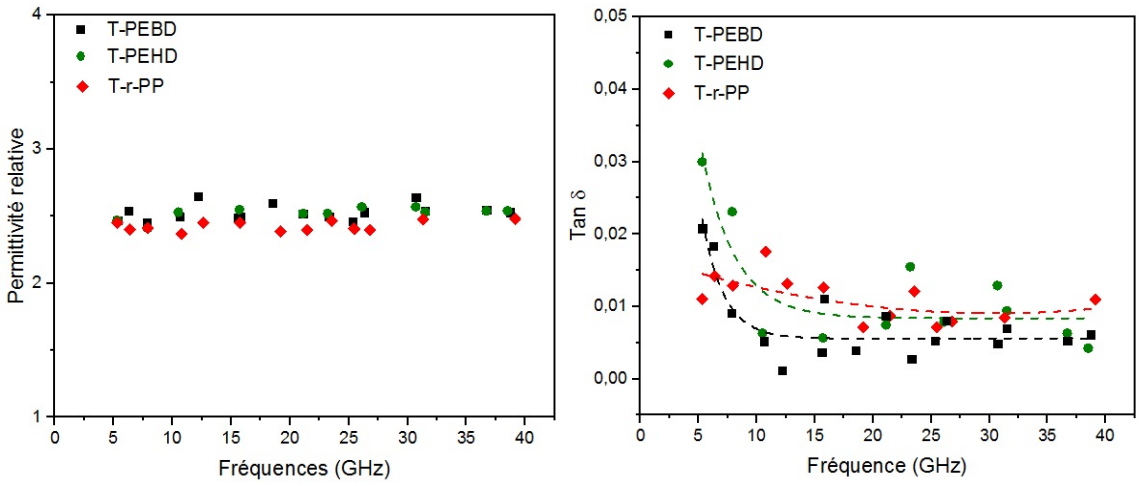

(a) (b)

Figure 33 : Propriétés diélectriques (a) permittivité relative (b) tan δ des mélanges T-PEBD, T-PEHD et T-r-PP [14]

Une optimisation et caractérisation de plusieurs types d'antennes dans la bande X (8 GHz – 12 GHz) est réalisées à partir des films développés et caractérisés dans cette étude. Ces mesures ont permis de valider le protocole de fabrication de l'antenne mis en place. La mesure du coefficient de réflexion S_{11} de l'antenne T-r-PP est en très bon accord avec les simulations HFSS (cf. figure 34). La figure 34 montre également les diagrammes de rayonnement de l'antenne planaire à base de T-r-PP. Les composantes principales et croisées ont été tracées dans les deux plans de l'antenne E et H. Nous notons deux larges lobes centraux en composantes principales pour les plans H et E. Les valeurs négatives en dessous de -20 dB en composantes croisées confirment bien la polarisation linéaire de l'antenne planaire fabriquée.

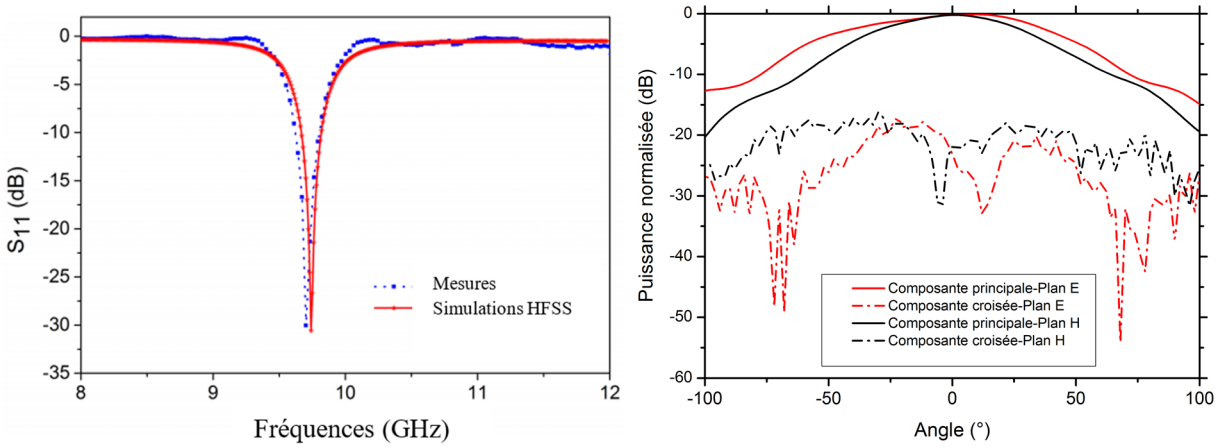

Figure 34 : Mesure et simulation HFSS du coefficient de réflexion S11 et le diagramme de rayonnement de l'antenne planaire à base de T-r-PP

5 Autres activités scientifiques

- Membre du comité scientifique et du comité d'organisation de la Journée du Club Optique et Micro-Ondes (JCOM 2015) de la Société Française d'Optique à Nantes le 12 juin 2015, avec 65 participants.

- Membre du comité d'organisation du Workshop on Advanced ADCs à La Baule le 16 décembre 2015, dont deux participants de la DGA, deux de Thales, un de l'Université de Paris VI (UPMC), un de Drexel University (Philadelphie, USA) et deux de l'Université de Nantes.

- Membre du comité scientifique de la conférence internationale "International Conference on Computing and Wireless Communication systems (ICCWCS)" depuis 2017 à ce jour (autour de 200 participants/an).

- Membre du comité scientifique de la conférence internationale "International Conference on Functional Materials and Renewable Energies (COFMER)", depuis 2019 à ce jour (autour de 150 participants).

- Président du comité scientifique et du comité d'organisation de la Journée des Doctorants (JDOC) de l'École Doctorale MathSTIC (MASTIC) à Nantes depuis 2022, avec plus de 70 présentations orales et posters chaque année.

- Présentation du projet "capteurs de pression artérielle sans fil implantables de grande précision et autonomie" lors de la première Rencontre Innovation autour du thème "Dispositifs médicaux" organisé par l'Université de Nantes et le Centre Hospitalier Universitaire de Nantes le 3 Juillet 2018.

  (https://www.univ-nantes.fr/developper-votre-entreprise/rencontres-innovation-dispositifs-medicaux-1ere-edition)

- Communication, auprès de plusieurs représentants industriels, présentée au World Electronics Forum 2017 à Angers :

  R. Seveno, T. Dufay, B. Guiffard, **M. El Gibari**, J. Le Scornec, J-C. Thomas, P.J. Cottinet, M. Lallart, L. Petit, V. Le Cam, "Flexible Electro-Active Materials", World Electronics Forum 2017, 24-28 Octobre 2017, Angers, France. (Id : hal-01714979)

- Relecture pour plusieurs revues internationales :

  IEEE Microwave and Wireless Components Letters,
  Journal of Infrared, Millimeter, and Terahertz Waves,
  Journal of Engineering Research and Reports,
  Sensors and Actuators: A. Physical
  Sensors, MDPI
  Biomedical Signal Processing and Control
  European Microwave Week (EuMW 2024 et 2025)

6 Publications et production scientifique (noms des doctorants soulignés)

Articles dans des revues internationales à comités de lecture	20
Chapitre dans ouvrage	1
Brevet international	1
Communications dans des conférences internationales à comité de lecture avec acte	46
Communications dans des conférences nationales à comité de lecture avec acte	4
Communications dans des conférences nationales	14

6.1 Articles dans des revues internationales à comités de lecture référencées

1. **M. El Gibari**, D. Averty, C. Lupi, H. W. Li and S. Toutain "Ultra-wideband GCPW-MS-GCPW driven electrode for low-cost and wide range application electro-optic modulators", *Microwave and Optical Technology Letters*, Vol. 52, issue 2, pp. 1078-1082, Mai 2010. (doi: 10.1002/mop.25112)
2. **M. El Gibari**, D. Averty, C. Lupi, M. Brunet, H. W. Li and S. Toutain "Ultra-broad bandwidth and low-loss GCPW-MS transitions on low-k substrates", *Electronics Letters*, Vol. 46, issue 13, pp. 931-933, 2010. (doi: 10.1049/el.2010.0986)
3. **M. El Gibari**, D. Averty, C. Lupi, H. W. Li and S. Toutain "Ultra-wideband GCPW-MS transitions to characterize components based on thin polymer", *Electronics Letters*, Vol. 47, issue 9, pp. 553-555, 2011. (doi: 10.1049/el.2010.3745)
4. **M. El Gibari**, D. Averty, M. Hlabwax, J-P. Vilcot and H. W. Li, "Comprehensive study of ultra-broadband GCPW-MS transition on thin films", *Microwave and Optical Technology Letters*, Vol. 57, issue 9, pp. 2041-2045, 2015. (doi: 10.1002/mop.29273)
5. M. Hadjloum, **M. El Gibari**, S. Ginestar, H. W. Li, A. S. Daryoush, "Via-Hole Less Broadband Grounded Coplanar to Coupled Microstrip Transition for up to 40 GHz", *Progress In Electromagnetics Research Letters*, vol. 56, pp.47-51, 2015. (doi:10.2528/PIERL15060404)
6. **M. El Gibari**, D. Averty, M. Halbwax, J.-P. Vilcot, H. W. Li, "Comprehensive study of ultra-broadband GCPW-MS transitions on thin films", *Microwave and Optical Technology Letters,* vol. 57, n° 9, pp. 2041-2045, 2015. (doi: 10.1002/mop.29273)
7. M. Hadjloum, **M. El Gibari**, H. W. Li et A. S. Daryoush, "An ultra-wideband dielectric material characterization method using grounded coplanar waveguide and genetic algorithm optimization", *Applied Physics Letters*, vol. 117, issue 14, pp. 142908, 2015. (https://doi.org/10.1063/1.4933019)
8. **M. El Gibari**, H. W. Li, "A Comparative Study between Via-Hole and Via-Free Grounded Coplanar Waveguide to Microstrip Transitions on Thin Polymer Substrate", *International Journal of Antennas and Propagation*, vol. 2015, Article ID 481768, 7 pages, 2015. (http://dx.doi.org/10.1155/2015/481768)

9. M. Hadjloum, **M. El Gibari**, H. W. Li, A. S. Daryoush, "Design challenges of EO polymer based leaky waveguide deflector for 40 Gs/s all-optical analog-to-digital converters", *Optics Communications,* vol. 373, pp. 82-90, 2016. (https://doi.org/10.1016/j.optcom.2015.10.009)
10. M. Hadjloum, **M. El Gibari**, H. W. Li, A. S. Daryoush, "Leaky waveguide deflector for 40 Gs/s all-optical analog-to-digital converters", *Journal of The Franklin Institute,* vol. 354, pp. 8710-8720, 2017. (http://dx.doi.org/10.1016/j.jfranklin.2016.10.042)
11. M. Hadjloum, **M. El Gibari**, H. W. Li, A. S. Daryoush, "Broadband Capacitively Grounded Coplanar to Coupled Microstrip Transition for Planar Microwave Photonic Components", *International Journal of Microwave and Wireless Technologies*, vol. 9, issue 4, pp. 815-819, 2017. (https://doi.org/10.1017/S1759078716000969)
12. K. Receveur, K.Wei, M. Hadjloum, **M. EL Gibari**, A. De Rossi, H.W. Li, A. S. Daryoush, "Sensitivity improvement of broadband electro-optic polymer-based optical phase modulator using 1D and 2D photonic crystal structures", *Chinese Optics Letters, OSA Publishing*, vol. 15, issue 1, pp. 010003 (5 pages), 2017. (doi: 10.3788/COL201715.010003)
13. M. Hadjloum, **M. El Gibari**, H. W. Li, A. S. Daryoush, "Improvement of both Bandwidth and Driving Voltage of Polymer Phase Modulators Using Buried In-Plane Coupled Micro-Strip Driving Electrodes", *Journal of Applied Physics*, vol. 121, issue 23, 0.1063/1.4985285, 2017. (http://dx.doi.org/10.1063/1.4985285)
14. D. Palessonga, **M. El Gibari**, S. Ginestar, H. Terrisse, B. Guiffard, A. Kassiba and H. W. Li "Bandwidth Improvement of Microwave Photonic Components Based on Electro-Optic Polymers loaded with TiO2 Nanoparticles", *Applied Physics A*, vol. 123, issue 8, Article 542, 2017. (https://doi.org/10.1007/s00339-017-1154-4)
15. R. Seveno, T. Dufay, **M. El Gibari**, B. Guiffard, H. W. Li, S. Morsli, A. Pichon et E. Tanguy, "Teach the basics of electricity by the use of a flexible piezoelectric generator", *Physics Education, IOP Publishing*, 2018, 53 (4), pp.045015. (doi: 10.1088/1361-6552/aabf27)
16. B. Guiffard, M. Saadeh, P. Frère, R. Seveno, **M. El Gibari**, T. Sghaier, V. Merupo et A. Kassiba "Potentialities of flexoelectric effect in soft polymer films for electromechanical applications", *Journal of Physics: Conference Series, IOP Publishing,* 2019, 1322, pp.012041. (doi: 10.1088/1742-6596/1322/1/012041)
17. T. Sghaier, **M. El Gibari** et B. Guiffard, "New low loss soft thermoplastic blends for microwave applications", *Journal of Physics D: Applied Physics, IOP Publishing*, 2020, 53 (13), pp.135003. (doi: 10.1088/1361-6463/ab5756)
18. P. -V. Dugue, **M. El Gibari**, M. Halbwax, S. Ginestar, V. Avramovic, J.-P. Vilcot et H. W. Li, "A new equivalent circuit scheme for grounded back-to-back GCPW-MS-GCPW transitions fabricated on a thin low-k substrate", Progress In Electromagnetics Research Letters, vol. 95, pp.33-42 56, 2021. (doi: 10.2528/PIERL20093003)
19. S. Adrar, **M. El Gibari**, P. Saillant, J-C Thomas et R. Seveno, " Development of flexible piezoelectric sole with wireless communication for medical application", *Biomedical Signal Processing and Control,* vol. 85, 104878, ISSN 1746-8094, 2023. (doi : https://doi.org/10.1016/j.bspc.2023.104878)
20. **M. El Gibari**, S. M. D. Mbacke, B. Lauzier, C. Gauthier et H. W. Li, " A simple and effective method to compensate the thermal drift of implantable blood pressure sensors", *Sensors and Actuators A: Physical,* vol. 376, 115615, ISSN 0924-4247, 2024. (doi : https://doi.org/10.1016/j.sna.2024.115615)

6.2 Ouvrage

1. **M. El Gibari**, D. Averty, C. Lupi, Y. Mahe, H. W. Li et S. Toutain, "Coplanar-microstrip

transitions for ultra-wideband communications", INTECH, Chapitre dans ouvrage "Ultra Wideband Communications: Novel Trends", 2011. (doi: 10.5772/16893)

6.3 Brevet

M. El Gibari (40%), S. Toutain (15%), H. W. Li (15%), D. Averty (15%), C. Lupi (15%), "Composant hyperfréquence commandé par un système d'électrodes coplanaires blindées, et procédé de fabrication correspondant", Brevet international WO2013186316A1 : dépôt en France par l'Université de Nantes le 13 juin 2012 et publication le 07 mai 2015 (US20150125107A1)

6.4 Conférences internationales à comités de lecture et actes

1. **M. El Gibari**, C. Lupi, D. Averty et H. W. Li, "Optimisation des paramètres de réalisation d'un modulateur électro-optique à Base de Polymères pour les télécommunications à fibre" *Congrès Méditerranéen des Télécommunications et exposition (CMT 2008)*, Mars 2008, Tanger, Maroc. (Id : hal-01149980)
2. **M. El Gibari**, D. Averty, C. Lupi, H. W. Li and S. Toutain "Ultra-wideband GCPW-MS-GCPW transitions on Si wafers for microwave photonic components", *17th Telecommunications Forum TELFOR 09*, 24-26 November 2009, Belgrade, Serbia. (ISBN 978-86-7466-375-2).
3. **M. El Gibari**, D. Averty, C. Lupi, H. W. Li and S. Toutain "Improvement of the performances of GCPW transmission lines and GCPW-MS transitions on low permittivity substrates for broadband applications", *5th International Conference on Microwaves, Antenna Propagation and Remote Sensing (ICMARS - 2009)*, 19-21 December 2009, Jodhpur, India. (Id: hal-01150170)
4. **M. El Gibari**, Y. Mahé, D. Averty, C. Lupi, H. W. Li "Ultra-wideband transitions for connectorizing microwave photonic components based on thin polymer and driven by microstrip electrode", *IEEE MTT-S German Microwave Conference (GeMiC 2011)*, 14-16 Mars 2011, Darmstadt, Allemagne. (ISBN:978-3-9812668-2-5)
5. **M. El Gibari**, Y. Scudeller, J.P. Landesman "Investigating thermal proprieties of GaAs / INP laser diode structures with a pulsed technique", *Proceedings in the 17th International Worshop on Thermal Investigations of ICs and Systems*, Paris, France, 27-29 September 2011. (ISBN: 978-2-35500-018-8).
6. **M. El Gibari**, C. Lupi, Y. Scudeller, J.P. Landesman "Optical spectroscopy for thermal diagnostic of GaAs / INP laser diodes", *Proceedings in the 17th International Worshop on Thermal Investigations of ICs and Systems*, Paris, France, 27-29 September 2011. (ISBN: 978-2-35500-018-8).
7. M. Hadjloum, **M. El Gibari**, H. W. Li, A. S. Daryoush "Leaky Waveguide Deflector for 40 GS/s All-Optical ADC" *2014 IEEE Benjamin Franklin Symposium on Microwave and Antenna Sub- Systems for Radar, Telecommunications, and Biomedical Applications* (BenMAS 2014), 26 Sept. 2014, Philadelphie, USA. (Doi: 10.1109/BenMAS.2014.7529454)
8. M. Hadjloum, **M. El Gibari**, H.W. Gundel, H.W. Li, A.S. Daryoush "Ultra-Wideband GCPW-CMS-GCPW Transition for Characterization of All-optical ADCs Based on Leaky Waveguide Deflector", *22nd Telecommunications Forum (TELFOR 2014)*, 25-27 November 2014, Belgrade, Serbia. (Doi: 10.1109/TELFOR.2014.7034423)
9. M. Hadjloum, **M. El Gibari**, M. Halbwax, J.-P. Vilcot, H. W. Li, A. S. Daryoush, "40 GSPS All Optical ADC with ENOB of 6.6 using EO Polymer Optical Deflector and Spatial Quantizer", *IEEE Microwave Photonics,* 25-29 Oct. 2015, Paphos, Chypres. (doi: 10.1109/MWP.2015.7356670)

10. **M. El Gibari**, S. Bretin, M. Hadjloum, P. Derval, H. W. Li, **"**Coplanar Waveguide to Microstrip Transition in Thin Polymer Film for Characterization and Packaging of Microwave Photonic Components", *IEEE TELFOR*, Nov. 2015, Belgrade, Serbie. (doi: 10.1109/TELFOR.2015.7377537)

11. M. Hadjloum, **M. El Gibari**, H. W. Li, A. S. Daryoush, "Electrode Structure for both Poling and Driving of the Electro-Optic Polymer in an Analog-to-Digital Converter based on an Optical Deflector", *IEEE TELFOR*, Nov. 2015, Belgrade, Serbie. (doi: 10.1109/TELFOR.2015.7377531)

12. D. Palessonga, **M. El Gibari**, S. Ginestar, H. Terrisse, B. Guiffard, A. Kassiba, H. W. Li, "Tuning of Microwave and Optical Properties of the Electro-Optic Polymer PMMA-DR1 by Loading with SiC Nanoparticles for Optimization of Photonic Microwave Components", *IEEE TELFOR 2015*, 24-25 Nov. 2015, Belgrade, Serbie. (doi: 10.1109/TELFOR.2015.7377523)

13. M. Hadjloum, **M. El Gibari**, G. Lirzin, H. W. Li, A. S. Daryoush, "Study of an Electro-Optic Polymers Leaky Waveguide Deflector and its Microwave access across a GCPW to CMS transition for realizing a 40 GSPS AOADC", *IEEE International Conference on Microwave and Photonics (ICMAP 2015)*, 11-13 Dec. 2015, Dhanbad, Inde. (doi: 10.1109/ICMAP.2015.7408700)

14. **M. El Gibari**, M. Hadjloum, H. W. Li, **"**Conductor-Backed Coplanar Waveguide to Microstrip Transition on BCB Polymer Thin Film with Bandwidth over 60 GHz", *IEEE ICMAP 2015*, 11-13 Dec. 2015, Dhanbad, Inde. (doi: 10.1109/ICMAP.2015.7408757)

15. M. Hadjloum, **M. El Gibari**, H. W. Li, A. S. Daryoush, "Microwave and Optical Design Optimization of Polymer Phase Modulators with Over 40 GHz BW", *IEEE ICMAP 2015*, 11-13 Dec. 2015, Dhanbad, Inde. (doi: 10.1109/ICMAP.2015.7408725)

16. M. Hadjloum, **M. El Gibari**, H. W. Li, A. S. Daryoush, "Study of an Electro-Optic Leaky Waveguide Deflector for Application in All-Optical Analog-to-Digital Converters", *Progress In Electromagnetics Research Symposium* (PIERS 2016), 8-11 Aug. 2016, Shanghai, China. (doi: 10.1109/PIERS.2016.7734907)

17. **M. El Gibari**, S. Bretin, M. Hadjloum, P. Derval, G. Lirzin, H. W. Li, "Design and realization of high-performance microwave and millimeter wave band-pass filters on thin polymer films", *PIERS* 2016, 8-11 Aug. 2016, Shanghai, China. (doi: 10.1109/PIERS.2016.7735362)

18. D. Palessonga, **M. El Gibari**, S. Ginestar, H. Terrisse, B. Guiffard, A. Kassiba, H. W. Li, "TiO_2 Nanoparticles Loading on the Microwave and Optical Properties of the Electro-Optic Polymer PMMA-DR1 for Optimization of Microwave Photonic Components", *PIERS* 2016, 8-11 Aug. 2016, Shanghai, China. (doi: 10.1109/PIERS.2016.7734349)

19. **M. El Gibari**, S. Bretin, P. Derval, S. Ginestar, G. Lirzin, H. W. Li, "Conception and realization of highly selective band-pass filters in Ka-band built on thin polymer films", *IEEE International Conference on Microelectronics* (ICM), 10-13 Dec. 2017, Beirut, Lebanon. (doi: 10.1109/ICM.2017.8268896)

20. **M. El Gibari**, C. Le Bleis, G. Lirzin, B. Lauzier, S. Ginestar, J. Tissier, M. Latrach, C. Gautier, H. W. Li, "Thermal drift compensation of piezoresistive implantable blood pressure sensors with low cost analog solutions", *IEEE International Conference on Microelectronics* (ICM), 10-13 Dec. 2017, Beirut, Lebanon. (doi: 10.1109/ICM.2017.8268895)

21. Y. Ouellaf, **M. El Gibari**, P. Bertoncini, E. Abisset-Chavanne, O. Chauvet et H. W. LI, "Functional properties improvement of electro-optic polymers by loading them with nanoparticles", *French-Australian Friendly: Advanced Materials Workshop, 30* Juin 2017, Le Mans. (Id : hal-01830933)

22. P. -V. Dugue, **M. El Gibari**, J.-P. Vilcot et H. W. Li, “Study of the near field from an electro-optic leaky waveguide for application in all-optical analog-to-digital converters”, *PhotonIcs & Electromagnetics Research Symposium (PIERS)*, Juin 2019, Rome, Italy. (Id : hal-02166906)

23. P. -V. Dugue, **M. El Gibari**, M. Halbwax, M. Hadjloum, J.-P. Vilcot et H. W. Li, "A new method of dielectric characterization using a genetic algorithm and a coplanar waveguide on bilayer films", *PhotonIcs & Electromagnetics Research Symposium (PIERS)*, Juin 2019, Rome, Italy. (Id : hal-02166881)

24. J. Le Scornec, **M. El Gibari,** R. Seveno, B. Guiffard et V. Le Cam, " Influence de la structure des électrodes interdigitées sur les micro-générateurs piézoélectriques", *International Conference on Functional Materials and Renewable Energies (COFMER'03),* Apr 2019, Marrakech, Maroc. (Id : hal-02108527)

25. R. Seveno, T. Dufay, B. Guiffard, J. Le Scornec, **M. El Gibari,** S. Carpy, J. –C. Thomas, P. –J. Cottinet, M. Lallart, L. Petit et V. Le Cam, "Films piézoélectriques flexibles pour la récupération d’énergie", *International Conference on Functional Materials and Renewable Energies (COFMER'03),* Apr 2019, Marrakech, Maroc. (Id : hal-02108475)

26. R. Seveno, J. Le Scornec, B. Guiffard, V. Le Cam, **M. El Gibari,** J. –C. Thomas, P. –J. Cottinet, M. Lallart et L. Petit, "Flexible PZT thin films prepared by Chemical Solution Deposition process", *International Workshop on Piezoelectric Materials and Applications in Actuators 2019 (IWPMA2019),* Oct 2019, Lyon, France. (Id : hal-02316660)

27. T. Sghaier, **M. El Gibari** et B. Guiffard, "Ring resonator characterization at microwave frequencies of a novel soft dielectric", *PhotonIcs & Electromagnetics Research Symposium (PIERS)*, Juin 2019, Rome, Italy. (Id : hal-02172039)

28. T. Sghaier, **M. El Gibari** et B. Guiffard, "Characterization methodology up to 40 GHz of new low loss soft dielectric thermoplastic films for microwave applications", *2019 International Conference on Electromagnetics in Advanced Applications (ICEAA),* Sept 2019, *pp.1296-1299, Granada, Spain*. (doi : 10.1109/ICEAA.2019.8878915)

29. P. -V. Dugue, **M. El Gibari**, k. Heggarty, C. Larat, J.-P. Vilcot et H. W. Li, "In depth study of optical behavior of a novel leaky waveguide deflector", *IEEE Telecommunications Forum TELFOR 2020*, 24-25 Nov. 2020, Belgrade, Serbia. (doi: 10.1109/TELFOR51502.2020.9306629)

30. S. M. D. Mbacke, **M. El Gibari**, B. Lauzier, C. Gauthier et H. W. Li, "Analog, compact and economical solution for the compensation of implantable piezoresistive blood pressure sensors for wireless medical monitoring", *IEEE Telecommunications Forum TELFOR 2020*, 24-25 Nov. 2020, Belgrade, Serbia. (doi: 10.1109/TELFOR51502.2020.9306571)

31. S. M. D. Mbacke, **M. El Gibari**, B. Lauzier, C. Gauthier et H. W. Li, "Cost-effective and compact analog compensation method of thermal drift of implantable piezoresistive blood pressure sensors", *SI: Printemps de la cardiologie 2020 (Digital conference)*, vol. 12 (2-4), pp.218-219, Oct 2020, Grenoble, France. (doi: 10.1016/j.acvdsp.2020.03.050)

32. Z. Jradi, **M. El Gibari**, H. W. Li et O. Chauvet, "Electro optic nanocomposites for high performance microwave photonic applications", *IEEE Telecommunications Forum TELFOR 2020*, 24-25 Nov. 2020, Belgrade, Serbia. (doi: 10.1109/TELFOR51502.2020.9306635)

33. Z. Jradi, **M. El Gibari**, H. W. Li et O. Chauvet, "Electro-optic nanocomposites for high performance microwave photonic applications", *C’Nano 2020, Nov 2021, Toulouse, France.* (Id : hal-03512523)

34. S. M. D. Mbacke, **M. El Gibari**, B. Lauzier, C. Gauthier et H. W. Li, "Implantable Blood Pressure Sensors with Analogic Thermal Drift Compensation", *8th International Symposium*

on Sensor Science, May 2021, Dresde (Fully online event), Germany. pp.34. (doi: 10.3390/I3S2021Dresden-10126)

35. S. Adrar, **M. El Gibari**, P. Saillant, A. Chambellan, M. Jubeau et R. Seveno, "Flexible Piezoelectric Thin Films for Podiatric Sensors with Wireless Communication", *8th International Symposium on Sensor Science,* May 2021, Dresde (Fully online event), Germany. pp.48. (doi: 10.3390/I3S2021Dresden-10127)
36. S. Adrar, **M. El Gibari**, M. Yoen, J. C. Thomas et R. Seveno, "Mechanical characterization of a piezoelectric sensor for podiatrist applications", *IEEE International Systems Conference (SysCon), 25-28* April 2022, Montreal, Canada. (doi: 10.1109/SysCon53536.2022.9773897)
37. M. Khaiaf-Belghiti, **M. El Gibari**, A. Rhallabi et A. El Fallah-Serghrouchni, "Development and Optimization of Gas Sensors for Ammonia detection", *IEEE Telecommunications Forum TELFOR 2024*, 26-27 Nov. 2024, Belgrade, Serbia. (doi: 10.1109/TELFOR63250.2024.10819182)
38. A. Bakkali, J. Zbitou, **M. El Gibari**, A. Oukaira et S. Khoulji, "A New Configuration Diplexer for RF Harvesting Applications", *International Conference on Functional Materials and Renewable Energies (COFMER'05)*, April 15-17th, 2025, Tanger, Maroc. (doi.org/10.1051/epjconf/202532601003)
39. S. El Maimouni, F. Aytouna, J. Zbitou, **M. El Gibari**, et S. Khoulji, "A Novel Configuration of a Reconfigurable Planar BandPass Filter For Wireless Power Transfer", *International Conference on Functional Materials and Renewable Energies (COFMER'05)*, April 15-17th, 2025, Tanger, Maroc. (doi.org/10.1051/epjconf/202532601004)
40. Y. Esshaimi, F. Aytouna, J. Zbitou, **M. El Gibari**, et R. Er-rebyiy, "Design of RFID Tag Antenna for Logistics Applications in the Renewable Energy Sector", *International Conference on Functional Materials and Renewable Energies (COFMER'05)*, April 15-17th, 2025, Tanger, Maroc. (doi.org/10.1051/epjconf/202532605008)
41. Z. Errachidi, J. Zbitou, **M. El Gibari**, et N. Chahboun, "Novel UHF RFID Tag Structure Based on Polycarbonate Material, for Renewable Energy Applications", *International Conference on Functional Materials and Renewable Energies (COFMER'05)*, April 15-17th, 2025, Tangier, Maroc. (doi.org/10.1051/epjconf/202532605009)
42. B. Laakel Stinou, J. Zbitou, **M. El Gibari**, A. Oukaira, S. Ginestar et A. Lakhssassi, "A Design of a Compact Coplanar Low Pass Filter for THz applications ", International Conference on Innovative Research in Applied Science, Engineering and Technology (IRASET 2025), 15 - 16 May 2025, Fez, Morocco. (doi: 10.1109/IRASET64571.2025.11008092)

À paraitre en 2025 :

43. Z. Errachidi, J. Zbitou, **M. El Gibari**, M. Mashagbeh et N. Chahboun, "A Novel Miniature Circular Eye-inspired UHF RFID Tag Antenna Design", PhotonIcs & Electromagnetics Research Symposium (PIERS 2025), 4 - 8 May 2025, Abu Dhabi, UAE.
44. M. Guermal, J. Zbitou, **M. El Gibari**, F. Aytouna, A. Oukaira et A. Lakhssassi, "A Novel Design and Optimization of a Multi-section Coupler for Microwave Radar Systems", PhotonIcs & Electromagnetics Research Symposium (PIERS 2025), 4 - 8 May 2025, Abu Dhabi, UAE.
45. A. Bakkali, J. Zbitou, **M. El Gibari**, A. Oukaira et S. Khoulji, "Novel Design of a 5.8 GHz Bandpass Filter for RF Energy Harvesting Applications", PhotonIcs & Electromagnetics Research Symposium (PIERS 2025), 4 - 8 May 2025, Abu Dhabi, UAE.

46. M. Khaiaf-Belghiti, **M. El Gibari**, B. El khamlichi, A. Rhallabi et A. El Fallah-Serghrouchni, "Conception and Realization of Microwave Sensor for Efficient Hydrogen Detection", PhotonIcs & Electromagnetics Research Symposium (PIERS 2025), 4 - 8 May 2025, Abu Dhabi, UAE.
47. A. Merainani, Y. Mahe, **M. El Gibari** et T. Razban, "Modeling of Transparent Mesh Technology --- Wideband Dispersion Model from Scattering Matrix", PhotonIcs & Electromagnetics Research Symposium (PIERS 2025), 4 - 8 May 2025, Abu Dhabi, UAE.

6.5 Conférences nationales à comités de lecture et actes

1. **M. El Gibari**, D. Averty, C. Lupi, H. W. Li et S. Toutain, "Transition CPW-MS ultra large bande sans via et application à la caractérisation de dispositifs opto-hyperfréquences sur polymère" *Journées Nationales Microondes (JNM)*, 27-29 mai 2009, Grenoble. (Id : hal-01150177)
2. **M. El Gibari**, D. Averty, Y. Mahé et H. W. Li, "Transition CPW-MS ultra large pour la connectorisation de composants sur polymère", *Journées Nationales Microondes (JNM)*, pp. J3-DP-P101, 5-17 mai 2013, Paris. (Id : hal-01092774)
3. T. Sghaier, **M. El Gibari** et B. Guiffard, "Mélanges élastomères thermoplastiques souples à faible pertes diélectriques pour applications antennaires en bande X", *Journées Nationales Microondes (JNM)*, May 2019, Caen. (Id : hal-02172021)
4. P. -V. Dugue, **M. El Gibari**, M. Halbwax, S. Ginestar, J.-P. Vilcot et H. W. Li, "Etude et réalisation d'une transition GCPW-MS-GCPW avec via-hole sur couche mince en polymère", *Journées Nationales Microondes (JNM), pp 347, May 2019, Caen.* (Id : hal-02479395)

6.6 Conférences nationales

1. **M. El Gibari**, C. Lupi, Y. Scudeller, J.P. Landesman, "Caractérisation thermique d'émetteurs électro-optiques : des matériaux aux assemblages" *Journée thématique « Caractérisations thermo-physiques et applications microélectroniques »*, Société Française de Thermique, 18 novembre 2011, Orléans, France.
2. **M. El Gibari**, B. Belkerk, C. Lupi, Y. Scudeller, J.P. Landesman "Caractérisation thermique d'émetteurs électro-optiques : des matériaux aux assemblages" *Journée thématique « Caractérisations thermo-physiques et applications microélectroniques »*, Société Française de Thermique, 18 novembre 2011, Orléans, France.
3. K. R. P. Auguste, M. Halbwax, **M. El Gibari**, S. Pavy, J.-F. Legier, D. Averty, H. W. Gundel, J.-P. Vilcot, H. W. Li, "Caractérisations électro-optique et hyperfréquence de matériaux polymères en vue de la réalisation de modulateurs de type Mach-Zehnder" *Journée du Club Optique Micro-Ondes (JCOM)*, Villeneuve d'Ascq Juin 2012. (Id : hal-00797734)
4. **M. El Gibari**, D. Averty, M. Halbwax, J-P. Vilcot and H. W. Li, "Transition coplanaire-microruban ultra-large bande pour la caractérisation de composants opto-hyperfréquence" *GDR onde*, 17-18 janvier 2013, Grenoble, France. (Id : hal-01092768)
5. M. Hadjloum, **M. El Gibari**, A. S. Daryoush, H. Gundel, H. W. Li, "Conversion analogique-numérique des signaux hyperfréquences à base de polymères électro-optiques dopés avec des nanoparticules", *JCOM,* Lannion, 19 juin 2014. (Id : hal-01073109)
6. S. Bretin, M. Hadjloum, **M. El Gibari**, H. W. Li, "Transition coplanaire-microruban large bande pour le packaging d'un composant opto-hyperfréquence", *JCOM,* Nantes, 12 juin 2015. (Id : hal-01163717)

7. M. Hadjloum, **M. El Gibari**, A. S. Daryoush, H. W. Li, "Conception d'un déflecteur à guide d'onde à fuite électro-optique pour un convertisseur analogique-numérique tout optique fonctionnant à 40 Géch/s", *JCOM,* Nantes, 12 juin 2015. (Id : hal-01163718)
8. D. Palessonga, **M. El Gibari**, S. Ginestar, H. Terrisse, A. Kassiba, H. W. Li, "Mise en forme et caractérisation de polymères électro-optiques incorporant des nanoparticules", *JCOM,* Nantes, 12 juin 2015. (Id : hal-01163714)
9. M. Hadjloum, **M. El Gibari**, H. W. Li, A. S. Daryoush, "Advances on all-optical ADCs based on a polymer leaky waveguide deflector", W*orkshop on advanced ADCs*, Dec 2015, La Baule, France. (Id: hal-01251332)
10. D. Palessonga, **M. El Gibari**, S. Ginestar, H. Terrisse, B. Guiffard, A. Kassiba, H. W. Li, "Amélioration de la bande passante des composants opto-hyperfréquences basés sur des polymères électro-optiques chargés de nanoparticules de TiO_2", *JCOM,* Limoges, 3 juillet 2017. (Id : hal-01558091)
11. Y. Ouellaf, **M. El Gibari**, P. Bertoncini, S. Ginestar, E. Abisset-Chavanne, O. Chauvet et H. W. LI, "Amélioration de la dispersion de nanoparticules dans des polymères en combinant l'utilisation de sonication et de tensio-actifs ", *Journées annuelles GFP Ouest et réseau SPEED au Mans*, 24 mai 2018. (Id : hal-01830925)
12. P. -V. Dugue, **M. El Gibari**, M. Halbwax, J. Le Meur, S. Ginestar, K. Heggarty, J.-P. Vilcot et H. W. Li, "Premiers résultats de l'étude d'un déflecteur électro-optique sur polymères en vue de la réalisation d'un convertisseur analogique numérique tout-optique", *JCOM*, Toulouse, Juillet 2018. (Id : hal-01830878)
13. P. -V. Dugue, **M. El Gibari**, M. Halbwax, S. Ginestar, J.-P. Vilcot et H. W. Li, "Etude d'un déflecteur électro-optique à base d'un guide à fuite sur polymères et d'un élément optique diffractif", *JCOM*, Brest, Juin 2019. (Id : hal-02479414)
14. P. -V. Dugue, **M. El Gibari**, k. Heggarty, C. Larat, J.-P. Vilcot et H. W. Li, "Approximation analytique du faisceau de fuite d'un déflecteur électro-optique à base d'un guide sur polymères", *JCOM*, Paris, Juin 2021. (Id : hal-03512149)

7 Responsabilités collectives

7.1 Responsabilités administratives

7.1.1 Responsabilité du Fablab

Depuis juin 2019, je suis responsable du Fablab de l'UFR Sciences et Techniques. Le budget annuel est autour de 20k€.

Le Fablab est un atelier collaboratif offrant des outils et des facilités de fabrication numérique et de prototypage les plus exhaustives possibles. C'est un espace contributif où l'on va, de manière non exhaustive :

- Concevoir, prototyper, fabriquer, réparer... à l'aide des équipements mis à disposition.
- Promouvoir l'apprentissage par le « faire », notamment en développant des capacités d'analyse et de conception, et par la fabrication ou la modification d'objets.
- Favoriser la diffusion et la transmission de connaissances, de savoir-faire et de savoir-être entre pairs notamment par la documentation, l'entre-aide et la bienveillance.
- Faciliter l'innovation technique, économique, sociale, sociétale et environnementale ainsi que l'expérimentation et l'apprentissage par la pratique.
- Encourager les actions responsables et durables en interaction avec l'environnement technique, naturel, économique, social et sociétal.
- Favoriser la collaboration et l'entraide, ainsi que le croisement et l'échange tant transdisciplinaires (art, science, technique, culture, etc.) que Trans-générationnels.
- Participer à la création de communs (documentation open-source, logiciels libres...).

Le Fablab de l'UFR Sciences et Techniques sert à la fois pour :

- Des activités liées aux enseignements.
- Des projets extrascolaires et associatifs.
- Des activités de recherche.
- Des expérimentations.
- Des workshops et des temps d'échanges.

Pour plus d'informations : https://sciences-techniques.univ-nantes.fr/vie-du-campus-vie-etudiante/fablab

7.1.2 Responsabilité à l'école doctorale MASTIC

Depuis septembre 2021 je suis responsable des manifestations scientifiques à l'école doctorale MathSTIC (MASTIC depuis Sept. 2022).

- Organisation de la journée de la rentrée des nouveaux doctorants.
- Organisation de la journée des doctorants (JDOC) (en 2022 présentations de 60 doctorants sous forme de présentations orales et posters)
- Organisation des journées scientifiques et conférences

7.1.3 Coordinateur du concours national « Faites de la Science »

Le concours national "Faites de la Science" est organisé par la CDUS (Conférence des Doyens et directeurs des UFR Scientifiques de France). Il s'adresse aux élèves de tous les lycées et collèges français. L'objectif est de leur donner le goût des sciences en les mobilisant sur des projets scientifiques ou technologiques faisant appel à l'esprit de découverte et au travail en groupe. Ils sont pour cela encadrés par leurs enseignants et l'approche expérimentale est privilégiée. Tous les ans, le meilleur projet présenté lors des différentes finales régionales est sélectionné pour participer à la finale nationale.

Sous la présidence de la Doyenne de l'UFR Sciences et Techniques, j'ai organisé à la fois la finale locale, qui regroupe les établissements de la Loire-Atlantique et la Vendée, le 17 avril 2024 et également la finale de la 17e édition du concours national "Faites de la science" qui a eu lieu sur notre campus de l'UFR Sciences et Techniques, pour la première fois depuis l'existante de ce concours, du 6 au 8 juin 2024.

Plusieurs Doyens (nes), Vice-Présidents de Nantes Université, représentants de l'Académie de Nantes et rectorat, représentants de Nantes métropole et responsables politiques étaient présents pour participer aux jurys et au remise des prix à la fin des deux concours.

Le budget de ces deux concours est de 65 k€

Voici une liste de quelques taches réalisées avec mon équipe de manière non exhaustive :

- Recherche de partenaires et sponsors en lien avec l'équipe du pole communication de la faculté
- Organisation logistique des différentes équipes participantes (emplacements, équipements, bourse, hébergement, repas, etc…)
- Mise en place du programme des deux concours
- Mise en place de la composition et rotation du jury pour le concours local (15 membres) et pour le concours national (42 membres)
- Rédaction du livret d'accueil pour les participants et pour les jurys

- Réponse aux différents mails : 2000 mails traités
- …..

7.1.4 Autres responsabilités

- Membre du conseil de gestion de l'UFR Sciences et Techniques depuis 2024
- Membre du conseil de scientifique de l'UFR Sciences et Techniques depuis 2020.
- Responsable de Licence 2 SPI (Science Pour l'Ingénieur) parcours EEA
- Membre de la commission pédagogique de L3 EEA, de M1 EEA et de M2 CISE (depuis 2012).
- Membre du jury de M2 CISE (depuis 2013), de M1 EEA (depuis 2012), de L3 EEA (2013-2019) et de L2 Sciences Pour l'Ingénieur (2014-2019).
- Membre du conseil de perfectionnement du Master EEA depuis 2017.
- Membre suppléant du conseil de département de physique de l'UFR Sciences et Techniques depuis 2021.
- Coordinateur régional du concours "Faites de la Science".

8 Projet de recherche

Dans le cadre de mon projet de recherche, je souhaite concentrer mes travaux autour des applications, dispositifs et systèmes hyperfréquence, compte tenu de leur rôle de plus en plus crucial dans divers secteurs technologiques comme les télécommunications mobiles (xG), le Wi-Fi, les radars, les capteurs, et bien d'autres encore d'une part et autour des capteurs biomédicaux avec pour ambition de contribuer aux technologies de santé du futur d'autre part. Le premier objectif s'aligne parfaitement avec la stratégie du laboratoire IETR, qui vise à renforcer et recentrer les compétences des enseignants-chercheurs dans le domaine des antennes et des circuits RF (passifs et actifs), afin de positionner le laboratoire au cœur des futurs enjeux de connectivité, notamment dans les architectures antennaires et les circuits micro-ondes et millimétriques associés. Le second objectif s'inscrit pleinement dans le cadre du défi sociétal porté par la Région Pays de la Loire et Nantes Université autour de la santé du futur.

Voici les actions que je mène actuellement et que je souhaite développer dans l'avenir :

8.1 Modélisation d'une technologie transparente grillagée : Application à la conception d'antennes et de circuits radiofréquences.

Fort de mes compétences acquises dans mes travaux antérieurs, je me suis rapproché de l'équipe STAR du laboratoire pour co-encadrer une thèse entamée en janvier 2024 sous la direction du Pr. Tchanguiz Razban et avec Yann Mahé comme co-encadrant. La thèse porte sur la modélisation d'une technologie transparente grillagée, visant comme application la conception d'antennes et de circuits radiofréquences.

En effet, le développement d'antennes et de circuits optiquement transparents est important, voire crucial dans certains cas, pour les intégrer discrètement dans des surfaces telles que les fenêtres de bâtiments, les vitres de voitures, ou encore les smartphones, tout en minimisant leur impact visuel. La conception de front-ends radio sur des matériaux transparents devient donc essentielle pour allier discrétion et efficacité. Les solutions de métallisation en maillage offrent un bon compromis entre transparence et performances à haute fréquence. Cependant, les dimensions des cellules de maillage, très petites par rapport aux longueurs d'onde, modifient les paramètres de dispersion des structures. Les recherches antérieures montrent qu'il est nécessaire de repenser la modélisation des structures maillées, car les modèles existants pour la conception d'antennes ne sont pas adaptés à ce type de structures. De plus, le processus de maillage, pour les outils de simulations électromagnétiques 3D, nécessite un grand nombre de cellules de maillage augmentant ainsi le temps de calcul et les simulateurs 1D se révèlent inefficaces pour les structures maillées, faute de modèles analytiques appropriés.

Dans ce projet, notre objectif est de développer un nouveau modèle mathématique capable de représenter avec précision le comportement des lignes de transmission maillées (comme le

microruban) sur une bande de fréquences allant jusqu'à 40 GHz. Nous cherchons également à modéliser l'impact de la forme et des propriétés physiques de ces structures sur leurs performances, en associant des calculs analytiques avec des modèles existants pour les lignes de transmission traditionnelles. L'objectif final est de faire évoluer les modèles classiques de dispersion validés pour les structures opaques et d'évaluer dans quelle mesure ils peuvent être adaptés aux solutions grillagées. À terme, nous arriverons à modéliser le comportement de structures grillagées simples (lignes et discontinuités, filtres, adaptation d'impédance, cellules actives, ...) en identifiant les paramètres équivalents (impédance caractéristique, dispersion du mode de propagation, paramètres de discontinuités) en fonction de la géométrie de la structure et des paramètres physiques de la technologie d'appui.

Cette activité contribuera en partie à relever les défis scientifiques à venir (miniaturisation, montée en fréquence et en débit) tout en répondant aux enjeux sociétaux de la transformation numérique et des transitions énergétiques, environnementales et sanitaires.

8.2 Synergie internationale pour l'innovation en hyperfréquences et santé connectée

Dans le cadre d'une dynamique de coopération scientifique internationale, j'ai invité le Pr. Jamal Zbitou, enseignant-chercheur à l'École Nationale des Sciences Appliquées (ENSA) de Tétouan, relevant de l'Université Abdelmalek Essaâdi (Maroc), à effectuer une mission en tant que professeur invité au sein du laboratoire IETR. Cette mission, d'une durée d'un mois, s'est déroulée en mars 2025. Elle a permis de poser les bases d'une collaboration prometteuse entre plusieurs institutions académiques : l'IETR, l'Université Abdelmalek Essaâdi, l'IMN de Nantes et le laboratoire REI 4.0 (Laboratoire de robotique, électronique et industrie 4.0) de l'Université de Moncton au Canada.

Dans le cadre de cette collaboration, l'accent a été mis sur la conception de circuits hyperfréquences associés à des antennes innovantes, notamment pour des applications avancées (5G et bande millimétrique) ainsi que du développement de capteurs intelligents pour des applications en santé. À titre d'exemple, plusieurs topologies de filtres passe-bande sélectifs ont été réalisées autour de 3,5 GHz et 5,8 GHz, ainsi que des coupleurs et filtres passe-bande autour de 24 GHz et 28 GHz. Ces dispositifs ont été fabriqués sur des substrats commerciaux de type RO4003 et RT5880 en salle blanche, et les caractérisations ont été menées avec succès.

À ce jour, cette collaboration a déjà donné lieu à 7 communications dans des conférences internationales. Plusieurs articles sont également en cours de rédaction, en vue de leur soumission prochaine dans des revues scientifiques de rang A.

Nous envisageons désormais d'étendre nos travaux de recherche à la conception de circuits associés aux antennes sur couches minces (≈ 20 µm) en polymère BCB (benzocyclobutène), un matériau largement utilisé en hyperfréquence en raison de ses excellentes propriétés diélectriques : ($\varepsilon_r = 2{,}77$, $\tan\delta = 0{,}007$).

À l'issue de cette mission, une intention de collaboration a été formalisée entre nos deux institutions, ouvrant des perspectives prometteuses en matière de co-diplômation, de coopération pédagogique et de projets de recherche conjoints. Dans ce cadre, et en partenariat avec l'IMN et l'Université Abdelmalek Essaâdi, j'ai déposé, en tant que coordinateur, un projet PHC Toubkal 2026 portant sur la conception et la réalisation de capteurs sans fil intelligents pour des applications en santé. Nous sommes actuellement en attente des résultats de cette soumission.

Concernant le laboratoire REI 4.0 de l'Université de Moncton au Canada, j'ai invité le Pr. Aziz Oukaira à séjourner une semaine au sein du laboratoire IETR, du 12 au 17 mai 2025, afin de découvrir nos activités de recherche et d'explorer des perspectives de collaboration. Cette coopération portera principalement sur le développement de circuits RF associés aux antennes et leur intégration dans divers systèmes, ainsi que sur les capteurs intelligents, avec un accent particulier sur les applications dédiées à la santé du futur. Nous collaborons déjà à distance et présenterons ensemble trois communications lors de deux conférences internationales : une à COFMER'05 (du 15 au 17 avril 2025) et deux à PIERS 2025 (du 4 au 8 mai 2025).

8.3 Capteur à base structures résonantes pour la détection de l'hydrogène vert et l'ammoniac

Bien que le marché propose déjà une large gamme de capteurs couvrant divers secteurs comme l'automobile, la domotique, l'instrumentation médicale, l'énergie, ainsi que l'industrie chimique et agroalimentaire, le besoin de nouvelles familles de capteurs, alliant précision, faible coût, faible consommation d'énergie et miniaturisation, devient de plus en plus pressant pour économiser de l'énergie et accompagner le déploiement de l'Intelligence Artificielle.

Pour répondre à ce besoin, j'ai débuté l'encadrement d'une seconde thèse (septembre 2024) dans le cadre d'une collaboration avec le Centre International d'Intelligence Artificielle (Ai-Movement) à l'École Polytechnique Mohammed VI (UM6P) au Maroc. Cette thèse en cotutelle, co-encadrée par moi sous la direction de Pr. Ahmed Rhallabi (IMN) et Pr. Amal El Fallah Seghrouchni (Ai-Movement), a pour objectif de réaliser un capteur de gaz intelligent basé sur des oxydes métalliques déposés par la technique PVD (Physical Vapor Deposition), conçu à partir de structures résonantes opérant autour de 10 GHz.

En effet, les capteurs de gaz suscitent un intérêt croissant, notamment ceux capables de réaliser des mesures en temps réel, de préférence à distance. Ces caractéristiques leur confèrent une grande agilité, facilitant leur intégration dans des systèmes embarqués capables de transmettre un volume important de données. C'est pourquoi ce travail représente un axe stratégique majeur pour le groupe OCP (Office Chérifien des Phosphates), notamment pour la détection de l'hydrogène vert et de l'ammoniac, essentiels dans les domaines de la nutrition des plantes et des engrais à base de phosphate.

Dans ce contexte, nous proposons de développer un capteur de détection de gaz basé sur des oxydes métalliques tels que le dioxyde de titane (TiO_2) ou le trioxyde de tungstène (WO3), qui

constitueront la couche active du capteur. L'impact de la composition chimique de ces matériaux, déposés par la technique PVD, sur leurs propriétés électriques en hyperfréquence sera étudié. Sur la base de ces résultats, la conception et la fabrication du capteur, reposant sur une structure résonante, seront réalisées en s'appuyant sur des simulations électromagnétiques 3D. Enfin, une phase d'étalonnage du capteur sera menée pour analyser le décalage de la fréquence de résonance en fonction de la concentration du gaz sélectionné sur la surface du capteur.

Une fois les capteurs réalisés, nous intégrerons l'intelligence artificielle pour améliorer leurs performances en optimisant leur précision, leur sensibilité et leur facilité de détection. Grâce à des algorithmes d'apprentissage automatique (machine learning), l'intelligence artificielle analysera les signaux bruts des capteurs, en supprimant le bruit et en mettant en évidence les caractéristiques clés permettant d'identifier les gaz présents avec une plus grande précision. De plus, elle facilitera la classification de différents types de gaz, même dans des environnements complexes où plusieurs gaz peuvent être présents simultanément.

L'intelligence artificielle pourra également quantifier les concentrations de gaz, détecter des anomalies en temps réel, et ajuster le capteur en fonction des variations environnementales, telles que l'humidité ou la température. En combinant ces capteurs avec des capacités d'intelligence artificielle, nous visons à créer des systèmes de détection de gaz plus intelligents, réactifs et fiables, adaptés à des conditions variées et changeantes.

8.4 Capteur de pression artérielle miniaturisé implantable et compensé en température

Les capteurs de pression artérielle précis, fiables et compacts sont d'une importance cruciale pour les essais précliniques effectués sur des animaux, car ces essais représentent une étape clé avant les essais cliniques pour validation de nouveaux traitements contre les maladies cardiovasculaires chez l'humain. Ces capteurs permettent de mesurer en temps réel les variations de la pression sanguine, fournissant ainsi des données précieuses pour évaluer l'efficacité et la sécurité des traitements expérimentaux.

Toutefois, un des principaux défis dans l'utilisation de ces capteurs réside dans leur caractère implantable. Une fois placés à l'intérieur du corps de l'animal, ils sont exposés à des variations internes de température, résultant des changements physiologiques, de l'environnement ou des effets secondaires des traitements testés. Ces fluctuations de la température corporelle influencent directement la précision des mesures, comme les propriétés des matériaux des capteurs ainsi que les conditions de mesure peuvent être altérées par les changements de température.

Pour développer des capteurs performants, il faut s'affranchir des variations de la température, soit par le choix des matériaux adaptés et innovants, soit en intégrant des systèmes de compensation thermique. Cela permettrait non seulement d'améliorer la précision des données recueillies, mais aussi d'accroître la fiabilité des essais, réduisant ainsi le besoin d'ajustements expérimentaux ou de recalibrations fréquentes. L'objectif final étant de minimiser les erreurs de mesure tout en optimisant

les résultats des tests précliniques, garantissant ainsi une meilleure transition vers les essais cliniques.

À ce jour, aucun capteur miniaturisé implantable compensé en température n'existe. Mon objectif est de développer des capteurs de ce type, non seulement miniaturisés pour être compatibles avec de petits animaux tels que les rats et les souris, mais aussi dotés d'un module de transmission sans fil. Plus précisément, il s'agira de réduire la dérive thermique à moins de 3 mmHg dans une plage de température de 34°C à 39°C, avec une autonomie de 90 jours et une transmission de données sur une distance de 5 à 10 mètres. Cette ambition permettra de dépasser largement l'état de l'art. À titre de comparaison, l'implant commercialisé par la société emka TECHNOLOGIES présente une dérive de 5 mmHg et une autonomie de seulement 40 jours.

Ma collaboration avec l'équipe de biologie cardiaque de l'Institut du Thorax à Nantes et emka TECHNOLOGIES a permis de développer et valider une méthode innovante pour extraire les paramètres d'un capteur piézorésistif et modéliser leurs variations en fonction de la pression et de la température. Cette méthode permet d'optimiser le réglage du circuit de compensation afin de réduire les dérives thermiques d'un ensemble de sondes, évitant ainsi une calibration individuelle chronophage et coûteuse. De plus, elle offre la possibilité d'étudier rapidement différents circuits comportant des composants sensibles à la température. Dans la suite de cette collaboration, l'IETR continuera à apporter, d'une part, son expertise en électronique pour la compensation des dérives thermiques à l'aide de circuits analogiques économes en énergie et, d'autre part, en systèmes antennaires pour la transmission de données sans fil. Ce travail s'insère clairement dans l'axe Bioélectronique sans fil de l'IETR.

Dans le cadre de l'édition 2025 des appels à projets de l'ANR, j'ai soumis, en tant que coordinateur, un projet ANR PRC. Ce projet vise à concevoir et réaliser des capteurs de pression artérielle innovants, miniaturisés et implantables, spécifiquement destinés à la surveillance physiologique chez les petits animaux. Le consortium réunissait plusieurs partenaires académiques de renom : l'IETR (Nantes Université et ENS de Rennes), le laboratoire GPM (UMR CNRS 6634 – Université de Rouen), l'IEMN (UMR CNRS 8520 – Université de Lille), ainsi que l'Institut du Thorax (UMR 6291 – Nantes Université). Bien que le projet ait reçu des retours très positifs de la part des experts évaluateurs, il n'a malheureusement pas été retenu lors de cette session. Convaincus de la pertinence scientifique et sociétale de cette recherche, nous avons décidé de retravailler la proposition et de la soumettre à nouveau dans le cadre de l'édition 2026 de l'ANR.

9 Références bibliographiques

[1] D. Chen, H. R. Fetterman, A. Chen, W. H. Steier, L. R. Dalton, W. Wang, ans Y. Shi, "Demonstration of 110 GHz electro-optic polymer modulators", Appl. Phys. Lett., vol. 70, no 25, pp. 3335-3337, 1997.

[2] Y. Shi, C. Zhang, H. Zhang, J. H. Bechtel, L. R. Dalton, B. H. Robinson and W. H. Steier, "Low (sub-1-volt) halfwave voltage polymeric electro-optic modulators achieved by controlling chromophore shape", Science, vol. 288, no 5463, pp. 119–122, 2000.

[3] A. S. Daryoush, X. Hou and W. Rosen, "All-optical ADC and its applications in future communication satellites", IEEE International Topical Meeting on Microwave Photonics (MWP 2004), pp. 182-185, 2004.

[4] X. Hou, "A Leaky Waveguide All-Optical Analog-to-Digital Converter", Thèse de dortorat, Drexel University, 2004.

[5] L. Zhu; K.L. Melde, "On-wafer measurement of microstrip-based circuits with a broadband vialess transition", IEEE Transactions on Advanced Packaging, vol. 29, no. 3, pp. 654-659, 2006

[6] M. El Gibari, D. Averty, C. Lupi, Y. M. H. Li and S. Toutain, "Coplanar-microstrip transitions for ultra-wideband communications, ultra-wideband communications: novel trends - antennas and propagation", ISBN 978-953-307-452-8, INTECH, 2011.

[7] M. Hadjloum, M. El Gibari, S. Ginestar, H. W. Li, A. S. Daryoush, "Via-Hole Less Broadband Grounded Coplanar to Coupled Microstrip Transition for up to 40 GHz", Progress In Electromagnetics Research Letters, vol. 56, pp.47-51, 2015.

[8] 11. M. Hadjloum, M. El Gibari, H. W. Li, A. S. Daryoush, "Broadband Capacitively Grounded Coplanar to Coupled Microstrip Transition for Planar Microwave Photonic Components", International Journal of Microwave and Wireless Technologies, vol. 9, issue 4, pp. 815-819, 2017.

[9] P. -V. Dugue, M. El Gibari, M. Halbwax, S. Ginestar, V. Avramovic, J.-P. Vilcot et H. W. Li, "A new equivalent circuit scheme for grounded back-to-back GCPW-MS-GCPW transitions fabricated on a thin low-k substrate", Progress In Electromagnetics Research Letters, vol. 95, pp.33-42 56, 2021.

[10] D. Palessonga, M. El Gibari, S. Ginestar, H. Terrisse, B. Guiffard, A. Kassiba and H. W. Li "Bandwidth Improvement of Microwave Photonic Components Based on Electro-Optic Polymers loaded with TiO2 Nanoparticles", Applied Physics A, vol. 123, issue 8, Article 542, 2017.

[11] Z. Jradi, M. El Gibari, H. W. Li et O. Chauvet, "Electro optic nanocomposites for high performance microwave photonic applications", IEEE Telecommunications Forum TELFOR 2020, 24-25 Nov. 2020, Belgrade, Serbia.

[12] M. El Gibari, S. M. D. Mbacke, B. Lauzier, C. Gauthier et H. W. Li, " A simple and effective method to compensate the thermal drift of implantable blood pressure sensors", Sensors and Actuators A: Physical, vol. 376, 115615, ISSN 0924-4247, 2024.

[13] S. Adrar, M. El Gibari, P. Saillant, J-C Thomas et R. Seveno, " Development of flexible piezoelectric sole with wireless communication for medical application", Biomedical Signal Processing and Control, vol. 85, 104878, ISSN 1746-8094, 2023.

[14] T. Sghaier, M. El Gibari et B. Guiffard, “New low loss soft thermoplastic blends for microwave applications”, Journal of Physics D: Applied Physics, IOP Publishing, 53 (13), pp.135003, 2020.

10 Publications principales

1- M. El Gibari, D. Averty, M. Hlabwax, J-P. Vilcot and H. W. Li, “Comprehensive study of ultra-broadband GCPW-MS transition on thin films”, Microwave and Optical Technology Letters, Vol. 57, issue 9, pp. 2041-2045, 2015

Cet article présente des transitions GCPW-MS-GCPW (coplanaires-microruban back to back) realisées sur une couche mince de polymère BCB de 20 µm. Ces transitions présentent une bande passante expérimentale de 82 GHz, avec une fréquence de coupure basse exceptionnelle de 1,5 GHz et une perte d'insertion de seulement 0,5 dB. Ces performances remarquables sont obtenues sans l'utilisation de vias ni de structuration du plan de masse inférieur. Cette configuration simplifie la fabrication et la caractérisation, grâce à l'utilisation de sondes coplanaires, de dispositifs micro-ondes basés sur des matériaux en couches minces, où la ligne microruban sert d'électrode de commande. C’est le cas, par exemple, des modulateurs électro-optiques sur polymère dont les chromophores sont orientés par effet corona.

2- M. Hadjloum, **M. El Gibari**, H. W. Li et A. S. Daryoush, “An ultra-wideband dielectric material characterization method using grounded coplanar waveguide and genetic algorithm optimization”, Applied Physics Letters, vol. 117, issue 14, pp. 142908, 2015

Dans cet article, nous avons développé une nouvelle méthode numérique pour extraire la permittivité complexe des matériaux utilisés dans le domaine opto-hyperfréquence sur une bande de fréquence ultra-large. Cette méthode est basée sur la minimisation de l’erreur globale entre le paramètre de transmission S21 mesuré et celui simulé par HFSS par un processus itératif d’une ligne coplanaire blindée (GCPW pour Grounded Co-Planar Waveguide). Pour une bonne sensibilité, le module et la phase de S21 sont utilisés pour définir le bon critère de convergence. Un algorithme génétique d’optimisation globale, implémenté sous Matlab, a été utilisé afin d’accélérer la convergence et par conséquent réduire le temps d’extraction de la permittivité complexe. La faisabilité de cette technique a été validée jusqu'à 40 GHz sur le polymère BCB de faible permittivité et de faible tangente des pertes. La méthode a été ensuite utilisée pour caractériser des matériaux utilisés dans les applications opto-hyperfréquences.

3- M. Hadjloum, **M. El Gibari**, H. W. Li, A. S. Daryoush, “Design challenges of EO polymer based leaky waveguide deflector for 40 Gs/s all-optical analog-to-digital converters”, Optics Communications, vol. 373, pp. 82-90, 2016

La conception et l'optimisation des performances d'un convertisseur analogique-numérique tout optique est présenté dans cet article. La conception hyperfréquence et optique approfondie du déflecteur basé sur un guide d’onde à fuite, brique de base pour le convertisseur, utilisant un polymère électro-optique est ainsi présenté dans ce papier. Ce déflecteur optique convertit chaque variation

d'amplitude analogique de la tension RF en une variation angulaire de la direction du faisceau émergent. Cette variation angulaire est quantifiée grâce à un masque de codage suivi d'une matrice de photodétecteurs. L'étude a permis d'obtenir le meilleur compris possible entre la résolution et la bande passante du convertisseur en utilisant une technique innovante pour la compensation des pertes hyperfréquences liées à la propagation d'une part et d'accorder les vitesses de phases des ondes optique et hyperfréquence d'autre part. En outre, afin de faciliter les accès optique et hyperfréquence, une transition présentant une très large bande passante expérimentale (> 22 GHz) entre une ligne coplanaire (CPW) et l'électrode de commande de déflecteur en microruban couplée (CMS). Cette transition CPW-CMS a été optimisé sans via et sans motif dans le plan de masse. Avec un coefficient électro-optique de 350 pm/V, le déflecteur conçu devrait permettre à un convertisseur tout optique de fonctionner sur 44 Géch/s avec une résolution de 6,5 bits et une consommation électrique de seulement 4W avec un système adapté à 50 Ω.

4- D. Palessonga, **M. El Gibari**, S. Ginestar, H. Terrisse, B. Guiffard, A. Kassiba and H. W. Li "Bandwidth Improvement of Microwave Photonic Components Based on Electro-Optic Polymers loaded with TiO2 Nanoparticles", Applied Physics A, vol. 123, issue 8, Article 542, 2017

Cet article étudie l'influence de la charge des nanoparticules de dioxyde de titane (TiO_2) sur les propriétés hyperfréquences et optiques des polymères électro-optique. L'étude a montré la possibilité d'ajuster l'indice de réfraction ainsi que la constante diélectrique du polymère dans le but d'optimiser la bande passante des composants opto-hyperfréquence comme les modulateurs et les convertisseurs analogiques numériques. Avec 1 à 3% de nanoparticules de TiO_2 incorporées de façon homogène dans le polymère, la constante diélectrique varie de 2,73 à 3,40 sur la gamme 400 MHz - 10 GHz, et l'indice de réfraction passe de 1,483 à 1,488 à la longueur d'onde de 1539,6 nm. Par exemple, avec une longueur d'interaction électro-optique de 2 cm (longueur typique des modulateurs électro-optique), la bande passante des modulateurs pourrait être portée à 258 GHz en chargeant le polymère PMMA-DR1 avec 1% de nanoparticules de TiO_2. Il a également été constaté que l'ajout des nanoparticules pourrait améliorer la réponse électro-optique des polymères polarisés, représentée par l'intensité du signal de génération de la seconde harmonique (SHG). Ce dernier présente une multiplication par plus de trois en chargeant le polymère PMMA-DR1 avec 2 % des nanoparticules TiO_2.

5- T. Sghaier, **M. El Gibari** et B. Guiffard, "New low loss soft thermoplastic blends for microwave applications", Journal of Physics D: Applied Physics, IOP Publishing, 53 (13), pp.135003, 2020

Dans cet article, deux mélanges élastomères thermoplastiques souples à base de polypropylène (PP) et de polyéthylène (LDPE), basse densité, ont été fabriqués et caractérisés. Ces étapes de fabrication et de caractérisation sont présentées en détails. La méthode de caractérisation diélectrique à base des anneaux résonateurs a été adaptée pour pouvoir mesurer la constante diélectrique et la tangente des pertes des films réalisés jusqu'à 40 GHz. La réalisation et la caractérisation des antennes

patchs dans la bande X (8 GHz -12 GHz) ont permis de mettre en évidence la potentialité de ce nouveau concept des mélanges thermoplastiques souples. Ainsi les propriétés d'antenne mesurées : le gain, la directivité et l'efficacité ont été calculés à partir du diagramme de rayonnement mesuré et sont de 4,6. dB, 7,7 dB et 46 % respectivement pour le mélange à base de PP et de 4,8 dB, 8,1 dB et 51 % pour le mélange à base de LDPE.

6- S. Adrar, M. El Gibari, P. Saillant, J-C Thomas et R. Seveno, "Development of flexible piezoelectric sole with wireless communication for medical application", Biomedical Signal Processing and Control, vol. 85, 104878, ISSN 1746-8094, 2023

L'article s'inscrit dans les thématiques de recherche liées à la santé du futur en particulier les systèmes de suivi du patient à domicile via des outils adaptés à sa pathologie. Dans ce cadre, la conception et la réalisation d'une semelle connectée afin de détecter la présence d'anomalies au niveau du pied caractérisées par un trouble de la marche. La collaboration avec un podologue est un point supplémentaire dans cette étude, elle permet de définir ou mieux des zones de pression significative du pied pour analyser les données et les transformer en informations médicalement exploitables. La semelle réalisée contient plusieurs capteurs piézoélectriques sensibles à la pression développée entièrement au laboratoire IETR. Les données obtenues avec la déformation de ces capteurs seront envoyées directement par Bluetooth à l'aide d'une carte d'acquisition sans fil, les informations sont automatiquement enregistrées sur un cloud sécurisé dans lequel le médecin a accès à tout moment.

7- M. El Gibari, S. M. D. Mbacke, B. Lauzier, C. Gauthier et H. W. Li, " A simple and effective method to compensate the thermal drift of implantable blood pressure sensors", Sensors and Actuators A: Physical, vol. 376, 115615, ISSN 0924-4247, 2024

Cet article présente une étude approfondie de capteurs de pression artérielle implantables, basés sur une sonde comportant quatre piézorésistances. Une méthode innovante combinant à la fois des mesures et des calculs a été développée, permettant d'extraire les valeurs de chaque piézorésistance sans détériorer la sonde. Cette étude a conduit à la création d'un modèle de simulation dans le logiciel Cadence/Pspice, qui prend en compte les variations de la piézorésistance en fonction de la température et de la pression. La simulation du capteur permet ainsi de tester rapidement l'efficacité du circuit de compensation avant sa réalisation pratique. Une fois les dérives thermiques quantifiées, un circuit de compensation à base de transistors PNP a été développé pour corriger ces dérives. Cette technique de compensation analogique présente plusieurs avantages : faible coût, compacité, et faible consommation énergétique. Expérimentalement, elle a prouvé son efficacité, réduisant la dérive thermique du capteur de 9,97 mmHg/°C sans compensation à 2,12 mmHg/°C après compensation, à une pression de 300 mmHg. Cette méthode a été validée expérimentalement sur trois niveaux de pression : 0, 100, 200 et 300 mmHg.

TABLE 1 Radiation Pattern Characteristics

Frequency (MHz)	2400		2440		2480	
Plane (ϕ)	0°	90°	0°	90°	0°	90°
$HPBW_{simulated}$	24°	24°	24°	23°	23.5°	22.5°
$HPBW_{measured}$	27.5°	27°	26°	25°	25°	23.5°
$SLL_{simulated}$ (dB)	−20.8	−20.3	−19.8	−20.4	−19.1	−19.5
$SLL_{measured}$ (dB)	−18.3	−19.5	−18.2	−19.8	−18	−19

metal screws. The overall dimensions of the antenna are $Lg = 40$ cm, $Wg = 41$ cm, $h_{air} = 5$ mm.

The array was simulated and optimized using the electromagnetic simulator: Computer Simulation Technology's Microwave Studio [13].

3. SIMULATED AND MEASUREMENT RESULTS

The antenna was designed, simulated, and manufactured using a FR4 substrate, which present as main characteristics: dielectric constant $\varepsilon_r = 4.4$, thickness $h = 1.6$ mm, and loss tangent $tg\delta = 0.02$. The FR4 structure is suspended over an air layer with $h_{air} = 5$ mm. The prototype is shown in Figure 4.

The developed array was characterized for its main aspects: reflection coefficient, polarization, and radiation pattern.

3.1. Impedance Adaptation

To show the impact of the changes in the dielectric constant of the FR-4 material in the impedance adaptation of the antenna, it was simulated for different variations of the ε_{rFR4} around the initial value 4.4, and the results are presented in the Figure 5.

Although have been made variations in the dielectric constant of FR4, close to 10%, the antenna adaptation keeps good results, and a considerable bandwidth.

Another important aspect is the impact of some changes in the air layer thickness during the fabrication process. Some simulations were made changing the h_{air} around 5 mm, and the results are reported in the Figure 6.

According to the Figure 6 is concluded that small variations in the air layer thickness, have a reduced or negligible impact in the antenna adaptation, and its bandwidth.

The antenna prototype was measured, and good agreements with the simulated results were obtained. The Figure 7 shows the comparison between the simulated and measured S_{11} of the antenna.

Assuming as a criterion for an impedance matching an $S_{11} < -10$ dB, the antenna has an impedance bandwidth of 300 MHz.

3.2. Radiation Pattern

Figures 8–10 illustrates the simulated and measured radiation pattern of the developed antenna, for the central and the edges of the interest frequency band. Each Figure contains the two components of the electric field, simulated and measured, in the two main orthogonal planes, and the main characteristics are resumed in the Table 1.

It is evident the good agreement among the simulated and measured results. In terms of HPBW of the antenna has around 26°, which agrees with the initial prospects. Also the measured side lobes follows the simulated results, and are always lower than the requirements. The measured gain of the antenna is 16.21 dBi.

4. CONCLUSION

The developed nonuniform antenna array, consisting of a 12 printed patches with an excitation distribution based on Dolph-Chebyshev polynomials, presents the required characteristics. This array presents a low cost and simple structure, with desensitization to the FR4 properties. The antenna can be applied in the Wi-Fi communications, in particular to sports venues, covering a given sector. Its wide input adaptation bandwidth of 300 MHz covers the entire 2.4 GHz Wi-Fi band, and the reduced sides lobes allow lower the interferences.

ACKNOWLEDGMENT

This work is funded by National Funds through FCT- Fundação para a Ciência e a Tecnologia under the project PEst-OE/EEI/LA0008/2013.

REFERENCES

1. W.S. Kaswiati and J. Suryana, Design and realization of planar bowtie dipole array antenna with dual-polarization at 2.4 GHz frequency for Wi-Fi access point application, In: 7th International Conference on Telecommunication Systems, Services, and Applications (TSSA), 2012, pp. 218–222.
2. N. Li, W. Chen, and Z. Feng, A switched sector beam planar antenna, In: IEEE International Symposium Antennas and Propagation Society, Vol. 1A, Washington, DC, 2005, pp. 230–233.
3. Y.-H. He and J.-S. Li, A novel multi-band array antenna for WLAN/WiMAX applications, In: 4th IEEE International Symposium on Microwave, Antenna, Propagation, and EMC Technologies for Wireless Communications (MAPE), 2011, pp. 246–248.
4. Y.-Z. Yin, J.-P. Ma, Y.-J. Zhao, H.-L. Zheng, and Y.-M. Guo, Wideband printed dipole antenna for wireless LAN, In: IEEE International Symposium, Antennas and Propagation, Vol. 2B, Washington, DC, 2005, pp. 568–571.
5. K.K. Chan, H.C. Chin, W.L. Lim, and H. Kwee, A very low profile and high efficiency antenna array for WLAN at S-Band, In: Asia-Pacific Microwave Conference (APMC), 2008, pp. 1–4.
6. W.K. Toh, X.G. Qing, and Z.N. Chen, A planar dualband antenna array, IEEE Trans Antennas Propag 59 (2011), 833–838.
7. C.A. Balanis, Antenna theory: Analysis and design, 3rd ed., Wiley, Hoboken, NJ, 2005, pp. 1–117.
8. C.L. Dolph, A current distribution for broadside arrays which optimizes the relationship between beam width and side-lobe level, Proc IRE 34 (1946), 335–348.
9. Y.J. Yoon and B. Kim, A new formula for effective dielectric constant in multi-dielectric layer microstrip structure, In: IEEE Conference on Electrical Performance of Electronic Packaging, 2000, pp. 163–167.
10. T. Varum, J. Matos, P. Pinho, and R. Abreu, Non-uniform broadband circularly polarized antenna array for vehicular communications, Submitted.
11. E.J. Wilkinson, An n-way hybrid power divider, IRE Trans Microwave Theory Tech 8 (1960), 116–118.
12. L.I. Parad and R.L. Moynihan, Split-tee power divider, IEEE Trans Microwave Theory Tech 13 (1965), 91–95.
13. CST Microwave Studio, 3D EM Simulation Software, Computer Simulation Technology, Framingham, MA. Available at: http://www.cst.com.

COMPREHENSIVE STUDY OF ULTRA BROADBAND GCPW-MS TRANSITION ON THIN FILMS

Mohammed El-Gibari,[1] Dominique Averty,[1] Mathieu Halbwax,[2] Jean-Pierre Vilcot,[2] and Hongwu Li[1]

[1] Institute of Electronics and Telecommunications of Rennes, University of Nantes, 2 rue de la Houssinière, BP 92208, 44322 Nantes Cedex 3, France; Corresponding author: mohammed.el-gibari@univ-nantes.fr

[2] Institute of Electronics, Microelectronics and Nanotechnology, Avenue Poincaré–BP 60069, 59652 Villeneuve d'Ascq, France

Received 10 February 2015

ABSTRACT: *Back-to-back GCPW-MS-GCPW (Grounded Coplanar Waveguide-Microstrip lines) transitions realized on benzocyclobutene*

polymer thin films (20 μm) and using copper metallization are presented in this article. The achieved experimental bandwidth is 82 GHz with a remarkably lower cutoff frequency of only 1.5 GHz and insertion loss of 0.5 dB. This performance is obtained without neither making via holes in the substrate nor patterning the bottom ground plane. These transitions make easier and faster manufacturing and characterization, by means of coplanar probes, of microwave devices realized from materials in thin film and whose driving electrode is a MS line. © 2015 Wiley Periodicals, Inc. Microwave Opt Technol Lett 57:2041–2045, 2015; View this article online at wileyonlinelibrary.com. DOI 10.1002/mop.29273

Key words: *Grounded coplanar waveguide-microstrip transition; photonic microwave components; polymer; thin films*

1. INTRODUCTION

Nowadays optics is penetrating into metropolitan access networks, so the data transmission bit-rate can be guaranteed regardless the distance between the subscriber and the central office [1]. Low-cost and broadband optical modulators are then required to popularize high bit-rate transmission. Electro-optic (EO) polymers collect the required properties for realizing such modulators. In general, chromophore molecules responsible for EO effect in polymer are oriented perpendicularly to the substrate. Consequently, the electric field of the modulation signal must be applied in the same direction with a microstrip (MS) line. Taking into account the constraints relative to optical and microwave propagations as well as EO interaction, the MS width is of 10 of μm for polymer substrate of 10 of μm thick. Coplanar-microstrip (CPW-MS) transitions are then necessary to connect such devices directly to outside world.

In these transitions, we could physically connect the bottom MS ground plane and the top CPW ground plane using via-holes [2] to obtain ground continuity. However, this technique is complex to realize, especially in case of polymer modulators in which the dielectric materials are constituted by polymers sensitive to photolithography chemistry. Moreover, this technique would make the fabrication longer and the component more expensive because of additional processing steps. Via-free transitions are then an attractive solution [3–5] as they avoid processing on these polymers, making components simpler and cheaper to realize, and characterize.

We report a comprehensive study of via-free GCPW-MS-GCPW transition on thin films dedicated to components driven by MS electrodes, such as EO modulators based on polymer materials. In the second Section, we describe first the principle of such via-free transition. Experimental validation and discussion of obtained results will be presented in the third Section. We will explain, in the fourth Section, the conception rules of such transitions according to desired applications. Some prospects for increasing the GCPW-MS transition bandwidth will be given in the Conclusion.

2. PRINCIPLE OF VIA FREE GCPW-MS-GCPW TRANSITION

The structure of GCPW-MS-GCPW transition studied in this article is shown in Figure 1. A full plate ground plane is first deposited on a silicon wafer. A thin polymer film is then deposited over the full plate ground plane; it simulates the optical waveguide part. On the top surface of the polymer, both the MS line (mimicking the electrode of the functional device) and the CPW pads are realized. The impedance between the bottom and top ground planes decreases with increasing frequency of the driving signal owing to capacitive coupling between them. So they can get short-circuited at high frequencies resulting the signal brought to CPW probe to be applied between the bottom ground plane and the MS line.

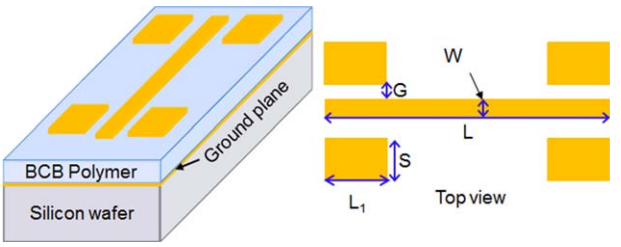

Figure 1 The studied back-to-back GCPW-MS-GCPW transitions. [Color figure can be viewed in the online issue, which is available at wileyonlinelibrary.com]

In this GCPW structure, the electric field propagation spreads into three modes due to the bottom ground plane below CPW section [5]: CPW mode, MS mode, and coplanar MS mode (CPM). In particular, this latter CPM is excited between the bottom and top ground planes. The CPM mode causes resonance peaks in the S_{21} parameter curve by diverting input electromagnetic energy from the CPW mode, so limiting the transition bandwidth. Appropriate parameters should be chosen for the structure to reduce the excitation of CPM mode. The thinness of the polymer substrate presents a triple advantage (i) it can easily create a short-circuit between the bottom and top ground planes by capacitive effect, (ii) it facilitates the conversion of the CPW mode into MS mode, and (iii) it pushes the CPM mode toward high frequencies [3].

3. EXPERIMENTAL AND SIMULATION RESULTS

The polymer film consists in a 20 μm-thick Benzocyclobutene (BCB) material. Its dielectric constant (ε_r) is 2.7 and its loss tangent (tanδ) varies from 0.008 to 0.02 [6]. It is deposited by spin-coating over a 365 μm-thick silicon wafer that was previously full wafer coated with a 2 μm-thick Cu ground plane. Advanced design system from Agilent was used to calculate the different dimensions of both MS and GCPW sections to obtain 50 Ω characteristic impedance. First, the MS line strip was calculated to be 54 μm wide (W). This dimension has been kept unchanged for the central conductor of the CPW line, achieving so a 25 μm wide gap (G). Top metallization is also made using a 2 μm-thick Cu film deposited using evaporation technique and shadow masking. The influence of different parameters on transition performance will be presented in the following.

S-parameters have been measured using an Agilent 8510C vector network analyzer (45 MHz to 110 GHz) and Cascade i110-AGSG125 probes (110 GHz bandwidth, 125 μm pitch). The calibration technique used is the LRRM (Line-Reflect-Reflect-Match) method using a Cascade ISS-104-783 calibration substrate, the whole system being controlled by Wincal Cascade software. All simulation results were obtained using the three-dimensional full-wave electromagnetic field analysis software HFSS V. 15. To get as close as possible to experimental procedure, coplanar probes were represented by the lumped port model issued from their datasheet.

3.1. Influence of the CPW Pads

Figure 2 presents the measurement and simulation results of GCPW-MS-GCPW transition with two different CPW ground pad surfaces $S.L1 = 4$ mm^2 ($S = 2$ mm and $L1 = 2$ mm) and $S.L1 = 1$ mm^2 ($S = 1$ mm and $L1 = 1$ mm). We note a very good agreement between experimental and simulation results.

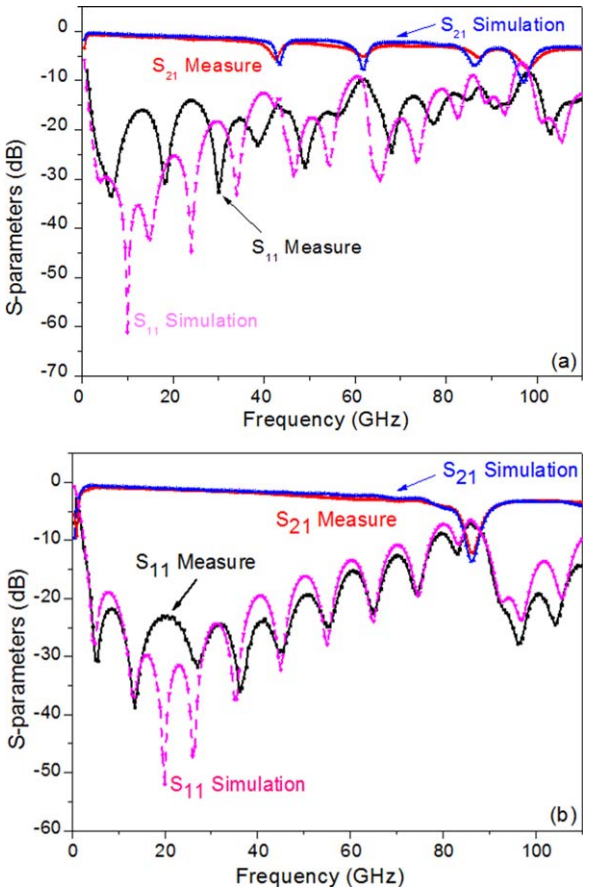

Figure 2 Measured and simulated S-parameters for back-to-back GCPW-MS-GCPW transitions of $L = 1$ cm. (a) $S.L1 = 4$ mm^2 ($S = 2$ mm and $L1 = 2$ mm), (b) $S.L1 = 1$ mm^2 ($S = 1$ mm and $L1 = 1$ mm). [Color figure can be viewed in the online issue, which is available at wileyonlinelibrary.com]

By reducing the pads surface from 4 to 1 mm^2, the upper cutoff frequency can be increased from 41.5 to 79.5 GHz but the lower cutoff frequency rises from 0.5 to 1.5 GHz.

3.2. Influence of the MS Length

The MS length L is in general determined by the associated device functionality. Figure 3 presents the measurement and simulation results obtained for different lengths, $L = 5$, 10, 15, and 20 mm; the coplanar ground pad surface ($S.L1$) is here fixed to 1 mm^2. The results show that the bandwidth of the GCPW-MS-GCPW transition varies significantly as a function of the structure length. Indeed, for the four considered increasing lengths, the bandwidth is 82, 78, 64, and 49 GHz and the insertion losses are 0.5, 0.9, 1.3, and 1.9 dB, respectively. The lower cutoff frequency remains at 1.5 GHz for all structures due to the same coplanar ground pad surface. As the negative slope of the transmission coefficient increases rapidly with the length L because of dielectric loss, the upper cutoff frequency is limited by the dielectric losses for larger lengths, 15 and 20 mm, and it is limited by the CPM mode resonance peak for the short ones, 5 and 10 mm.

The radiation losses have also an impact on the transition bandwidth. These radiation losses can be obtained by calculating $(1-|S_{11}|^2-|S_{21}|^2)$, where S-parameters are expressed in linear magnitude. Figure 3(e) and 3(f) present, respectively, the deduced radiated losses calculated with measured and simulated S-parameters, partly due to the energy leakage related to the CPM mode excitation.

3.3. Copper Metallization

The significant performance improvement of the transitions reported in this article compared with previous ones made with gold and aluminum metallization can be attributed to copper metallization. Conversely, the copper conductivity (5.96×10^7 S/m) is largely higher than that of gold (4.10×10^7 S/m) and aluminum (3.50×10^7 S/m). Conversely, copper has better adherence to BCB polymer, so a thicker metallization can be done, which in turn increases the bandwidth and reduces the insertion losses.

It was feared that copper oxidizes and diffuses into polymer which would result in the reduction of the effective metallization thickness and degradation of the loss tangent of the polymer substrate. Finally, none of these degradations seemed to take place or, at least if existing, they were not enough serious to impact significantly the transition performances 1-year later as S-parameter measurements gave same results. The transitions reported in this article were kept at room temperature on a shelf in an office, without special precautions. Copper oxidation and polymer degradation could take place if they are subjected to high temperatures and/or strong electric fields and/or high humidity.

4. DESIGN RULES

As it was seen in the previous Section 3.3, GCPW-MS-GCPW transition performances depend on transition parameters. The upper and lower cutoff frequencies vary often oppositely when one geometrical parameter is changed. So, some design rules shall be followed to optimize the transition parameters according to their respective applications.

4.1. Lower Cutoff Frequency

By considering the bottom ground plane and the CPW top ground pads as plane capacitors with a capacitance $C = \frac{S.\ L1\ \varepsilon_0\varepsilon_r}{h}$ and assuming that the voltage between the MS and the bottom ground plane can be calculated using voltage divider theorem, the 3 dB lower cutoff frequency f_L is approximately given by the following formula $f_L = \frac{h}{100\pi\ S.L1\ \varepsilon_0\varepsilon_r}$. The larger the dimensions of the CPW pads (width S and length $L1$) are compared with the distance h between the bottom ground plane and the CPW pads (equal to the dielectric substrate thickness), the more accurate is the above expression. With increasing CPW pads surface and/or dielectric substrate of higher permittivity and/or decreasing dielectric thickness, the capacitance C rises, the impedance between the bottom ground plane and the pads becomes smaller, so the lower cutoff frequency decreases. So, if one wants to reduce the lower cutoff frequency, he should increase the pads surface and/or chose high-k dielectric substrate and/or reduce the substrate thickness h.

4.2. Upper Cutoff Frequency

The transmission coefficient decreases with increasing frequency due essentially to the following factors: transition length, dielectric loss tangent or CPM mode excitation. The two first factors make S_{21} parameter decreases smoothly as a function of frequency while the CPM mode makes it decrease roughly due to its resonant nature. The dielectric material and the transition length are often determined by the functional device, so one should optimize the geometrical dimensions of the transitions to obtain the largest bandwidth possible.

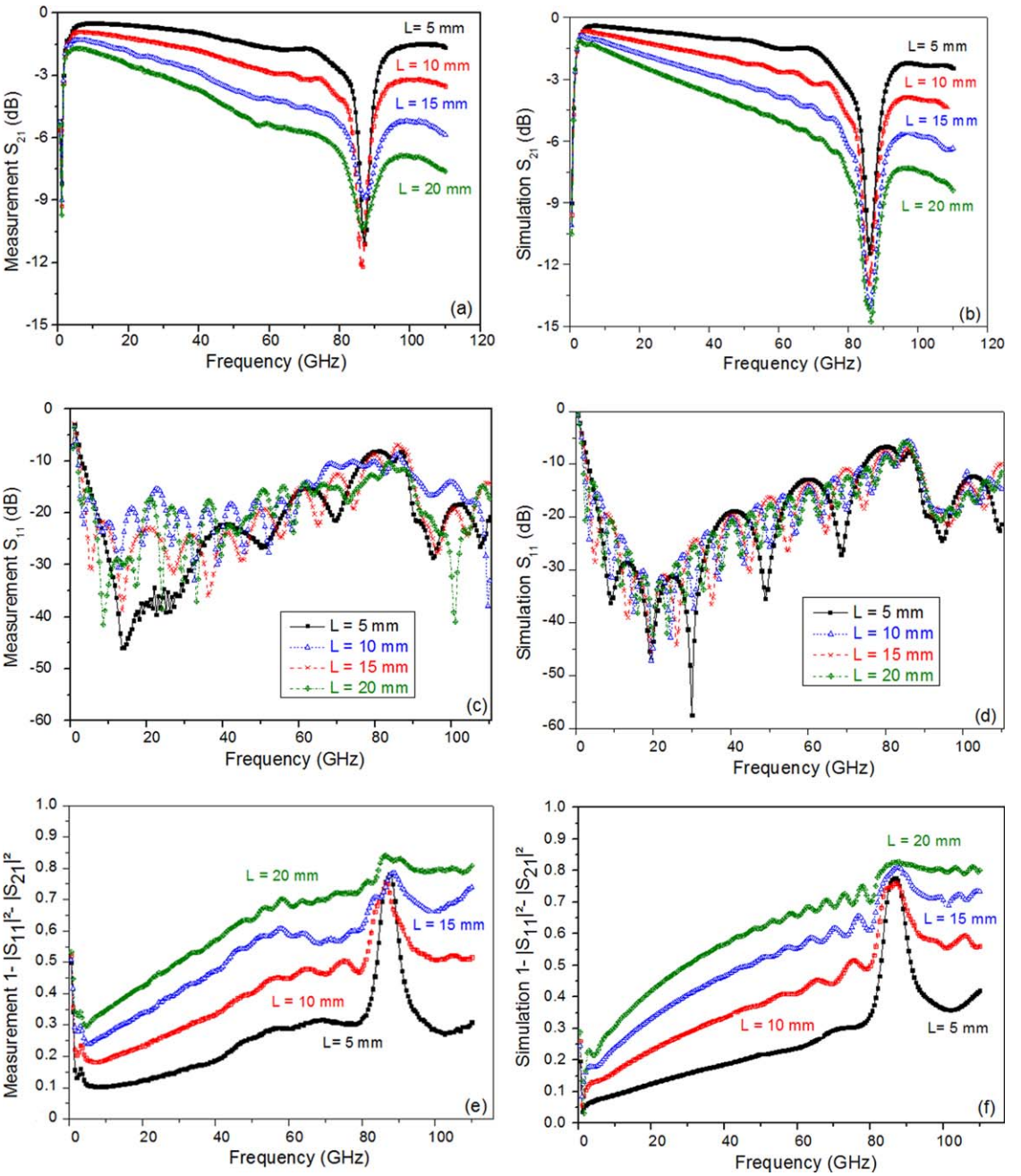

Figure 3 Results of the back-to-back GCPW-MS-GCPW transitions for different structure lengths ($L = 5$, 10, 15, and 20 mm). (a) Measured transmission coefficient (S_{21}), (b) Simulated transmission coefficient (S_{21}), (c) Measured return losses (S_{11}), (d) Simulated return losses (S_{11}), (e) Radiation losses calculated with measured *S*-parameters, (f) Radiation losses calculated with simulated *S*-parameters. [Color figure can be viewed in the online issue, which is available at wileyonlinelibrary.com]

The CPM mode is due to resonance between the bottom ground plane of MS line and CPW top ground pads and it fixes the higher border of the transition bandwidth. Its excitation frequency is given by the relation Eq. (1) [7]:

$$f_{mn} = \frac{c}{2\sqrt{\varepsilon_r}}\left[\left(\frac{m}{S}\right)^2 + \left(\frac{n}{L1}\right)^2\right]^{0.5} \quad (1)$$

Where c is the free-space light velocity, ε_r is the dielectric constant, $L1$ and S are respectively the length and the width of the CPW pads, m and n are integers representing the mode indexes. Figure 4 shows the field distribution at the resonance frequencies, in the top view of GCPW-MS transition, for the mode ($f_{10} = f_{01}$) in the left and the mode f_{11} in the right. At the resonances frequencies, the CPM mode is excited, the energy is clearly localized between the coplanar ground pads and the MS ground plane instead of propagating along the center strip, resulting in the drop in transmission and so the dip on the S_{21} parameter, which is clearly shown in Figure 5. The electric field profile at 10 GHz—outside any resonance peak—is displayed in Figure 5(a) and at 88 GHz corresponding to the resonance frequency $f_{10} = f_{01}$ in Figure 5(b).

According to Eq. (1), the upper cutoff frequency value decreases with increasing pad sizes S and $L1$ as well as increasing substrate permittivity ε_r. If one wants to push it to large values, one should use small CPW pads and low-k substrate material. As

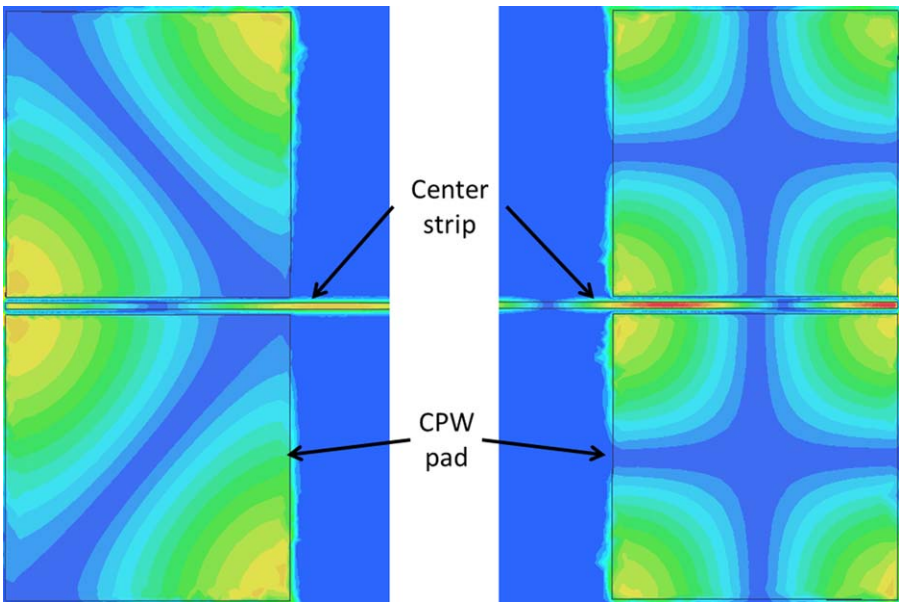

Figure 4 Electrical field distribution at resonance peak in the top view of the GCPW-MS transition: $m = 1$ and $n = 0$ at the left-hand side and $m = 1$ and $n = 1$ at the right-hand side. [Color figure can be viewed in the online issue, which is available at wileyonlinelibrary.com]

the lower cutoff frequency depends on the pads surface and the upper cutoff frequency depends on the (maximum) pads sizes, square pads allow obtaining the broad bandwidth possible with given substrate material and thickness.

5. CONCLUSION

In this article, we have shown that the via-free back-to-back GCPW-MS-GCPW transition can achieve a very large bandwidth of 75 GHz and a lower cutoff frequency of only 2 GHz. Indeed, this last is obtained thanks to substrate thinness, its low permittivity with BCB polymer, and design optimization, but also due to high conductivity of copper and its good adherence to BCB polymer. To our best knowledge, 75 GHz-bandwidth has never been achieved so far by via-free GCPW-MS-GCPW transitions. In addition to experimental and theoretical results, we have explained the guideline for optimization of transitions according to desired applications. We will study the influence of high temperatures (until 200°C), humidity and applied electrical fields on possible copper oxidization and diffusion into polymers. These transitions simple and cheap to produce will facilitate the characterization and the connectorization of components using MS driving electrodes.

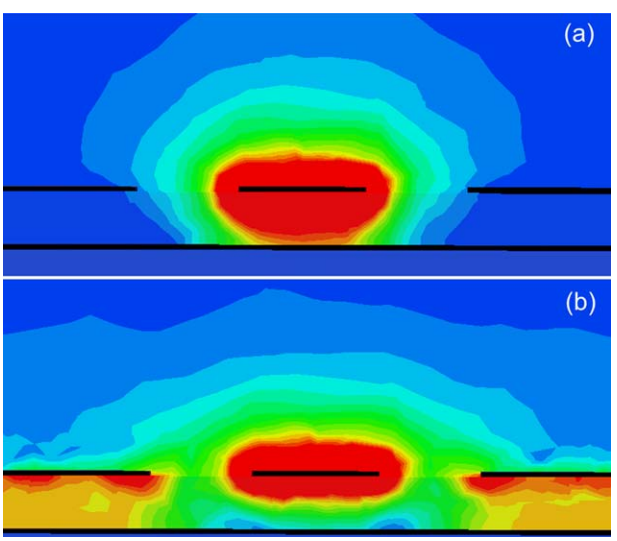

Figure 5 Electrical field distributions in the input of the GCPW-MS transition at (a) 10 GHz (frequency outside any CPM resonance) (b) 88 GHz (frequency at a CPM resonance). [Color figure can be viewed in the online issue, which is available at wileyonlinelibrary.com]

ACKNOWLEDGMENT

The authors wish to thank Vanessa Avramovic with the Institute of Electronics, Microelectronics and Nanotechnology (IEMN) for the measurements of *S*-parameters of the presented transitions.

REFERENCES

1. M.G. Larrode, A.M.J. Koonen, and J.J.V. Olmos, Overcomming modal bandwidth limitation in radio-over-multimode fiber links, IEEE Photo Technol Lett 18 (2006), 2428–2430.
2. R.N. Simons, Coplanar waveguide circuits, components and systems, Wiley, New York, NY, 2001.
3. M. El gibari, D. Averty, C. Lupi, H.W. Li, and S. Toutain, Ultra-wideband GCPW-MS-GCPW driven electrode for low-cost and wide range application electro-optic modulators, Microwave Opt Technol Lett 52 (2010), 1078–1082.
4. M. El gibari, D. Averty, C. Lupi, M. Brunet, H.W. Li, and S. Toutain, Ultra-broad bandwidth and low-loss GCPW-MS transitions on low-k substrates, Electron Lett 46 (2010), 931–933.
5. J.-P. Raskin, G. Gauthier, L.P. Kathei, and G.M. Rebeiz, Mode conversion at GCPW-to-microstrip-line transitions, IEEE Trans Microwave Theory Tech 48 (2000), 158–161.
6. M.D. Janezic, D.F. Williams, V. Blaschke, A. Karamcheti, and C.S. Chang, Permittivity characterization of low-k thin films from transmission-line measurements, IEEE Trans Microwave Theory Tech 51 (2003), 132–136.
7. W.H. Haydl, Resonance phenomena and power loss in conductor-backed coplanar structures, IEEE Microwave Guided Wave Lett 10 (2000), 514–516.

An ultra-wideband dielectric material characterization method using grounded coplanar waveguide and genetic algorithm optimization

Massinissa Hadjloum,[1] Mohammed El Gibari,[1] Hongwu Li,[1] and Afshin S. Daryoush[2]
[1]*Faculté des Sciences et Techniques, Institut d'Electronique et de Télécommunications de Rennes, Lunam Université, Université de Nantes, 2 Chemin de la Houssinière, BP 92208, 44322 Nantes cedex 3, France*
[2]*Department of ECE, Drexel University, 3141 Chestnut St. Philadelphia, Pennsylvania 19104, USA*

(Received 12 July 2015; accepted 30 September 2015; published online 8 October 2015)

An ultra-wideband complex permittivity extraction method is reported here using numerical fitting of scattering parameters to measured results. A grounded coplanar waveguide transmission line is realized on an unknown dielectric material, whose dielectric constant and loss tangent are extracted by the best fitting of the simulated magnitude, $|S_{21}|$, and phase, ϕ_{21}, of forward scattering parameter using an electromagnetic full-wave simulator (high frequency structure simulator) to the measured results. The genetic algorithm is employed for optimum rapid extraction, where errors between the numerically simulated and measured S_{21} ($|S_{21}|$ and ϕ_{21}) are minimized in an iterative manner. As long as the convergence criterion is not satisfied, modifications to dielectric properties are made with this genetic algorithm implemented in Matlab. Feasibility of this extraction technique is validated on benzocyclobutane polymer from 10 MHz to 40 GHz. © *2015 AIP Publishing LLC*.
[http://dx.doi.org/10.1063/1.4933019]

Design of passive microwave circuits and antennas requires knowledge of intrinsic characteristics of dielectric materials used in the physical realization of these components. The relative complex permittivity of various dielectrics, $\varepsilon_r^* = \varepsilon_r(1 - j\tan\delta)$, is the most practical parameter in the design of microwave components. The real dielectric constant (ε_r) is indispensable for optimization of various important parameters, such as characteristic impedance, bandwidth and phase velocity of RF signals, while the loss tangent, $\tan\delta$, is required for predicting RF losses and circuit efficiency in these components. In addition, for wideband applications, these parameter values are required over the whole operating frequency bands.

Diverse methods have been reported for complex dielectric constant measurement in literature.[1–6] Each one is adapted for a given frequency range and a given range of values for ε_r and $\tan\delta$. Capacitive[1] and resonant cavities[2] are the most popular techniques for narrow frequency band characterization due to their accuracy and simplicity of implementation. For wideband dielectric characterization, methods based on transmission lines are better suited. Microstrip (MS) lines have been widely used for broadband dielectric constant measurement, where the dielectric under test (DUT) can be used either as a substrate[3] or a superstrate[4] of the MS line. Bernard and Gautray put the material to characterize on the top of a MS ring resonator,[4] resulting in a resonant frequency change depending on the complex permittivity of the DUT. The use of coplanar waveguide (CPW) instead of MS lines has been investigated by Hinojosa *et al.*[5] The CPW configuration is advantageous over the MS line at high frequencies due its non-dispersive characteristic impedance/phase velocity and reduced radiation losses, thereby improving the dielectric constant extraction accuracy over a wider frequency band.

All of these reported methods[1–5] are based on measurement of transmission and/or reflection coefficients (S_{21}, S_{11}) or complex propagation constant (γ) and/or characteristic impedance (Z_c), whose analytical formulas are used to extract complex permittivity of dielectric materials. As analytical models are valid for a limited frequency range, the extracted values are also valid over a limited frequency range. However, Tofighi and Daryoush[6] employed the electromagnetic wave numerical modeling using finite element method (FEM) (e.g., High Frequency Structure Simulator, HFSS) to extract the complex permittivity of biological matters up to 50 GHz. Their broadband extraction approach, however, employed scattering measurement and fitting of the MS lines coupled to biological samples under test through a small circular aperture made in the ground planes of the MS lines.

In this paper, we present an original extraction approach of complex permittivity of dielectrics over an ultra-wideband (UWB) using numerical modeling of Grounded Co-Planar Waveguide (GCPW) on thin DUT. This measurement structure allows an excellent interaction of electromagnetic waves with the DUT and presents even less dispersion than the CPW line. A thin film of the DUT is used as a substrate for the GCPW. To make our technique accurate over an UWB, we avoid using any analytical models whose validity is always restricted by various modeling approximations. The FEM based full electromagnetic wave simulator HFSS is employed to simulate the scattering parameters of the DUT and best fits it to the measurement results. Other numerical modeling methods, such as Finite-Difference Time-Domain (FDTD) or Method of Moments (MoM), can be used for the electromagnetic modeling of the GCPW structure with different modeling accuracy and computation time. The magnitude and phase of the transmission coefficient, S_{21}, are calculated with an initially estimated relative permittivity and loss tangent and then compared with the measured ones; a fitness function parameter, Δ, is evaluated, which is defined as a sum of weighted differences between simulated and measured S_{21}-parameters. The accepted extracted values of

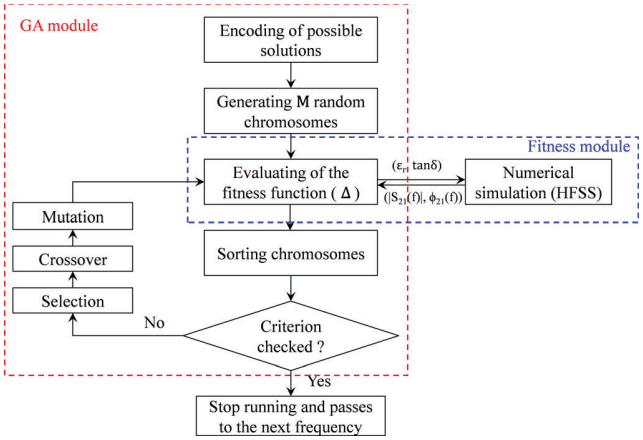

FIG. 1. Flowchart of complex permittivity extraction for dielectric substrates by combining the electromagnetic simulation using the HFSS software and the GA for optimized extraction convergence.

ε_r and $\tan\delta$ are those that reduce Δ below a certain threshold. An optimization algorithm (e.g., genetic algorithm) was employed in order to reduce the total extraction time for this optimization problem with the two unknown variables of ε_r and $\tan\delta$. Local optimization methods, such as gradient or random search, are fastest but they are susceptible to getting stuck in local minimum. Global optimization algorithms tend to be slow than local methods, but are more accurate at finding a global minimum solution. For this work, we have employed the global minimization method using genetic algorithm (GA).

Optimization based on GA has already been used in the multivariable electromagnetic problems, particularly, for optimization of the geometrical parameters of antenna structures.[7–9] However, the GA has not been much applied in material characterization procedures. Zhang *et al.*[10] have used GA combined with analytical models for extracting dispersion characteristic of dielectric material up to 10 GHz. The validation of the proposed dielectric characterization method was carried out only up to 40 GHz due to our current measurement band limitations in the employed Vector Network Analyzer (VNA) and CPW probes for this extraction procedure. However, this extraction method is valid for any frequency range as long as an accurate FEM numerical simulation is performed using the appropriate frequency dependent meshing.

The dielectric characterization technique developed in this paper is based on adjustment of ε_r and $\tan\delta$ values that minimizes aggregate error between simulated and measured values of $|S_{21}(f)|$ and $\phi_{21}(f)$ for each frequency. The extraction technique was implemented in Matlab. A main application manages the GA module, fitness module, and data exchange between the GA and HFSS, as described in the flowchart of Figure 1. The fitness module compares the numerically simulated using HFSS and the measured S_{21}-parameters of the GCPW structure to evaluate the fitness function

$$\Delta = \frac{1}{2}\left[\sum_f \sqrt{\left[|S_{21}(f)|_{meas} - |S_{21}(f,\ \varepsilon_r,\ \tan\delta)|_{sim}\right]^2} + \frac{1}{\pi}\sum_f \sqrt{\left[\phi_{21}(f)_{meas} - \phi_{21}(f,\ \varepsilon_r,\ \tan\delta)_{sim}\right]^2}\right], \quad (1)$$

where $|S_{21}(f)|_{meas}$ and $|S_{21}(f,\ \varepsilon_r,\ \tan\delta)|_{sim}$ are the measured and simulated linear magnitude of the S_{21}-parameter, respectively, while $\phi_{21}(f)_{meas}$ and $\phi_{21}(f,\ \varepsilon_r,\ \tan\delta)_{sim}$ are the measured and simulated phase of the S_{21}-paramter respectively. The fitness function is defined as the absolute magnitude difference plus the normalized absolute phase difference of the measured and simulated S_{21}-parameters. Convergence is done when the fitness function Δ is below a defined threshold. If the convergence criterion is not satisfied, the GA module generates another complex dielectric constant to re-calculate the S_{21}-parameters of the GCPW structure that could lead to a smaller Δ. This process is iteratively performed to globally reduce Δ and lead to an acceptable extracted value of the complex dielectric constant.

The GA searching for an optimum complex dielectric constant is based on genetic mechanisms and stochastic operators.[9] It relies on evolution of the estimated ε_r and $\tan\delta$ population during some number of iterations until meeting a stopping criterion, as shown in the GA module of Figure 1. An initial population of ε_r and $\tan\delta$ is generated randomly with a good dispersion in the predefined solutions domain. All possible values of ε_r and $\tan\delta$ are represented in binary code and called genes, a gene ε_r and a gene $\tan\delta$ constitute a chromosome $(\varepsilon_r, \tan\delta)$. In our approach, the dielectric characterization is considered as an optimization problem with two unknown variables. For each chromosome $(\varepsilon_r, \tan\delta)_i$, $i = 1, 2, \ldots, M$, where M is the chromosomes number of the population, an associated fitness function is evaluated using the Equation (1). Then, chromosomes are sorted from the best to the worst in terms of their fitness function. Least fit chromosomes are rejected, and the best fits are authorized to recur. A crossover operator is then applied on the survived chromosomes to produce the next offspring chromosomes. The number of reproduced chromosomes is equal to that of the rejected chromosomes to keep the total number constant. Mutation on randomly selected chromosomes is applied to avoid local convergence. Fitness function Δ is reevaluated for offspring and mutated chromosomes.

The predefined searching domain of each parameter (i.e., ε_r or $\tan\delta$) contains 2^N values, where N is the number of bits of a gene, so that each possible N-bit binary code (i.e., gene) has its corresponding solution value of the parameter ε_r or $\tan\delta$. The population size M is chosen according to the size of the searching area. We have chosen $M = 20$ chromosomes which represent 0.5% of 4096 possible combinations over the searching area (e.g., ε_r values are distributed from 2.02 to 5.17 and $\tan\delta$ values from 0.0005 to 0.032, i.e., 2^6 values for ε_r and 2^6 values for $\tan\delta$). Convergence is achieved quickly in terms of the number of iterations (i.e., an average of 10 iterations) for an imposed stopping criterion of $\Delta < 0.05$, which was determined by a compromise between precision and computation time in our case. As the GA works with the binary code of the parameters rather than parameters themselves, the best chromosome (i.e., ε_r and $\tan\delta$) is decoded after this convergence is reached.

Complex dielectric constant is determined as a function of frequency f_j over a frequency range. For each frequency f_j, segments of $|S_{21}(f)|$ and $\phi_{21}(f)$ plots around f_j are used for evaluating the fitness function rather than the only values

$|S_{21}(f_j)|$ and $\phi_{21}(f_j)$ at f_j. In fact, a fitting vector with 200 values allows a more accurate extraction of the complex dielectric constant.

To validate our extraction method, a commercially-available polymer benzocyclobutane (BCB 3022–63) material[11] is employed as the DUT with well-known dielectric properties.[12–14] This dielectric substrate widely used in microelectronics has the manufacturer recommended dielectric constant and loss tangent values of around 2.7 (at 1–20 GHz) and 0.0008 (at 1 MHz) respectively.

The GCPW is fabricated on a silicon wafer coated with a 200 nm thick aluminum using sputtering apparatus (Alliance Concept AC450). Aluminum is used as ground plane due to its good resistance to corrosion during the BCB curing step. A 40 μm thick BCB polymer layer is then spin-coated and cured in an oven at 250 °C for 60 min. An adhesion promoter, AP3000,[15] is used prior to BCB coating to improve adhesion of the BCB on the aluminum layer. The upper metallic strips of GCPW are manufactured by depositing an 800 nm thick layer of copper using the AC450 and then etching the CPW patterns by a photolithography process using a mask aligner (Karl Suss MJB[16]) to end up with the geometry depicted in Figure 2. The measured dimensions of the fabricated GCPW are: dielectric thickness $h = 40\ \mu$m, coplanar gap $G = 78.9\ \mu$m, center strip width $W = 81.6\ \mu$m, lateral ground width $W_g = 9.9$ mm, copper thickness $t = 800$ nm, and length $L = 2.2$ mm.

Bandwidth of dielectric characterization methods can not only be limited by the used analytical models but also by the used measurement cell. For example, the capacitive method is limited to a few GHz because of dispersion.[1] In this developed technique, the employed GCPW (cf. Figure 2) provides better characteristics in terms of dispersion and radiation losses at high frequencies than the CPW and MS lines. Moreover, the full plate bottom ground plane and the thinness of the dielectric layer are two key specifications enabling an accurate extraction of the dielectric constant over an UWB frequency range.

The measured amplitude and phase of S_{21}-parameters versus frequency are depicted in Figure 3. The on-wafer measurements are performed for the fabricated GCPW using an Agilent E8364B VNA, which are shown in inset of Figure 3. Cascade CPW probes (I40-A-GSG-250) with a ground pad width of 12 μm and a pitch of 250 μm along with its calibration kit (Cascade AE-101-190) are used for calibration of the

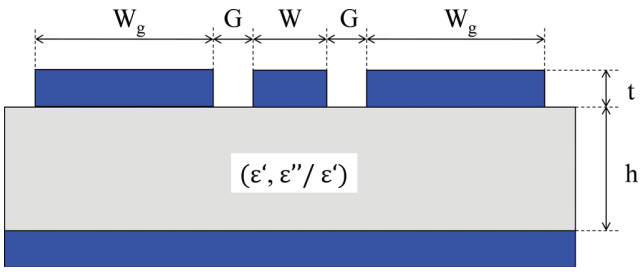

FIG. 2. Cross section of the conductor-backed coplanar waveguide used for method validation fabricated on thin film of BCB polymer. Length $L = 2.2$ mm, dielectric substrate thickness $h = 40\ \mu$m, gap $G = 78.9\ \mu$m, center strip width $W = 81.6\ \mu$m, ground strip width $W_g = 9.9$ mm, and copper thickness $t = 800$ nm.

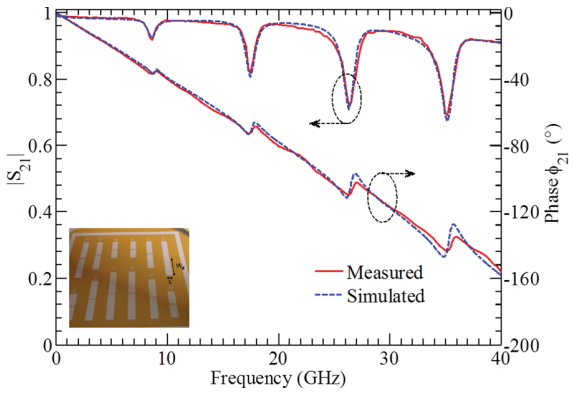

FIG. 3. Comparison of measured and simulated (with $\varepsilon_r = 2.77$ and $\tan\delta = 0.007$) of the linear magnitude and the phase of S_{21}-parameter as a function of frequency for the 2.2 mm long GCPW test structure on BCB polymer used to extract complex relative dielectric constant.

VNA up to 40 GHz using the Wincal software. Four resonance peaks are also observed in the $|S_{21}|$ response over the frequency band to 40 GHz. These resonance peaks are caused by leakage of energy between lateral and bottom ground pads of the GCPW. A higher accuracy extraction of complex dielectric constant is achieved due to these resonance frequencies in a manner similar to a cavity based system.[2] The resonance frequencies depend on ε_r, and the geometry as follows:

$$f_{mn} = \frac{c}{2\sqrt{\varepsilon_r}}\left[\left(\frac{m}{W_g}\right)^2 + \left(\frac{n}{L}\right)^2\right]^{1/2}, \qquad (2)$$

where parameters W_g and L are the lateral grounds width and length of the GCPW, respectively, m and n are integers representing the mode indices, and c is the free-space light velocity. The number and location of resonance peaks can be optimized by choosing appropriate values for the parameters W_g and L for the given dielectric constant. The measured resonance frequencies of $f_{10} = 8.73$ GHz, $f_{20} = 17.58$ GHz, $f_{30} = 26.59$, and $f_{40} = 35.52$ GHz correspond to high order modes occurrence. The resonance depth and width depends on $\tan\delta$. Large width W_g and length L increase the number of resonance peaks, so extraction accuracy but require long simulation time for each chromosome; hence, a compromise is made between simulation time and extraction accuracy due to finite computation resources.

The developed Matlab script controls calculation of S_{21}-parameters of the GCPW using HFSS for each chromosome (ε_r, $\tan\delta$) generated by the GA module. The permittivity extraction process is automated. For quick and accurate convergence, two parameters must be chosen appropriately: range of values for ε_r and $\tan\delta$, and the convergence criterion for the fitting function Δ. Comparison of the measured and simulated S_{21}-parameters is depicted in Figure 3 for the extracted value of $\varepsilon_r = 2.77$ and $\tan\delta = 0.007$. An accurate fit is achieved within a reasonable number of iterations. A number of chromosomes could meet the imposed stopping criterion of $\Delta < 0.05$ in GA. As shown in Figure 4, the extracted real dielectric constant is within the range of 2.72 and 2.87 and the loss tangent between 0.003 and 0.0085 over the frequency band from 2.5 GHz to 40 GHz. Rather than using a variation method to identify sensitivity and error analysis,[17]

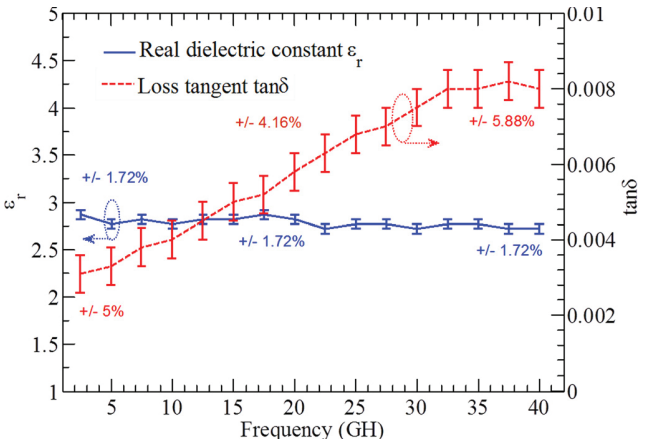

FIG. 4. Accuracy of the extracted complex dielectric constant (relative dielectric constant, ε_r, and loss tangent, tan δ) of BCB polymer, as a function of frequency.

the numerically estimated statistical variation of the best fit extractions is performed among different sets as depicted in Figure 4, where an accuracy of 1.72% for the real dielectric constant and 5.88% for the loss tangent are assigned to the results. The measured ε_r and tan δ are in agreement with the values reported in literature.

Dielectric characterization method was presented in this letter. Numerical simulations by HFSS were used to overcome bandwidth limitations due to the analytical model approximations. GA allows quick global convergence by avoiding local convergence. The process of dielectric constant extraction is automatized in a Matlab-script by controlling both numerical simulations in HFSS and the GA optimization. Validation of this method was made using a GCPW on a thin BCB polymer film over 10–40 GHz, and the obtained results are in good agreement with BCB properties reported in literature.[12–14] The presented results in this paper are limited to 40 GHz because of the measurement instrument limitations (i.e., VNA and CPW probes). However, our approach can extract complex dielectric constant over frequency band beyond 40 GHz due to the non-dispersive characteristics of the GCPW. In addition, full plate bottom ground metallization acts as screen to hide any wafer imperfections, so not only cheap silicon wafers can be used to mechanically support the substrate but also no prior wafer characterization is required. On the other hand, as shown in Figure 3, the GCPW configuration provides the possibility of generating resonances in the S_{21}-parameter, which could be used for high sensitivity extraction in a manner similar to the resonant cavities.[2] Moreover, there are extra manufacturing steps for ground plane metallization and connections between top ground pads and the grounded substrate.

[1]C. J. Mathai, S. Saravanan, M. R. Anantharaman, S. Venkitachalam, and S. Jayalekshmi, J. Phys. Appl. Phys. **35**, 240 (2002).
[2]D. C. Dube, M. T. Lanagan, J. H. Kim, and S. J. Jang, J. Appl. Phys. **63**, 2466 (1988).
[3]G. E. Ponchak and A. N. Downey, IEEE Trans. Compon., Packag., Manuf. Technol., Part B **21**, 171 (1998).
[4]P. A. Bernard and J. M. Gautray, IEEE Trans. Microwave Theory Tech. **39**, 592 (1991).
[5]J. Hinojosa, K. Lmimouni, S. Lepilliet, and G. Dambrine, Microwave Opt. Technol. Lett. **33**, 176 (2002).
[6]M. R. Tofighi and A. S. Daryoush, IEEE Trans. Microwave Theory and Tech. **50**, 2217 (2002).
[7]F. J. Villegas, T. Cwik, Y. Rahmat-Samii, and M. Manteghi, IEEE Trans. Antennas Propag. **52**, 2424 (2004).
[8]S. Sun, Y. Lv, J. Zhang, Z. Zhao, and F. Ruan, in International Conference on Microwave and Millimeter Wave Technology, 2010.
[9]R. L. Haupt, IEEE Antennas Propag. Mag. **37**, 7 (1995).
[10]J. Zhang, M. Y. Koledintseva, J. L. Drewniak, D. J. Pommerenke, R. E. DuBroff, Z. Yang, W. Cheng, K. N. Rozanov, G. Antonini, and A. Orlandi, IEEE Trans. Electromagn. Compat. **50**, 704 (2008).
[11]See http://www.dow.com/cyclotene/prod/302263.htm for cyclotene advanced electronics resins.
[12]S. Seok, N. Rolland, and P.-A. Rolland, IEEE Trans. Microwave Theory Tech. **55**, 1040 (2007).
[13]A. Modafe, N. Ghalichechian, B. Kleber, and R. Ghodssi, IEEE Trans. Device Mater. Reliab. **4**, 495 (2004).
[14]S. Costanzo, F. Venneri, A. Borgia, I. Venneri, and G. Di Massa, IET Sci., Meas. Technol. **5**, 134 (2011).
[15]See http://www.dow.com/cyclotene/prod/ap3000.htm for cyclotene advanced electronics resins—AP3000 adhesion promoter.
[16]See http://www.suss.com/en/products-solutions/products/mask-aligner for SUSS Microtech Mask Aligner.
[17]M. R. Tofighi and A. S. Daryoush, IEEE Trans. Instrum. Meas. **58**, 2316 (2009).

Optics Communications 373 (2016) 82–90

Contents lists available at ScienceDirect

Optics Communications

journal homepage: www.elsevier.com/locate/optcom

Design challenges of EO polymer based leaky waveguide deflector for 40 Gs/s all-optical analog-to-digital converters

Massinissa Hadjloum [a,*], Mohammed El Gibari [a], Hongwu Li [a], Afshin S. Daryoush [b]

[a] Lunam Université, Université de Nantes, UMR CNRS 6164: Institut d'Electronique et de Télécommunications de Rennes, Faculté des Sciences et Techniques, 2 Chemin de la Houssinière, BP 92208, 44322 Nantes cedex 3, France
[b] Department of ECE, Drexel University, Philadelphia, PA 19104, USA

ARTICLE INFO

Article history:
Received 17 March 2015
Received in revised form
29 September 2015
Accepted 1 October 2015
Available online 27 October 2015

Keywords:
All-optical analog-to-digital converter
Leaky waveguide deflector
Electro-optic polymer
GCPW-CMS transitions
Pre-emphasis technique
Effective number of bits
Spatial filter

ABSTRACT

Design challenges and performance optimization of an all-optical analog-to-digital converter (AOADC) is presented here. The paper addresses both microwave and optical design of a leaky waveguide optical deflector using electro-optic (E–O) polymer. The optical deflector converts magnitude variation of the applied RF voltage into variation of deflection angle out of a leaky waveguide optical beam using the linear E–O effect (Pockels effect) as part of the E–O polymer based optical waveguide. This variation of deflection angle as result of the applied RF signal is then quantized using optical windows followed by an array of high-speed photodetectors. We optimized the leakage coefficient of the leaky waveguide and its physical length to achieve the best trade-off between bandwidth and the deflected optical beam resolution, by improving the phase velocity matching between lightwave and microwave on one hand and using pre-emphasis technique to compensate for the RF signal attenuation on the other hand. In addition, for ease of access from both optical and RF perspective, a via-hole less broad bandwidth transition is designed between coplanar pads and coupled microstrip (CPW-CMS) driving electrodes. With the best reported E–O coefficient of 350 pm/V, the designed E–O deflector should allow an AOADC operating over 44 giga-samples-per-seconds with an estimated effective resolution of 6.5 bits on RF signals with Nyquist bandwidth of 22 GHz. The overall DC power consumption of all components used in this AOADC is of order of 4 W and is dominated by power consumption in the power amplifier to generate a 20 V RF voltage in 50 Ohm system. A higher sampling rate can be achieved at similar bits of resolution by interleaving a number of this elementary AOADC at the expense of a higher power consumption.

1. Introduction

High speed analog-to-digital converters (ADCs) are key components for enhancing high speed communications systems, such as broadband satellites at millimeter wave frequencies [1] and extremely high-throughput wireless systems [2]. Tens of gigahertz ADCs are required to cope with the increasing need of real time digital signal processing (DSP) of broad bandwidth analog RF signal in direct digital receivers. However, electronic ADCs have inherent difficulties in reaching high bandwidth with appropriate resolution [3] because of timing jitters of the electronic clocks. The real-time oscilloscope LabMaster 10 Zi–A built by LeCroy is claimed to have until 100-GHz bandwidth with a 240 GS/s sampling rate [4]; however, all real-time oscilloscopes operating over 10 GHz currently are based on multiple interleaved ADC that employs a lower sampling rate ADC [5] as their elementary unit ADC. In the same way, 56-GS/s 8-bit ADC by Fujitsu is built with 320 interleaved 175-MS/s 8-bit ADCs [6]. Interleaving is a very attractive and efficient technique to increase sampling rate and could in principle be applied to many ADC even though it results in a higher complexity, more noise, and high power-consumption for the same effective number of bits (ENoB). The interleaved ADC suffer from matching problems in time between each interleaved elementary ADCs; moreover, K. Poulton [7] predicted that not all ADCs could be interleaved and Rohde & Schwarz opted to develop a single flash ADC with 8 bits of resolution that samples at 10 GS/s and 7 ENoB in its R&S@RTO Series real-time oscilloscopes [8]. According to the latest survey of the ADC performances in July 2015 by Murmann [9], the fastest single-channel flash ADC was reported by W. Cheng et al. [10] and it operates with direct conversion rate up to 40 GS/s but only 3 bits resolution. The targeted performance of AOADC presented in this paper is with a sampling rate of 44 GS/s and a 6.5 bits resolution that results in a resolution-sampling rate product of 3.98×10^{12} LSBs-Hz, which is an order of magnitude higher than the fastest single-channel electronic flash ADCs with 3.2×10^{11} LSBs-Hz. Current research on electric ADCs

* Corresponding author.
E-mail address: massinissa.hadjloum@univ-nantes.fr (M. Hadjloum).

http://dx.doi.org/10.1016/j.optcom.2015.10.009
0030-4018/

focuses on reduction of power consumption and active area [11]. Optical ADCs take advantage of much lower optical clock jitters available from mode-locked laser (MLL) to achieve tens of giga-samples-per-second (GSPS) rates with high resolution by avoiding the aperture jitter limits of the electronic ADC. All-optical ADCs (AOADCs) perform both sampling and quantization in optical domain, as opposed to hybrid ADCs where usually sampling is done in optical domain and quantization in electrical domain [12]. The AOADC reported in this paper operates in spatial domain, using an electro-optic (E–O) polymer based leaky waveguide deflector, by converting magnitude of input analog voltage into angular displacement of a leaky optical beam. The amount of deflected optical beam power impinging on each optical window is the same for each applied RF voltage level and results in the same amplitude for each digitized bit; hence, it does not suffer from quantization errors observed in other ADC. The AOADC is designed to operate at Nyquist sampling rate of 40 GSPS with effective number of bit resolution of over 6.5 bits (i.e., 90 quantization levels), on instantaneous signal bandwidth of 22 GHz.

E–O polymers based leaky waveguide deflectors are selected over E–O crystals because of its ultra high-speed operation, a better phase velocity matching between traveling optical and electric waves due to a smaller difference in index of refraction at RF and optical frequencies, and manufacturing compatibility with Si-Photonics. RF bandwidth of 110 GHz is demonstrated for stabile E–O polymer based optical Mach–Zehnder (MZ) modulators [13]. In addition, the progress in chromophore synthesis and high efficiency poling allow obtaining polymers with E–O coefficient up to 350 pm/V [14], while the E–O coefficient of the widely used inorganic crystals in commercial MZ modulators, such as $LiNbO_3$, is only 31 pm/V.

The operation principle of the AOADC is explained in the Section 2, while the Section 3 addresses bandwidth optimization by improving velocity matching between microwave and optical wave and resolution optimization by compensating for the RF electric field attenuation using pre-emphasis filtering of CMS electrodes. Finally, the via hole free back-to-back GCPW-CMS-GCPW microwave transitions from external RF coaxial probe transition to planar transmission lines are presented in the Section 4 that results in both velocity matching and uniform RF field distribution along the optical waveguide.

2. Principle of AOADC using leaky waveguide E–O deflector

Fig. 1 depicts the principle of the spatial-sampling AOADC based on leaky waveguide E–O deflector, where short optical pulses at GSPS rates from MLL are being spatially deflected using an E–O polymer based leaky waveguide deflector, and quantization is attained by illuminating the deflected optical pulses on an spatial optical filter that is realized based on a selected binary coding mask. The short optical pulses samples the applied RF signal by deflecting the light in the E–O polymer based optical deflector and then passed through optical windows, which are used for quantization by detecting deflected light beam using an array (e.g., 8×3 for a 3 bit quantizer) of ultra high-speed photodetectors. The MLL generates short pulses of the order of picoseconds and of timing jitters below 100 fs at repetition rate of over 40 GHz to achieve Nyquist sampling of 40 GSPS for an RF signal with a maximum bandwidth of 20 GHz. The minimum required optical power of MLL is about 15 mW with DC and drive RF mode-locking power consumption of under 100 mW [15]. The E–O deflector steers the optical beam from the MLL into a direction according to the magnitude of the RF signal.

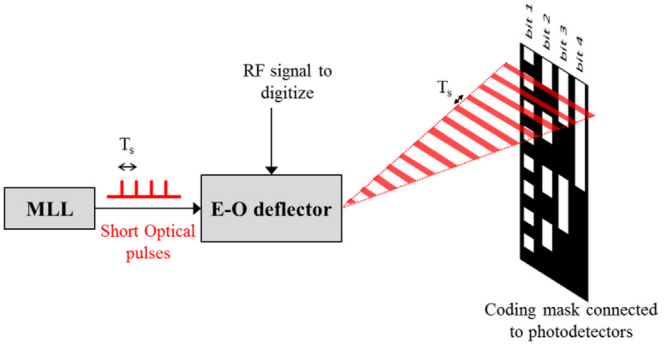

Fig. 1. : Principle diagram of AOADC working in spatial domain based on E–O deflector.

The optical waveguide deflector converts the RF voltage variation into angular deflection angles of the leaky beam; therefore, the position of each sampling pulse on the coding mask varies as a function of the magnitude of the applied RF analog signal. Low speed (sub-milliseconds) optical deflectors have been developed for optical scanners, laser printers, and photocopiers, but the leaky optical waveguide deflector is designed for a very high-speed (sub-nanoseconds) operation. In fact, the leaky waveguide deflector with sub-nanoseconds deflection speeds is a critical component of this proposed GSPS AOADC, where its RF bandwidth determines the Nyquist sampling bandwidth. Moreover, the diffracted optical beamwidth and the maximum optical deflection angle of this optical deflector define the effective number of bits of this spatial sampling AOADC. These features make the design aspects of optical deflector somewhat challenging.

The quantization of the proposed AOADC is based on optical spatial filtering using a coding mask, as depicted in Fig. 1. The apertures of the optical spatial filter collect the angular information by an array of photodetectors mounted behind the array of apertures. High-speed photodectetors of RF bandwidth above 20 GHz are necessary for quantizing the sampled RF signal at the MLL wavelengths. The binary decisions of logics “0” and “1” for each aperture corresponding to a given bit is performed after the photodetection of the deflected short optical pulses across an array of optical spatial filter apertures. For a 7 bit AOADC, a 128×7 array of photodetectors are required. When the deflection angle points to a specific row of photodetectors, then the binary on or off optical window pattern quantizes the RF signal. The logic bit “1” (e.g., a photocurrent of about mA for about mW optical power out of optical deflector) is considered when the detected photocurrent is above a set threshold (e.g., about 10 μA) and logic bit “0” (e.g., dark reverse channel current of 100 nA) is set to be well below threshold well below (e.g., about 10 μA). In addition to the binary coding masks, the Gray coding masks could also be realized to improve accuracy of quantization process by changing the distribution of the optical windows across photodetector array.

3. Geometry and design of leaky waveguide deflector

Physical geometry of the E–O polymer based optical deflected is depicted in Fig. 2. In the design and performance simulation of this optical deflector, three-dimensional (3D) optical modeling is performed using beam propagation method (BPM) in the integrated optics simulator of OptiBPM, a commercial CAD tool developed by Optiwave Systems Inc. The BPM solver employs finite difference solution of Maxwell's equations in place of partial derivatives and it is a computationally intensive program that accurately calculates a very wide range of optical devices. A commercial CAD tool developed by Ansys Inc, High Frequency Structure Simulator, is employed for full wave microwave modeling of E–O deflector. The numerical simulation and design optimization

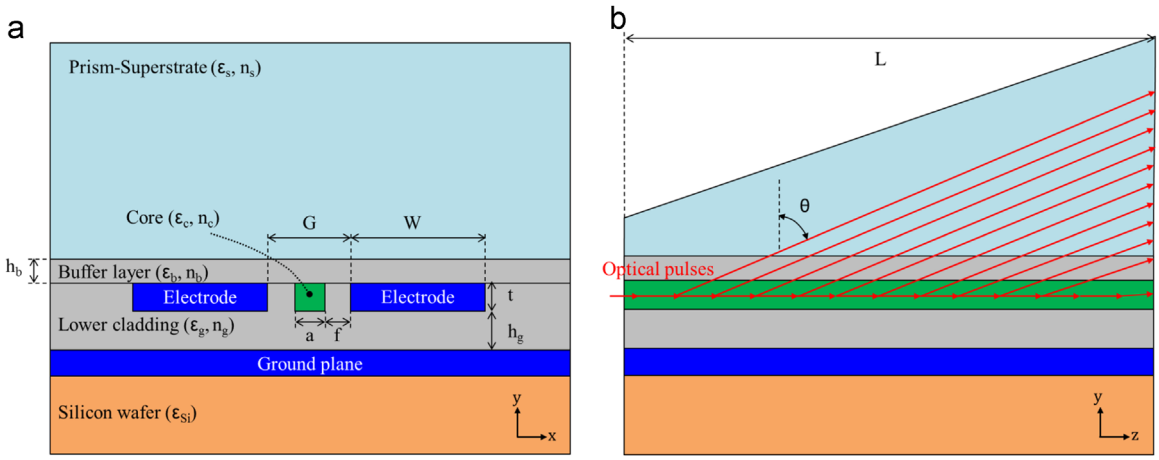

Fig. 2. The optical leaky waveguide deflector on silicon wafer. (a) Cross section. (b) Longitudinal section.

is performed by solving Maxwell's equations at discrete nodal points on tetrahedron meshes using the finite element method (FEM).

The leaky waveguide deflector of the AOADC has a structure similar to that of a conventional optical phase modulators, except that the top cladding (buffer layer) is thin enough and covered by a prism-superstrate (cf. Fig. 2), whose refractive index n_s is greater than the effective index n_{eff} of the waveguide. The applied RF signal causes change in index of refraction of the E–O polymer based optical waveguide and hence changes the refracted wave angle. Nonetheless, tail of the optical field extends into the superstrate due to dispersion relationship of waves in the optical waveguide of substrate and superstrate. Since normal component of the wave Poynting vector in superstrate has a real part, then energy leaks out of the optical waveguide from superstrate, while the wave vector also propagates along the longitudinal direction of the optical waveguide, as depicted in Fig. 2b. The modulation bandwidth and resolution of the AOADC is sensitive to the thickness of the buffer layer h_b, index of refraction difference between core and cladding regions of optical waveguide, and the material absorption losses at optical and microwave frequencies.

Since a multi-mode waveguide deflector would lead to broadening of the leaked out optical beam, then the leaky waveguide deflector requires remaining single-mode for a narrow optical beamwidth that leads to a high-resolution AOADC. In fact in leaky waveguide supporting multiple modes, every mode corresponds to a different effective index, and consequently every mode leaks at different angle θ (cf. shown in Fig. 2b) determined using Snell–Descartes' law of refraction:

$$\sin\theta = (n_{eff}/n_s) \tag{1}$$

Single-mode operation of optical waveguides at a given operating wavelength critically depends on the waveguide dimensions and the index contrast between the core and the upper and lower claddings. Several criteria must be considered when choosing the cladding material. First of all, its refractive index must be lower than that of the core E–O polymer but should have an appropriate value. In fact, high index contrast allows reducing the driving voltage by reducing the gap G between electrodes (cf. Fig. 2.a). However, too high contrast index involves a small core section, thus resulting in lower light confinement factor Γ. In addition, the cladding material must be chemically and thermally compatible with the core E–O polymer.

In order to realize a realistically high-performance AOADC that is based on leaky waveguide deflector, we assume the polymer used as core material has an E–O coefficient of 350 pm/V, as reported by Huang et al. [14]. Unfortunately the microwave and optical characteristics of this polymer is not reported in [14], hence the design is based known polymer PMMI (e.g., a host matrix polymer for the chromophore reported in [16]) to emulate an optical deflector realized using the-state-of-art E–O coefficient of 350 pm/V. The refractive index of the E–O polymer is $n_c=1.63$ with dielectric constant of $\varepsilon_c=3.15$. Lower cladding and buffer layer are with refractive index of $n_g=n_b=1.56$ and dielectric constant of $\varepsilon_c=\varepsilon_b=3.2$ (i.e., typical values for NOA63 polymer), and superstrate is in glass with $n_s=1.7$ and $\varepsilon_s=5$. All refractive indices values are considered at center wavelength of about $\lambda_0=1550$ nm and the single-mode operation of the leaky optical waveguide is achieved with 1.8 μmx1.8 μm cross-section for the square optical core. When short optical pulses from the MLL are provided using single mode optical fiber to the optical deflector, the square cross section provides a 71% light confinement in the core region and is better mode matched with spherical lensed single mode optical fibers than the rectangular waveguides.

The width f of the sidewalls between metallic RF electrodes and optical core (cf. Fig. 2a) has an impact on both light confinement and electric field for a given applied RF voltage. If distance f is too short, the optical field would not decay enough at the sidewall/electrode interfaces and lightwave would experience additional Ohmic losses due to finite conductivity of metallic electrodes; while a large separation of f results in a higher gap, G, between two coupled strips since $G=a+2f$. A larger gap leads to a higher RF voltage for a required electric field and associated deflection angle of the leaky waveguide per Eq. 1. A design compromise is made between these two limiting factors of applied voltage and lightwave confinement with selection of $f=1.2$ μm, where for a gap of $G=4.2$ μm the optical intensity decays below 1% at the sidewall/electrode interfaces.

The effective index achieved is $n_{eff}=1.5882$ with the selected material properties and dimensions, giving rise to a leaky angle $\theta=1.2061$ rad (or 69°) in absence of E–O effect ($V_{RF}=0$ V). When a RF voltage is applied, a variation of the effective index is induced via Pockels effect of $\Delta n_{eff}(z)=\frac{1}{2}n_{eff_0}^3 r_{eo}\Gamma E(z)$, where $E(z)$ is the electrical field along the propagation axis at the position z, Γ is the overlap between electrical and optical fields, $n_{eff_0}$is the effective index when $V_{RF}=0$ V and r_{eo} is the electro-optic coefficient. The resulting effective index in the core is hence expressed as:

$$n_{eff} = n_{eff_o} + \Delta n_{eff} = n_{eff_o} + \frac{1}{2}n_{eff_0}^3 r_{eo}\Gamma E(z) \tag{2}$$

This index variation modifies leaky lightwave direction by $\Delta\theta$, which can be expressed from derivative of θ with respect to n_{eff} in relation (1) by:

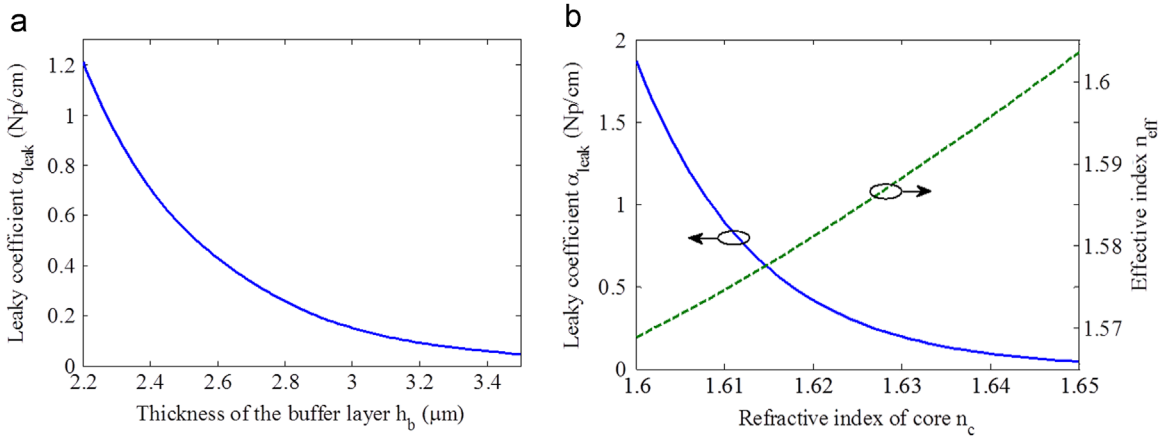

Fig. 3. : (a) Influence of the buffer layer thickness on the leaky wave coefficient with core of side $a=1.8$ μm and refractive index $n_c=1.63$ and lower cladding and buffer layer refractive index $n_g=n_b=1.56$ at wavelength $\lambda_0=1.55$ μm. (b) Influence of the refractive index of core on leaky wave coefficient with buffer layer thickness of $h_b=2.9$ μm.

$$\Delta\theta = \frac{\Delta n_{eff}}{n_s \cos\theta} = \frac{n_{eff_0}^3 r_{eo}\Gamma E(z)}{2n_s \cos\theta} \quad (3)$$

Eq. (3) demonstrates that the angular sweep $\Delta\theta$ is proportional to the applied electric field E(z); therefore, the input RF voltage is linearly mapped into angular deflection of optical beam.

3.1. Bandwidth consideration of leaky waveguide deflector

The leaky waveguide deflector should been designed to obtain the best possible velocity matching between optical and electrical waves, so each optical pulse is "accompanied" by the same traveling electric field to experience the same induced E–O effect along the waveguide at all applied RF frequencies. The velocity mismatch of the E–O deflector limits the modulation bandwidth since the modulation bandwidth is inversely proportional to [17]:

$$\Delta f = \frac{2c}{\pi\left|n_{eff} - \sqrt{\varepsilon_{RF}}\right|L}, \quad (4)$$

where c is the speed of light in free space, L is the length of the optical deflector, and ε_{RF} is the microwave effective dielectric constant. The silicon substrate for the E–O deflector is selected for its low cost integration with RF electronics circuits, good flatness, stiffness, and capability being cleaved following an accurate direction since light injection requires good input waveguide facets, but the high dielectric constant silicon wafer ($\varepsilon_{Si}=11.9$) will undoubtedly slows down the RF signal propagation wave velocity. Therefore, in order to eliminate velocity mismatch caused by high dielectric constant of silicon wafer, a metallic ground plane is set between silicon wafer and lower cladding (in NOA63) to screen the silicon as depicted in Fig. 2a. The metallic screen thus isolates the RF electric field from Si substrate, which permits to reduce considerably effective permittivity of ε_{RF}, down to 3.6 instead of 6.4 in absence of metallic ground plane. As result of a better velocity matching due to ground plane shielding, the modulation bandwidth consequently increases from 10.1 GHz to 30.9 GHz for an E–O deflector of length $L=2$ cm.

The velocity matching will not only improve the optical deflector bandwidth, but also its resolution, as the reduction in the timing jitters of MLL optical pulses and any excessive microwave attenuation. Indeed, a better velocity matching will allow a longer length for the optical deflector waveguide, which results in a narrower beamwidth; moreover, the leaky lightwave will be focused on even finer line due to constructive interference between in-phase elementary leaky optical fields generated along the waveguide. The narrower optical beamwidth increases the number of resolvable lines (i.e., quantization levels) focused on the coding mask and therefore improving the effective number of resolution bits of the AOADC. However, RF attenuations should be reduced to maintain a uniform RF electric field across the optical waveguide and maximize its resolution by using a longer optical deflector waveguide. To achieve this performance improvement, we present an original pre-emphasis technique to compensate the RF attenuation in the following sub-section.

3.2. Leaky wave divergence angle of $\delta\theta$ in lossy RF transmission lines

The number of resolved lines on the coding mask N is given by the following formula:

$$N = \Delta/\delta\theta \quad (5)$$

where $\Delta\theta$ is the total angular deflection swing according to the Eq. (3) and $\delta\theta$ is the divergence angle of leakage beam. The number of resolution bits $b=\log_2 N$. As the electro-optic coefficient of the E–O polymer enhances a larger Δ is obtained and the diffraction angle $\delta\theta$ decreases as a longer optical deflector is employed.

However, the leaky beam divergence $\delta\theta$ depends upon lightwave attenuation coefficient α_{opt}, leakage coefficient α_{leak}, length of the optical waveguide L due to diffraction, and RF attenuation coefficient α_{RF}. Particularly, different deflection angles are caused by different E–O effect over the waveguide length according to Eq. (1) and Eq. (2). The total angular deflection swing $\Delta\theta$ of the deflected beam is proportional to both maximum voltage swing of the RF signal and the E–O coefficient of polymer. For a given $\Delta\theta$ of the deflected beam, one should reduce the leaky beam divergence to increase the resolution, so the effective leaky waveguide length L_{eff} must be close to L, thus ensuring a small leaky wave beamwidth from optical diffraction. A weak leaky wave condition can be achieved by controlling the leaky coefficient α_{leak}, which varies depending on index contrast $\Delta n = n_c - n_b$ and the thickness of the buffer layer, h_b. Fig. 3a renders the influence of h_b on α_{leak}, where a thicker buffer layer results in a smaller leaky wave coefficient. For a smaller leaky waveguide coefficient the optical wave travels a longer distance over the optical waveguide and results in a smaller optical beamwidth for the diffracted beam, as the wave exits prism superstrate. However, a longer deflector reduces the modulation bandwidth due to velocity mismatch between the electrical and optical waves (cf. Eq. 4). Hence, a design compromise is made between the resolution and the bandwidth of the AOADC.

Many types of polymer materials with high E–O coefficient can be used for core of the E–O deflector. Their refractive indices range generally between 1.60 and 1.65. The dependency of the leaky coefficient on the refractive index of core E–O material is depicted

as solid line in Fig. 3b. Leaky coefficient drops with increasing index contrast between the core and the buffer layer as the optical wave is confined more in the core of the waveguide with a higher index contrast. This reduction in the optical field into the prism superstrate results in a reduced optical leakage coefficient. The effective index increases with core index as shown by the dashed lines in Fig. 3b. When the materials of the E–O deflector are selected, one can adjust the leaky coefficient at will by choosing an appropriate buffer layer thickness.

By summing the contribution at each segment dz of the waveguide to the optical leaky wave and taking into account optical and RF losses, the total leaky lightwave ψ at the deflection angle θ is given by the following integral:

$$\psi = \alpha_{leak} A e^{-jk_s r} \int_0^L \exp\left\{\left[-(\alpha_{leak} + \alpha_{opt}) - j(\beta - k_s \sin\theta)\right] z\right\} dz, \quad (6)$$

where A is the magnitude of the input lightwave in the waveguide at the origin $z=0$, $\beta = kn_{eff}$ is the phase constant of the lightwave in the waveguide, where $k = 2\pi/\lambda_0$ is the optical wavenumber in free space; α_{opt} is the total optical losses caused by material absorption and waveguide imperfection (roughness in particular). Note that E_o is the magnitude of the RF field at the input port of the coupled microstrip (CMS) electrodes, and r is a position in superstrate. The phase propagation constant β can be expressed as a function of the longitudinal position z and the RF attenuation coefficient α_{RF} as:

$$\beta = k\left(n_{eff_o} + \frac{1}{2} n^3_{eff_0} r_{eo} \Gamma E_o e^{-\alpha_{RF} z}\right) \quad (7)$$

By incorporating Eq. (7) into Eq. (6), the total leaky optical field at the deflection angle θ is then rewritten in the following integral:

$$\psi = \alpha_{leak} A e^{-jk_s r} \int_0^L \exp\left\{\left[-(\alpha_{leak} + \alpha_{opt}) - jk(n_{eff_o} - n_s \sin\theta)\right] z\right\} \exp\left[-j\frac{1}{2} k n^3_{eff_o} r_{eo} \Gamma E_o \exp(-\alpha_{RF} z) z\right] dz. \quad (8)$$

The influence of various parameters on the resolution has been studied with the help of Eq. (8) and numerically calculated (cf. Fig. 4) using the mathematical program Matlab. The peak in Fig. 4a corresponds to the normalized optical intensity of the leaky lightwave in function of output beam angle θ without any E–O effect, when $V_{RF} = 0$ V. This result has been obtained with waveguide length $L=2$ cm and leaky coefficient $\alpha_{leak}=0.1$ Np/cm. For a small value of the leaky coefficient α_{leak}, typically comprised between 0.1 and 0.2 Np/cm, optical losses have a little impact on the divergence $\delta\theta$ of leaky beam. The high leakage coefficient leads to a larger diffracted optical beam divergence angle as the effective waveguide length L_{eff} is reduced (cf. Fig. 4b). Any increase of optical losses results also in an increase of the beam divergence via reduction of the effective waveguide length. Optical losses can be further mitigated by choosing a small leaky coefficient.

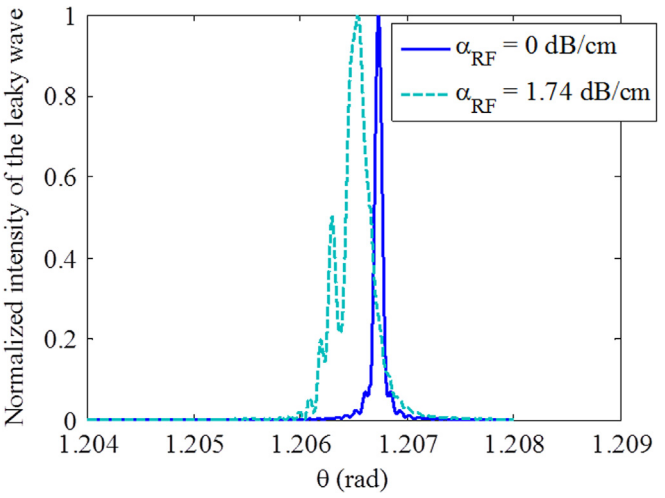

Fig. 5. : Influence of microwave losses on the beam divergence δθ. Results obtained with leaky coefficient $\alpha_{leak}=0.2$ Np/cm, effective index $n_{eff_0}=1.5882$, waveguide length $L=3$ cm and RF voltage $V_{RF}=10$ V.

Microwave attenuation degrades the resolution of an AOADC based on leaky waveguide deflector by angular broadening the optical leaky beam (i.e., making optical beam more divergent), as shown in Fig. 5. If microwave losses are negligible by setting $\alpha_{RF}=0$ in the term $e^{-j\frac{1}{2}kn^3_{eff_o} r_{eo}\Gamma E_o e^{-\alpha_{RF} z} z}$ of Eq. (8), then the leaky beams throughout the interaction length L arrive in phase at the prism and air interface of superstrate. This deflected output beams are focused at the output of the E–O deflector using a cylindrical lens. The contributions of deflected beam are added by constructive interference of the leaky wave along length L, which results in a narrow beam represented by the peak in solid line in Fig. 5. The peak beamwidth is only limited by diffraction. However, in reality, microwave losses are never null and cause enlargement of the leaky beam because the electrical field reduces over the waveguide length, so both the phase and the deflection direction of elementary leaky optical fields change from a point to another

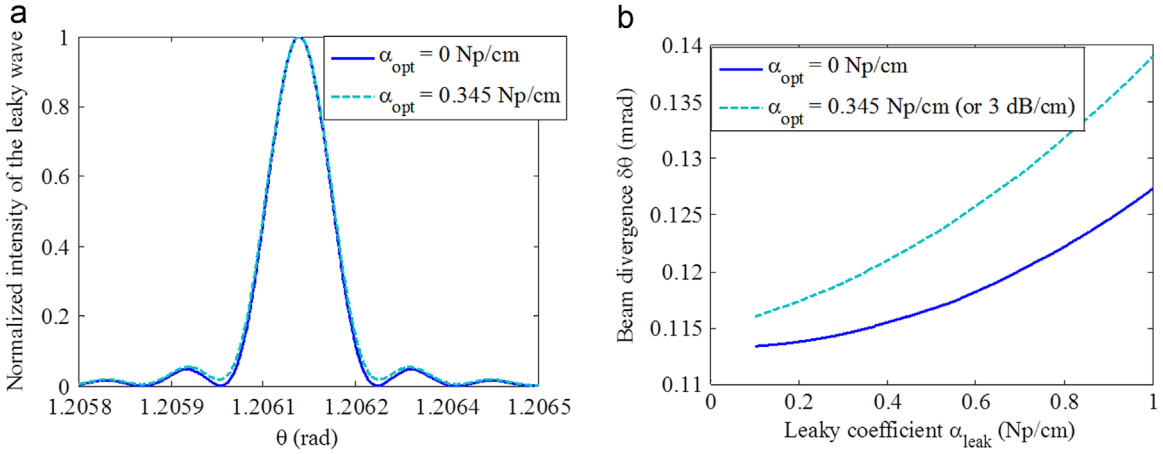

Fig. 4. : (a) Normalized intensity of the optical leaky wave in function of output beam angle θ when leaky coefficient is $\alpha_{leak}=0.1$ Np/cm, effective index of $n_{eff_0}=1.5882$, waveguide length of $L=2$ cm and electrical field $E_0=0$; (b) Influence of the leaky coefficient α_{leak} on beam divergence $\delta\theta$.

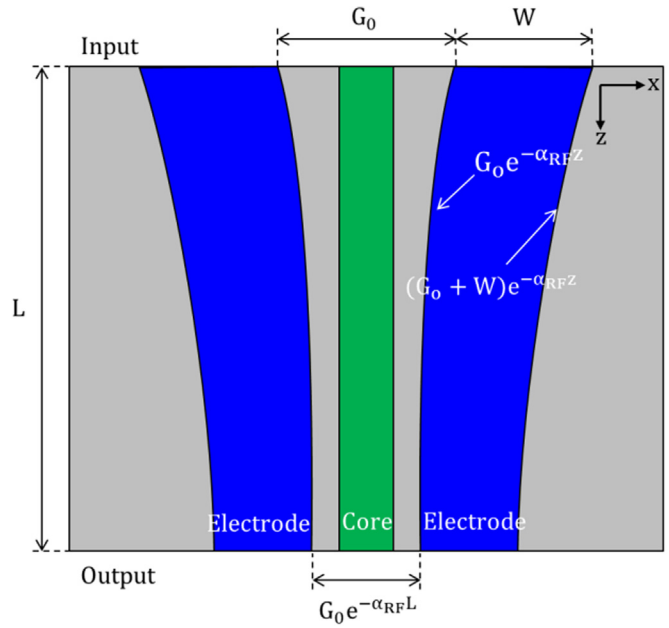

Fig. 6. : Modified CMS strips shape and gap to pre-emphasize the electric field along the propagation direction z.

along the waveguide axis. When focused by the cylindrical lens, the local leaky beams are added with different phase shifts, giving rise to an enlarged main peak with the secondary peaks depicted in dashed line in Fig. 5. This broadening of the leaky wave beamwidth is more pronounced with increasing waveguide length L due to the none-negligible RF losses. We overcome the RF propagation losses using a pre-emphasis technique.

3.3. *Pre-emphasis filter design of the electric field*

Since RF voltage applied between the two strips decays exponentially along the propagation axis *z*, electric field decays also exponentially along the propagation axis *z*. The RF electric field along with a constant gap G_0 in a classical CMS electrode:

$$E(z) = \frac{V_{RF}(z)}{G_0} = \frac{V_0 e^{-\alpha_{RF} z}}{G_0} \tag{9}$$

To negate any electric field decay, it is proposed to design a pre-emphasis filter by exponentially reducing the gap between the two strips along the axis *z*, as shown in Fig. 6. Conceptually this change in gap is equivalent to mathematically multiply the denominator in Eq. (9) by the factor $e^{-\alpha_{gap} z}$ as expressed by:

$$E = \frac{V_{RF}(z)}{G(z)} = \frac{V_0 e^{-\alpha_{gap} z}}{G_0 e^{-\alpha_{RF} z}} = \frac{V_0}{G_0} e^{(\alpha_{RF} - \alpha_{gap}) z} \tag{10}$$

Therefore, the pre-emphasized E field will be uniform, when $\alpha_{gap} = \alpha_{RF}$. To keep the characteristic impedance matched to 50 Ω along the propagation axis *z*, the strips width W is also reduced exponentially in the same manner as the gap (cf. Fig. 6).

However, microwave losses increase with frequency, as shown in Fig. 7, the bandwidth is limited over which the compensation improves significantly the E–O deflector performances. Indeed, when the compensation is performed at a given frequency f_c, electric field is slightly magnified at lower frequencies ($f < f_c$) thus still causing variation of electric field. The frequency where exact compensation is made (i. e. $\alpha_{gap} = \alpha_{RF}(f_c)$) must be chosen as a compromise between significant improvement at the high frequencies (i.e., $f > f_c$) and small distortions at the lower frequencies (i.e., $f < f_c$), according to frequency range for which resolution improvement is looked for by the pre-emphasis filtering method.

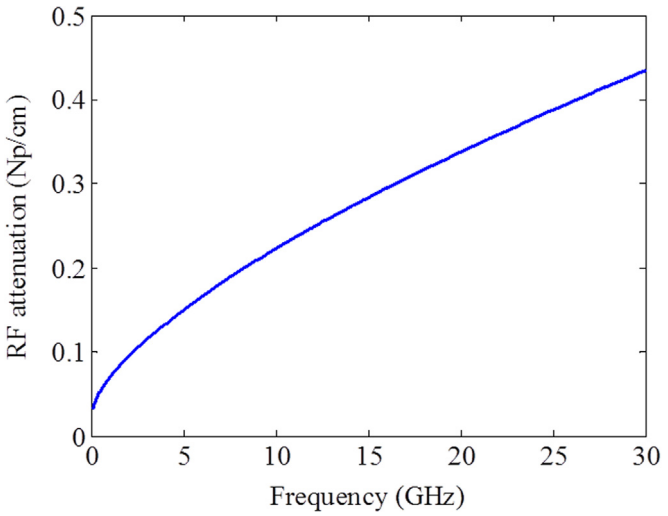

Fig. 7. : RF attenuations coefficient in the E–O deflector made with polymers PMMI (tangent loss of $\varepsilon''/\varepsilon' = 10^{-3}$) as core material and NOA65 or NOA73 (tangent loss of $\varepsilon''/\varepsilon' = 2.2 \times 10^{-2}$) as cladding and buffer material, superstrate in glass ($\varepsilon''/\varepsilon' = 10^{-5}$) and electrodes in copper (electrical conductivity of $\sigma = 5.8 \times 107$ S/m) for CMS strips.

With the microwave properties of the polymers PMMI (tangent loss of $\varepsilon''/\varepsilon' = 10^{-3}$) as core material, NOA63 or NOA73 (tangent loss of $\varepsilon''/\varepsilon' = 2.2 \times 10^{-2}$) as cladding and buffer material, superstrate prism in glass ($\varepsilon''/\varepsilon' = 10^{-5}$), and CMS strips electrodes using copper (electrical conductivity of $\sigma = 5.8 \times 10^7$ S/m), the RF attenuation coefficient α_{RF} as frequency function is plotted in Fig. 7. These polymers are chosen for leaky waveguide deflector due to their good index contrast ($n_c = 1.63$ vs $n_g = n_b = 1.56$), low material loss tangent, and good mechanical adhesion.

Fig. 8a displays the simulated magnitude of electric field in the optical core center at the frequencies 5, 10 and 20 GHz for constant strips width $W = 50$ μm and gap $G_0 = 4.2$ μm along the *z* axis. These curves show an exponential decay of the electric field intensity throughout *z* axis, which causes of the leaky wave beamwidth broadening as displayed by dashed lines in Fig. 5. The reason for this broadening of beamwidth is due to changing of both phase and local direction of leaky optical field from one point to another over the waveguide length.

Fig. 8b shows the magnitude of electric field, for the frequencies 5, 10 and 20 GHz in center of the optical core, when the gap between the two strips decay exponentially with a decay coefficient $\alpha_{gap} = 0.22$ Np/cm for 10 GHz frequency (or 1.91 dB/cm, cf. Fig. 7). The resulting electric field in the core region is constant over the waveguide length at the frequencies around 10 GHz, slowly decaying at 20 GHz (0.058 Np/cm) and weakly enhanced at 5 GHz (0.040 Np/cm). This compensation allows limiting to a very small level the electric field variation in the frequency band from 5 up to 20 GHz, which reduces considerably the divergence of leaky beam $\delta\theta$ as explained before. Therefore, this pre-emphasis improves the achieved effective resolution bits of the designed AOADC.

3.4. *Total angular sweep of* $\Delta\theta$

In Fig. 9a renders plot the two deflected beam peaks corresponding respectively to maximum applied voltages $V_{RF} = \pm 20$ V. The spacing between them corresponds to the total angular sweep $\Delta\theta$. This result has been obtained using Eq. (8) with waveguide length $L = 3$ cm, optical losses $\alpha_{opt} = 0.345$ Np/cm, RF losses $\alpha_{RF} = 0.01$ Np/cm (after RF attenuation compensation technique described in Section 3.3). A leaky coefficient $\alpha_{leak} = 0.10$ Np/cm, E–O coefficient $r_{eo} = 350$ pm/V, and gap between the two strips at the

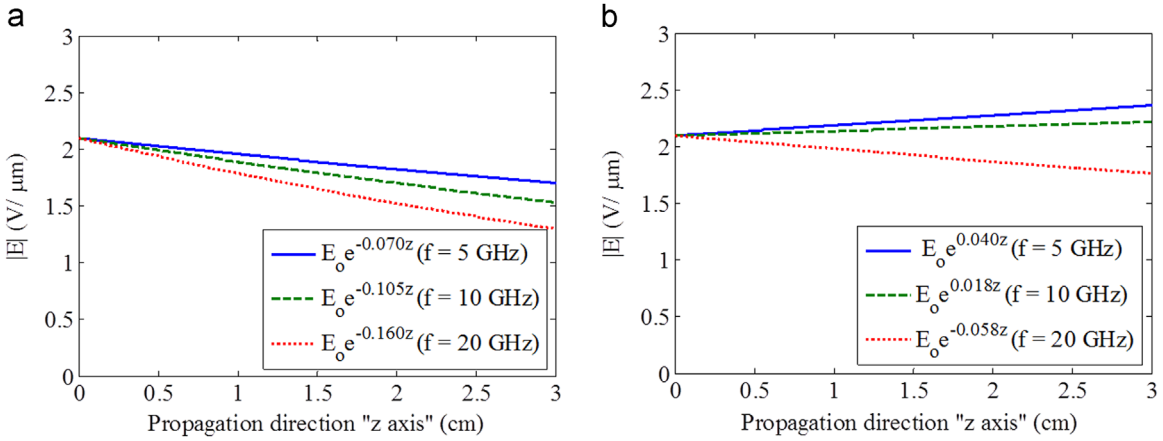

Fig. 8. : Electric field in the center of core region. (a) E–O Deflector with classical CMS line (constant gap). (b) E–O deflector with gap decaying CMS line.

waveguide input side $G_0=4.2$ μm are also employed with an overlap integral $\Gamma=100\%$ between the RF and optical fields.

The dashed line in Fig. 9b shows that when electric field attenuation is zero, the resolution is proportional to both E–O coefficient and the applied electric field. Therefore, the output angle displacement varies linearly with the applied RF voltage, so the applied voltage is linearly translated into angular displacement in the spatial domain. However under the above conditions, when considering non-zero attenuation, as shown by solid line in Fig. 9b, resolution N remains proportional to the E–O coefficient for values up to 200 pm/V. The resolution reaches an optimum value of about 73 quantization levels for 240 pm/V and then decreases beyond that level because of leaky beam angular enlargement due to interference between phase-shifted elementary leaky optical fields generated along the waveguide caused by electric field variation. In such a case, then we should reduce leaky waveguide length to achieve a higher resolution by minimizing overall phase-shift induced interference along the optical waveguide.

3.5. Optimal length of the leaky waveguide deflector

The divergence angle of the deflected optical beam from the leaky waveguide is limited by two main factors: (i) diffraction, which its impact is weakened when increasing waveguide length L; and (ii) deflection angle dispersion of the leaky wave beamwidth due to the RF field attenuation, whose the effect is increased with a longer waveguide. Actually, with short leaky waveguide, electric field variation is still small and its influence is negligible compared to diffraction effect, and therefore, in this range of length ($L<2$ cm for $r_{eo}=350$ pm/V) resolvable lines number increases proportionally with length L, as shown in Fig. 10. However depending on the strength of E–O coefficient, diffraction influence and electric field attenuation are reversed after optical deflector length of about 2 cm. The optimal length L is 2 cm for an E–O polymer with $r_{eo}=350$ pm/V, as shown in Fig. 10, leading to $N=90$ lines, which corresponds to 6.5, as the effective number of bits.

4. Microwave accesses of the E–O deflector

Using the realized traveling wave configuration with characteristic impedance of Z_0, the E–O deflector must be excited by RF matched source and load impedances of Z_S and Z_L respectively. The CMS line is designed for impedance matching to $Z_0=Z_S=Z_L=50\ \Omega$ and on the other hand, for velocity-matching between microwave and optical wave allowing operation bandwidth of over 30 GHz. The achieved characteristic impedance of Z_0 depends not only on the geometric parameters of the CMS line, but also on all the surrounding materials. The gap G between CMS electrodes is fixed by optical core width and sidewalls width. Manufacturing of core and electrodes channels can be made using reactive ion etching (RIE), which is the most common method for fabrication of the

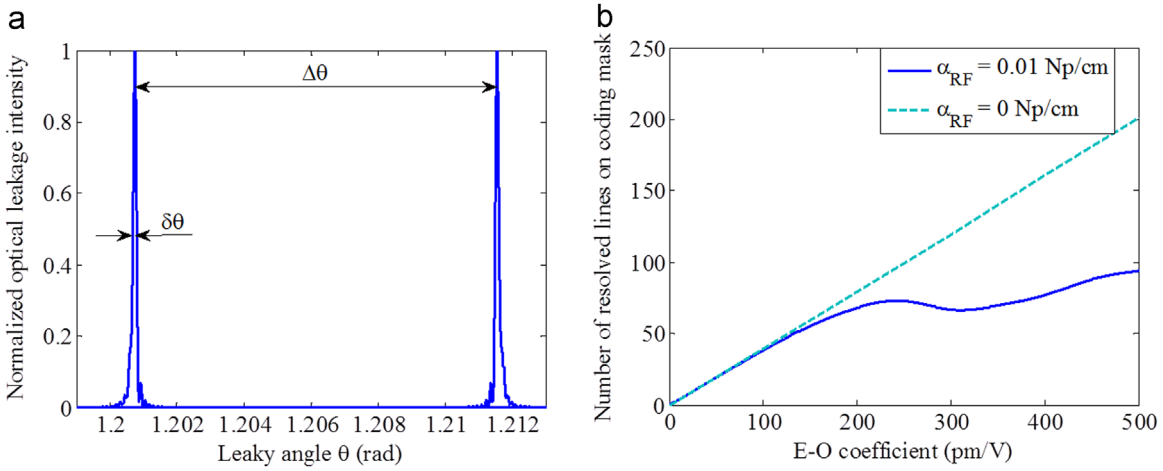

Fig. 9. : Simulation results obtained with Eq. (8) with $L=3$ cm, $\alpha_{opt}=0.345$ Np/cm, $\alpha_{RF}=0.01$ Np/cm (after RF attenuation compensation), $\alpha_{leak}=0.1$ Np/cm, $\Gamma=100\%$, $V_{RF}=\pm 20$ V and gap between strips $G_0=4.2$ μm. (a) Leaky intensity peaks for applied voltages $V=-20$ and $+20$ V and $r_{eo}=350$ pm/V. (b) Number of resolved lines on the coding mask versus E–O coefficient.

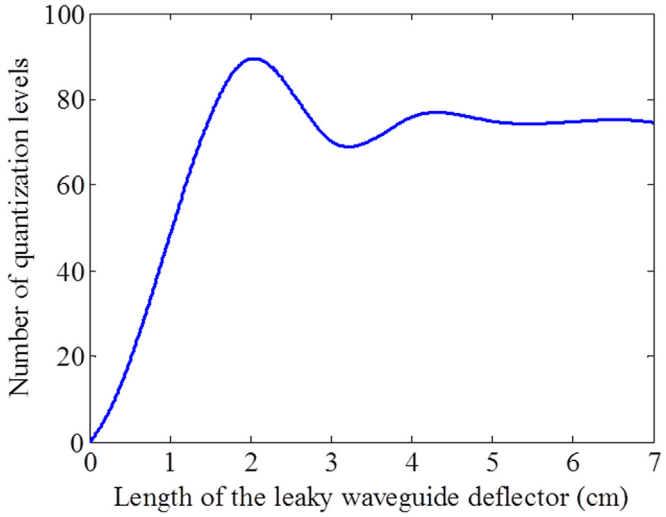

Fig. 10. : Number of quantization levels (resolved lines on coding mask) versus leaky waveguide deflector length with $V_{RF}=\pm 20$ V, $\alpha_{leak}=0.1$ Np/cm, $\alpha_{RF}=0.01$ Np/cm, $\alpha_{opt}=0.345$ Np/cm and $r_{eo}=350$ pm/V.

optical waveguides.

Both connectorized and on-wafer characterization of the E–O deflector require coplanar (CPW) microwave interconnects or the use of GSG (Ground-Signal-Ground) probes from a probe station to assure reliable electrical contacts that is compatible with coplanar transmission lines. A transition between coplanar and coupled microstrip line (CPW-CMS) is thus required to characterize components driven by the CMS line with the CPW probe station.

In the designed E-O deflector, both the optical waveguide core (with square side of $a=1.8$ μm) and the traveling wave electrodes (separated by gap of 4.2 μm at the input side) are in the same *xz* plane, as shown by the cross section in Fig. 2a. Compared with the case, where optical core is below the strips [18], this configuration allows better optical and electrical waves overlap, Γ. In fact a $\Gamma=61\%$ instead of 40% as estimated in the last design. In addition, this configuration reduces the number of technological steps by manufacturing both core and strips channels at the same technological step. However, coupling of the optical pluses from the MLL into the optical waveguide core and applying a microwave signal onto electrodes by the same side is not feasible because of mechanical limitations of accommodating both optical fiber (diameter of ~120 μm) and probe head (~3 mm). It's then necessary to bend the electrodes away from the optical input for separating the optical access points from the microwave access points, as illustrated in Fig. 11. Optical access is feasible because of constraints related to dimensions of optical core. Nevertheless, a direct CPW-CMS transition (all strips in the same level) would make one ground strip of the CMS line intersect with the optical waveguide core, which is obviously unacceptable. Our solution consists of

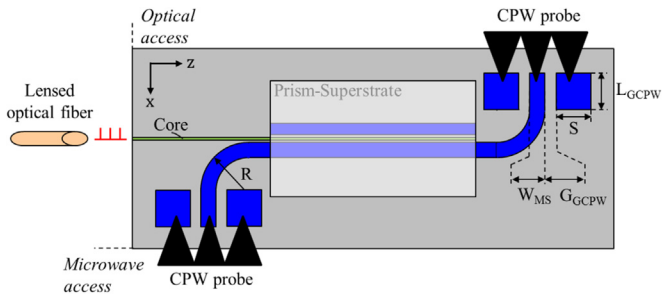

Fig. 11. : Diagram of the via-free transitions permitting applying electrical voltage to the CMS electrodes without intersecting E–O leaky waveguide.

making a virtually grounded at RF frequencies by capacitive effect of the lateral ground pads of the input GCPW section with the bottom ground plane; and then have the bottom ground plane capacitively coupled with the ground strip of the CMS line (cf. Fig. 11). In this topology the electromagnetic energy is first transferred from the input GCPW section to the bent MS line section (GCPW-MS) then from the bent MS section to the CMS line (MS-CMS).

We present in this section design and performance prediction of a back-to-back GCPW-CMS-GCPW transition for feeding the E–O deflector (cf. Fig. 11) with the CPW probes. The E-O deflector is located in the CMS section of the transition. Built on an optimum thin substrate (lower cladding in Fig. 2a) of $h_g=20$ μm in NOA63 ($\varepsilon'=3.2$ and $\varepsilon''/\varepsilon'=0.022$) to realize velocity-matching (cf. sub-Section 3.1). As both the GCPW and MS sections are built in 20 μm NOA65 polymer and the CMS section in NOA65 and PMMI E–O polymer, we use the software Linecalc from the Agilent's Advanced Design System (ADS) to determine the strip width in MS section and the gap in GCPW section for matching their characteristic impedances Z_{o_MS} and Z_{o_GCPW} to 50 Ω. In CMS section, iterative HFSS simulations are performed to determine optimum CMS strips width W_0 from the gap $G_0=4.2$ μm at the input side chosen in Section 3 for a lower cladding thickness $h_g=20$ μm and buffer layer thickness $h_b=3.2$ (for $\alpha_{leak}=0.1$ Np/cm) in NOA63 and the superstrate thickness h_{sup} of a few centimeters in glass.

Parasitic resonances in the GCPW structures were analyzed in [19], while studying GCPW-MS-GCPW transitions bandwidth. Energy in GCPW line can propagate into three modes owing to the bottom ground plane: in addition to the MS and CPW modes, a coplanar microstrip mode (CPM) is excited between bottom ground plane and coplanar pads, causing energy to escape from the CPW mode and giving rise to resonance peaks in the insertion loss plot of S_{21}-parameter curve (cf. Fig. 11). Low effective permittivity ε_{RF} pushes parasitic resonances to very high frequencies, according to Eq. (11) giving their approximate resonance frequencies using cavity model equation [20]:

$$f_{mn}=\frac{c}{2\sqrt{\varepsilon_g}}\left[\left(\frac{m}{S}\right)^2+\left(\frac{n}{L_{GCPW}}\right)^2\right]^{1/2} \tag{11}$$

where S and L_{GCPW} are GCPW ground pads width and length, as shown in Fig. 11, ε_g is relative permittivity of lower cladding, m and n are the mode integers. Parameters S and L_{GCPW} determine parasitic peaks frequency on $|S_{21}|$-parameter curve; in addition, they have an important influence on low cut-off frequency of the bandwidth. Indeed, pad surface areas of $A=S\cdot L_{GCPW}$ determines capacitive effect between CPW pads and full plate bottom ground plane. To reduce the lower cut-off frequency as small as possible without affecting significantly the higher cut-off frequency, the width and length of pads are optimized to $S=L_{GCPW}=1$ mm, so CPW mode can be stabilized and converted to MS mode in the bent section of the MS line.

Fig. 12 presents microwave bandwidth of designed E–O deflector including the via-free GCPW-CMS-GCPW transition (cf. Fig. 11). According to these results, E–O deflector can operate over the frequency range from 1.5 to 22.3 GHz. Due to the capacitive effect, this transition has a high upper cut-off frequency (22.3 GHz for an E–O deflector of length $L=2$ cm) and is easy to realize (without via-holes and without pattering bottom ground plane) resulting in a lower manufacturing cost over a via-hole based structures. However, this solution doesn't allow digitizing RF signals below 1.5 GHz due to a high insertion loss of the E–O deflector (cf. Fig. 12). Via-holes can be made between top ground pads of the GCPW line and bottom ground plane to enable a low-pass operation up to 22.3 GHz.

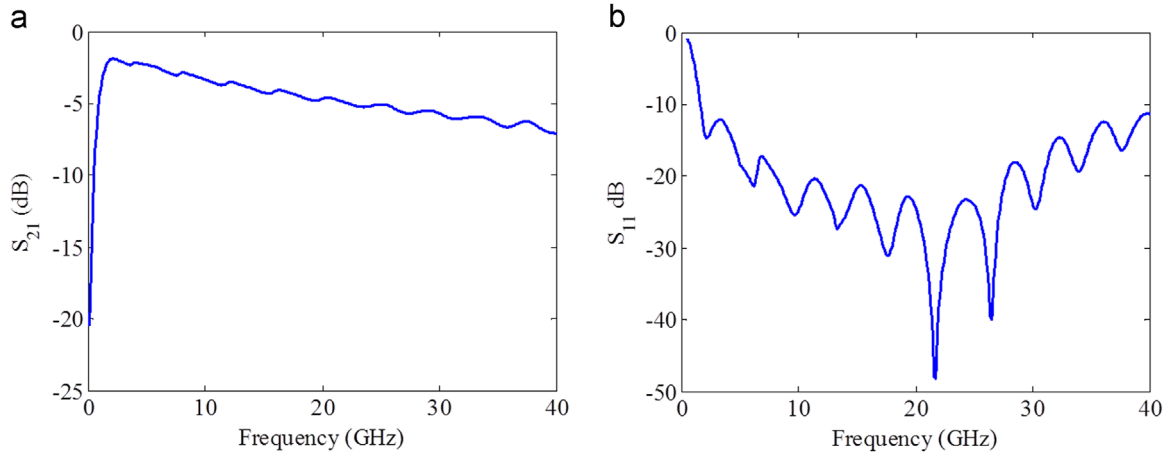

Fig. 12. : S_{21} and S_{11} parameters for CMS section of length $L=2$ cm.

5. Conclusions

Design of a leaky waveguide deflector is presented in this paper for implementation of a 44GSPS AOADC. The design of leaky waveguide deflector is based on low RF loss material with optical loss of $\alpha_{opt} < 0.345$ Np/cm and high E–O coefficient $r_{eo}=350$ pm/V to achieve 6.5 effective bits of resolution. An optimum leaky waveguide deflector length of $L=2$ cm and pre-emphasis technique allowing compensation of RF wave losses. Broad bandwidth up to 22.3 GHz is reached due to a good velocity matching between microwave and band GCPW-CMS-GCPW transition is discussed with a bandwidth of 1.5 to 22.3 GHz for applying RF signal to the E–O deflector, while providing access for the lensed fiber optical input from a MLL. The DC power consumption of this AOAD is dominated by the 4 W consumed in a 50 Ω load as result of providing a sinusoidal peak RF voltage of 20 V to the CMS electrodes of the E–O deflector. A100% efficiency is theoretically possible, when the Class C power amplifiers are employed, while the Class B push-pull power amplifiers with 78% efficiency are also feasible, resulting still under 5 W of total power consumption. The other sources of power consumption are less significant compared to the power amplifier and the optical deflector, as the reported optical sampler uses under 100 mW for clock and optical output power of 30 mW using low jitters optical clocks from the MLL. In addition a 7 bit optical quantizer consumes under 50 mW, when only one row of 7 photodetectors out of 128×7 photodetector array are being illuminated by about 5 mW of deflected optical beam impinges on to the optical windows. The future EO material improvements to the anticipated level of 1200 pm/V will undoubtedly lower the required RF voltage and result in a power consumption of about 0.5 W, while it provides sampling rate over 44 GSPS with resolution of approaching 8 bits.

Acknowledgment

The authors would like to thank the Region of Pays de la Loire for its support through the project ADC PolyNano (Grant No. 2013 10079). Moreover, the authors greatly appreciated numerous discussions and helpful recommendations by Prof. Gundel, Prof. Guiffard and Dr Ginestar on practical implementation of EO-Polymer based leaky waveguide optical deflector in the project.

References

[1] A.S. Daryoush, X. Hou, W. Rosen, All-optical ADC and its applications in future communication satellites, IEEE Int. Top. Meet. Microw. Photon. (2004) 182–185.
[2] L. Verma, M. Fakharzadeh, S. Choi, WiFi on Steroids: 802.11ac and 802.11ad, IEEE Wirel. Commun. (2013) 30–35.
[3] M. El-Chammas, B. Murmann, A 12-GS/s 81-mW 5-bit Time-Interleaved Flash ADC With Background Timing Skew Calibration, IEEE J. Solid-State Circuits 46 (4) (2011) 838–847.
[4] ⟨http://cdn.teledynelecroy.com/files/pdf/labmaster-10zi-a-datasheet.pdf⟩.
[5] P.J. Pupalaikis, B. Yamrone, R. Delbue, A.S. Khanna, K. Doshi, B. Bhat, A. Sureka, Technologies for Very High Bandwidth Real-time Oscilloscopes, Invit. Lect. IEEE Bipolar/BiCMOS Circuits Technol. Meet. (2014) 128–135 , BCTM.
[6] P. Bower, I. Dedic, High speed converters and DSP for 100 G and beyond, Opt. Fiber Technol. (2011) 467–471.
[7] K. Plouton Time-Interleaved ADCs, Past and Future IEEE International Solid State Circuits Conerence, Feb 10, 2009.
[8] Rohde & Schwarz, Oscilloscope Fundamentals, 2014. Available: https://www.conres.com/test-equipment/wp-content/uploads/sites/4/2014/04/oscilloscope fundamentals.pdf.
[9] B. Murmann, ADC performance survey 1997-2015 (July 2015), [Online]. Available: ⟨http://web.stanford.edu/~murmann/adcsurvey.html⟩.
[10] W. Cheng, W. Ali, M.-J. Choi, K. Liu, T. Tat, D. Devendorf, L. Linder, Ronald Stevens, A 3b 40GS/s ADC-DAC in 0.12 μm SiGe, IEEE Int. Solid-State Circuits Conf. (2004) 262–263.
[11] J.-H. Tsai, H.-H. Wang, Y.-C. Yen, C.-M. Lai, Y.-J. Chen, P.-C. Huang, P.-H. Hsieh, H. Chen, C.-C. Lee, A 0.003 mm^2 10 b 240 MSPs 0.7 mW SAR ADC in 28 nm CMOS With digital error correction and correlated-reversed switching, IEEE J. Solid-State Circuits 50 (6) (2004) 1382–1398.
[12] Y. Han, B. Jalali, Photonic time-stretched analog-to-digital converter: fundamental concepts and practical considerations, IEEE J. Light Technol. 21 (12) (2003) 3085–3103.
[13] D. Chen, H.R. Fetterman, A. Chen, W.H. Steier, L.R. Dalton, W. Wang, Y. Shi, Demonstration of 110 GHz electro-optic polymer modulators, Appl. Phys. Lett. 70 (25) (1997) 3335–3337.
[14] S. Huang, T.-D. Kim, J. Luo, S.K. Hau, Z. Shi, X.-H. Zhou, H.-L. Yip, A.K.-Y. Jen, Highly efficient electro-optic polymers through improved poling using a thin TiO_2-modified transparent electrode, Appl. Phys. Lett. 96 (24) (2010) 1–3 243311.
[15] S. Arahira, N. Mineo, K. Tachibana, Y. Ogawa, 40 GHz hybrid mode-locked laser diode module operated at ultra-low RF power with impedance-matching circuit, Electron. Lett. 39 (3) (2003) 287–289.
[16] X. Wang, C.-Y. Lin, S. Chakravarty, J. Luo, A.K.-Y. Jen, R.T. Chen, Effective in-device r_{33} of 735 pm/V on electro-optic polymer infiltrated silicon photonic crystal slot waveguides, Opt. Lett. 36 (6) (2012) 882–884.
[17] B.M.A. Rahman, V. Haxha, S. Haxha, K.T.V. Grattan, Design optimization of polymer electrooptic modulators, J. light. Technol. 24 (9) (2006) 3506–3513.
[18] X. Hou, A. Leaky, Waveguide All-Optical Analog-to-Digital Converter, Drexel University, Pheladelphia, PA, 2004, PhD Thesis.
[19] J.-P. Raskin, G. Gauthier, L.P. Katehi, G.M. Rebeiz, Mode conversion at GCPW-to-microstrip-line transitions, IEEE Trans. Microw. Theory Technol. 48 (1) (2000) 158–161.
[20] W.H. Haydl, On the use of vias in conductor-backed coplanar circuits, IEEE Trans. Microw. Theory Technol. 50 (6) (2002) 1571–1577.

Appl. Phys. A (2017) 123:542
DOI 10.1007/s00339-017-1154-4

Applied Physics A
Materials Science & Processing

Bandwidth improvement of microwave photonic components based on electro-optic polymers loaded with TiO_2 nanoparticles

D. Palessonga[1] · M. El Gibari[1] · S. Ginestar[1] · H. Terrisse[2] · B. Guiffard[1] · A. Kassiba[3] · H. W. Li[1]

Received: 15 February 2017 / Accepted: 18 July 2017 / Published online: 25 July 2017

Abstract Electro-optic (EO) polymers offer a very attractive possibility of realizing low-cost microwave photonic components with a wide bandwidth and a low driving voltage, thanks to a low dispersion from microwave to optical frequency of polymeric materials on the one hand, and the progress in the synthesis of high hyperpolarizability chromophores on the other hand. This paper studies the influence of titanium dioxide (TiO_2) nanoparticle loading on the microwave and optical properties of EO polymers. Thus, poly(methyl methacrylate) (PMMA) and disperse red 1 (DR1) are used as host polymer and guest EO chromophore, respectively. With 1–3% TiO_2 nanoparticle homogeneously incorporated in the polymer, the dielectric constant varies from 2.73 to 3.40 over the 400 MHz–10 GHz range, and the refractive index increases from 1.483 to 1.488 at the wavelength of 1539.6 nm. It is shown that fine tuning of dielectric constant and refractive index could allow improvement of the microwave photonic component bandwidth. For example, with an EO interaction length $L = 2$ cm (typical length of EO modulators), the ultimate modulator bandwidth could be raised to 258 GHz by loading PMMA–DR1 EO polymer with 1% wt of TiO_2 nanoparticles. It is also found that loading polymer with nanoparticles could improve the EO response of poled polymers, represented by the intensity of the second-harmonic-generation (SHG) signal. The latter presents more than a threefold increase by loading PMMA–DR1 EO polymer with 2% wt TiO_2 nanoparticles.

✉ D. Palessonga
den-god-frez.palessonga@etu.univ-nantes.fr

H. Terrisse
Helene.Terrisse@univ-nantes.fr

A. Kassiba
kassiba@univ-lemans.fr

[1] Université Bretagne Loire (UBL), Institut d'Electronique et de Télécommunications de Rennes (IETR), UMR CNRS 6164, Université de Nantes, 2, rue de la Houssinière, BP 92208, 44322 Nantes cedex, France

[2] UBL, Institut des Matériaux Jean Rouxel (IMN), UMR CNRS 6502, Université de Nantes, 2, rue de la Houssinière, BP 32229, 44322 Nantes cedex, France

[3] UBL, Institut des Molécules et Matériaux du Mans (IMMM), UMR CNRS 6283, Université du Maine, 72085 Le Mans cedex 9, France

1 Introduction

Data exchange in networks increases more and more due to the development of multimedia content and the growth in the number of users. Therefore, the required transmission rate of telecommunication networks and/or the carrier frequency should be increased, even though microwave photonic components offer bandwidths and transmission rates much higher than their electrical counterparts. As the direct modulation bandwidth of lasers is limited to 20 GHz, it is necessary to use external modulators for modulation above 20 GHz. Today, more than 90% of Mach–Zehnder modulators are based on the very popular electro-optic (EO) inorganic crystal lithium niobate ($LiNbO_3$). However, due to its intrinsic properties, the driving voltage of the modulators ranges from 2 to 10 V [1] and the bandwidth is limited below 40 GHz [2]. Polymers are emerging as new promising materials for microwave photonic devices, thanks to a good velocity matching between microwave and lightwave signals in polymeric materials and also the progress in the synthesis of high hyperpolarizability chromophores. The EO coefficient of polymers may reach up to 350 pm/V [3], which is much higher than 31 pm/V, that of

the inorganic crystal $LiNbO_3$. Besides, sub-volt driving voltage has been achieved with a polymer modulator [4]. Even though EO polymers allow reaching, in principle, microwave photonic components of higher bandwidth than $LiNbO_3$ [4], it is necessary to work out universal techniques of tuning permittivity and refractive index to increase the bandwidth, regardless of polymers chosen according to their other good characteristics, such as low optical and dielectric losses, appropriate chemical, and mechanical properties. These results allow to adjust the optical properties of the materials used to obtain the best possible design of microwave photonic components such as modulators and all-optical analog-to-digital converters (ADC) based on EO polymers [5, 6]. Indeed, it is possible to get a polymer composite P' by loading a polymer P with a desired refractive index difference between P and P', typically between 0.02 and 0.08 according to the required core dimension of optical waveguides made with P and P'. When these polymers P' and P are respectively used as core and cladding materials of optical waveguides, by adjusting the nanoparticle content, one can either make their mode size closer to that of optical fibers to improve their coupling efficiency, or reduce waveguide width, and consequently the distance between electrodes located at both sides of the waveguide, resulting in lower driving voltages while keeping the required electric field. In addition, as both the core and the cladding of the waveguides are made with EO polymers P' and P, the effective EO effect should be increased compared to waveguides whose only core is in the EO polymer, because EO effect is experienced by lightwave in both core and cladding.

In this paper, we show that the permittivity and the refractive index of EO polymers can be adjusted by loading them with nanoparticles to improve the phase velocity matching between the lightwave and the microwave signals. For our study, the classical polymer poly(methyl methacrylate) (PMMA), which displays good thermal stability, optical clarity and excellent weather and chemical resistance [7], and disperse red 1 (DR1), are used as host polymer and EO chromophore, respectively. Titanium dioxide (TiO_2) nanoparticles are selected as fillers due to the transparency of TiO_2 at the telecommunication wavelength, also because Prakash et al. reported in 2011 that loss tangent diminishes from 0.22 to 0.03 by loading 3% TiO_2 nanoparticles into PMMA at 1 MHz [8]. We investigated the changes of the relative permittivity and the loss tangent of PMMA filled or not with DR1 chromophore over the frequency range between 400 MHz and 10 GHz, as a function of TiO_2 nanoparticle content. In addition, the refractive index of the neat and TiO_2-loaded polymer films was measured at 1306.7 and 1539.6 nm wavelengths. Afterwards, the interest of tuning permittivity and refractive index with TiO_2 nanoparticle loading is shown through theoretical demonstration of bandwidth improvement of EO polymer modulators. We also investigated the influence of TiO_2 nanoparticle loading on the EO characteristic of EO polymer. To this end, the second-harmonic generation (SHG) signal amplitude of the PMMA–DR1–*x*wt%TiO_2 polymer composite was measured.

2 Experimental section

2.1 Thin film preparation

1,1,2-Trichloroethane (TCA) was used for dissolving PMMA matrix and DR1 dye (both commercialized by Sigma-Aldrich), and dispersing TiO_2 nanoparticles with a primary size of 30 nm and an approximately spherical shape supplied by Nanostructured & Amorphous Materials, Inc.

Loading protocols were optimized to homogeneously disperse TiO_2 nanoparticles in the neat PMMA and PMMA–DR1 polymers (see Fig. 1). PMMA was first dissolved by magnetic stirring in TCA for at least 2 h, and then when necessary DR1 dye was added to obtain a first solution after magnetic stirring for 1 h. A second solution was obtained by dispersing TiO_2 nanoparticles in TCA using an ultrasonic probe for 2 min 30 s with an acoustic power density $P = 75$ W/cm^2 and a duty cycle $\alpha = 33\%$. The final solution of PMMA–TiO_2 or PMMA–DR1–TiO_2 was obtained by mixing the two previous solutions. A second sonication was performed for 2 min with $P = 105$ W/cm^2 and $\alpha = 33\%$, for homogenizing the final solution. Dynamic light scattering (DLS) technique was used to control the dispersion quality of the TiO_2 nanoparticles and the stability of the suspension by measuring the size of nanoparticle agglomerates. This control is important since composite thin films which are deposited from the final solution will exhibit a dispersion quality of

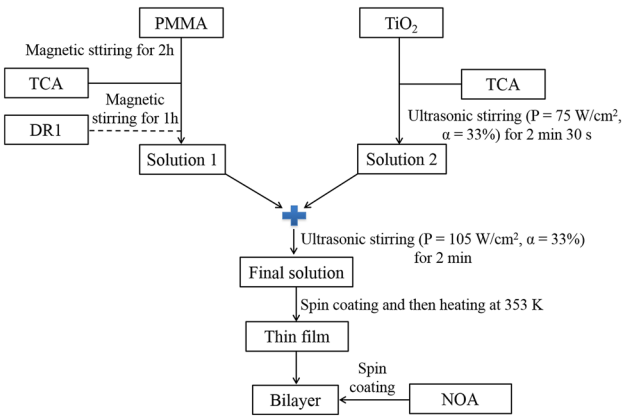

Fig. 1 Schematic diagram representing the preparation of thin films

TiO_2 reflecting the quality of the solution. The measurements were performed using the Zetasizer Nano ZS system supplied by Malvern Instruments SA. The suspensions, presenting a viscosity of approximately 2 mPas at the temperature of 295 K, were put in quartz cells supplied by Hellma Group. In the aim to be sure of the repeatability of the results, six successive measurements were performed on every solution. Figure 2 shows the volume-based size distribution of TiO_2 particles in polymer with TCA, which presents two agglomerate populations, the first one ranging from 100 to 170 nm and the second one from 250 to 470 nm. It is worth noting that the first population is largely predominant in the suspension since the second one disappears in the number-based distribution (see Fig. 3). These results indicate that TiO_2 nanoparticles (individual size: 30 nm) are rather well dispersed in the final solution containing mainly small agglomerates. Nano-composite films, filled or not with DR1, were deposited by spin-coating from the final solution onto different substrates presented in the further sections and cured at 353 K for 30 min. The thickness of thin films ($\sim$1 µm) was measured using a mechanical profilometer. As onset of inhomogeneity of the solution PMMA–DR1 was observed for dye contents above 15 wt% [9], we fixed the concentration of DR1 in the host polymer at 14 wt% and the TiO_2 nanoparticle concentration in the host polymer between 1 and 3 wt%.

As nanoparticle dispersion in solid films is in usual different from that in solvent, transmission electron microscopy (TEM) and optical microscopy were used to assess the dispersion of nanoparticles in the thin films elaborated. Figure 4a, b shows the actual dispersion state of nanoparticles in PMMA thin films. Both images reveal large agglomerates of TiO_2 nanoparticles. The optical microscopy image also reveals high dispersity of agglomerate size. The size of the biggest agglomerates achieves 400 nm and that of the smallest ones is approximately

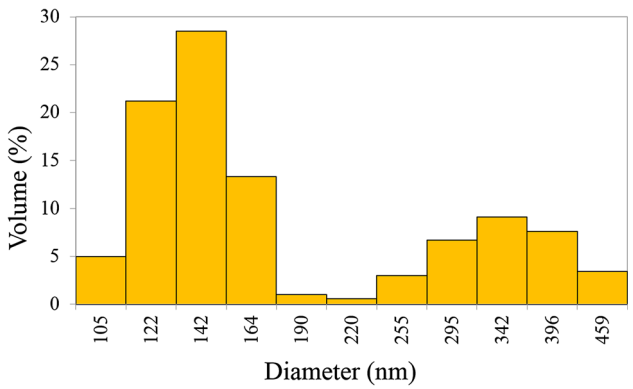

Fig. 2 Particle volume-based size distribution in polymer/TCA solution

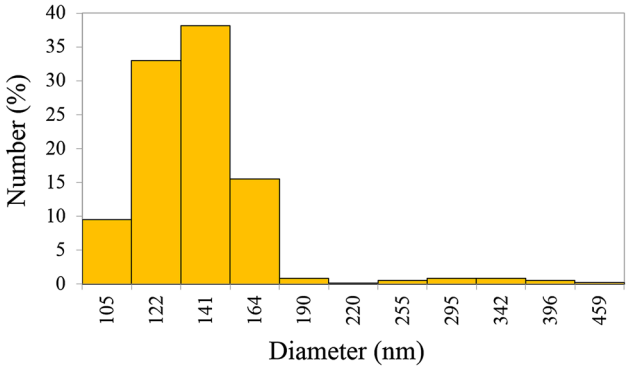

Fig. 3 Particle number-based size distribution in polymer/TCA solution

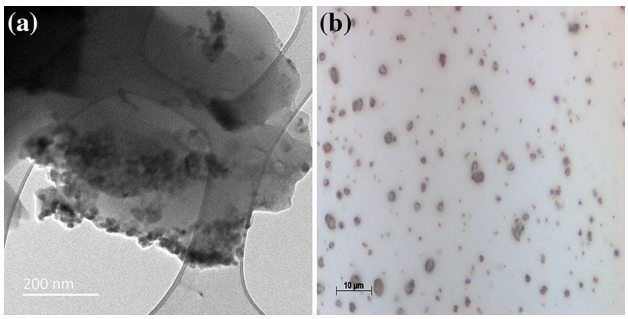

Fig. 4 Dispersion of TiO_2 nanoparticles in PMMA thin films: **a** TEM image and **b** optical microscopy image of PMMA–1wt%TiO_2

100 nm. However, it can be observed in Fig. 4a that large agglomerates are composed of smaller grains. These findings are in agreement with results of DLS investigations.

It is worth noting that thin films elaborated in this study are optically transparent due to the transparency of PMMA from about 380 to 2000 nm, even though there are two absorption bands at about 300 nm and about 490 nm in DR1–PMMA [10, 11]. Additionally, Yuwono et al. reported in 2003 that PMMA–TiO_2 thin film is transparent in the visible region (390–700 nm) [12]. We would like to remind that TiO_2 nanoparticles were chosen for this study due to the transparency of TiO_2 at the telecommunication wavelength of 1550 nm [13].

For the measurement of the complex dielectric constant and EO properties, a top electrode was sputtered onto the film. The top electrode for EO properties was sputtered using a shadow masking. For the measurement of dielectric properties, the top electrode was patterned by photolithography process followed by chemical etching. As acetone solvent used in the photolithography can readily dissolve the polymer film, acetone-resistant buffer layer and NOA81 resin from Norland were deposited onto the polymer film before depositing the top metal layer to protect the dielectric film. Naturally, the buffer layers were kept in all film structures.

This buffer layer offers a relative easiness of technological processing. Figure 5 shows a scanning electron microscopy (SEM) image of the polymer film and the buffer layer deposited onto the polymer film without degrading it.

2.2 Microwave and optical characterization

Complex dielectric constant (relative permittivity and loss tangent) measurements were performed from the complex reflection coefficient measured onto metal–insulator–metal (MIM) capacitors including the dielectric material to characterize (see Fig. 6). In the MIM technique [14], the dielectric film was deposited onto a metal ground layer (1 µm thick) on a glass substrate and capped with another metal layer (copper in our case). The top metal layer (1 µm thick) was then patterned into suitable test structures by photolithography. The reflection coefficient measurement was performed using a vector network analyzer (VNA) Agilent E8364B in the frequency range from 400 MHz to 10 GHz with GSG (Ground-Signal-Ground) probes from Cascade Microtech (bandwidth 40 GHz, pitch 400 µm, and pad 30 µm). One-port full calibration (open, short, load) was performed using a substrate CSR-4 calibration kit from Cascade Microtech. All the experimental setup was controlled by Wincal 4.5 software from Cascade Microtech. Figure 7 shows the top buffer layer in NOA 81 resin added to the basic test structure to protect the polymer layer.

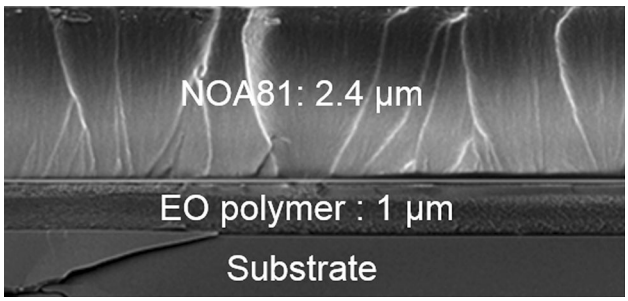

Fig. 5 SEM image of the polymer film and the buffer layer deposited onto the polymer film

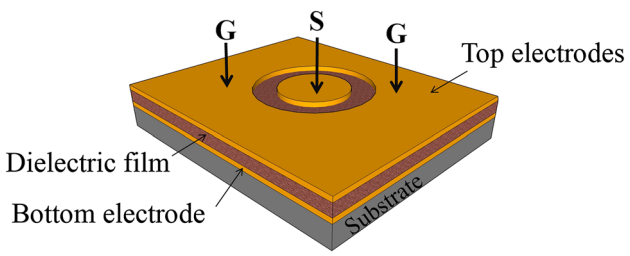

Fig. 6 Structure of a MIM capacitor suitable for microwave measurements using a GSG wafer probe

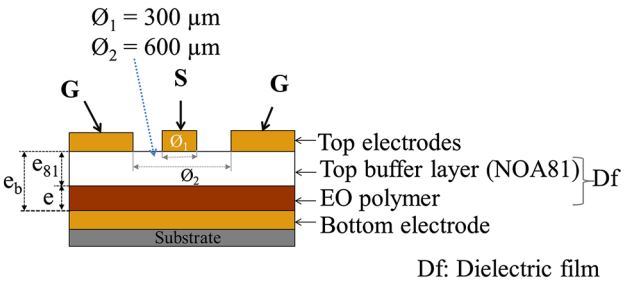

Fig. 7 Cross-sectional view of a MIM capacitor including a top buffer layer in NOA 81 resin to protect the EO polymer from acetone. Diameters $\varnothing_1 = 300$ µm and $\varnothing_2 = 600$ µm, *bottom* electrode on a 2.5 × 2.5 cm glass substrate

The electrical model of the MIM structure is given by two capacitors (C1 and C2) in series, where C1 is the capacitance between the circular patch S and the bottom electrode and C2 the capacitance between the top ground electrode G and the bottom electrode. As the area of the circular patch S is much smaller than that of the top ground electrode G (see Fig. 6), C1 is much lower than C2, therefore, the response of the whole circuit is dominated only by the capacitance C1, approximating the equivalent capacitance C by C1 results in an error less than 0.1%. The impedance (Z) of the test structure is given by the following formula [14]:

$$Z = Z_0 \frac{1 + \Gamma}{1 - \Gamma} \tag{1}$$

where $Z_0 = 50\ \Omega$ is the input impedance of the VNA and Γ is the measured complex reflection coefficient. The capacitance and the loss tangent of the materials under test are given respectively by the formulas (2) and (3). The dielectric constant was deduced from the MIM capacitive method formula (4):

$$C = \mathrm{Re}\left[\frac{1}{j\omega Z}\right] \tag{2}$$

$$\tan\delta = -\frac{\mathrm{Re}[Z]}{\mathrm{Im}[Z]} \tag{3}$$

$$\varepsilon_r = \frac{4eC}{\varepsilon_0 \pi \phi_1^2} \tag{4}$$

As the dielectric film in the MIM capacitor is constituted of the PMMA-based polymer and NOA81 resin buffer layer, the effective dielectric constant and loss tangent of the bilayer film are determined from the reflection coefficient measurement, the microwave properties of the PMMA-based polymer are extracted by following these steps:

1. Determination of the effective capacitance and loss tangent of the bilayer film constituted of the PMMA-based polymer and the NOA81 buffer layer.
2. Determination of the dielectric constant and the loss tangent of the NOA81 buffer layer.

3. Extraction of the capacitance and the loss tangent of the PMMA-based polymer using the formulas (5) and (6). The dielectric constant was deducted using formula (7)

$$C = -\frac{C_b C_{81}}{C_b - C_{81}} \tag{5}$$

$$\tan\delta = \frac{e_b \tan\delta_b - e_{81}\tan\delta_{81}}{e} \tag{6}$$

$$\varepsilon_r = \frac{4eC}{\varepsilon_0 \pi \phi_1^2} \tag{7}$$

where C and tan δ are respectively the capacitance and the loss tangent of the polymer layer to characterize, C_b and tan δ_b those of the bilayer (polymer material and NOA81), C_{81} and tan δ_{81} those of NOA81 layer, finally, e, e_b, and e_{81} the thicknesses of the polymer material layer, polymer material/NOA81 bilayer, and NOA81 layer; ε_0. the vacuum permittivity and ϕ_1 the diameter of the circular patch S.

For optical characterization, the refractive index measurements were performed at two telecommunication wavelengths, namely 1306.7 and 1539.6 nm, using a 2010/M prism coupler from Metricon, based on m-line spectroscopy method [15].

2.3 EO modulator bandwidth study

The bandwidth is a key element to qualify microwave photonic components such as EO modulators or ADC converters. This bandwidth can be determined by the following formula [6]:

$$f_{\max} = \frac{2c}{\pi L |n_{\text{eff}} - \sqrt{\varepsilon_{\text{eff}}}|} \tag{8}$$

In this equation, c is the free-space light velocity, L is the EO interaction length, n_{eff} and ε_{eff} are respectively the effective refractive index and the effective dielectric constant of the propagated mode.

To increase this bandwidth, two possibilities may be envisaged: the reduction of the interaction length L or the improvement of velocity matching between lightwave and microwave signals. The last one corresponds to the reduction of the difference between the square root of the effective dielectric constant and the effective refractive index. However, the driving voltage V_π of EO modulators is inversely proportional to the interaction length

$$V_\pi = \frac{\lambda d}{n_{\text{eff}}^3 r_{33} \Gamma L} \tag{9}$$

where λ is the light wavelength in the free-space, d is the distance between electrodes, r_{33} is the EO coefficient and Γ is the field overlap between lightwave and microwave signals. Consequently, the reduction of the length L leads to an increase of the driving voltage. This effect on V_π is a drawback for reducing electric consumption and facilitating broadband driver design. Therefore, a good velocity matching is preferred to improve the bandwidth.

To show the influence of the velocity matching, we consider a phase modulator based on EO polymers and driven by a microstrip line (see Fig. 8):

In this configuration, as core and cladding materials have often similar dielectric properties, the effective dielectric constant can be approximated by the following formula [16]:

$$\varepsilon_{\text{eff}} = \frac{\varepsilon_r + 1}{2} + \frac{\varepsilon_r - 1}{2}\frac{1}{\sqrt{1 + \frac{12d}{W}}} \tag{10}$$

where ε_r is the dielectric constant, d and W are respectively the thickness of the dielectric thin film and the width of the microstrip conductor. The characteristic impedance of microstrip line must be around 50 Ω to avoid reflection of the driving microwave signal. Thus, the chosen dimensions are:

$W = 26\,\mu\text{m}$ and $d = 10\,\mu\text{m}$.

2.4 EO characterization

To investigate the EO characteristics of poled polymer loaded with TiO_2, the SHG signal amplitude of PMMA–DR1–$x$wt%TiO_2 with $x = 1, 2$ samples was measured by reflection of a p-polarized fundamental beam on a thin film. The pump beam and SHG wavelengths were 1064 and 532 nm, respectively. The materials were transparent at the pump beam wavelength. The pump beam incidence angle toward the thin film samples was $\theta = 45°$. The excitation light polarization angle was controlled using a half wave

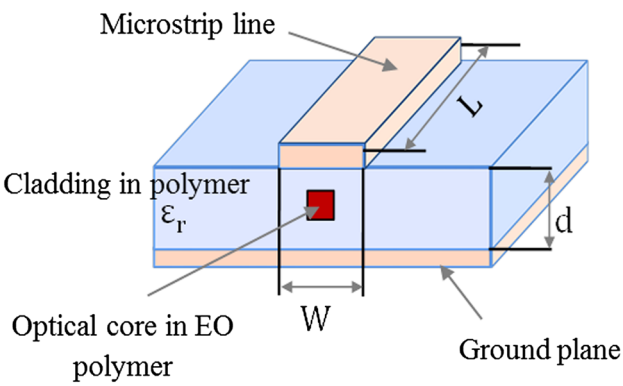

Fig. 8 Sketch of an EO phase modulator based on EO polymer driven by a microstrip line

plate, while the SHG polarization was resolved using a Glan-Laser prism.

The films were realized onto a glass substrate covered by thin indium tin oxide (ITO) film (100 nm thick) which serves as a bottom electrode for the EO investigations. The EO polymer was initially centrosymmetric, which precludes nonlinear effects. Non-centrosymmetry is induced by thermally assisted electric field poling. As a matter of fact, high DC electric field appliance is necessary to align guest chromophores in polar order and activate the second-order nonlinearity. A gold electrode (150 nm thick) was sputtered on top of the polymer films for contact poling between the two poling electrodes. Second-order nonlinear optical susceptibility was induced in the polymers after annealing at temperatures above the glass transition temperature of the polymer.

The poling procedure of PMMA–DR1–TiO_2 films to generate SHG signal classically implies the insertion of an additional (buffer) layer between top electrode and EO polymer to delay the onset of catastrophic breakdown [17] (see Fig. 9). The EO response of poled polymers, represented by the value of the SHG, depends on the poling DC electric field actually applied to the EO polymer layer. This poling field is chosen to be as large as possible and is carefully adjusted to be weaker than that corresponding to the dielectric breakdown of the polymer. To optimize the poling electric field value, the resistivity of the EO polymer must be much higher than that of the top buffer layer. For the bilayer films, a corrected formula expression was used to calculate the poling voltage really applied to the EO polymer layer [18]:

$$V_{eo} = \frac{e_0}{\frac{\rho_t}{\rho_0} e_t + e_0} V \tag{11}$$

V is the voltage applied to the poling contact electrodes, e_t and ρ_t are, respectively, the thickness and the resistivity of the cladding layer, e_0 and ρ_0 are, respectively, the thickness and resistivity of the active layer (the EO polymer layer).

The materials were annealed at 100 °C for 20 min using a hotplate. The poling field applied to the EO polymer layer was about 110 V/μm. The sample was then cooled to room temperature and the poling field was finally switched off. Measurements of SHG signal amplitude were performed subsequent to the poling (after switching off the poling field) and the day after the poling.

3 Results and discussion

3.1 Dielectric properties

The relative permittivity ε_r and the loss tangent tan δ of different PMMA-based polymers and NOA81 resin were extracted from measurements up to 10 GHz. They are displayed in Figs. 10 and 11 as a function of frequency and TiO_2 concentration.

Figure 10 shows that the relative permittivity ε_r of the PMMA-based polymers increases with TiO_2 loading with roughly the same variation in the whole frequency range, because of the quasi-independence of ε_r upon frequency. For example, the relative permittivity at 3 GHz is 2.62 and 2.73, 3.13 and 3.40 for respectively pure PMMA and PMMA-$x$wt%TiO_2 with $x = 1, 2, 3$, respectively. It seems coherent that the PMMA loaded with TiO_2 nanoparticles has a higher relative permittivity than the polymer non-loaded because of the high dielectric constant of TiO_2 ($\sim$100) [8]. So, the effective permittivity increases with filler concentration. These results show that the relative permittivity of PMMA can be continuously tuned by incorporating TiO_2 nanoparticles.

The dielectric loss tangent also increases with TiO_2 content but the variation strongly depends on the frequency

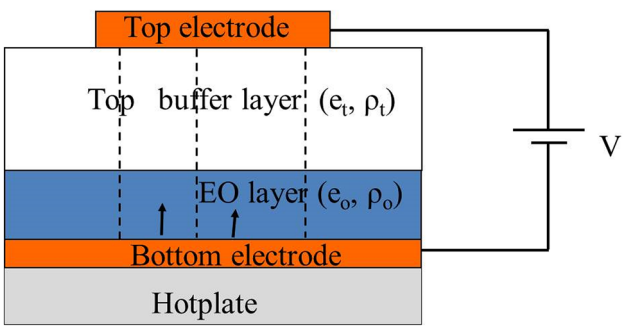

Fig. 9 Structure of contact poling between the two poling electrodes including a top buffer layer to protect the EO polymer from breakdown. Top electrode 1.5 × 1 cm and bottom electrode 2.5 × 2.5 cm

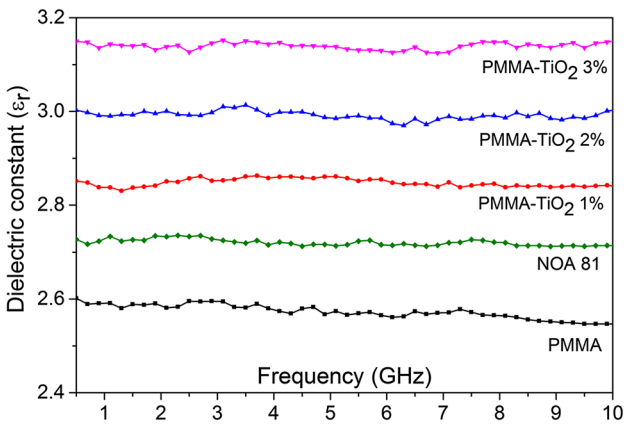

Fig. 10 Frequency dependence of the relative permittivity of PMMA polymer as a function of TiO_2 concentration

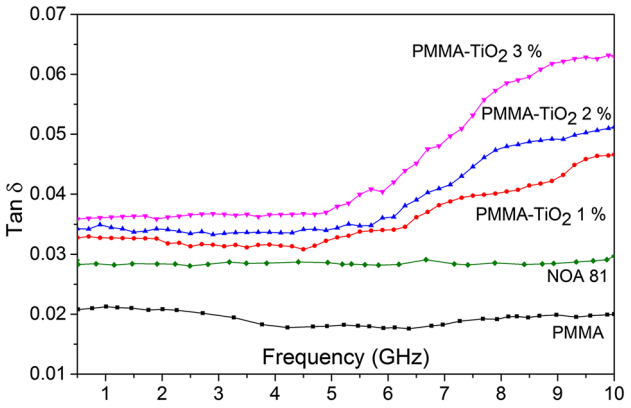

Fig. 11 Dielectric loss tangent of PMMA polymer as a function of the TiO_2 concentration

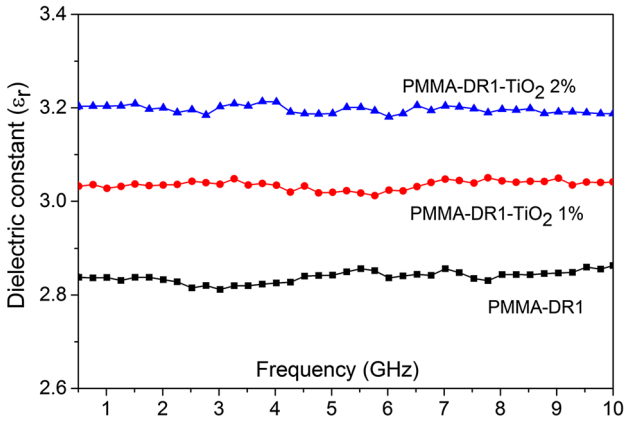

Fig. 12 Relative permittivity of EO polymer as a function of frequency for two TiO_2 nanoparticle concentrations

with a more pronounced increase of tan δ above $\sim$6 GHz (Fig. 11). The same behavior was already observed with carbon nanotubes in a two-component polymer by Liu et al. [19].

As already observed in the case of PMMA–*x*wt%TiO_2 polymers, the relative permittivity of the PMMA–DR1 films loaded with 1 and 2 wt% TiO_2 versus frequency exhibits the same trend in Fig. 12. The relative permittivity of the EO polymers can be also tuned by loading with TiO_2 nanoparticles. For instance, the relative permittivity at 3 GHz is 2.56, 2.87, and 3.14 for neat PMMA–DR1, PMMA–DR1–1wt%TiO_2, and PMMA–DR1–2wt%TiO_2, respectively. However, the measurement of relative permittivity of PMMA–DR1–3wt%TiO_2 gave aberrant values. That effect was attributed to the increase of surface roughness with TiO_2 nanoparticle content.

As shown in Fig. 13, the dielectric loss tangent of PMMA–DR1–*x*wt%TiO_2 also presents a similar variation to that of PMMA–*x*wt%TiO_2. G. Wan et al. reported [20] a similar dielectric loss increase with frequency from 13 GHz of paraffin loaded with carbon-coated TiO_2

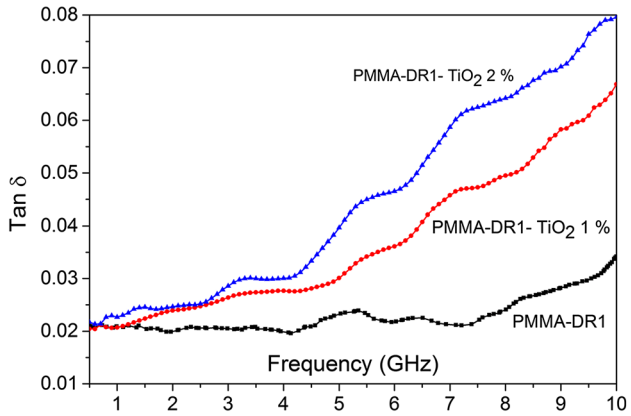

Fig. 13 Dielectric loss tangent of EO polymer as a function of frequency for two TiO_2 nanoparticle concentrations

nanocrystals. They explained that the existence of interfaces between different components of the nano-composite may give rise to interfacial polarization and associated relaxation, which could contribute to the enhanced dielectric loss. In our study, interfacial polarization due to interfaces between TiO_2 and PMMA could be responsible for dielectric loss increase with frequency from 6 GHz. With additional interfaces between TiO_2 and DR1, dielectric loss increase with frequency got worse.

Figures 14 and 15 give the variation of the relative permittivity and loss tangent measured at 3 GHz of PMMA–TiO_2 and PMMA–DR1–TIO_2 composite films as a function of weight fraction of TiO_2 nanoparticles. Both permittivity and loss tangent increase with increasing TiO_2 content. The lower and upper bounds of effective permittivity and loss tangent have been calculated using the Wiener bound model [21], which corresponds to the Lichtenecker model with α parameter $= 1$ and -1 [22]:

$$(\varepsilon^*_{\text{eff}})^{\alpha} = f_{\text{TiO}_2}(\varepsilon^*_{\text{TiO}_2})^{\alpha} + (1 - f_{\text{TiO}_2})(\varepsilon^*_{\text{polymer}})^{\alpha} \quad (12)$$

where $\varepsilon^*_{\text{eff}}$ is the effective complex permittivity of the two-phase composite film, $\varepsilon^*_{\text{TiO}_2}$ and $\varepsilon^*_{\text{polymer}}$ are the complex permittivities of TiO_2 nanoparticles and PMMA or PMMA–DR1 polymer matrix, respectively, and f_{TiO_2} is the volume fraction of TiO_2. The relative permittivity and loss tangent values for TiO_2 used for the effective permittivity calculation are 100 and 0.13, respectively.

Even if it is not very accurate, this model is one of the theoretical mixing rules useful to estimate the effective complex permittivity of composite materials made of two dielectric components (TiO_2 inclusions in a polymer matrix, in the present study). For both dielectric constant and loss tangent, it is found that every measured value is within the limits of the lower and upper bounds of the Wiener model, which means that the validity condition (homogeneity condition) is fulfilled [23]. However, a rather

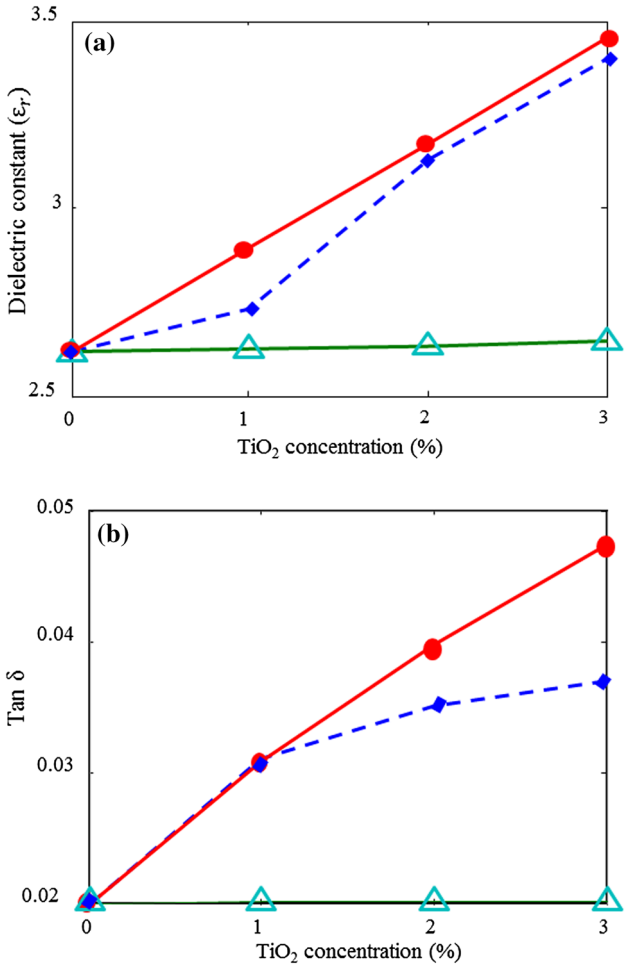

Fig. 14 Evolution of the dielectric properties at 3 GHz of PMMA-based composite versus TiO_2 content: **a** relative permittivity and **b** tanδ of PMMA–*x*%TiO_2, (*blue-filled diamond*) measured data, (*green-unfilled triangle*) calculated lower effective dielectric data using Wiener bound model, (*red-filled circle*) calculated upper effective dielectric data using Wiener bound model

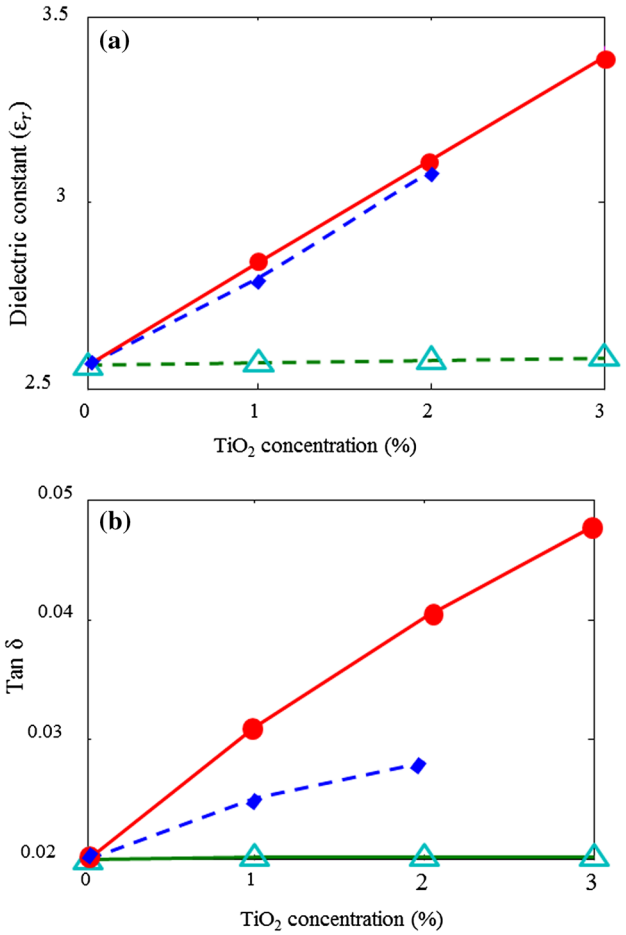

Fig. 15 Evolution of the dielectric properties at 3 GHz of PMMA-based composite versus TiO_2 content: **a** relative permittivity and **b** tan δ of PMMA–DR1–x %TiO_2. (*blue-filled diamond*) Measured data, (*green-unfilled triangle*) calculated lower effective dielectric data using Wiener bound model, (*red-filled circle*) Calculated upper effective dielectric data using Wiener bound model

good agreement is found between measured permittivity and the upper bound values.

3.2 Measurement of refractive index

Figures 16 and 17 present the measurement results of the refractive index of the studied materials at the two wavelengths. These figures show that the refractive index increases with TiO_2 nanoparticle loading. For example, the refractive index is 1.501, 1.504, 1.509, and 1.514 at 1539.6 nm for respectively PMMA–DR1, and PMMA–DR1 loaded by TiO_2 nanoparticles of 1, 2, and 3 wt%.

It seems coherent that PMMA–DR1 loaded with TiO_2 nanoparticles has a higher refractive index than unloaded

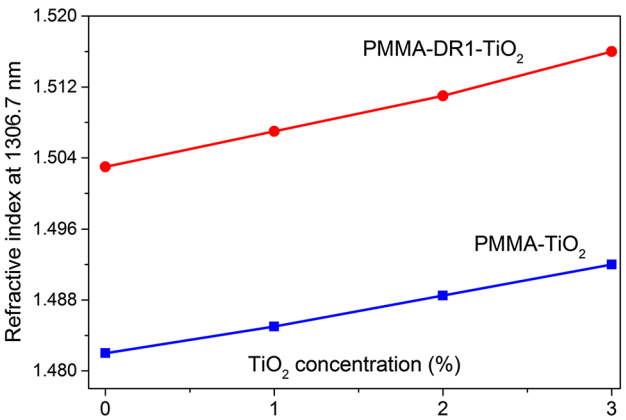

Fig. 16 Refractive index of the studied materials at the wavelength of 1306.7 nm

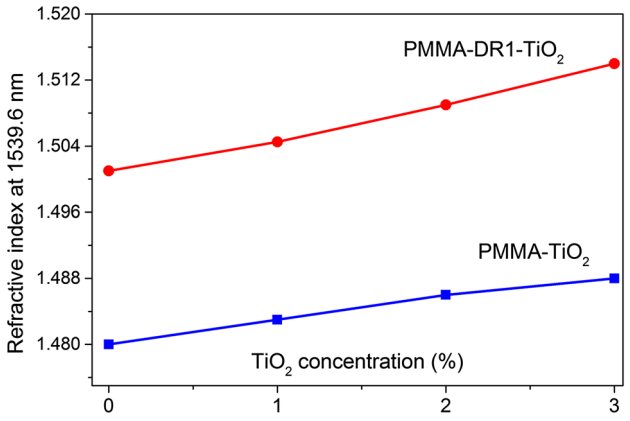

Fig. 17 Refractive index of the studied materials at the wavelength of 1539.6 nm

EO polymer, as the refractive index of the bulk TiO_2 is around 2.2 [24], larger than that of PMMA–DR1 which is 1.503 at the wavelength of 1306.7 nm and 1.501 at the wavelength of 1539.6 nm (see Figs. 16, 17).

3.2.1 Improvement of EO modulator bandwidth

Figure 18 shows that the use of EO polymer loaded with TiO_2 nanoparticles allows to reduce the difference $|n_{\text{eff}} - \sqrt{\varepsilon_{\text{eff}}}|$. We observe that the optimal loading is around 1 wt% of TiO_2 nanoparticles in the host polymer. This loading leads to an excellent velocity matching (see Fig. 18) due to a very low difference $|n_{\text{eff}} - \sqrt{\varepsilon_{\text{eff}}}| = 3.7 \times 10^{-2}$. The bandwidth of microwave photonic components based on EO polymer PMMA–DR1 could be very large. For example, with $L = 2$ cm (typical length of EO modulators), the modulation bandwidth would achieve 258 GHz if it was not limited by dielectric and conductor losses. Finally, for a given desired bandwidth, the EO interaction length can be increased due to a better velocity matching between lightwave and microwave signals, resulting in a lower driving voltage.

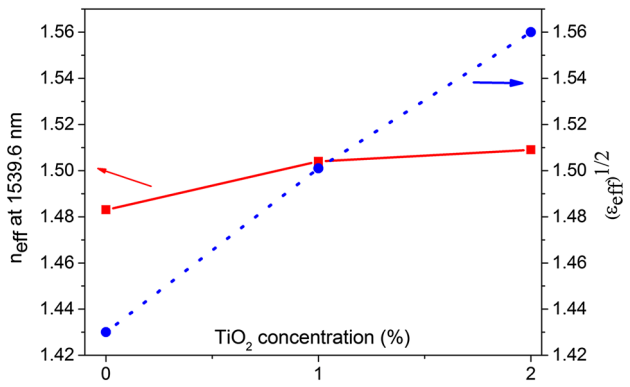

Fig. 18 Improvement of velocity matching by loading PMMA-based EO polymers with TiO_2 nanoparticles

3.2.2 EO characteristic

Figure 19 shows that 1 day after poling, the SHG response of the three samples reaches stable values, indicating that substantial and remanent ordering of DR1 chromophores occurred and the polymer films have become permanently poled. Measurements also show the increase of SHG intensity with the TiO_2 loading: 12, 25, and 40 for unloaded PMMA–DR1, PMMA–1 wt%–DR1, and PMMA–2 wt%-DR1, respectively. This demonstrates that the poling efficiency of PMMA–DR1 and possibly the EO coefficient r_{33} is improved by TiO_2 loading. This interesting effect with TiO_2 incorporation in the EO polymer matrix may originate from a space charge phenomenon. As a matter of fact, during the poling step, these charges (generally electrons) may not only be trapped and accumulated by structural interfaces in the matrix but also in the vicinity of TiO_2 nanoparticles, yielding high local electric field densities, thus promoting DR1 molecule's long-range ordering. This interpretation seems consistent with space charge effect at the origin of enhanced electric field-induced strain of polymer films filled with nano-objects such as SiC nanowires [25] or carbon nanotubes [26].

4 Conclusion

In this paper, we present a study of the influence of TiO_2 nanoparticle loading on the microwave and optical properties of the classical PMMA polymer filled or not with DR1 EO dye. The MIM capacitor method has been used for determining the microwave properties from 400 to 10 GHz and the M-line method for the refractive index at wavelengths near 1.3 and 1.55 μm.

The investigation has shown that both the dielectric constant and the refractive index of PMMA and PMMA–DR1 films may be finely tuned by incorporating TiO_2

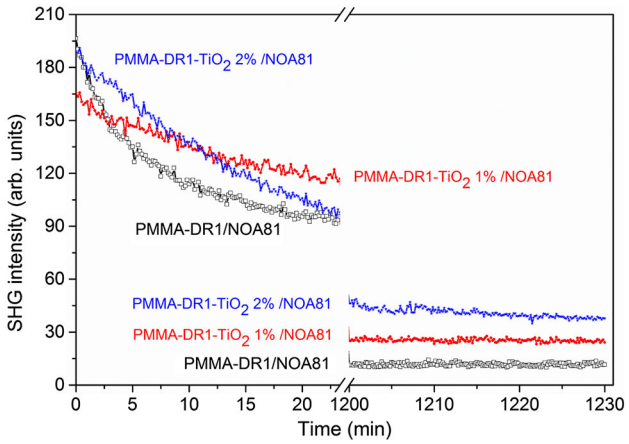

Fig. 19 Relaxation of the SHG intensity of bilayer films

nanoparticles, while loss tangent are significantly increased, especially above 6 GHz. At 3 GHz, 1 wt% of TiO_2 nanoparticle loading increases the dielectric constant of PMMA from 2.62 to 2.73 and that of PMMA–DR1 from 2.56 to 2.87. The refractive index of PMMA moves from 1.48 to 1.485 at the wavelength of 1539.6 nm by loading it with 1 wt% of TiO_2 nanoparticles and that of PMMA–DR1 from 1.501 to 1.504.

Through optimization of velocity matching between the microwave and lightwave signals by loading PMMA–DR1 EO polymer with 1 wt% of TiO_2 nanoparticles, the ultimate EO interaction bandwidth was raised to 258 GHz for a phase modulator of $L = 2$ cm. However, the effective modulation bandwidth is limited by the dielectric losses of the used EO polymers. Therefore, next key step is to find out appropriate low-loss loading nanoparticles permitting to reduce dielectric losses of EO polymers. Regarding the EO effect of PMMA–DR1 polymers, it has been proven through SHG signal amplitude that the poling efficiency could be improved with TiO_2 loading. This effect is interpreted in terms of space charge effect, amplified by the presence of TiO_2 particles, acting as charge traps. Therefore, the future work will be also devoted to the measurement of space charges profile in the polymer films and the EO coefficient r_{33} to quantify the beneficial effect of TiO_2 loading on the EO properties. If the EO coefficient r_{33} is increased, interaction length L can be reduced and dielectric losses become less critical.

Acknowledgements The authors would like to thank Dr. Anthony Rousseau who is with Institut des Molécules et Matériaux du Mans (IMMM) for the TEM image. The financial support of region Pays de la Loire under the Project ADC PolyNano is gratefully acknowledged.

References

1. L. Arizmendi, Phys. Status Solidi A **201**, 253–283 (2004)
2. W.K. Burns, M.M. Howerton, R.P. Moeller, R. Krahenbuhl, R.W. McElhanon, A.S. Greenblatt, J. Light. Technol. **17**, 2551–2555 (1999)
3. S. Huang, T.-D. Kim, J. Luo, S.K. Hau, Z. Shi, X.-H. Zhou, H.-L. Yip, A.K.-Y. Jen, Appl. Phys. Lett. **96**, 243311–243313 (2010)
4. D.M.Y. Enami, Appl. Phys. Lett. **91**, 093505 (2007)
5. M. Hadjloum, M. El Gibari, H.W. Li, A.S. Daryoush, Opt. Commun. **373**, 82–90 (2016)
6. B.M.A. Rahman, V. Haxha, S. Haxha, K.T.V. Grattan, J. Light. Technol. **24**, 3506–3513 (2006)
7. S. Gross, D. Camozzo, V. Di Noto, L. Armelao, E. Tondello, Eur. Polym. J. **43**, 673–696 (2007)
8. R.R. Prakash, S. Pandiarajan, P. Venkatesh, N. Kamaraj, in Emerging Trends in Electrical and Computer Technology, 2011 International Conference on, 46–49 (2011)
9. M.G. Kuzyk, C.W. Dirk, J.E. Sohn, JOSA B **7**, 842–858 (1990)
10. B. Derkowska-Zielinska, O. Krupka, A. Wachowiak, V. Smokal, A. Grabowski, in Transparent Optical Networks, 2015 17th International Conference on, 1–3 (2015)
11. T. Pliska, W.-R. Cho, A.-C. Le Duff, V. Ricci, A. Otomo, M. Canva, P. Raimond, F. Kajzar, J. Opt. Soc. Am. B **17**, 1554–1564 (2000)
12. A.H. Yuwono, J. Xue, J. Wang, H.I. Elim, W. Ji, Y. Li, T.J. White, J. Mater. Chem. **13**, 1475–1479 (2003)
13. C.C. Evans, C. Liu, J. Suntivich, Opt. Express **23**, 11160–11169 (2015)
14. Z. Ma, Andrew J. Becker, P. Polakos, H. Huggins, J. Pastalan, H. Wu, K. Watts, Y.H. Wong, P. Mankiewic, Electr. Dev. IEEE Trans. **45**, 1811–1816 (1998)
15. T. Schneider, PhD Thesis, Université de Nantes, France, 2006
16. D.M. Pozar, *Microwave engineering*, 4th edn. (Wiley, Hoboken, 2012)
17. K. R. Philippe-Auguste, PhD Thesis, Université de Nantes, France, 2012
18. J.G. Grote, J. Phys. Chem. B **108**, 8584–8591 (2004)
19. L. Liu, Z.H. Yang, L.B. Kong, W.Y. Yin, S. Wang, Appl. Phys. A **108**, 843–848 (2012)
20. G. Wan, L. Yu, X. Peng, G. Wang, X. Huang, H. Zhao, Y. Qin, RSC Adv **5**, 77443–77448 (2015)
21. K. Karkkainen, A. Sihvola, K. Nikoskinen, I.E.E.E. Trans, Geosci. Remote Sens. **39**, 1013–1018 (2001)
22. A.V. Goncharenko, V.Z. Lozovski, E.F. Venger, Opt. Commun. **174**, 19–32 (2000)
23. B.M. Suleiman, Appl. Phys. A **99**, 223–228 (2010)
24. M. Yoshida, M. Lal, N.D. Kumar, P.N. Prasad, J. Mater. Sci. **32**, 4047–4051 (1997)
25. B. Guiffard, D. Guyomar, L. Seveyrat, Y. Chowanek, M. Bechelany, D. Comu, P. Miele, J. Phys. D Appl. Phys. **42**, 055503 (2009)
26. B. Guiffard, L. Seveyrat, G. Sebald, D. Guyomar, J. Phys. D Appl. Phys. **39**, 3053–3057 (2006)

IOP Publishing
Journal of Physics D: Applied Physics
J. Phys. D: Appl. Phys. **53** (2020) 135003 (12pp)
https://doi.org/10.1088/1361-6463/ab5756

New low loss soft thermoplastic blends for microwave applications

Tessnim Sghaier, Mohammed El Gibari[1] and Benoit Guiffard[1]

IETR, UMR CNRS 6164, University of Nantes, Nantes, France

E-mail: benoit.guiffard@univ-nantes.fr and mohammed.el-gibari@univ-nantes.fr

Received 7 July 2019, revised 28 October 2019
Accepted for publication 13 November 2019
Published 22 January 2020

Abstract

All organic soft dielectrics are growing more and more interest in the electronic industry owing to their light weight, low cost and the flexibility they yield compared to the rigid devices. In the specific field of microwave communicating devices planar printed (patch) antennas on a soft dielectric substrate are sought for their conformability and advantageous compactness. In this article, two soft thermoplastic elastomer blends based on polypropylene (PP) or low-density polyethylene (LDPE) were tested. The fabrication process and the established characterization steps have been fully presented. More specifically, in order to characterize the dielectric film up to 40 GHz, the microstrip ring resonator with coplanar waveguide access has been adapted to a new configuration specimen sample. The results of the characterizations obtained showed very encouraging performances for microwave applications. Indeed, the measured dielectric constant and loss tangent up to 40 GHz were found to be $\varepsilon_r \approx 2.45$ and $\tan\delta \approx 0.01$ for both blends. The fabrication and the radiation characteristics of a patch antenna on a new performing PP or LDPE-based elastomer blends as the soft dielectric substrate was demonstrated and analysed. The proof of the concept of the investigated device consists of a microstrip patch antenna with an operation frequency of about 10 GHz. These dielectric features render the polyolefin based blends very promising as a soft material for microwave engineering, which is confirmed by the measured antenna properties: the gain, the directivity as well as the efficiency have been calculated from the measured radiation pattern and were recorded as 4.6 dB, 7.7 dB and 46% respectively for the r-PP based blend and 4.8 dB, 8.1 dB and 51% for the LDPE based blend.

Keywords: X-band, soft thermoplastic elastomer, ring resonator, relative permittivity, dielectric loss, microstrip patch antenna, photolithography

(Some figures may appear in colour only in the online journal)

1. Introduction

Recently, the conversion from the wired to the wireless technology has given momentum for developing new concepts and new materials adapted for wireless communication. Thereby, printed antennas and more specifically, microstrip antennas play a paramount role in the wireless communication since they ensure the signal noise reduction of the communication. The modern communication systems and technologies at the X band (8–12 GHz) are supported by different types of antennas such as compact antennas and more precisely planar patch antenna that are widely used owing to their large signal to noise ratio, low profile and low cost [1].

Moreover, the need for compact, lighter components introduced new soft polymeric materials to replace rigid ones used in the electronic components for the wireless technology. In that aspect, patch antennas which are the fundamental components of today wireless technology are no exception, where the need for a soft patch antenna substrate is necessary, as in the field of wearable electronics for developing shape able sensory skins, for instance. A flexible soft substrate offers conformability in comparison to their rigid counterparts;

[1] Authors to whom any correspondence should be addressed.

moreover a soft dielectric-based patch antenna presents more versatility because polymers can generally be easily moulded onto desired shapes.

Soft polymeric materials have been considered for the dielectric substrate to replace rigid ones that are currently used e.g.: ceramic or glass fibers based composites [2–8], Although a valuable research has been done as far as polymeric film based materials are concerned for patch antenna, some inherent structural and electrical features of a large amount of the investigated materials do not lead to an easy and mechanically efficient antenna integration. One of the main drawbacks of the polymeric materials is a weak adhesion with metal layer, acting as radiating patch. In fact, strong adhesion between soft substrate and metal patch is a critical issue, both in terms of mechanical and the radio frequency performances of the antenna. Besides, the relatively weak efficiency of the final antenna device is also due to the dissipative nature of most studied elastomeric polymers. But a lot of research is still going on in order to solve the problems of their integration and efficiency so that the flexible antenna can withstand the same operations conditions as the commercial ones and can be integrated into more innovative complex devices such as curved radar sections, sensors, and target acquisition systems [9].

The dielectric substrate plays a paramount role in optimizing the performance of microwave components. Microwave antennas are concrete examples whose properties of the substrate determine the quality of the radiation of the antenna. From that perspective, developing a performing soft substrate for antenna is still challenging due to the quite high dielectric loss factor ($\tan\delta > 0.01$) [10] of some previously studied soft polymers at 1 GHz. We aim to develop a patch antenna based on soft dielectric at X band, which is of interest in many military and medical applications. In fact, different groups have worked on developing patch antenna based on a soft dielectric polymer [11–16]. In this context, Hage-Ali *et al* [16] developed a technical process for depositing an array of patch antennas on a polydimethylsiloxane (PDMS) substrate, which efficiency and gain have been measured 28% and 12 dBi respectively at 55 GHz. In another study, Baron *et al* [17] developed a microstrip patch antenna based on thermoplastic polyurethane (TPU) and measurement in anechoic chamber has shown a gain and an efficiency of 3.25 dBi and 30% at 10 GHz. In the latter study, the patch antenna had quite acceptable performance considering the dielectric loss of TPU substrate which reached 0.1 (10%) at 10 GHz. It was then necessary to develop a supported TPU membrane configuration above an air cavity to reduce the global losses and enhance the radiation properties of the patch antenna.

A polymeric material with favourable dielectric properties more specifically with low dielectric loss is of crucial importance. The fabrication and the implementation of electronic junction of antenna involve deposition of metals and chemical etching to define the final shape of the patch, and the choice of the material should take into account the aforesaid conditions. Moreover, since pure polymers generally exhibit high dielectric loss and do not have good chemical resistance, blend based polymer films permit to obtain a tailored material to overcome limits exhibited by the pure polymers such as improving the resistance to chemical solvents or introducing new properties. In this work, we introduce an α-polyolefin based blend as a dielectric substrate for a patch antenna that exhibits flexibility with a Young's modulus of ~4 MPa and that is chemically resistant to solvents. Although both blends are sought for their electrical properties [18] and are widely used in different industrial sectors such in high voltage insulation cable, the fabrication of a patch antenna at the X band based on polypropylene (PP) or polyethylene based soft dielectric substrate has never been reported, to our knowledge. Moreover, the polymeric blend has shown that it can withstand different methods of copper deposition such as sputtering and chemical etching and finally it was implemented in a microstrip patch antenna with good radiating performances mainly thanks to low dielectric loss ($\leqslant$1% at the X band).

The paper is organised as follows. After the introduction, section 2 presents the type and the preparation of the studied polymer blends and the different structural and dielectric characterisation procedures. Section 3 gives the experimental results and associated discussion and section 4 is specifically devoted to the preparation and radiation characteristics of the polymer blend-based patch antennas, followed by a conclusion.

2. Materials and methods

The developed soft dielectric material for this study is a thermoplastic elastomer (TPE) blend composed of three major constituents: styrene–ethylene–butadiene–styrene SEBS triblock copolymer (30% Styrene, high molecular weight from Taipol)—where the rigid blocks of styrene parts are dispersed in the rubber part made of ethylene butadiene and the rubber part is sealed by the styrene blocks-, white mineral oil, acting as a plasticizer and a polyolefin. Two blends where all the components were fixed except for the polyolefin part: one blend contains random polypropylene (r-PP) with a density of 0.902 purchased from TOTAL petrochemicals company and will be identified as r-PP blend, and the second blend contains LDPE (density: 0.917, purchased from Polimeri Europe company), identified as a low-density polyethylene (LDPE) blend. By introducing the oil, the final thermoplastic elastomer system (TPE) constitutes a soft blend with enhanced overall fluidity. The selected SEBS (high molecular weight) is used in electrical applications and as compatibilizer. The polyolefins were chosen since they are standard non polar polyolefins used in cable insulation. The blend was composed of 50% of oil, 26% of SEBS, 16% of polyolefin and 8% of calcium carbonate. The TPE were prepared via injection process, where the components of the blend are mixed together under varying temperatures (~190°–210 °C) in a single screw machine with a rotating speed of 300 rpm. The process of fabrication does not include any volatile chemical solvents.

Once the mixture is realized and the blends are obtained in the form of pellets, a set of physico-chemical characterization of SEBS, polyolefin and blend films was performed in order to assess the compatibilities and possible interactions between

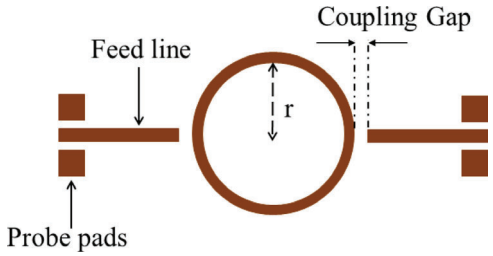

Figure 1. Schematic view of the shape of the ring resonator with GCPW for high frequency measurement up to 40 GHz with the probe station.

the components. The blend specimens were hot-melted into $2.5 \times 2.5\,\mathrm{cm}^2$ samples.

The Fourier transformer Infrared analysis spectra of the films were recorded using a Perkin Elmer Spectrum 2000 FTIR spectrometer in the transmission mode in the $400\,\mathrm{cm}^{-1}$ to the $4000\,\mathrm{cm}^{-1}$ range. A background scan of the air was first made then the samples were scanned under the same conditions.

X-ray diffraction (XRD) patterns were determined by using a Bruker D8 Advance diffractometer at room temperature in the reflection mode. The Cu-Kα radiation ($\lambda = 0.154\,18\,\mathrm{nm}$) was used. The LDPE-TPE blend and the r-PP-TPE blend films were put over copper and stainless steel plate as rigid substrate, respectively. The blends were also characterized by differential scanning calorimetry (DSC) with a DSC Perkin Elmer apparatus where samples were subjected to heat/cooling increment of 5 °C min^{-1} under a constant nitrogen atmospheric pressure. The data extracted from the curve such as the melting temperature T_m is a crucial parameter in the process of thermoforming when preparing the samples for the dielectric characterization.

The measurement of the dielectric parameters (capacitance and dielectric loss factor tan δ) between 1 kHz and 10 kHz have been carried out using an impedance analyser (Agilent HP 4194A) and by developing a metal–insulator–metal (MIM) configuration of $2.5 \times 2.5\,\mathrm{cm}^2$ samples where the polymer film is the dielectric layer, the copper layer as the top electrode of a 1 μm thickness and stainless steel as the bottom one of 205 μm thickness. The top electrode was deposited by DC sputtering using AC450 Alliance Concept sputter at 50 W, over the entire surface of the sample or within circular shadow mask to form a disk of a radius of 0.5 cm.

The dielectric permittivity was calculated by using formula (1):

$$\varepsilon_\mathrm{r} = \frac{hC}{S\varepsilon_0} \tag{1}$$

where h and ε_r are the thickness and the relative permittivity of the dielectric substrate respectively, ε_0 is the vacuum permittivity, C is the capacitance measured by the impedance meter and S is the surface of the top electrode.

The determination of the relative permittivity and loss tangent for soft substrate at microwave frequency band is a mandatory step before fabricating any high frequency components for several reasons. At higher frequencies, the characterization process becomes more intricate in as much as conveying good performance at high frequencies becomes challenging. So forth, establishing the correct method is crucial to obtain accurate values of the dielectric parameters of the sample. Thereupon, different methods have been thoroughly studied [10, 19, 20] and the microstrip ring resonator method has been selected for our measurements. This method has been exploited for different configurations such as liquid crystal polymers [20–23]. For our study, to be able to characterize our samples, we have adapted the resonator ring method by adding grounded coplanar waveguide (GCPW) for microwave access as described below [24]. The ring resonator method is a technique that was developed for microwave circuits and was first established in 1969 by Marcatili [22] and was mainly used for characterizing liquid crystal polymers. The principle of the technique consists in exciting the ring by filling it with incident wavelengths through a waveguide that is coupled to the ring. The wavelengths are propagated into the loop of the ring and are transmitted to the output waveguide. An output power is a result of resonating constructive interferences that are collected at the output beam. The spectrum displays the extinction of each resonant wavelength [25].

The dimensions of the ring resonator were calculated by high frequency structure simulation (HFSS) software. The ring was shaped on the metalized samples by using photolithography as shown in figure 1.

The ring resonator dimensions such as the coupling gap as well as the radius of the ring were adapted to the thickness of the polymer film and its dielectric properties measured as explained previously.

The samples used for the microwave and patch antenna characterisations were prepared from $2.5 \times 2.5\,\mathrm{cm}^2$ polymer film/stainless steel substrate bilayers, with a DC sputtered top copper electrode of 1.5 μm thickness, covering the whole surface.

It may be noted that the conductivity of the metallic radiating patch must be as high as possible and the thickness of the deposited layer must be at least equivalent to one skin depth at the operating frequency, otherwise metal losses prevent from good radiation. For instance, for a 10 GHz operating patch antenna with a copper patch, the skin depth—minimum metal thickness for antenna radiation—is equal to 0.92 μm [10]. Besides, the generally weak adhesion between polymers and metals due to their chemical incompatibility is often a crucial issue for microwave applications. Thus, any interface discontinuity between the polymeric film and the metal electrode will severely degrade the measurement quality. In this aspect, the copper was chosen thanks to its high electrical conductivity. Different techniques of metallization have been then investigated and are summed up in table 1.

So for our study, DC copper sputtering was selected since this technique permits to achieve better metal adhesion than evaporation technique and the operating temperature of the metal deposition (~50 °C instead of ~1000 °C for evaporation) is lower than the degradation temperature of polymers (~300 °C) in the case of sputtering. For deposited thickness of over 800 nm, it was found out that breaks times were necessary in order to release the residual stress and avoid micro cracks in the copper layer.

Table 1. Comparison of different techniques of metallization.

Metallization techniques	Evaporation	Electro-deposition	Direct current (DC) sputtering
Advantages	Relatively fast	Relatively fast	Good adhesion of copper
Drawbacks	Degradation of polymer under high temperature	Risk of metal oxidation Poor adhesion layer Need for seed layer	Time consuming

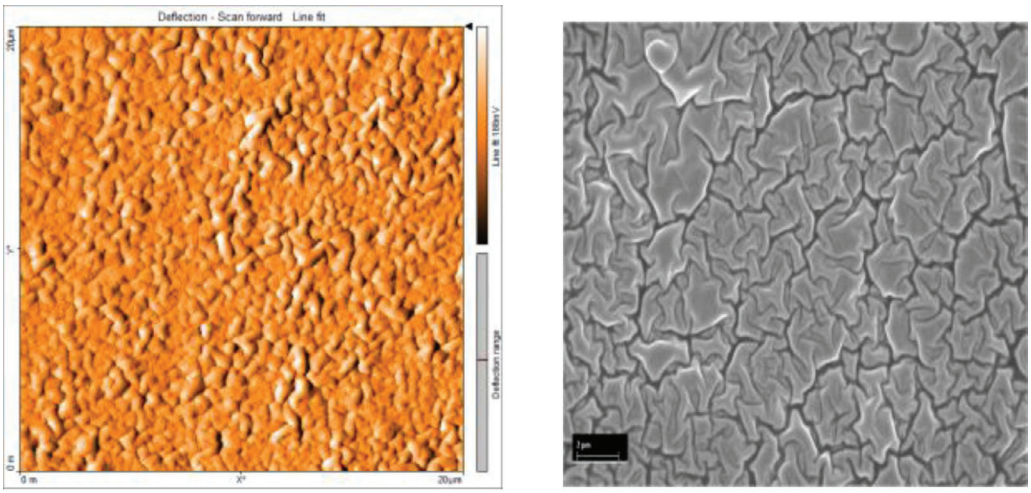

Figure 2. (a) AFM image (scanned surface dimensions: 20 × 20 μm^2), (b) SEM image (scanned dimensions: 14.7 × 14.7 nm^2) of 2 μm thick copper layer deposited on the r-PP based blend dielectric film.

The 1.5 μm thick metallized surface of the dielectric film was further investigated by microscopy in order to conclude on the homogeneity of the metal film. The atomic force microscopy (AFM) picture is consistent with the scanning electron microscope (SEM) picture for the r-PP based blend (figure 2). Copper tends to cover the polymeric film in the form of small islands superimposed on each other yielding a whole homogeneous layer that electrically conducts. Similar behaviour was also found for LDPE based blend.

The final structures of the ring resonator samples and the patch and microstrip line for the antenna (the latter is shown in section 4) were patterned via direct photolithography where a positive photoresist (S1818, Microposit) was spin coated on the metallized sample surface and then cured for 5 min at 90 °C. UV insulation step (to add the wavelength) of the samples was carried out for 26 s through a patterning mask. The active electrodes take the final shape by introducing the samples first into developer solution (MF 351, Microposit) and then by eliminating the copper in excess using a solution of iron chloride for 30 s each. The samples were washed with distilled water and dried before immersion in each solution. The final step of the device preparation consists in rinsing and removing the rest of the photosensitive resins by washing the device with acetone and alcohol.

For ring resonator microwave characterisation, the feed lines were connected to GCPW to facilitate the characterization of the sample by the ground–signal–ground (GSG) probe. The measurements were carried out using an Agilent E8364B vector network analyzer (VNA) (bandwidth from 10 MHz to 50 GHz) and Cascade ACP40-AW-GSG probes (40 GHz bandwidth, 500 μm pitch). For the calibration of the probe station, we used the short–open–load–through method with a Cascade ISS-104-783 calibration substrate. The whole test system was controlled using Wincal Cascade software.

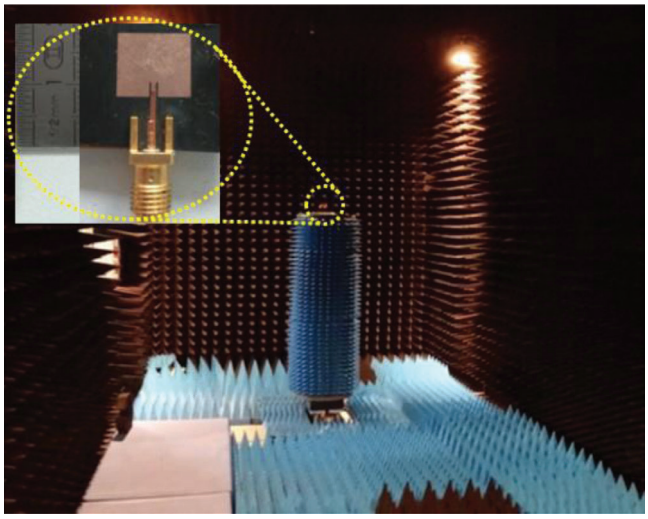

Figure 3. Microstrip patch antenna with inset feed line and SMA connector in anechoic room.

For the radiation characterisation of the polymer blend based patch antenna, the latter was excited via an inset microstrip

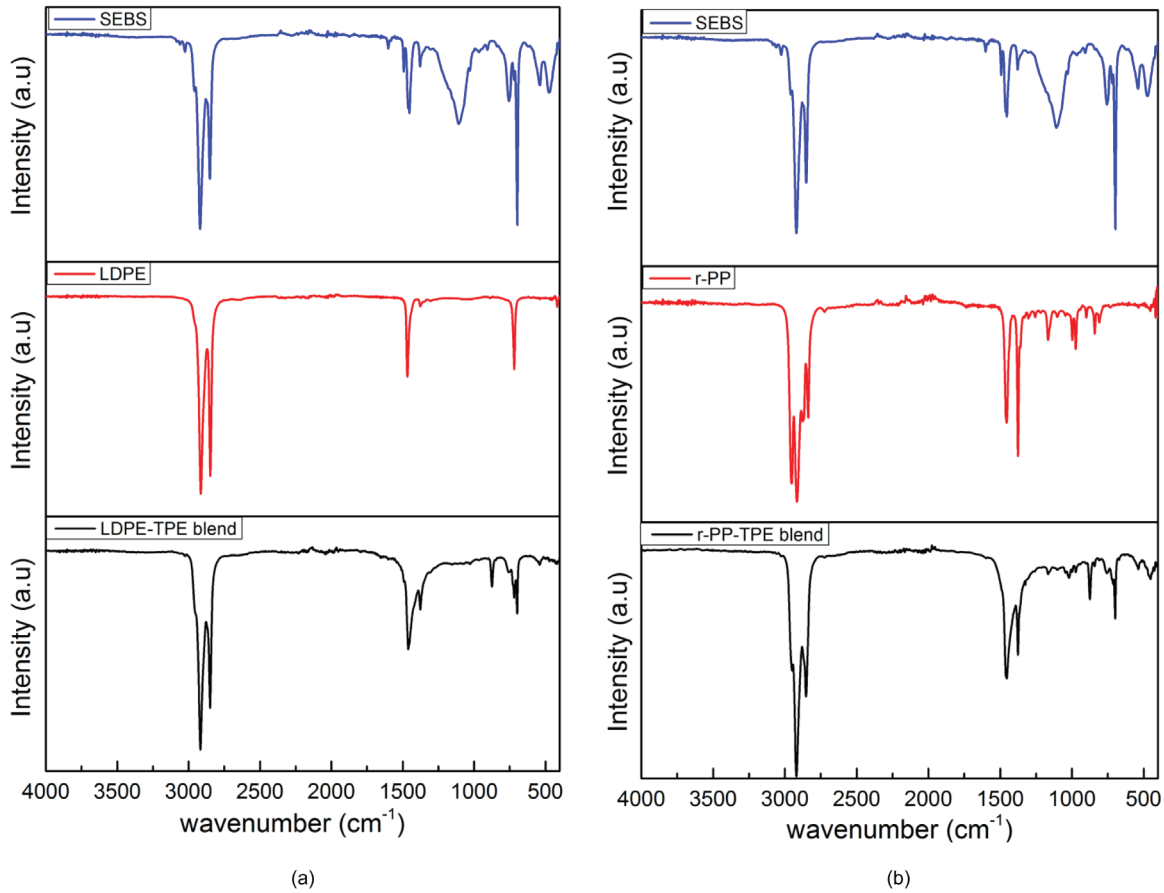

Figure 4. FTIR absorption spectra of (a) LDPE-blend, LDPE and SEBS, (b) r-PP-blend, r-PP, SEBS.

feedline using a SubMiniature version A (SMA) connectors. The proposed design of the inset microstrip line fed patch antenna was chosen because it provides easy manufacturing and is advantageous for being able to connect directly the antenna element to the impedance circuit and to avoid multilayer-board.

Measurements of the radiation pattern of the antenna have been made in a far-field millimeter wave anechoic chamber (figure 3). A source horn-shaped antenna was used as a reference and the patch antenna was installed on a rotary mast controlled by software and 5 m apart from the reference antenna. In order to determine the angle with a maximum gain, a sweep in frequency between 8 GHz and 12 GHz has been done. Once the value of the resonance frequency and the angle with the maximum gain are obtained, four plane configurations have been realized: co-polarization planes *E* and *H* and cross polarization planes *E* and *H* since the microstrip patch antenna is linearly polarized. The reflected signals by the tested antenna installed on the rotary mast and received by the horn antenna were recorded as a function of the angle in order to generate the radiation plot of each mentioned configuration.

3. Results and discussion

3.1. Physico-chemical characterisations

Figure 4 presents the FTIR absorption spectra of SEBS, LDPE, r-PP, LDPE-blend and r-PP-blend. The absorption peak in the

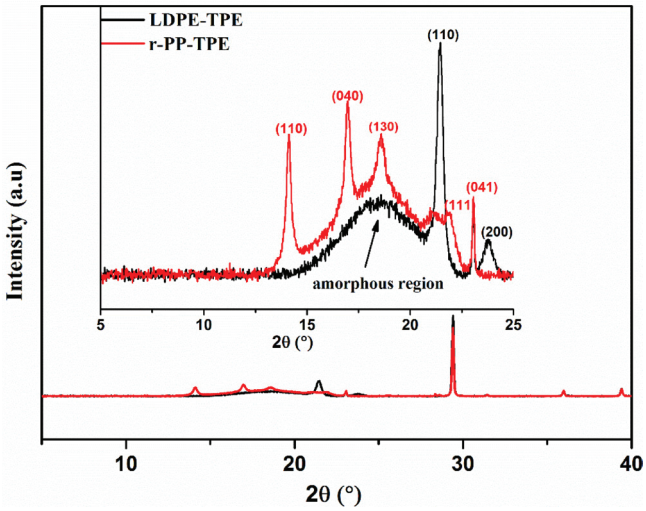

Figure 5. XRD patterns of LDPE-TPE and r-PP TPE based blends.

SEBS at 1107 cm^{-1} is not identified in the studies of the FTIR of SEBS and then might be due to the presence of additives in small quantities. This hypothesis is confirmed since it is not observed in the spectra of the blends. The other main peaks of the SEBS (3025 cm^{-1}, 1492 cm^{-1}, 756 cm^{-1}) which are not found as well in the spectrum of the blend is a result of the dispersion of the oil in the elastomeric phase of the SEBS the EB phase and thus inducing an irregular arrangement of the microdomains of the PS. The FTIR spectra confirm that

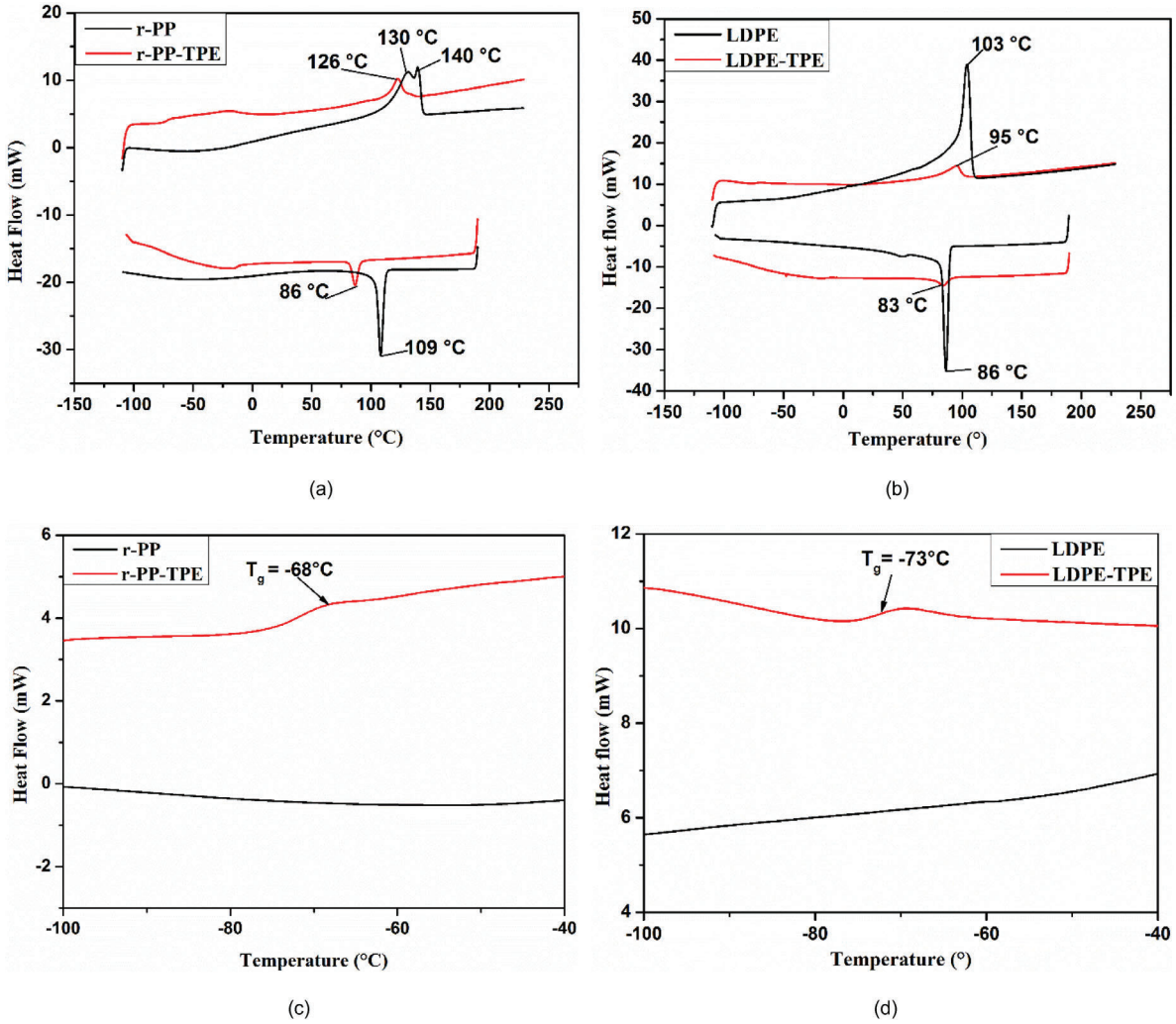

Figure 6. DSC curves of (a) r-PP-TPE and r-PP, (b) LDPE-TPE and LDPE, (c) zoomed-in area near T_g of the r-PP-TPE, (d) zoomed-in area near T_g of the LDPE-TPE.

no new chemical bond has formed in both blends since there is no new peak generated. A similar study of the same blends was reported in [26] The FTIR spectra of the LDPE blend and the r-PP blend show quasi similarities except the range of 1165 cm^{-1} and 808 cm^{-1} where the peaks at 1165 cm^{-1}, 997 cm^{-1} of the r-PP blend are assigned to parallel C–C chain stretching, CH_3 rocking, CH bending of the crystalline part of r-PP, 840 cm^{-1} corresponds to the parallel CH_2 rocking, C–CH_3 stretching of the crystalline part as well and 808 cm^{-1} is assigned to the perpendicular CH_2 rocking, C–C chain stretching, C–CH stretching in the crystalline domain of the r-PP [27].

Figure 5 shows the XRD patterns of LDPE-TPE and r-PP TPE based blends. All the peaks appearing above $2\theta = 25°$ relate to the rigid substrates.

The crystalline domains of the blends originate from the presence of LDPE and r-PP. The diffraction peaks of both polyolefins are detected in their respective blends when 2θ is between 10° and 25°. The corresponding peaks at 2θ equal to 14.28° (1 1 0), 17.14° (0 4 0), 18.92° (1 3 0), 21.40° (1 1 1) and 22.20° (0 4 1) are assigned to the presence of the PP α-form in the corresponding blend. In the LDPE based blend however not only is the intense peak of the LDPE ascribed to the presence of the orthorhombic lattice when $2\theta = 21.6°$ (1 1 0) and 23.9° (2 0 0), but also the amorphous part is detected in the range of 2θ: 12°–25° with characteristic broad peak. Considering that the peak area is proportional to the amount of the amorphous and the crystalline phases, we can assume that the amorphous region on the LDPE based blend is more present than in the r-PP blend, moreover when mixed to SEBS and oil to form blends the crystalline phase of both polyolefins remain stable.

Figure 6 shows the DSC curves of the two polyolefins and related blends. It is found that in the case of pure polyolefins, the melting peak is sharper. Moreover, the overall melting temperature is decreased in the case of the blends. Previous studies in [28] have shown that the decrease in melting temperature is explained by the lamellar thinning of the polyolefins crystal phase in the presence of the SEBS. The two observed melting peaks in the r-PP are due to the presence of the PP units and the ethylene units in the structure of the r-PP and which have different melting temperatures.

The temperature of glass transition T_g was determined at the half heat capacity C_p values of the heating curves. Only the values of the T_g of the soft block of the SEBS of each blend

Table 2. Summary of T_m and T_g of LDPE, r-PP, LDPE-TPE and r-PP-TPE.

	T_g (°C)	T_m (°C)	ΔH_m (J g^{-1})	Xc
LDPE	—	103	102	35%
r-PP	—	140, 130	85	41%
LDPE blend	−73	95	17	50%
r-PP blend	−68	126	10	36%

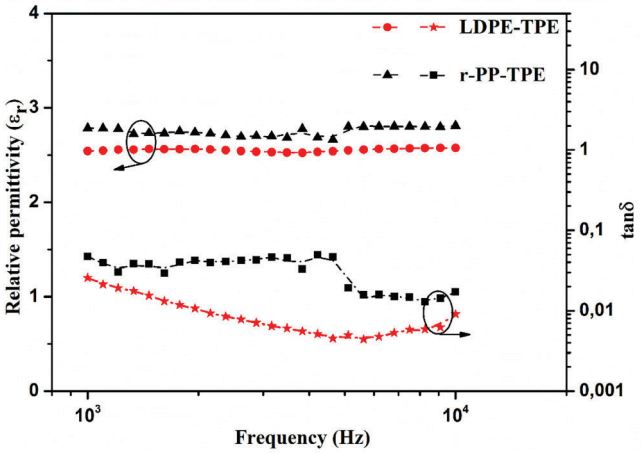

Figure 7. Relative permittivity and tan δ of the r-PP based blend and the LDPE based blend dielectric film as a function of frequency in the range of 10^3 Hz and 10^4 Hz.

could be recorded which were −73 °C and −68 °C for the LDPE based blend and for the r-PP based blend respectively.

As a plasticizer, the trapped oil in the olefinic block of the SEBS decreases the T_g value of the soft part of the SEBS which is ~55 °C for the EB block of a pure SEBS.

The degree of crystallinity X_C (or cristallinity) was determined with the following formula:

$$X_C = \frac{\Delta H_{mTPE}}{m_{olefin} \times \Delta H m_{olefin}} \quad (2)$$

where m_{olefin} is the mass fraction of the polyolefin and ΔHm_{olefin} and ΔHm_{TPE} and are the melting heat of 100% crystalline of the polyolefin and the polyolefin blend respectively; the values of the melting heat of complete crystalline polyolefin are reported to be 209 J g^{-1} and 286.7 J g^{-1} for the 100% crystalline r-PP [29] and LDPE, respectively [30].

The LDPE based blend shows higher crystallinity than the r-PP based blend (table 2). The crystallinity is an important parameter in the study of the dielectric losses of the blends. The crystalline phase in the semi crystalline polymers such as the LDPE or the r-PP has lower dielectric loss than the amorphous phase [19].

3.2. Dielectric characterisations

For each polymer blend, dielectric measurements were made on three to four samples and repeated three times, from which the mean value of the dielectric parameters

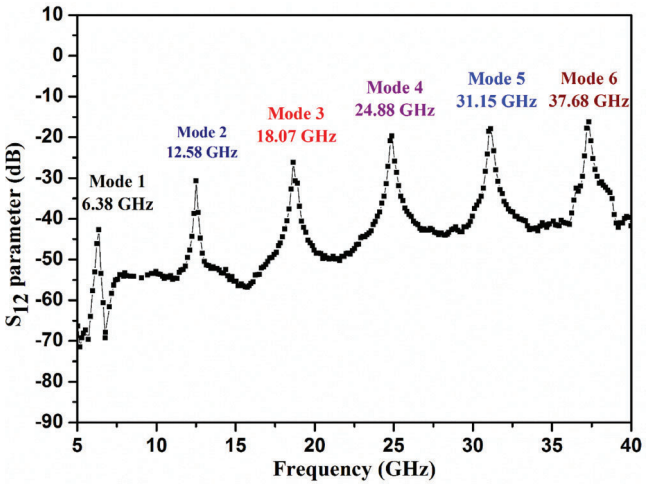

Figure 8. Measured transmission S_{12} parameter versus the frequency of a 220 μm thick r-PP blend dielectric film, the ring resonator parameters are $r = 4000$ μm, $S = 80$ μm, $W = 530$ μm.

was calculated. Figure 7 shows the frequency dependence of the relative permittivity in low frequency range [1–10] kHz. The relative permittivity exhibits a quasi-stable value around 2.82 for the r-PP blend and 2.65 for the LDPE based blend which are typical values of a non-polar polymer such as r-PP and LDPE containing blends [31]. The relative permittivity is an important property for optimizing the ring resonator dimensions for the characterization at higher frequencies. The loss tangent values are also roughly stable for both blends, even if lower values are observed for the LDPE-based blend.

Figure 8 shows the plotted results of the transmission signal also called the S_{12}-parameter versus frequency of the tested sample for a ring radius $r = 4000$ μm and a coupling gap of 80 μm. The thickness of the sample is 220 μm and the feed line width is W = 530 μm. In order to calculate the dielectric permittivity and the loss tangent at microwave frequencies, we restrict the calculation of the aforementioned properties at resonance frequencies (S_{12} peaks) observed in figure 8. Each peak corresponds to a resonant mode of the ring from which the dielectric properties are calculated.

To determine the dielectric properties of the blend, the relative permittivity and the loss tangent were extracted using formulas (3)–(12) [20–23, 32, 33].

So the effective dielectric constant is calculated as shown in formula (3):

$$\varepsilon_{eff} = \left(\frac{nc}{2\pi r f_0}\right)^2 \quad (3)$$

where n is the mode order, $c = \frac{1}{\sqrt{\mu_0 \varepsilon_0}}$ the speed of light, r_e is the effective ring radius equal to $r + \frac{W}{2}$ (W is the width of the ring) and f_0 is the resonance frequency. The relative permittivity is then calculated from the effective permittivity using the expression in formula (4)

$$\varepsilon_r = \frac{2\varepsilon_{eff} + M - 1}{M + 1}, \quad (4)$$

where

$$M = \sqrt{1 + 12\frac{H}{W_{\text{eff}}}}$$

and W_{eff} is the effective width of the line of the ring and is expressed in formula (5):

$$W_{\text{eff}} = W + \left(1.25\frac{t}{\pi}\right)\left(1 + \ln\frac{2h}{\pi}\right), \tag{5}$$

where W is the width of the ring, t and h are the thickness of the metal and the dielectric polymeric film respectively.

To calculate the loss tangent from the ring resonator we can get the value of the total attenuation and deduct the conduction loss and the radiation loss in order to determine the dielectric loss as shown in formula (6):

$$\alpha = \alpha_{\text{d}} + \alpha_{\text{c}} + \alpha_{\text{r}}, \tag{6}$$

where α the total attenuation factor, α_{d} the dielectric loss, α_{c} the conductive loss and α_{r} the radiation loss. The effect of this latter is observed in the optical frequencies and thus will be null since the measurements were conducted at microwave frequencies.

The total attenuation can also be calculated by formula (7) and is given in N_{p}/length:

$$\alpha = \frac{\pi}{Q_0\lambda_{\text{g}}}, \tag{7}$$

where λ_{g} the guided wavelength and the unloaded Q_0 factor that are calculated by formula (8):

$$Q_0 = \frac{Q_L}{1 - 10^{-\frac{La}{20}}}, \tag{8}$$

where La (dB) represents the measured insertion losses of the ring resonator at frequency resonance and Q_{L} is the loaded quality factor calculated by formula (9):

$$Q_{\text{L}} = \frac{f_0}{\Delta f_{-3\text{dB}}}, \tag{9}$$

where f_0 and Δf are the resonant frequency and the frequency bandwidth at 3 dB.

Then, we proceed with the calculation of the conductive attenuation α_{c} (dB m^{-1}) given by formula (10):

$$\alpha_{\text{c}} = \frac{8.68}{Z_0 h}\frac{R_{\text{s}}}{\left\{\frac{W_{\text{eff}}}{h} + \frac{2}{\pi}\ln\left[2\pi\exp\left(\frac{W_{\text{eff}}}{2h} + 0.94\right)\right]\right\}^2}\left[\frac{W_{\text{eff}}}{h} + \frac{W_{\text{eff}}/\pi h}{\frac{W_{\text{eff}}}{2h} + 0.94}\right] \times \left\{1 + \frac{h}{W_{\text{eff}}} + \frac{h}{\pi W_{\text{eff}}}\left[\ln\left(1 + \frac{2h}{t}\right) - \frac{1 - \frac{t}{h}}{1 + \frac{t}{2h}}\right]\right\}, \tag{10}$$

where Z_0 is the characteristic impedance of the microstrip line, t the copper thickness and Rs the surface roughness resistance calculated by thefollowing expression:

$$R_{\text{s}} = \sqrt{\frac{\pi\mu f}{\sigma}}, \tag{11}$$

where $\mu = 4\pi \cdot 10^{-7}$ H m^{-1} and σ the bulk conductivity of copper.

The loss tangent is then determined using the following expression, with λ_0 as the wavelength at resonant frequency f_0.

$$\tan\delta = \frac{\alpha_{\text{d}}\lambda_0}{27,3}\frac{(\varepsilon_{\text{r}} - 1)\sqrt{\varepsilon_{\text{eff}}}}{\varepsilon_{\text{r}}(\varepsilon_{\text{eff}-1})}. \tag{12}$$

The results of the dielectric properties corresponding to each peak from different resonator radii are shown in figure 9. The tested resonator radii were: 4, 5 and 6 mm for the LDPE based blend and 3, 4, 5 and 6 mm for the r-PP based blend. The relative permittivity values are similar and stable ($\varepsilon_{\text{r}} \approx 2.45$) for both blends, in the whole frequency range (0.5–40 GHz), as already observed in the 1 kHz–10 kHz range. Although there are some scattering in the experimental data, the dielectric loss curves of the two blends exhibit different trends. The LDPE based blend dielectric loss globally decreases with increasing frequency and the abrupt drop below 10 GHz is attributed to the dispersion at ~1 GHz, which is an inherent property of PE [34]. Whereas the dielectric loss factor of the r-PP based blend is roughly constant between 0.5–40 GHz. By taking the crystallinity (Xc) of both blends into account, the larger Xc in the case of the LDPE based blend contributes to the relatively smaller tan δ values since the dielectric loss in polymers often decreases with increasing degree of crystallinity [34]. Low loss tangent of LDPE blend in the low frequency range (1 kHz–10 kHz) shown in figure 7 may also originate from enhanced cristallinity.

Finally, the dielectric loss of the LDPE and r-PP blends exhibit similar trends as LDPE and PP respectively that were reported by Bur [34]. The mechanism of dielectric loss in LDPE at 1 GHz is explained by localized dipolar motion in the amorphous phase. The observed dielectric loss in the range of [0.1–1] GHz in the case of PP is reported to be due to the dispersed β relaxation that starts at 10^4 Hz. The study in [34] has reported as well on the effect of the crystalline phase on the dielectric loss.

It is interesting to note that the measured dielectric features of the two soft blends make these polymer formulations attractive for antenna applications, especially owing to the low dielectric loss value above 10 GHz, close to those of commercial rigid substrates.

4. Microwave application of the blends: patch antenna preparation and characterisation

To highlight the performance of the two new polymeric blends developed in this study, we chose the realization of a blend-based patch antenna.

The antenna based on PP or LDPE blend was designed to have an operation frequency of about 10 GHz. Since the latter is a function of the width and length of the patch and the dielectric properties of the substrate that have been already measured, HFSS simulations have been carried out in order to adapt the dimensions of the patch and the feed line to obtain a matching impedance of 50 Ω at 10 GHz. The geometry as well as the dimensions are detailed in table 3 and figure 10.

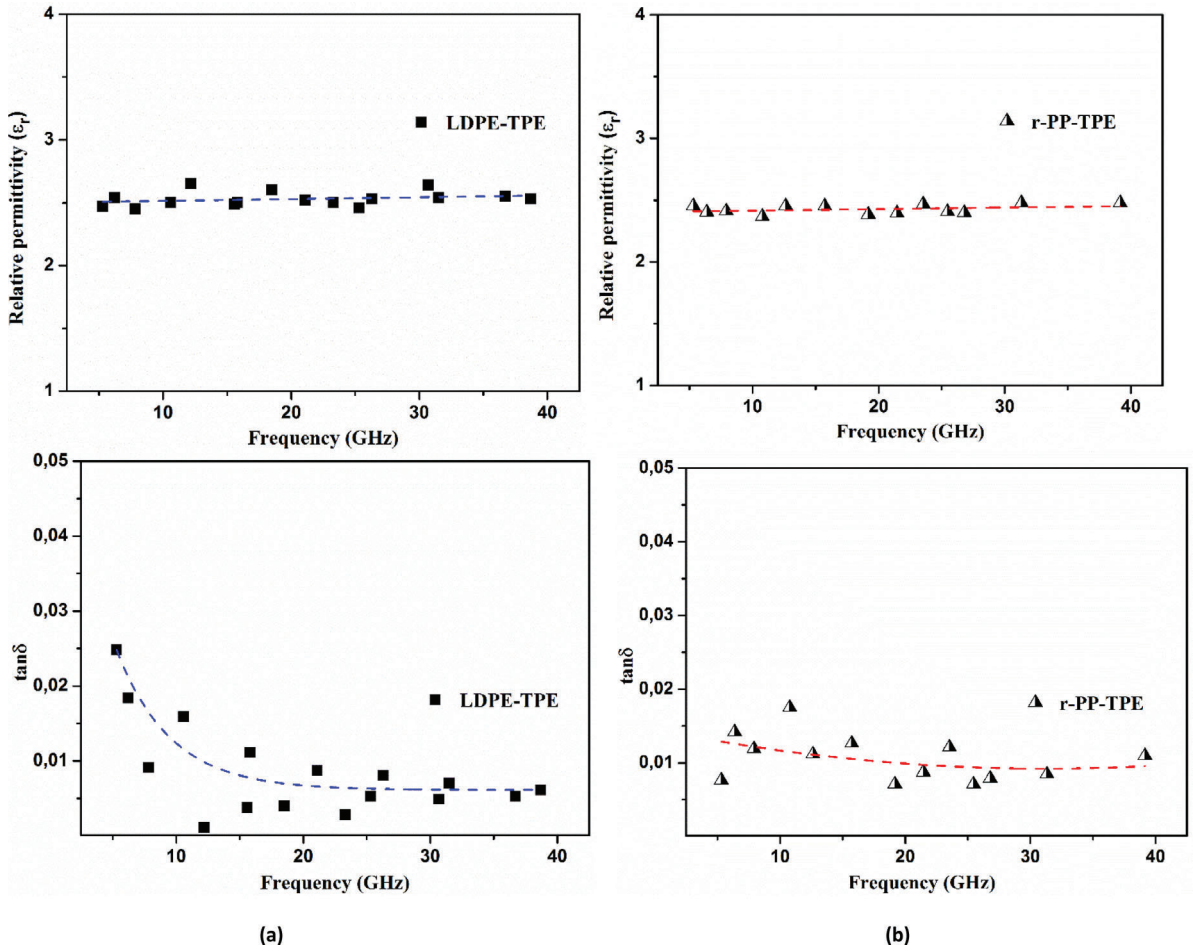

Figure 9. Dielectric properties versus frequency of (a) LDPE-TPE and (b) r-PP-TPE based blends.

Table 3. Summary of the dimensions of the designed microstrip patch antenna on a 220 μm thickness r-PP and LDPE based blend as dielectric film.

Parameter	W	L	Gap	L_2	W_p	L_p
Dimensions (μm)	635	10 000	800	2200	11 500	9700

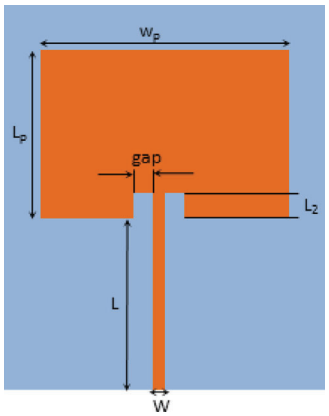

Figure 10. Top view of the geometry of the microstrip patch antenna.

The length of the metallized patch is $L_p = \frac{\lambda_g}{2}$; where λ_g is the effective wavelength.

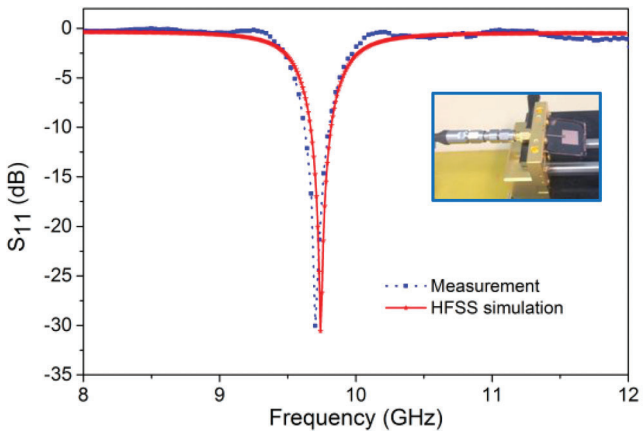

Figure 11. Measured and Simulated return loss measurement for the 50 Ω microstrip patch antenna on a 220 μm thick r-PP based blend dielectric with socket Anritsu® Universal test fixture 3680.

The step of measuring the antenna return loss was carried out before measuring the radiation pattern. This step is necessary to validate the impedance matching of the antenna and it consists in measuring the return power reflected by the antenna (S_{11} reflection parameter).

As shown in figure 11, a good agreement between measurement and HFSS simulated results is obtained. The experimental value of the return loss was noted as −30 dB at the

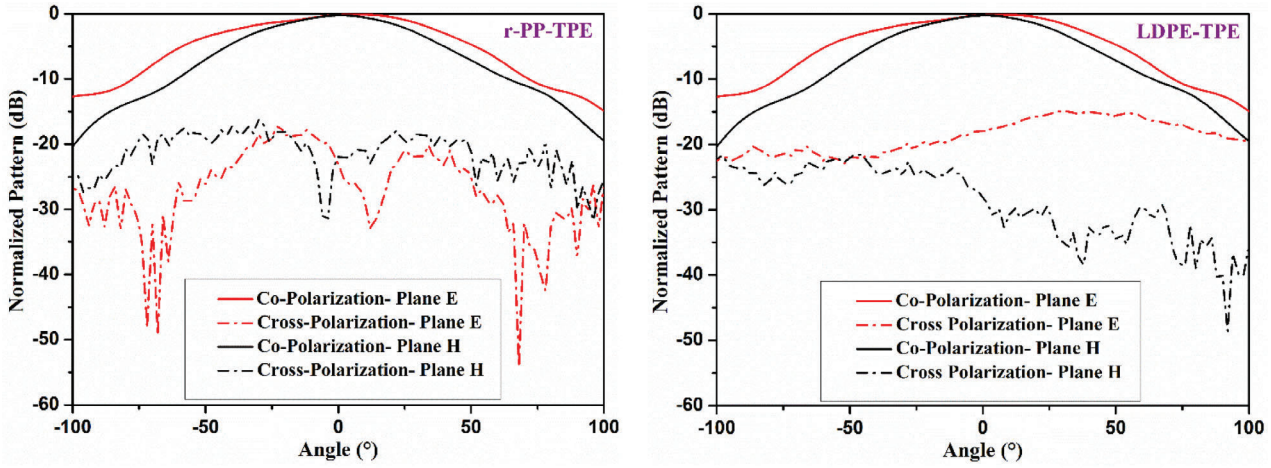

Figure 12. Measured radiation pattern of the (a) r-PP based microstrip patch antenna at 9.9 GHz, (b) LDPE based microstrip antenna at 9.8 GHz.

resonance frequency at $f_r = 9.8$ GHz for r-PP based blend and -26 dB at the resonance frequency of $f_r = 9.6$ GHz (table 5). Since it is considered in bibliography that a value of -10 dB or less is accepted as the limit for S_{11} peak, then the values obtained for our experimental and the narrow bandwidth for a return loss lower than -10 dB validate the good impedance matching of the tested system as a step before measuring the radiation efficiency of the developed antenna. This latter parameter will determine if the transmitted power is radiated or dissipated.

The radiation pattern of an antenna is a graph that describes how the antenna radiates the energy as a function of space. It designates the fluctuation of the power radiated by the antenna in all directions. The radiation is a function of the angle and noted as the antenna radiation in the far field.

The radiation of the antenna depends not only on the dielectric properties of the antenna but also on the microstrip line and the feed line position for higher frequencies. The substrate thickness h increases the gain to a certain limit but can also cause some undesirable effect like surface wave excitation that can deteriorate the radiation [35]. Figure 12 shows the normalized radiation pattern of radiation versus angle for the two blends. The values of the gain, directivity and efficiency have been determined from the radiation plots.

Since patch antennas are passive structures, they do not have a real gain; the radiation pattern was calculated and compared from a hypothetical isotropic antenna which is the broadband horn antenna.

The maximum gain was recorded at a resonance frequency of 9.9 GHz with a value of 4.56 dB for Co-polarization plane E. The radiation graph shows main lobs presence for the co-polarization planes. This result was expected since the microstrip antennas are linearly polarized.

The directivity of an antenna is the ratio of the maximum radiated power density over the average radiated power [35]. It is also a measure of how well the radiation of an antenna is concentrated, the higher the directivity, the narrower the radiation pattern is [36]. The directivity is calculated by:

Table 4. Bandwidth of plane E and plane H for r-PP and LDPE based blends.

	ΔE	ΔH
r-PP based blend	90°	60°
LDPE based blend	92°	63°

$$D(\theta,\varphi) = \frac{U(\theta,\varphi)}{U_0} = \frac{4\pi U(\theta,\varphi)}{P_{\text{rad}}} \tag{13}$$

where θ and φ are the spherical coordinates, $U(\theta,\varphi)$ is the radiation intensity of the antenna, U_0 and P_{rad} are the radiation intensity and the total power radiated of an isotropic antenna, respectively.

Since obtaining the 3D pattern is quite difficult in reality, an approximation is used for a pencil beam shaped pattern which is the case for a microstrip antenna. In that case, the directivity is calculated as follows:

$$D = 10\ \log\left(\frac{32\,400}{\Delta E \times \Delta H}\right) \tag{14}$$

where ΔH and ΔE are the measured aperture angles at –3 dB beam width which are given in table 4.

The slight dissymmetry in the plane E observed in the curves of figure 12 for both can be explained by the instability in the SMA connector during the rotation of the mast [37]. The directivity is 7.5 dB measured for the r-PP based blend and 8.1 dB for the LDPE based blend using formula (14).

The efficiency value takes into account the gain and the directivity of the antenna and is calculated as in formula (15):

$$\eta = 100 \times 10^{(G-D)/10}. \tag{15}$$

The calculated efficiency of the r-PP based blend antenna and the LDPE based blend antenna is 46% and 51%, respectively. Knowing that a 100% efficiency is obtained for an ideal system meaning with null dissipation effect with a lossless material, we can conclude that both values of efficiency are relatively better than that of comparable patch antennas based

Table 5. A comparative study of the properties of patch antenna on different flexible substrates.

	This work	This work	[15]	[38]	[17]
Electrode (radiating patch)/dielectric substrate	Copper/SEBS-PP-oil blend	Copper/SEBS-LDPE-oil blend	Gold/PDMS	Copper/extruded polystyrene	Gold/TPU
Resonance frequency	9.8 GHz	9.6 GHz	55 GHz	6.78 GHz	10 GHz
Thickness (μm)	220	220	20	2000	40
S_{11} (dB)	−30	−28	—	—	−25
Gain (dB)	4.56	4.88	12.3	4.7	3.25
Efficiency (%)	46	51	28	—	26,6%

on polymeric materials as shown in table 5. The observed improvement in the gain and the efficiency of the LDPE based antenna is assumed to be related to the slight reduction of the dielectric loss in the LDPE based blend as compared to the r-PP based blend.

5. Conclusion

In this paper, we report the study of two soft TPE blends for microwave antenna applications. The soft blend was composed of three constituents: triblock copolymer SEBS, PP or LDPE α-olefin and mineral oil acting as a plasticizer. Microwave characterization results showed a low loss tangent (~0.01 at 10 GHz) for both types of polyolefins with a slight dielectric loss decrease with LDPE especially for frequencies above 10 GHz. The blend shows a great potential to be further optimized by blending initially lower dielectric loss materials in order to still reduce the dielectric losses of the blend and prepared with high purity process presenting weaker dielectric loss at the microwave frequencies. Another possible way is to modify the global morphology by varying for instance the free volume or the porosity and thus minimize the interfacial polarization that contributes to the dielectric loss of the final blend.

For microwave application, the new soft TPE blends have been used as patch antenna substrates. First, we adapted the microstrip ring resonator method for the dielectric characterization at microwave frequencies of a soft blend film of 100–250 μm in thickness. The technology process of the developed microstrip patch antenna on a soft dielectric and the radiation pattern were fully detailed. Interestingly, a very good bonding was achieved between the sufficiently thick (>1 μm) sputtered patch copper and the two soft elastomer antenna substrates. From the viewpoint of radiation characteristics, a very good agreement between the experiment and the simulation of the return loss has been observed. Compared to previous studies where elastomer-based soft dielectric was used for the same type of antenna of similar frequencies as mentioned in [16, 17], the overall performances of the antenna in the present work is promising with a gain of 4.56 dB and 4.88 dB and an efficiency of 46% and 51% for the r-PP and LDPE based blends respectively at 10 GHz. This proof of concept is a key step to the next level which demonstrates the possibility of integrating the antenna on real electronic device system with flexible ground plane, in view of developing high sensitivity strain antenna sensor, for instance.

Acknowledgments

This work was supported by MCPP France.

We would like to thank Dr Stéphane Ginestar from IETR for SEM characterization.

ORCID iDs

Tessnim Sghaier https://orcid.org/0000-0003-1644-4864
Benoit Guiffard https://orcid.org/0000-0002-1337-4074

References

[1] Lee J S, Chuang C C and She C C 2009 *IEEE, Proc. 5th Advanced Int. Conf. on Telecommunications (Venice, Italy, 24–28 May)* p 15
[2] Eldek A A, Elsherbeni A Z and Smith C E 2005 *Microw. Opt. Technol. Lett.* **46** 36
[3] James J R, Hall P S and Wood C 1981 *Microstrip Antenna Theory and Design* (London: Peter Peregrinus) pp 103–9
[4] Verma A K and Nasimuddin 2002 *J. Microw. Optoelectron. Electromagn. Appl.* **2** 70–4
[5] Kumar G and Ray K P 2002 *Broadband Microstrip Antennas* (New York: Artech House)
[6] Dubey K A, Tripathi G C and Singh B 2011 *Global J. Res. Eng.* **11** 28
[7] Ang B K and Chung B K 2007 *Prog. Electromagn. Res.* **75** 397
[8] Asabegoudar V G and Vinoy K J 2009 *Prog. Electromagn. Res.* **90** 353
[9] Knott E F, Shaeffer J F and Tuley M T 2004 *Radar Cross Section* 2nd edn (Raleigh, NC: SciTech Publishing)
[10] Baron S, Nadaud K, Guiffard B, Sharaiha A and Seveyrat L 2015 *Appl. Phys. Lett.* **107** 092904
[11] Anagnostou D E, Gheethan A A, Amert A K and Whites K W 2010 *J. Disp. Technol.* **6** 558
[12] Khaleel H R, Al-Rizzo H M and Rucker D G 2012 *J. Disp. Technol.* **8** 91
[13] Goteti R, Jackson R and Ramadoss R 2006 *Antenna Wirel. Propag. Lett.* **5** 228–30
[14] Liu Q, Ford K L, Langley R, Robinson A and Lacour S P 2012 *6th European Conf. on Antennas and Propagation*

(EUCAP) (Prague, Czech Republic, *26–30 March)* (IEEE) pp 168–71
[15] Liu Q, Robinson A P, Ford K L, Langley R J and Lacour S P 2012 *Electron. Lett.* **48** 65
[16] Hage-Ali S, Tiercelin N, Coquet P, Sauleau R and Preobrazhensky V 2009 *IEEE AP-S Int. Symp. (Charleston)* p 4
[17] Baron S, Guiffard B and Sharaiha A 2014 *J. Michromech. Microeng.* **24** 075020
[18] Zha J W, Wang Y, Li W K, Wang S-J and Dang Z M 2017 *IEEE Trans. Dielectr. Electr. Insul.* **24** 1457
[19] Brosseau C, Quéffélec P and Talbot P 2001 *J. Appl. Phys.* **89** 4532
[20] Samanta K K and Robertson D 2006 *European Microwave Conf. (Paris, France*, *4–6 October 2005)* (IEEE)
[21] Zou G, Gronqvist H, Starski J P and Liu J 2002 *IEEE Trans. Adv. Packag.* **25** 503–8
[22] Hopkins R 2006 The microstrip ring resonator for characterising microwave materials *PhD Thesis* University of Surrey, Guildford
[23] Thompson D C, Tantot O, Jallageas H, Ponchak G E, Tentzeris M M and Papapolymerou J 2004 *IEEE Trans. Microw. Theory Tech.* **52** 1343
[24] El Gibari M, Averty D, Hlabwax M, Vilcot J-P and Li H W 2015 *Microw. Opt. Technol. Lett.* **57** 2041–5
[25] Girault P, Lorrain N, Poffo L, Guendouz M, Lemaitre J, Carré C, Gadonna M, Bosc D and Vignaud G 2015 *J. Appl. Phys.* **117** 104504
[26] Chen P, Gao X, Wang Y, Xu T, Fang Y and Zhang Z 2016 *Solar Energy Mater. Solar Cells* **149** 60–5
[27] Türkçü H N 2014 *Master Thesis* Bilkent University
[28] García M, Belem M, García P, Zavala D, Patricia N, Muñiz R, Gabriel J, Armenta R and Luis J 2013 *Polímeros* **23** 597–601
[29] Ribeiroa V F, Junior E C, Simõesa D N, Pittola M, Tomacheskia D and Santanac R M C 2019 *Mater. Res.* **22** e20180304
[30] Hitachi High-Tech 1986 DSC measurements of polyethylene: the correlation of polyethylene density and melting *Application Brief* No. 26
[31] Dang Z M, Zhang Y H and Tjong S C 2004 *Synth. Met.* **146** 79–84
[32] Rabus D G 2007 Ring resonators: theory and modeling *Integrated Ring Resonators* (*Springer Series in Optical Sciences*) vol 127 (Berlin: Springer)
[33] Pucel R A, Masse D J and Hartwig C P 1968 *IEEE Trans. Microw. Theory Tech.* **16** 342–50
[34] Bur A J 1985 *Polymer* **26** 963–77
[35] Orban D and Moernaut G J K 2009 The basics of patch antennas, updated *Report* RF Globalnet
[36] Petosa A 2013 *Frequency-Agile Antenna for Wireless Communications* (Boston, MA: SciTech Publishing) pp 7–21
[37] Kummer W H 1992 *Proc. IEEE* **80** 127
[38] Kalra P, Aastha and Sidhu E 2017 *Int. Conf. on Automatic Control and Dynamic Optimization Techniques (Pune, India*, *9–10 September 2016)* (IEEE) pp 775–8

Biomedical Signal Processing and Control 85 (2023) 104878

Contents lists available at ScienceDirect

Biomedical Signal Processing and Control

journal homepage: www.elsevier.com/locate/bspc

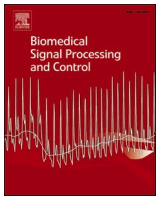

Development of flexible piezoelectric sole with wireless communication for medical application

Samia Adrar [a,*], Mohammed El Gibari [a], Philippe Saillant [b], Jean-Christophe Thomas [c], Raynald Seveno [a]

[a] University of Nantes: IETR Laboratory, Nantes, France
[b] University of Nantes: MIP Laboratory, Nantes, France
[c] University of Nantes: GeM Laboratory, Nantes, France

ARTICLE INFO

Keywords:
Piezoelectric sensor
Flexible piezoelectric materials
Wireless
Mechanical deformation
Gait
Point of-care devices

ABSTRACT

The subject of this article falls into the category of research themes on systems for medical applications with the objective of monitoring the patient at home via tools adapted to his pathology. In this context, we describe here the design of a sole for the analysis of the gait for detect the presence of anomalies in the foot characterized by a gait disorder, which can be related to a chronic disease. The collaboration with a podiatrist is an additional point in our study, it allows to define or better zones of significant pressure of the foot to analyze the data for transform these numeric values into medically exploitable information. The sole contains several pressure sensitive piezoelectric sensors developed at the IETR laboratory. The data obtained with the deformation of these sensors will be sent directly by Bluetooth using a wireless acquisition card, the information will automatically be saved on a cloud in which the doctor will have access at all times.

1. Introduction

A podiatrist is a health professional that treats foot-related infections (skin and angle). The variety of his skills allows him to design orthopedic insoles to treat problems associated to the foot posture or defect related to an imbalance in size between two feet. During the first visit, the podiatrist performs a clinical examination where the patient walks on a podiatry walking mat and data is saved for a later analysis. Generally, the walking mat has a length between 1 and 2 m. to get a data recording with the walking mat, it is necessary to do between 2 and 3 steps, which occurs an artificial walking that can generate mistakes of understanding for the walking analyze; and second problem is that the accuracy of information given by walking mat can decrease by the use of patient shoes, as demonstrated in Fig. 1. The "M" curve is flattened by the use of shoe which results in a loss of potentially useful information. To overcome these problems, pressure sensors can be directly inserted on the sole of the patient shoe. To avoid bothering that could disrupt walking, pressure sensors have to be as thin as possible, and flexible to prevent breaking during walking analyses. The objective of this article is to describe the realization (design and fabrication process) of a connected flexible sole which can be inserted in a patient's shoe and which can give similar "M" curve obtained by a walking mat without shoe.

The research carried out on the foot has given rise to several themes on gait monitoring devices, which has resulted in the appearance of several projects and start-ups that have worked on the design of connected soles for recording the walking. Connected soles like Digitsole [1] and FeetMe [2] allow you to have information relating to the activity such as the number of steps, the speed, the time of support and others. However, for medical treatment, a more personalized analysis of the foot is needed, starting with a consultation in the podiatrist's office. The specialist will carry out a series of examinations with different devices until the design of a suitable podiatric sole.

The connected soles marketed are standard, they have the same shape, the same thickness and the same characteristics. Industrial prototypes are made for sale on a large scale and do not consider the different foot pathologies, because the shape of the sole cannot be the same for a flat, hollow and normal foot, just as it cannot be the same for a person with a pronator, supinator or neural stride. Indeed, several elements are to be taken into consideration for the realization of a sole adapted to each person.

* Corresponding author.
E-mail addresses: Samia.Adrar@univ-nantes.fr (S. Adrar), Mohammed.El-Gibari@univ-nantes.fr (M. El Gibari), philippe.saillant@etu.univ-nantes.fr (P. Saillant), Jean-Christophe.Thomas@univ-nantes.fr (J.-C. Thomas), Raynald.Seveno@univ-nantes.fr (R. Seveno).

https://doi.org/10.1016/j.bspc.2023.104878
Received 16 November 2022; Received in revised form 1 February 2023; Accepted 18 March 2023
Available online 30 March 2023

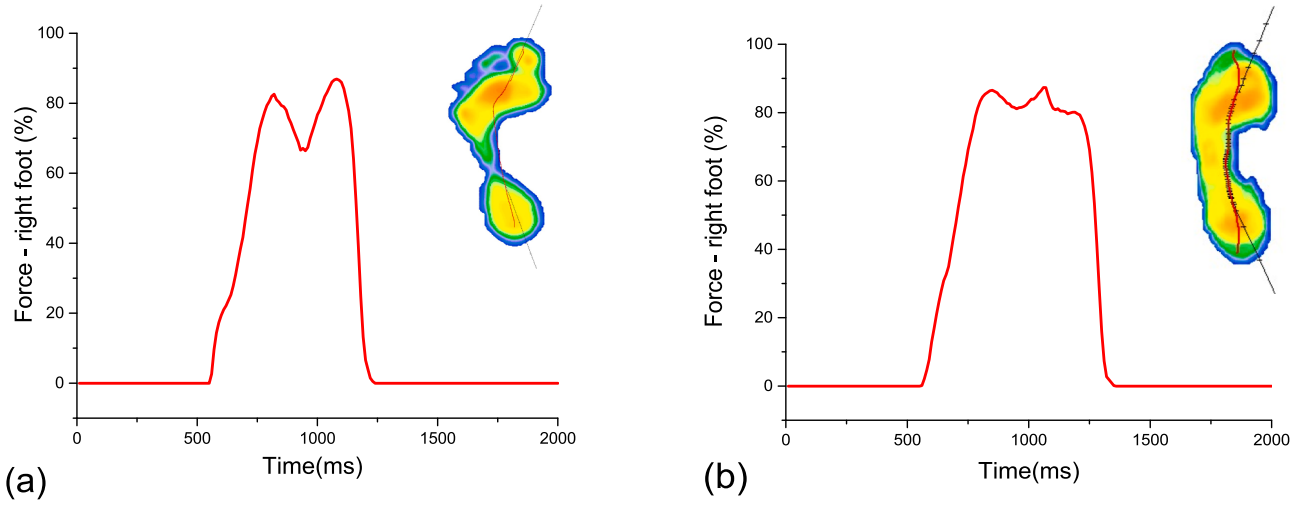

Fig. 1. "M" curves of two walking tests carried out with a podiatry walking mat, (a) without shoes and (b) with shoes.

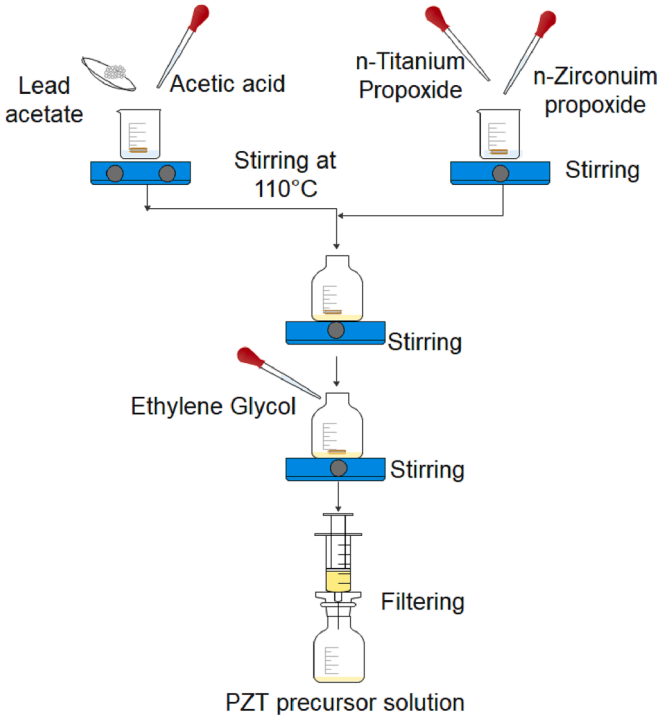

Fig. 2. Scheme of the manufacturing process for PZT thin films.

In order to identify important pressure zones, we used the thesis work of Laetitia Claverie [3] who carried out a study to define a method of placing sensors in the foot using a pressure platform (Win-pod®) which records plantar pressure data, and a force platform (AMTI) placed under Win-pod® to record the reaction force. Based on the results of his research we have identified the pressure zones for our sole prototype.

The mastery of the manufacturing process of flexible piezoelectric sensors, makes it possible to produce sensors with different sizes and shapes, a characteristic that will allow us to analyze the most remote and essential pressure points for the study. The process of depositing PZT solution on a flexible aluminum substrate is a technique patented by our laboratory [4]. Another important point in our project is based on the collaboration with a podiatrist, in addition to the technical aspects of the sole, it is interesting to have assistance and a medical vision for the interpretation of the results.

2. Device design and characterization

2.1. Flexible sensor

2.1.1. Realization of piezoelectric thin-film

The piezoelectric thin films for flexible sensors used in this study are fabricated in our laborratory as previously described [5,6]. This technology is based on the deposition of a thin layer of lead zirconate titanate oxide $Pb(Zr,Ti)O_3$ (PZT) on a flexible aluminum substrate, allowing of the fabrication of less than 15 μm-thickness pressure sensors that can be easily insert in a flexible sole. The simplicity of the Chemical Solution Deposition (CSD) process and availability of low-cost products present great advantages that make this technique easily transferable to industry.

The chemical process for the manufacture of these thin films contains

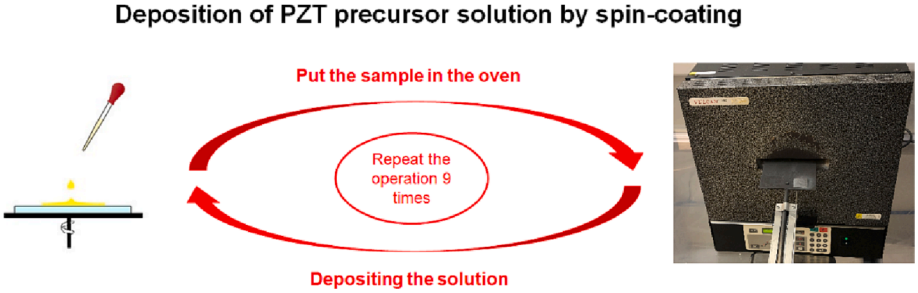

Fig 3. Depositing the precursor solution on the aluminum substrate.

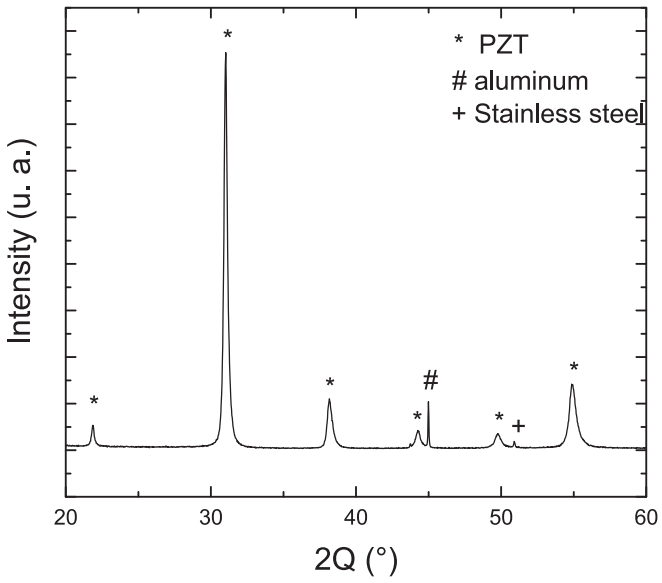

Fig. 4. X-ray diffraction pattern of PZT on aluminum substrate.

three steps, the preparation of the PZT precursor solution, the deposition on the aluminum substrate and the annealing step allowing the crystallization of the film. The chemical elements that go into the manufacture of the PZT thin films are detailed in Fig. 2. First, 7 ml of acetic acid CH_3COOH is mixed with 6.56 g of tri-hydrated lead acetate Pb $(CH_3CO_2)_2$ at a temperature of 110 °C. A second solution of zirconium n-propoxide quantity 4.26 g $Zr(C_3H_7O)_4$ mixed with 1.99 g titanium n-propoxide $Ti(C_3H_7O)_4$ at ambient temperature is then poured into the bottle of the first solution then mixed for a few minutes, 1.12 ml of ethylene glycol HO-$(CH_2)_2$-OH is added to the solution to prevent cracking of the film during heat treatment. In order to avoid the presence of agglomerates, the solution is then led to the filtering stage to obtain the final PZT precursor solution. Precursors quantities have been adjusted in order to obtained a 57/43 Zr/Ti ratio which provides good piezoelectric properties, this ratio has been optimized in other research work beforehand in our laboratory [7].

The next phase of the process consists in depositing the precursor solution on the aluminum substrate with a stainless-steel plate used as a support. The deposition of the precursor solution on the aluminum is carried out by spin-coating with a rotation of 6000 rpm for 20 s, then the sample must be directly put into an open air furnace at 650 °C [8] for 2 min, leading to the crystallization of the film in a rhombohedral perovskite structure with piezoelectric micro properties. Deposition and annealing steps are performed ten times to obtain a 3 µm PZT thin film (Fig. 3).

2.1.2. *Characterization by X-ray diffraction*

X-Ray Diffraction is used to analyse the crystallinity of the PZT films. In this study, the diffraction pattern of the PZT film was registered in a diffractogram using a Bruker D8 advance apparatus for an angle θ of 20°–60°, with a 0.03° step and a period of 30 min. The diffraction pattern obtained for the PZT thin film is presented in Fig. 4. The observed peaks correspond to a well crystalized PZT structure in the rhombohedral phase, and additional peaks correspond to aluminum substrate and stainless-steel holder. Moreover, this diffractogram confirms the absence of $A_2B_2O_7$ pyrochlore phase (usually observed at $2\theta = 29.6°$) which can appear during the annealing process. This parasitic cubic phase (non-piezoelectric) could decrease the electrical response of the sensor and the obtained diffraction pattern confirm the good crystallization of PZT in a crystalline structure suitable for piezoelectric properties.

In order to realize a piezoelectric sensor, rectangular top electrode of 300 nm aluminum layer is then deposited by thermal evaporation on the PZT surface for a 1.8 cm^2 area, aluminum substrate acting as the bottom electrode.

2.1.3. *Polarization of thin film*

After annealing treatment, PZT thin film has domains (with piezoelectric micro-properties) which are randomly oriented, leading to a zero macroscopic polarization (without piezoelectric macro-properties). It is necessary to align the domains in a same direction, by applying an electric field to the film, to obtain the piezoelectric sensor.

The polarization of the sample is carried out using the Sawyer-Tower circuit [9],10] described in Fig. 5. An amplified sinusoidal voltage with an amplitude V_1 and a frequency of 50 Hz is applied to the PZT film and a measurement capacitor ($C = 4.82\mu F$) whose applied voltage has an amplitude V_2. Both signals are observed with an oscilloscope and by using formulas (1) and (2), the P-E hysteresis loop can be obtained, where

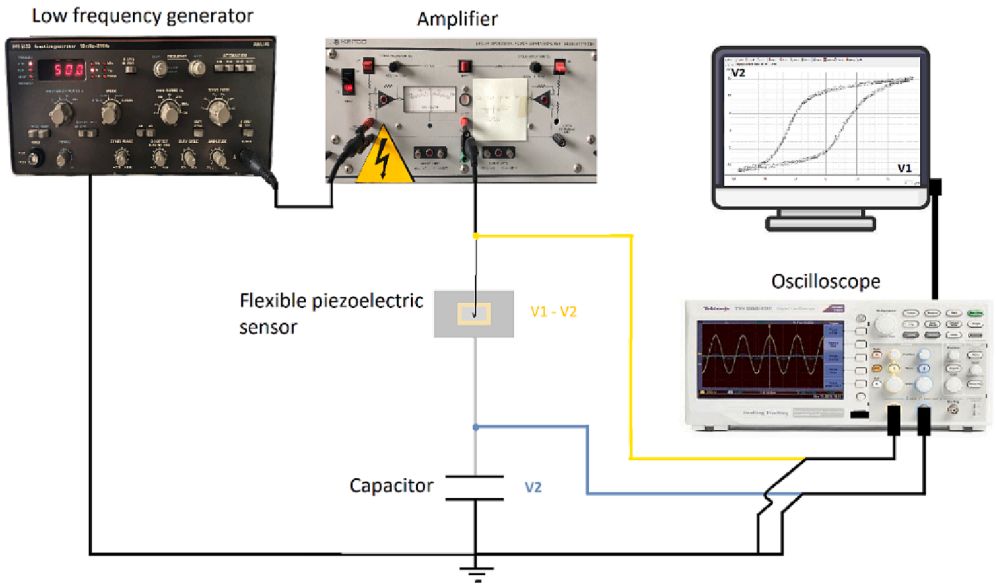

Fig. 5. Representation of the Sawyer-Tower circuit.

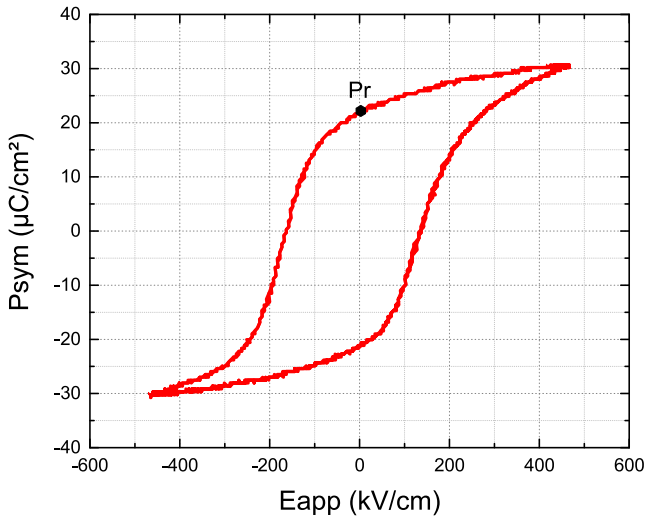

Fig. 6. Hysteresis loop of PZT thin film.

$$E_{app=}\frac{V_1 - V_2}{e} \tag{1}$$

$$P = \frac{C \times V_2}{S} \tag{2}$$

e is the PZT thickness, S the surface of the top electrode, and C the capacitance.

The Fig. 6 presents the P-E hysteresis cycle obtained after polarization by an applied electric field of 430 kV/cm. A Remnant polarization P_r of 21 µC/cm^2 is obtained, proving the good polarization of the PZT film and ensuring its macroscopic piezoelectric properties.

In order to protect the Al/PZT/Al piezoelectric sensor, the sensor is encapsulated by hot lamination between two foils of commercial polyethylene terephthalate (PET) 250 µm thick, which will play the role of the sole (Fig. 7). To recover the output signal of the sensor, conductive wires have been glued both on the bottom and top aluminum electrodes. To choose the type of connector, the flexibility of the materials, the resistance or the applied deformation and the ease of integration into the sole have been considered. The final choice is focused on stainless-steel fiber connectors [11] from Adafruit (ADA 640), which are conductive wire that have the ability to be flexible with a texture close to a sewing thread, thus making the sole more comfortable and more stress resistant.

The piezoelectric coefficient d_{31} for 3 µm of PZT is 12,8 pC/N, the value of the piezoelectric coefficient d_{31} depends on the crystallization temperature of PZT, the higher the temperature, the greater the value of the coefficient d_{31}. In the chosen configuration, the use of aluminum substrate limits the annealing temperature of the sample to 650 °C (melting point of aluminum is 660 °C). this manufacturing limit does not prevent the proper functioning of the sensors, whose output amplitudes can reach up to more than 500 mV.

In the literature, higher piezoelectric coefficients d31 are obtained by using other substrates whose melting temperature is important:

- With an Si(120 µm) [12] substrate and 3.3 µm of PZT the coefficient is 150 pC/N.
- With an MgO (NC) [13] substrate and 5 µm of PZT the coefficient is 48,6 pC/N.
- With an SiO_2 (1,06 µm) [14] substrate and 0.53 µm of PZT we obtain a coefficient of 127 pC/N.

there are also other types of piezoelectric materials such as zinc oxide (ZnO) and barium titanate (BT) [15] and many others [16], but PZT has the highest piezoelectric coefficients. The realization of sensors with thin layers of PZT deposited on an aluminum substrate makes it possible to have a compromise between a flexibility of the material and a good piezoelectric coefficient.

2.2. Mechanical characterization

2.2.1. Definition of the characteristic equation

The signal retrieved from the sensor must be converted into force for the analysis of the walking pattern [17]. The main work consists in finding the transfer function which links the applied stress (force) to the value at the output of the piezoelectric sensor.

Using the law of electromechanical behavior [18] (Fig. 8), and assuming that the external force will be applied on the z axis, the equation (3) and (4) give the electric displacement and the mechanical stress.

$$D_z = e_{31}\left(\varepsilon_{xx} + \varepsilon_{yy}\right) + e_{33}\varepsilon_{zz} + \epsilon_{33}E_z \tag{3}$$

$$\sigma_{zz} = c_{13}\left(\varepsilon_{xx} + \varepsilon_{yy}\right) + c_{33}\varepsilon_{zz} - e_{33}E_z = \frac{F}{S_{PZT}} \tag{4}$$

F $[N]$ load.
$S_{PZT}\,[m^2]$ sensor electrode surface.
σ $[Pa]$: mechanical stress.

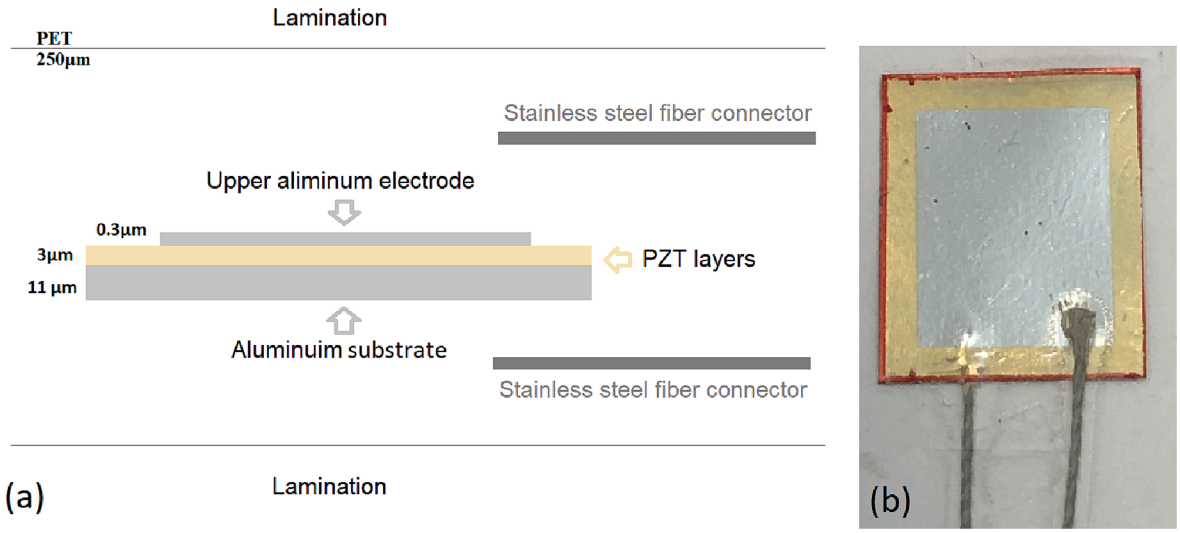

Fig. 7. Scheme of the different elements constituting the piezoelectric sensors (a), Flexible piezoelectric sensor (b).

$$\begin{Bmatrix} \sigma_{xx} \\ \sigma_{yy} \\ \sigma_{zz} \\ \sqrt{2}\sigma_{yz} \\ \sqrt{2}\sigma_{xz} \\ \sqrt{2}\sigma_{xy} \\ \hline D_x \\ D_y \\ D_z \end{Bmatrix} = \left[\begin{array}{cccccc|ccc} c_{11} & c_{12} & c_{13} & & & & & & -e_{31} \\ c_{12} & c_{11} & c_{13} & & & & & & -e_{31} \\ c_{13} & c_{13} & c_{33} & & & & & & -e_{33} \\ & & & c_{44} & & & & -e_{15} & \\ & & & & c_{44} & & -e_{15} & & \\ & & & & & c_{66} & & & \\ \hline & & & & e_{15} & & \epsilon_{11} & & \\ & & & e_{15} & & & & \epsilon_{22} & \\ e_{31} & e_{31} & e_{33} & & & & & & \epsilon_{33} \end{array}\right] \begin{Bmatrix} \epsilon_{xx} \\ \epsilon_{yy} \\ \epsilon_{zz} \\ \sqrt{2}\epsilon_{yz} \\ \sqrt{2}\epsilon_{xz} \\ \sqrt{2}\epsilon_{xy} \\ \hline E_x \\ E_y \\ E_z \end{Bmatrix}$$

Fig. 8. Electromechanical constitutive law [18].

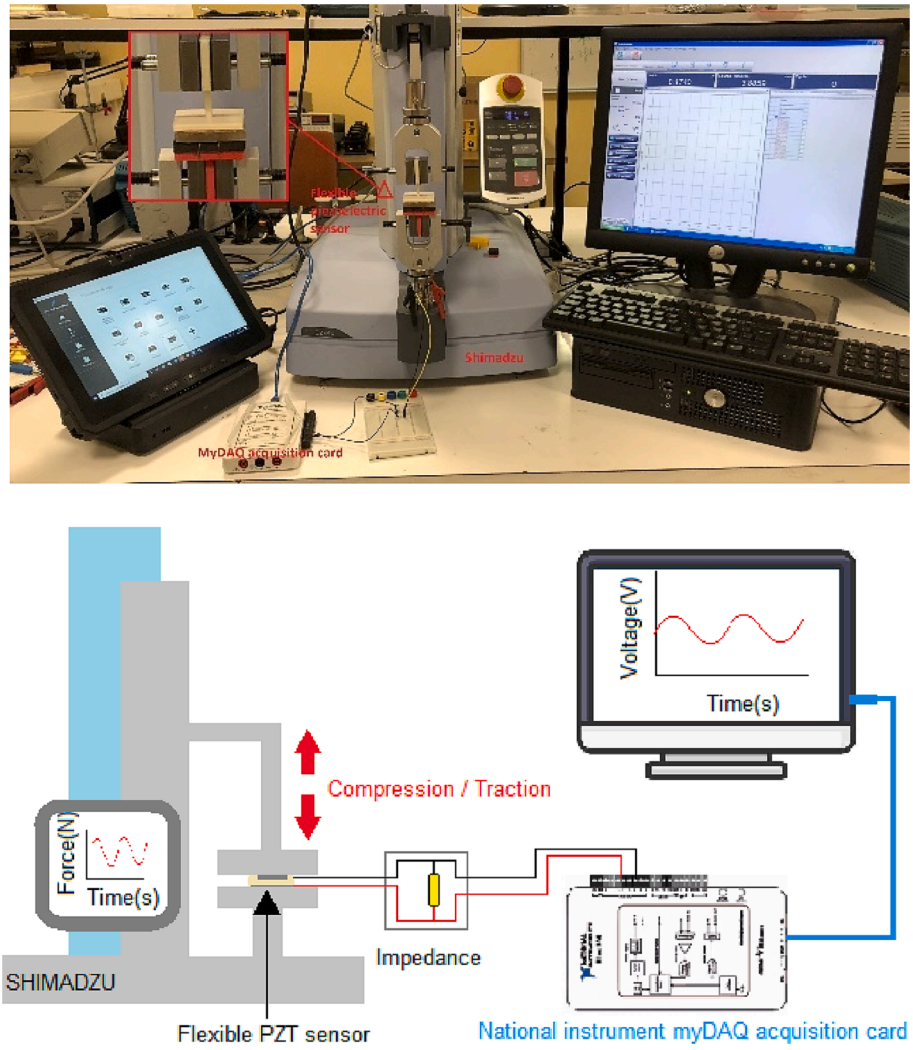

Fig. 9. Image and Scheme of the mechanical characterization for flexible piezoelectric sensor.

D $[C.m^{-2}]$: displacement of electric charge.
ε $[F.m^{-1}]$: mechanical strain.
E $[V.m^{-1}]$: electric field.
$c[Pa]$: stiffness constant.
e [A.s.m^2]: piezoelectric coefficient.

The reverse piezoelectric effect being negligible ($E_z = 0$), an approximate relation between the electric displacement and the external force will be used (Equation (5), the K factor being a characteristic of each realized sensors.

$$D_z \approx \frac{F}{K}\left[C.m^{-2}\right] \tag{5}$$

2.2.2. Determination of the K value

The system used to apply a controlled stress to the piezoelectric

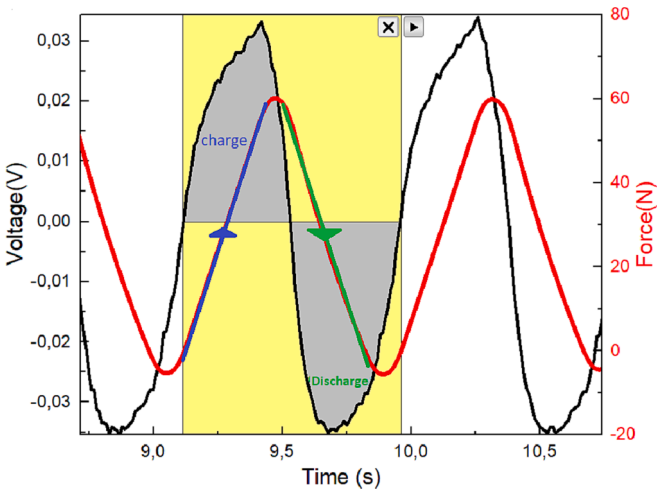

Fig. 10. Results of the data acquisition of the traction-compression system.

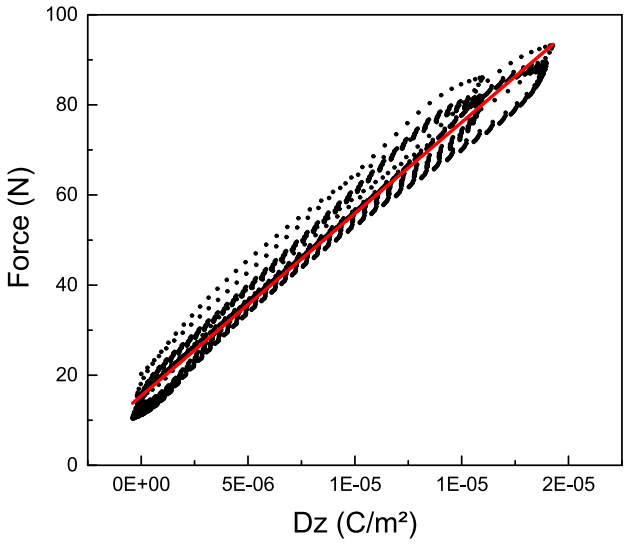

Fig. 11. Curve of the applied force *F* as a function of the electric displacement *Dz*.

sensor is the Shimadzu system [19]. It is a traction-compression machine which provides force data according to time, this machine makes possible to obtain the value of applied force (F) to the piezoelectric sensor. In addition, the sensor will be connected on a MyDAQ acquisition card from national instrument [20] to record its output signal, a resistor is also connected in parallel with the sensor in order to impose the impedance and calculate the displacement of the load D_z $[C.m^{-2}]$ (Fig. 9), allowing the determination of the *K* value.

The data obtained this way allow plotting the curves force F and output voltage V_{out} of the sensor versus time (see Fig. 10).

As the curve shows (Fig. 10), the compression represents the charge, and the traction represents the discharge. By integrating the output current of the sensor, the D_z value can be calculated.

In order to obtain the value of *K*, a linear model is used in the curve of the applied force *F* as a function of the electric displacement D_z (see Fig. 11).

The validation of the methodology was evaluated through reproducibility tests. The goal is to verify that the value of *K* is close to a constant by varying the value of the applied force (see Table1) for one sensor; measurements were carried out over a range of 40 N180 N. The results obtained show that the value of *K* vary with a standard deviation of 11 % for applied force greater than 100 N, which is quite reasonable for the dedicated application. For the sole containing several sensors, it is important to carry out the mechanical characterization for each sensor separately to define their corresponding *K* value.

In order to study the validity of the mechanical transfer function of the sensor and the value of the founded *K* coefficient, a test is carried out with the Shimadzu system in order to obtain two data sources: force value given by the sensor implanted in the Shimadzu device, and force value calculated from the output voltage of the piezoelectric sensor recorded by the MyDAQ card.

The two obtained curves are represented in the Fig. 12 and present the same aspect and almost the same amplitude with a difference of 4.3 %. If necessary, the *K* value of each sensor can be adjusted by this method.

2.3. Data transmission

2.3.1. Acquisition system circuit

The objective of this part is to retrieve the signal at the output of the sensor, the data will be sent by Bluetooth to our mobile phone which will save them in a backup space where the doctor can access at any time, the system must meet a few requirements in order to be able to acquire data without disturbing the patient during his daily activities.

The Adafruit feather nRF52 [21] is an acquisition card equipped with low energy Bluetooth technology (energy consumption 10 times less than classic Bluetooth). A BLE connection consists of only two devices, one called “central” (the NRF52 card) and the other called “peripheral”

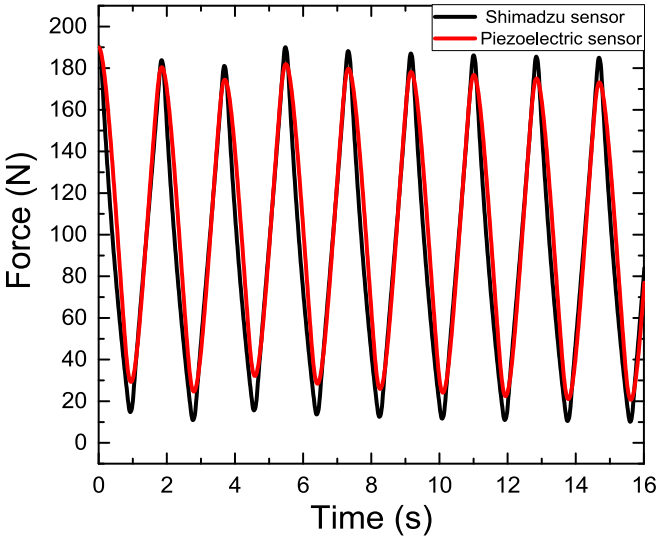

Fig. 12. Comparison of the applied force curve given by the Shimadzu sensor and the by the piezoelectric sensor.

Table 1
Values of the piezoelectric stiffness K obtained according to the variation of the applied force.

External force (N)	40	60	80	100	120	140	160	180
K ($N.m^2.C^{-1}$)	5.0E7	7.3E7	5.5E7	4.3E7	3.8E7	4.3E7	4.8E7	3.7E7
Standard deviation%				24 %				
Standard deviation% ≥ 100 N				11%				

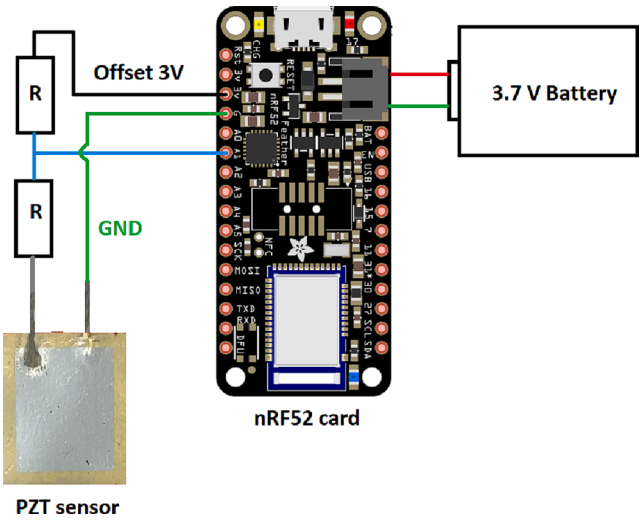

Fig. 13. Data acquisition system circuit.

(example: telephone). Each device communicates with the other over a given period called the "connection interval" (7.5 ms for Android and 11.25 ms for IOS) [22]. The Bluetooth (BLE) module integrated into the Adafruit feather nRF52 card allows communication with all Android and IOS devices, whose Bluetooth version includes low energy technology (available from Bluetooth version 4.0). To be able to test the Bluetooth of the card, an application developed by the company Adafruit feather is available in free access "Bluefruit LE Connect" has been installed on the telephone which is used (model Iphone 8). The acquisition time is fixed at 20 ms second to respect the proper functioning of the transmission (minimum 11.25 ms for IOS) and avoid data overlaps this card contains several analog inputs/outputs (for the use of several sensors) with a compatibility with all types of open access programming languages.

The nRF52 can acquire only the positive part of the signal provided by the sensor, but by using the 3 Volt output of the card, it allows to add an offset to the output signal of the sensor to record the entire signal. The tests carried out with configuration Fig. 13 works completely, the card can digitize the entire signal for a sensor.

The device carried out will contain several sensors positioned in different point of the sole, the second test to be carried out concerns the acquisition of data from several sensors connected to the acquisition card. The sensors connected to the card are also connected to the same offset supplied by output of the card (see Fig. 14).

2.3.2. Equivalent impedance of the circuit

The output voltages of piezoelectric sensors are very sensitive to the input impedance of the measurement device, so it is necessary to take into consideration the electrical characteristic of the sensor to choose the correct impedance of the circuit.

As shown in the Fig. 15, a Lego system is used to apply a sinusoidal variation of the amplitude of the strain to the flexible sensor. A variable load resistor R is connected in parallel to an oscilloscope for viewing and recording the output voltage as a function of the R value.

$$U_R = \frac{I_0\, R}{\sqrt{1 + (RC\omega)^2}} \tag{6}$$

R (load resistance), ω (pulsation), C (sensor capacitance), U_R (amplitude of the output voltage).

The experimental curve is shown in Fig. 16, following the equation (6). Conclusion is that a minimum of 1 MΩ is necessary to improve the amplitude of the output voltage of the sensor.

To choose the impedance of the acquisition system, it is necessary to find the equation that better describe the equivalent circuit corresponding to several sensors (example of 4 sensors presented in Fig. 17). The goal is to be able to vary the value of each resistance to control the impedance of the circuit.

The equivalent scheme makes it possible to define the impedance equation of the acquisition system.

$$R_{eq} = \frac{R}{4} + \frac{1}{\frac{1}{R_C} + \frac{4}{R}} \tag{7}$$

R: voltage divider resistors, R_C: nRF52 acquisition card impedance.

According to the output voltage presented in Fig. 16, the impedance will be taken at 1MΩ.

2.4. Realization of the sole

2.4.1. Definition of pressure points

In order to define the pressure points where the sensors will be placed in the sole, a plantar division algorithm [23] is used to identify the relevant pressure zones. As shown in Fig. 18, the algorithm divides the foot into 4 zones. They represent 30 % (heel area; segment A); 35 % (midfoot area; segment B); 20 % (forefoot area; segment C) and 15 % (toe area; segment D) of the total length of the foot. For the presented prototype, four sensors will be placed in the areas in which there is more interesting pressure points (segment A and C) (see Fig. 18).

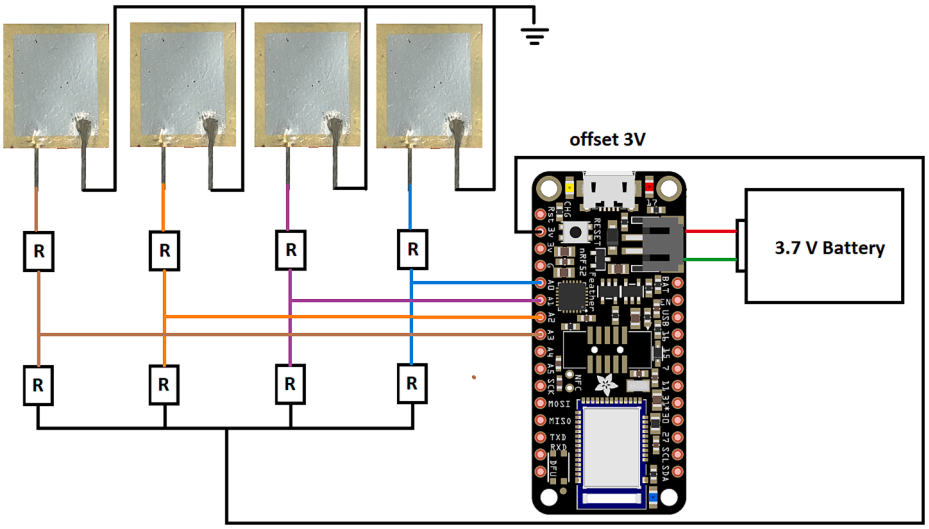

Fig. 14. Data acquisition system for four sensors.

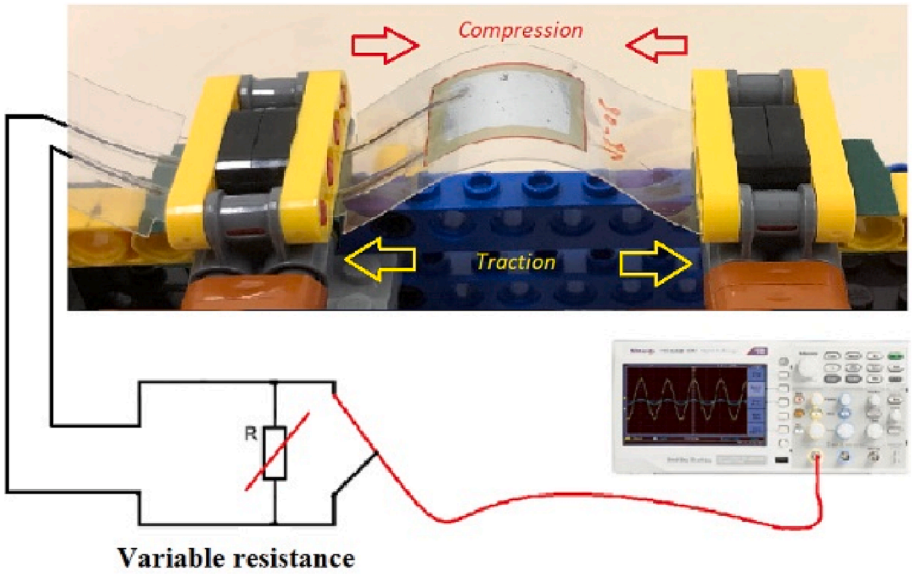

Fig. 15. Representation of the device used for measuring the output voltage of a sensor with the variation of load resistor.

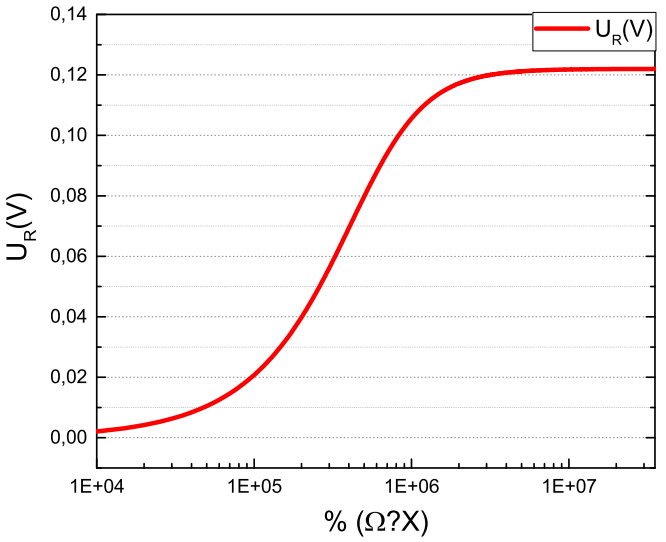

Fig. 16. Evolution of the output voltage of the flexible piezoelectric sensor according to the variation of the load resistance value.

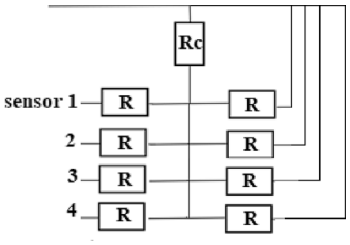

Fig. 17. Equivalent diagram of the data acquisition system with four sensors.

2.4.2. *Acquisition system box*

The definition of the acquisition system made it possible to realize the final box for the data transmission, this device includes the nRF52 acquisition card, the external resistance circuit made completely in PCB (printed circuit) to reduce the size and a battery 3.7 V lithium to power the system (Fig. 19).

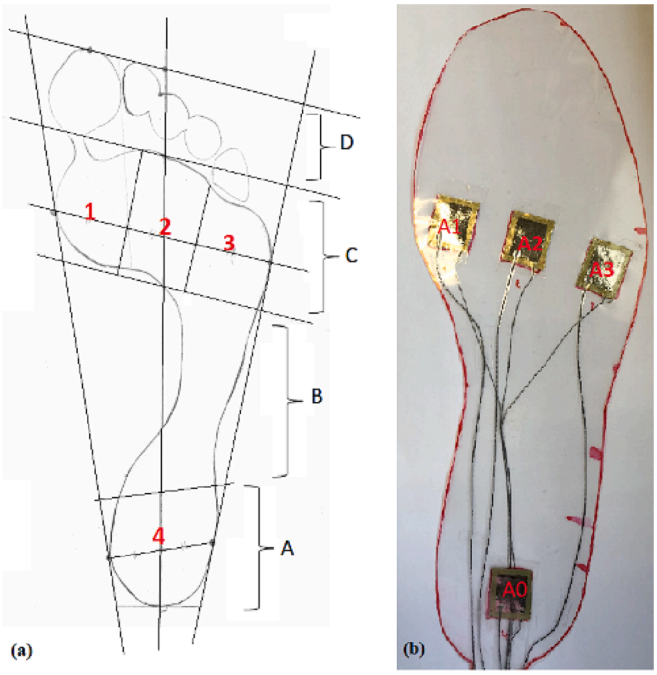

Fig. 18. (a) Plantar division on a footprint, (b) real sole made with 4 piezoelectric sensors.

The data transmission is carried out by Bluetooth, the Adafruit feather company provides digital platform and applications adapted to the used card, The Bluetooth LE Connect app [24] is a platform in which it is possible to display and save data.

3. Results and analysis

3.1. *Presentation of the gait analysis prototype*

The work carried out and presented previously leads to the realization of a prototype of a connected sole for the recording of walking, in which the sensors are placed in the support points chosen previously (see Fig. 20).

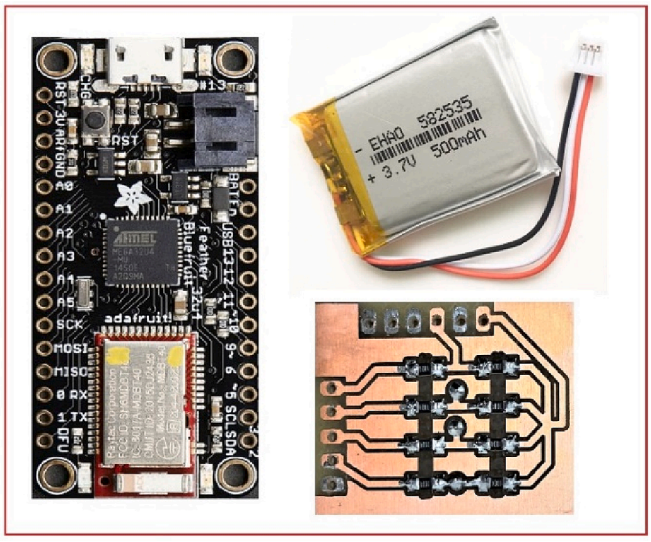

Fig. 19. Data acquisition system.

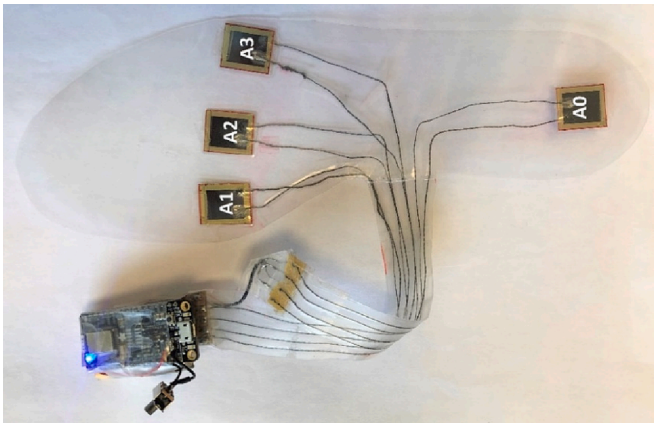

Fig. 20. Connected piezoelectric sole prototype.

Fig. 21. Prototype of a connected piezoelectric insole integrated into a shoe.

The use of PET makes possible to have flexible, light soles and an easy-to-handle material for the arrangement of the sensors. The lamination of the sole has helped to position the sensors in the pressure

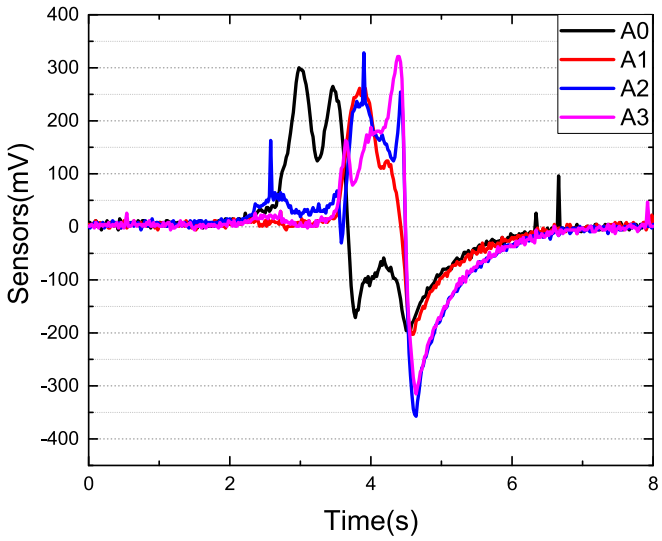

Fig. 22. Connected piezoelectric insole sensor outputs recorded.

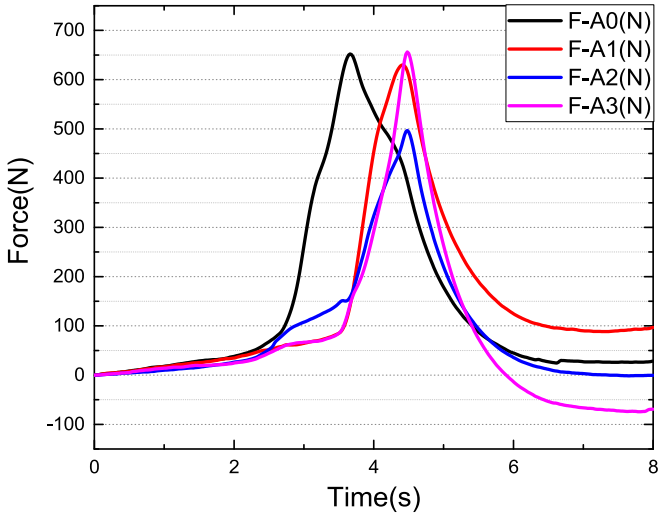

Fig. 23. Curves of sensors values converted into force.

points and to fix the connectors making the system more solid. The acquisition and transmission system, consisting mainly of the nRF52 card, allows sending data directly to a mobile phone in CSV format.

For our prototype, four sensors are used, and the four corresponding signals are recorded on the card inputs as A0, A1, A2 and A3, a small switch has been added to turn off the system and optimize the battery consume. For the walking tests, the sole is placed in a shoe as in Fig. 21.

3.1.1. *Achieve test result*

Walking tests were carried out with a connected sole on a healthy person, the data recorded and transmitted via Bluetooth to a smartphone make possible to draw the characteristic voltage curves for the four sensors during the walking cycle.

The recorded data of the output voltage for four sensors is represented in Fig. 22. By using the K value of each sensor, the applied force curves are plotted in Fig. 23, providing information on the support points of the foot.

The first analysis is that the support force between the heel (sensor A0) and the front of the foot (sensor A1, A2 and A3) is well distributed, the second analysis is that the support force between the two extremities of the foot (sensor A1 and sensor A3) are quite similar, therefore this person has a normal support distribution, this information can be used to

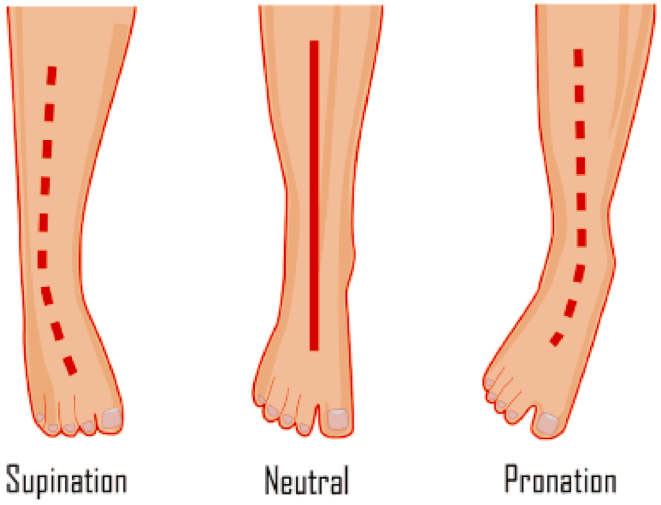

Fig. 24. Representation of the three types of support for the foot according to the angle of the ankle [26].

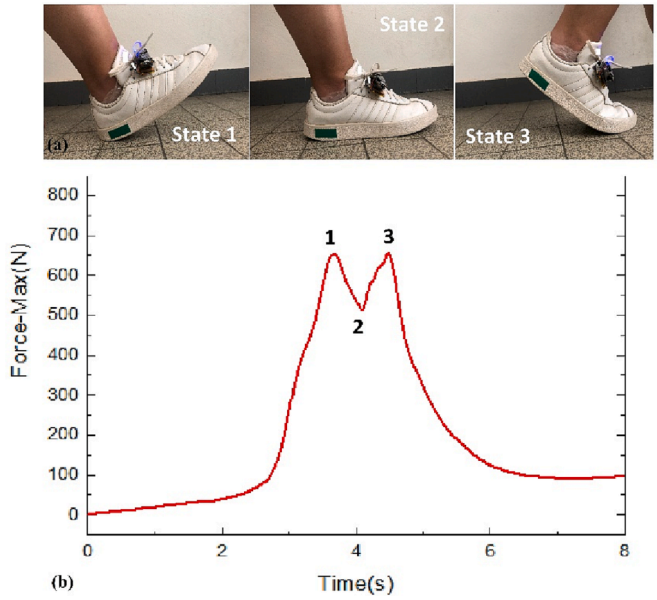

Fig. 25. (a) Image of the 3 stages of step and (b) Representation of the gait cycle curve.

detect the foot pronation and supination from neutral [25] to characterize the type of walking.

Ankle angle characterization is a very popular practice in the sports world, it makes it possible to make shoes more suitable for athletes and thereby improve their performance. The detection of this pathology relating to the points of support makes it possible to intervene more quickly and more effectively by curing the posture thus preventing against the incidences on the shins and problems of knee, back and many others (Fig. 24).

3.1.2. Gait evolution curve

The evolution curve of the gait cycle represents the progression of the foot in the different phases of the step progression [27]. There are three main stages, as shown in Fig. 25a, which define the step: state 1, the foot makes contact with the ground by the heel, the force of reaction to the ground is approximately equal to the weight of the body at normal speed and during this phase the center of gravity is located behind the heel; state 2, the foot is flat on the surface, the pressure is dispersed in all the

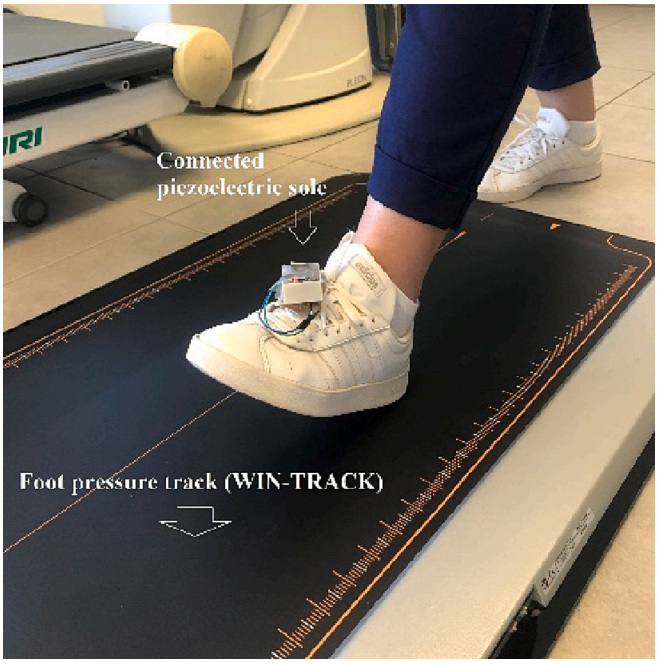

Fig. 26. Walking tests with a connected sole on a podiatric walking mat.

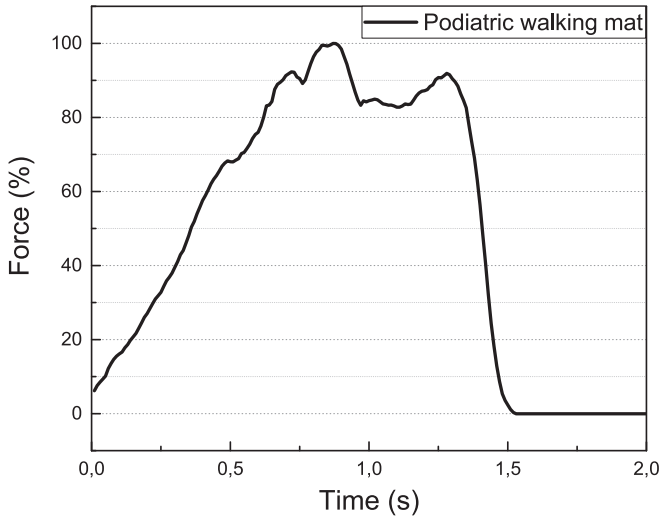

Fig. 27. Result of a walking test carried out with shoes on a podiatric walking mat.

feet and the center of gravity moves to the center of the foot, causing a small drop in force represented by the crus on the graph on Fig. 25b where the maximum force of the four sensors is plotted as a function of time; state 3 is also called the propulsive phase, in which all the pressure is moved to the front of the foot, thus rising to the initial weight of the person and positioning a new center of gravity.

The tests and analyzes carried out on a healthy person enabled the specialist to identify a model that fits the progress of the gait cycle [28], the model is used to compare between the different cycles, to identify anomalies and to intervene quickly and more effectively.

3.2. Comparison results with podiatric walking mats

The main objective of this part was to test the performance of connected sole by comparing it with a podiatric walking mat. A healthy person will walk with the connected sole integrated into his shoe on the

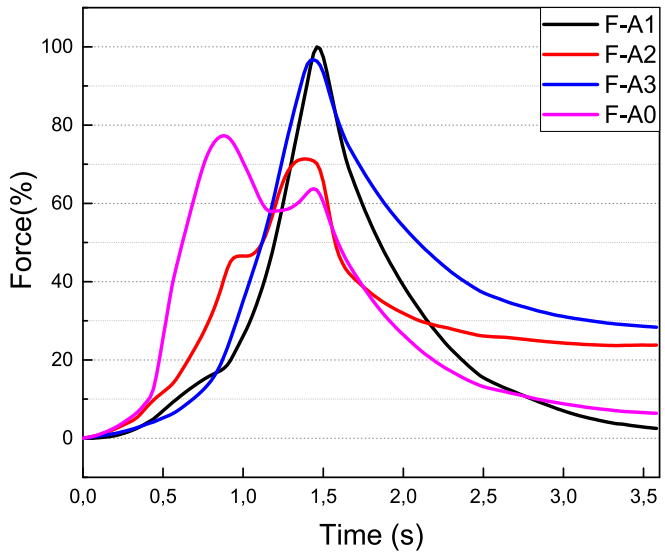

Fig. 28. Result of a walking test carried out with connected sole.

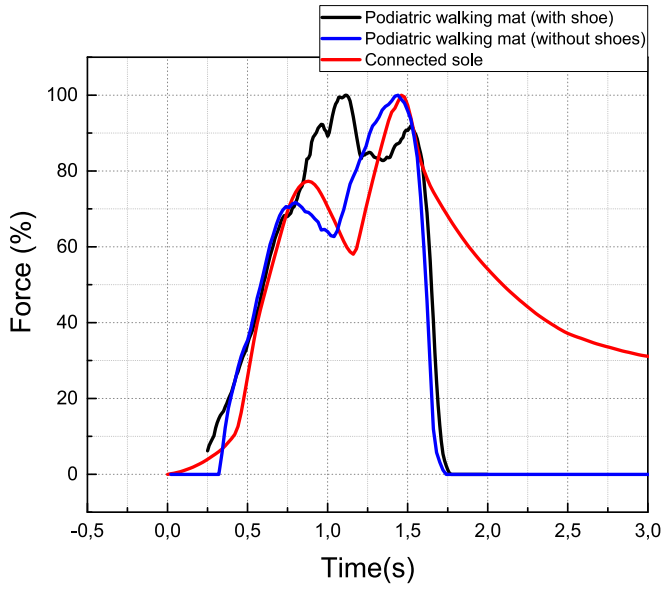

Fig. 29. Gait curves obtained with a walking mat and the connected sole integrated into the shoe superimposed on the gait curve without shoes.

podiatric walking mat, and at the same time the two systems will record the gait data (see Fig. 26).

In order to compare between the two devices, two curves corresponding to each system have been drawn using the data received as shown in the graphs (Fig. 27 and Fig. 28).

The Fig. 27 represents the results displayed of the walking test carried out with shoes on the pedometric walking mat, it is a normalized curve of variation of strength in percentage, there is a single graph which means that each point of the curve corresponds to the max enter the outputs of the active sensors for the same moment. As in the case of the Fig. 1 (b) the precision of the information given by the walking mat is disturbed by the use of the patient's shoes, the "M" curve is flattened by the use of shoes which leads to a loss of information.

The Fig. 28 represents the results of the walking test carried out with the connected sole. Four curves correspond to the four sensors integrated in the sole are displayed. The order of the appearance of the curves corresponds to the order of the excitation of each sensor during the step, the amplitude corresponds to the value of the normalized force

Table 2
Comparative table between two gait analysis systems (connected sole and Podiatric walking mat).

Characteristic	Connected Sole	Podiatric walking mat
Number of steps	Unlimited	$2 \leq$ steps ≤ 4
Output signal	Curve for each sensor (N)	Normalized force curve (%)
Adaptation to different foot morphologies	High	Low
Comfort and natural walking	High	Medium
System for remote monitoring	Yes	No
Manufacturing cost	Low	High

applied. The duration of the step is estimated at 1.5 s (based on the results in Fig. 27), for the curve of the sole the step is between 0.5 and 2 s, after two seconds, two sensors are still active (sensor A2 and sensor A3). To better compare between the different tests, we will overlap curves obtained with the sole and the ones obtained with the walking mat (see Fig. 29).

For a better comparison of both sole and walking mat, we presented the gait cycle curve of the connected sole with normalized values, considering the maximum points of the tension recorded for each instant (the maximum points between the four sensors for each instant). This curve is superposed on the curve recorded with the walking mat obtained for the same test. We have, in addition to the two curves, added the curve of the walk recorded on the walking mat without shoes, as shown on the Fig. 29. The curve obtained with the connected sole, show the same trend as that obtained with the walking mat without shoes. The "M" shape is more apparent on the red and the blue curves (connected sole and walking without shoes) than on the curve with shoes. For gait cycles recorded between 0.2 and 1.6 s, the blue and the red curves have the same dynamics, after 1.6 s the blue and black curve recorded with the walking mat returns to zero, while the red curve slowly discharges, this time can be reduced by modifying the size of the sensors to reduce the capacitance and the impedance of the equivalent circuit since ($\tau = RC$).

The results clearly show that by using the connected insole, we can reproduce the shape of the gait cycle curve recorded without a shoe. Modifications are planned on the connected sole system to solve the discharge problem and make the device more efficient.

A comparative table (see Table 2) is produced, containing characteristics of the two devices (connected sole and podiatric walking mat). The connected sole is an alternative device to the walking mat which contains functionalities allowing to analyze walking in real conditions with a direct contact with the foot, possibility of taking an unlimited number of steps and wireless transmission. In addition to these advantages, the connected piezoelectric insole is an easily transferable system to industry with the possibility of designing an insole for each person in order to correspond to different pathologies.

4. Conclusion

The work presented in this article consists in the realization of a connected sole based on flexible piezoelectric sensors manufactured entirely in our laboratory. One of the first objective was the characterization of the sensors to provide data that can be used by the podiatrist. The experimental tests carried out with the traction-compression system validate the transfer function defined from theoretical equations. The next part was to identify a data acquisition and transmission system. There are a multitude of cards that could be used, but we have set specifications in which we had to focus on three important parameters: an acquisition card with the smallest dimension, the least energy consumption and a card which has several analog input ports for the sensors. We chose to use the nRF52 card which satisfies all the conditions. It was also necessary to integrate an external circuit to adapt the impedance of the system and to add an offset for the recovery of the entire

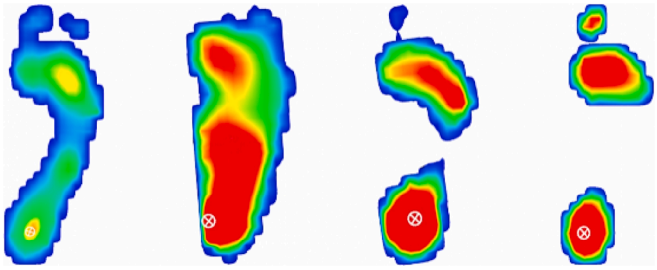

Fig. 30. Image corresponding to foot prints made with several patients [29].

signal. The collaboration with a podiatrist allowed the realization of a medical piezoelectric insole. We chose, for the first prototype, the use of four sensors placed in pressure zones previously defined with the specialist. The tests are carried out on a healthy person in order to first validate the device. The results obtained show that we can record the force applied for each sensor and reconstruct with these data the "M" curve of the gait cycle. This graph is used by the podiatrist to analyze the gait and performing diagnostics. This article has contributed to the realization of a feasibility study based on the use of flexible piezoelectric sensors in the realization of a connected sole for medical applications. The results obtained open the field to another prototype more personalized with more sensors, different sizes and different shapes for the realization of a personalized insole adapted to each patient.

5. Future works

The purpose of the work carried out in the article was to test the feasibility of the use of flexible piezoelectric sensor in the realization of connected sole. After validation of the device, the next study will take place on the realization of personalized sole for the analysis of walking person with a walking disorder, this part will be made in direct collaboration with the podiatrist and the patients.

The difficulty that the podiatrist has in making the diagnosis is linked to the diversity of the cases to be treated (Fig. 30) represented by varying and distinct fingerprints, mastering the manufacture of the sensors makes it possible to modify the size and the shape of the sensor and therefore to target areas that the podiatric walking mat cannot register.

CRediT authorship contribution statement

Samia Adrar: Writing – original draft, Methodology, Formal analysis. **Mohammed El Gibari:** Resources, Supervision, Writing – review & editing. **Philippe Saillant:** Methodology. **Jean-Christophe Thomas:** Formal analysis, Validation. **Raynald Seveno:** Conceptualization, Resources, Supervision, Funding acquisition, Writing – review & editing.

Declaration of Competing Interest

The authors declare that they have no known competing financial interests or personal relationships that could have appeared to influence the work reported in this paper.

Data availability

The authors are unable or have chosen not to specify which data has been used.

References

[1] Semelles connectées Digitsole Smart Insoles, https://www.decathlon.fr/p/semelles-connectees-digitsole-smart-insoles/_/R-p-X8655885 (accessed Jul. 06, 2022).

[2] FeetMe, CLINALLIANCE R&D, http://rd.clinalliance.fr/feetme (accessed Jul. 29, 2022).

[3] L. Claverie, Biofeedback pour l'optimisation de la locomotion : conception et validation d'un système embarqué d'évaluation de la locomotion à partir des pressions plantaires, phdthesis, Université Paul Sabatier - Toulouse III, 2017. Accessed: Jun. 27, 2022 [Online], Available: https://tel.archives-ouvertes.fr/tel-01902552.

[4] R. Seveno, B. Guiffard, T. Dufay, Procédé de fabrication d'un micro-générateur mécano-électrique flexible et micro-générateur correspondant, Sep. 16, 2016 Accessed: Jan. 20, 2023 [Online], Available: https://hal.science/hal-01396384.

[5] R. Seveno, D. Averty, Ultra light tunable capacitor based on PZT thin film deposited onto aluminium foil, J. Sol-Gel Sci. Technol. 68 (2) (2013) 175–179, https://doi.org/10.1007/s10971-013-3149-8.

[6] R. Seveno, J. Carbajo, T. Dufay, B. Guiffard, J.C. Thomas, Flexible PET/Al/PZT/Al/PET multi-layered composite for low frequency energy harvesting, J. Phys. D: Appl. Phys. 50 (16) (2017), 165502, https://doi.org/10.1088/1361-6463/aa6373.

[7] T. Dufay, B. Guiffard, J.-C. Thomas, R. Seveno, Transverse piezoelectric coefficient measurement of flexible lead zirconate titanate thin films, J. Appl. Phys. 117 (20) (2015), 204101, https://doi.org/10.1063/1.4921588.

[8] C.K. Kwok, S.B. Desu, Pyrochlore to perovskite phase transformation in sol-gel derived lead-zirconate-titanate thin films, Appl. Phys. Lett. 60 (12) (1992) 1430–1432, https://doi.org/10.1063/1.107312.

[9] R. Bouregba, G. Poullain, Numerical extraction of the true ferroelectric polarization due to switching domains from hysteresis loops measured using a Sawyer-Tower circuit, Ferroelectrics 274 (1) (2002) 165–181, https://doi.org/10.1080/00150190213947.

[10] R. Bouregba, B. Vilquin, G. Le Rhun, G. Poullain, B. Domenges, Sawyer–Tower hysteresis measurements on micron sized Pb(Zr, Ti)O3 capacitors, Rev. Sci. Instrum. 74 (10) (2003) 4429–4435, https://doi.org/10.1063/1.1606533.

[11] Prestashop 1.5, Bobine de fil conducteur mince 2 brins inoxydable - 23 m - Boutique Semageek, https://boutique.semageek.com/fr/382-bobine-de-fil-conducteur-mince-2-brins-inoxydable-23-m-3002830230968.html (accessed Jul. 25, 2022).

[12] T. Harigai, H. Adachi, E. Fujii, Vibration energy harvesting using highly (001)-oriented Pb(Zr, Ti)O3 thin film, J. Appl. Phys. 107 (9) (2010), 096101, https://doi.org/10.1063/1.3406253.

[13] I. Kanno et al., High efficiency energy harvester of transferred epitaxial PZT films on stainless steel sheets, in: 2010 IEEE 23rd International Conference on Micro Electro Mechanical Systems (MEMS), Jan. 2010, pp. 152–155, doi: 10.1109/MEMSYS.2010.5442542.

[14] A.J. Dick, Characterizing effective d31 values for PZT from the nonlinear oscillations of clamped-clamped micro-resonators, J. Mech. Eng. 59 (1) (2013) 50–55, https://doi.org/10.5545/sv-jme.2012.673.

[15] M. Vacca et al., Electric clock for nanomagnet logic circuits, 2014, pp. 73–110, doi: 10.1007/978-3-662-43722-3_5.

[16] M. Fraga, H. Furlan, R. Pessoa, M. Massi, Wide bandgap semiconductor thin films for piezoelectric and piezoresistive MEMS sensors applied at high temperatures: an overview, Microsyst. Technol. 20 (2013) 9–21, https://doi.org/10.1007/s00542-013-2029-z.

[17] S. Adrar, M. El Gibari, M. Yoen, J.-C. Thomas, R. Seveno, Mechanical characterization of a piezoelectric sensor for podiatrist applications, in: 2022 IEEE International Systems Conference (SysCon), Montreal, France, Apr. 2022, pp. 1–5, doi: 10.1109/SysCon53536.2022.9773897.

[18] Matériaux piézoélectriques - Caractérisation, modélisation et vibration - Michel Brissaud (EAN13: 9782880746926), EPFL Press, https://www.epflpress.org/produit/404/9782880746926/materiaux-piezoelectriques (accessed Jun. 21, 2021).

[19] Electromechanical Test Frames - Universal Testing | Shimadzu EZ-X, https://www.ssi.shimadzu.com/products/universal-tensile-testing/ez-x.html (accessed May 18, 2021).

[20] MyDAQ.pdf, Accessed: Jul. 22, 2020 [Online], Available: http://www.ni.com/pdf/manuals/373060g_0114.pdf.

[21] Bluefruit nRF52 Feather Learning Guide, Adafruit Learning System, https://learn.adafruit.com/bluefruit-nrf52-feather-learning-guide/introduction (accessed Apr. 15, 2020).

[22] Maximizing BLE throughput on iOS and Android, Punch Through, Apr. 03, 2016, https://punchthrough.com/maximizing-ble-throughput-on-ios-and-android/ (accessed Sep. 07, 2020).

[23] L. Claverie, A. Ille, P. Moretto, Validation of a method for dispatching discrete sensors on an insole for plantar pressure analysis, Comput. Methods Biomech. Biomed. Eng. 18 (sup1) (2015) 1908–1909, https://doi.org/10.1080/10255842.2015.1069563.

[24] Bluefruit LE connect for iOS and Android, Adafruit Learning System, https://learn.adafruit.com/bluefruit-le-connect/ios-setup (accessed Jun. 16, 2022).

[25] A Beginner's Guide to Pronation and Supination, https://www.flexispot.com/spine-care-center/understanding-your-feet:-a-beginners-guide-to-pronation-and-supination/ (accessed Jun. 07, 2022).

[26] Foot Levelers, Reservoir of HEALTH, http://reservoirofhealth.com/foot-levelers/ (accessed Jan. 19, 2023).

[27] A.V. Wiik, A. Aqil, M. Brevadt, G. Jones, J. Cobb, Abnormal ground reaction forces lead to a general decline in gait speed in knee osteoarthritis patients, World J. Orthop. 8 (4) (2017) 322–328, https://doi.org/10.5312/wjo.v8.i4.322.

[28] R. Haddas, K. Ju, Gait alteration in cervical spondylotic myelopathy elucidated by ground reaction forces, Spine 44 (2018) 1, https://doi.org/10.1097/BRS.0000000000002732.

[29] Empreinte. Types, ce qu'il dit sur vos pieds et comment il peut être analysé - Podoactiva. Leaders en podiatrie, Podoactiva. Líderes en Podología, Sep. 02, 2021, https://www.podoactiva.com/fr/blog/Que-dit-votre-empreinte-de-vous-et-comment-peut-elle-%C3%AAtre-analys%C3%A9e-%3F (accessed Jun. 08, 2022).

Sensors & Actuators: A. Physical 376 (2024) 115615

Contents lists available at ScienceDirect

Sensors and Actuators: A. Physical

journal homepage: www.journals.elsevier.com/sensors-and-actuators-a-physical

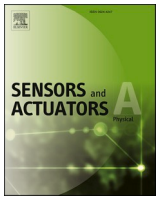

A simple and effective method to compensate the thermal drift of implantable blood pressure sensors

Mohammed El Gibari [a,*], Serigne Mbacke [a], Chantal Gauthier [b], Benjamin Lauzier [b], Hongwu Li [a]

[a] Nantes Université, CNRS, IETR UMR 6164, Pole Science et Technologie Faculté des Sciences et des Techniques, 2 Chemin de la Houssinière, BP 92208, Nantes cedex 3 44322, France
[b] Nantes Université, INSERM, CNRS, l'institut du thorax, INSERM UMR 1087/CNRS UMR 6291, 8 quai Moncousu, BP 70721, Nantes Cedex 1 44007, France

ARTICLE INFO

Keywords:
Piezoresistive sensor
Thermal drifts
Analog compensation
Simulation model
Piezoresistor extraction

ABSTRACT

This article presents a study of implantable blood pressure sensors based on a probe made up of four piezoresistors. An original method combining both measurements and calculations allows extracting the values of each piezoresistor without degrading the probe is developed. This study made it possible to create a simulation model in Cadence/Pspice electronic simulation software, considering the variation of the piezoresistor according to the temperature and the pressure. To our knowledge, no simulation model considering both the variation of the temperature and the pressure of each piezoresistor exists in the literature. So, the simulation of the sensor allows to quickly test the efficiency of the compensation circuit before its realization. Once the thermal drifts of the sensor have been quantified, a circuit based on PNP transistors is developed to compensate this thermal drift. This analog compensation technique ensures low cost, compactness and low power consumption. It proved experimentally effective in reducing thermal drift of the sensor. For example, the experimental thermal drift of the sensor is reduced from 9.97 mmHg/°C without compensation to 2.12 mmHg/°C after compensation at the pressure of 300 mmHg. This method has been validated with 3 pressure levels (0, 100, 200 and 300 mmHg).

1. Introduction

Implantable biomedical sensors for preclinical studies have been the subject of numerous preclinical studies in the last decade [1–3]. These studies are part of the fight against chronic cardiovascular diseases [4,5]. Among these sensors, piezoresistive blood pressure sensors play an essential part, especially in the prevention of cardiovascular diseases such as hypertension [6]. The key principle of the sensors is based on a thin silicon membrane that deforms when pressure is applied to its surface, resulting in resistance variation of piezoresistors on this latter. These probes have the advantage of being small in size and having good sensitivity [7,8]. But due to their silicon nature, they are easily affected by the temperature, which results in a thermal drift of their response [9,10]. Therefore, compensating the thermal drift of the sensor is essential to improve their performance. For that, numerous digital methods, software compensation methods and other methods are developed to compensate this thermal drift but the high cost of digital components and the high consumption limit their use in the long term, especially when the sensor is implanted [11–17]. Hardware compensation methods using analog circuitry to compensate the output signal of sensor are also widely proposed [18–24]. These methods have the advantage of being less energy-consuming and with a less complex conditioning circuit. These probes exhibit high reliability, low costs, and mass manufacturing capability for wide use.

In this paper, we present a detailed study of piezoresistive blood pressure sensors. We make a characteristic study of the arterial pressure sensor by quantifying the thermal drift with and without conditioning circuit. An original method combining both measurement and theoretical calculations allows extracting the value of the piezoresistors without degrading the sensor is presented. This then makes it possible to model the sensor with Cadence electronic simulation software, with the help of a special procedure to reproduce the behaviour of each piezoresistor. Once we got our sensor simulation model, we investigated an analog compensation method based on a PNP transistor. This method is effective in reducing the thermal drift of the sensor without increasing its size. This drift compensation method is then implemented and tested. And the measurement results are compared with those of the simulation.

* Corresponding author.
E-mail address: mohammed.el-gibari@univ-nantes.fr (M. El Gibari).

https://doi.org/10.1016/j.sna.2024.115615
Received 14 March 2023; Received in revised form 30 May 2024; Accepted 17 June 2024
Available online 21 June 2024

2. Materials and methods

In our study, the choice of the probe for the pressure sensor felt on the model NPB030 from Honeywell (cf. Fig. 1). These piezoresistive probes are widely used in industry for biomedical applications. They include a test body instrumented with strain gauges. Their operation is based on a silicon diaphragm which deforms when pressure is applied (cf. Fig. 1c). This deformation causes a change in the structure of the piezoresistors which are placed on the four sides of the diaphragm (cf. Fig. 1b). More details are given in our previous studies [25,26]. In this paper we developed a method for extracting the resistance of each piezoresistor as a function of temperature and pressure and we then created a simulation model to reproduce the experimental characteristics of the probe as a function of these two variables.

The main disadvantage of used piezoresistive pressure probes is the variation of piezoresistors with operating temperature, which considerably reduces the accuracy of the pressure measurement. For our biomedical application, this thermal drift must be less than 3 mmHg/°C in the temperature range of 34°C to 39°C. So, in order to develop thermal drift compensation techniques adapted to the piezoresistive probes considered, we first quantify the relative thermal drift of the probe without and with its conditioning circuit as indicated in Fig. 2a and Fig. 2b shows a photo of the complete sensor realized with the conditioning circuit.

3. Results and discussions

3.1. Thermal drift of the probe

Fig. 3 shows the output voltage (dV) of the probe, for different pressures, as a function of temperature. We can note that the voltage decreases with the temperature with a slope of −0.022 mV/°C at 0 mmHg for example. The average relative drift of probe thermal drift without conditioning and without compensation is around 0.35 %/°C whatever the pressure. It is calculated by dividing the output voltage variation (thermal drift) ΔdV by the average output voltage dV then by temperature variation ΔT. The relative drift of 0.35 %/°C corresponds to a drift of 2,65 mmHg/°C. The drift in voltage/°C is converted to mmHg/°C by dividing the ratio $\eta = \Delta V/\Delta P$ by the temperature slope kT of the output voltage curve, where ΔV is the output voltage variation corresponding to the pressure variation ΔP.

3.2. Thermal drift of the complete sensor

In order to assess the total drift of the sensor, the probe is associated with its conditioning circuit, consisting of a simple instrumentation amplifier realized with LM324 component (cf. Fig. 2a), for the temperature range from 34 °C to 39 °C for four pressure levels (0, 100, 200 and 300 mmHg). The output voltage V_{out}, is adjusted thanks to the offset (R_{offset}) and gain (R_{gain}) trimmers, from 300 mV to 1000 mV, for an applied pressure between (0–300 mmHg).

Fig. 4 shows that the voltage output decreases with the temperature, the relative drift represents 3.02 %/°C, 2.71 %/°C, 2.48 %/°C and 2.37 %/°C respectively at 0 mmHg, 100 mmHg, 200 mmHg and 300 mmHg which corresponds to a drift of 6.47 mmHg /°C (at 0 mmHg), 7.27 mmHg /°C (at 100 mmHg), 8.83 mmHg /°C (at 200 mmHg) and 9.97 mmHg /°C (at 300 mmHg). This result shows that the drift of the sensor is very large, which makes the pressure measurements dependent upon temperature. The compensation of this thermal drift is therefore essential to have precise and stable measurements over long periods despite natural or pathological variations in body temperature.

3.3. Extraction of piezoresistors of the probe

In this section, we will explain how to extract the value of each piezoresistor of the Wheatstone bridge as a function of temperature and pressure. The piezoresistors of the bridge are short-circuited according to different configurations (cf. Fig. 5). Each short-circuiting scheme results in an equation relating measured voltages and piezoresistors from Ohm's law. Four equations corresponding to four configurations allow determining the value of each piezoresistors as a function of temperature and pressure.

In the first configuration, the points A and D are short-circuited by the blue conductor and the voltages V_3 and V_4 are measured as a function of the temperature and the pressure. We obtain the following equations:

$$V_4 = \frac{R_2}{R_1 + R_2} Vcc \tag{1}$$

$$V_3 = \frac{R_1}{R_1 + R_2} Vcc = Vcc - V_4 \tag{2}$$

We derive from Eq. (1) and (2):

$$R_1 = R_2 \frac{V_3}{V_4} \tag{3}$$

In the same way, by short-circuiting points A and B, we derive equations relating the measured voltages across A and D (V_5) and across C and D (V_6) with the piezoresistors R_3 and R_4:

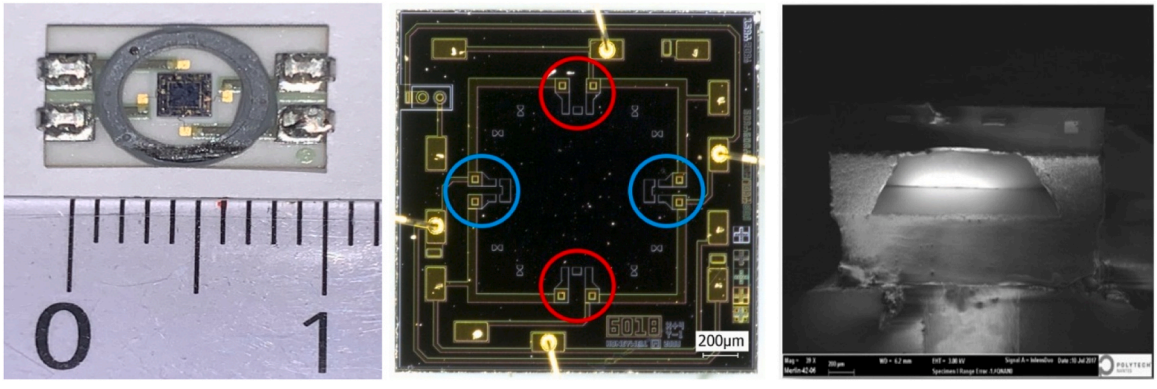

Fig. 1. The piezoresistive pressure probe used in our study: (a) without capsule, (b) Wheatstone bridge circuit of the probe observed using an optical microscope and (c) sectional view of the probe with a scanning electron microscope.

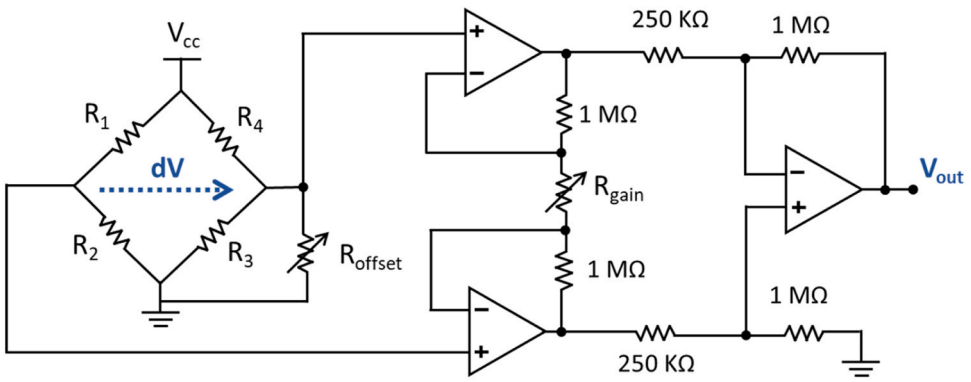

(a)

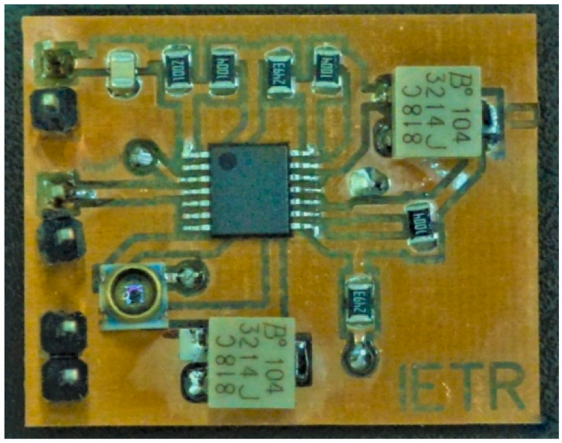

(b)

Fig. 2. Complete sensor: (a) probe with conditioning circuit (b) realisation electronic card.

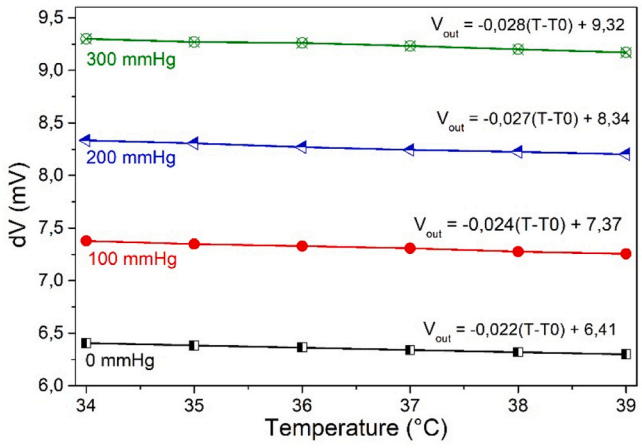

Fig. 3. Probe output voltage as a function of temperature without conditioning circuit, with T_0=34°C and supply voltage (V_{cc}) of 3 V.

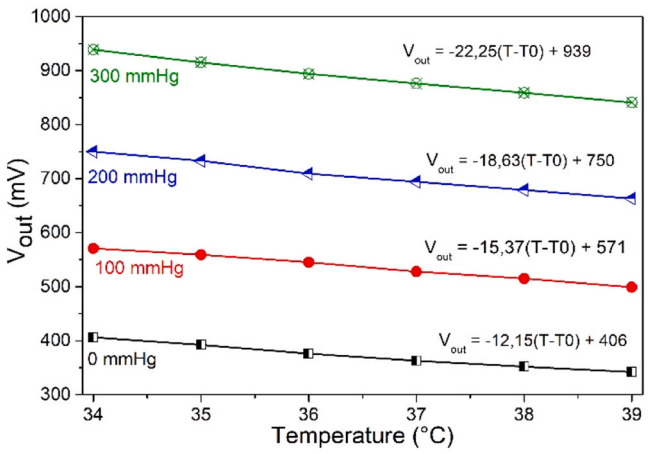

Fig. 4. Sensor voltage output as a function of temperature and pressure with amplification circuit, with T_0=34°C.

$$V_6 = \frac{R_3}{R_3 + R_4} Vcc \tag{4}$$

$$V_5 = \frac{R_4}{R_3 + R_4} Vcc \tag{5}$$

and

$$R_3 = R_4 \frac{V_6}{V_5} \tag{6}$$

With the Eqs. (3) and (6), we have:

$$(3)x(6) : R_1 R_3 = R_2 R_4 \frac{V_3 V_6}{V_4 V_5} \tag{A}$$

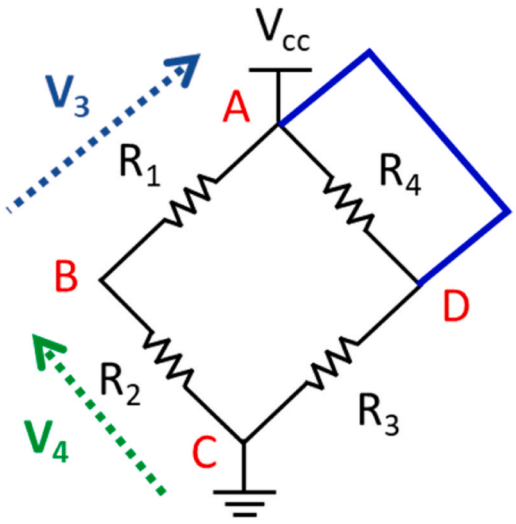

Fig. 5. First short-circuiting configuration of the piezoresistive probe.

$$(3)+(6): R_1+R_3=R_2\frac{V_3}{V_4}+R_4\frac{V_6}{V_5} \quad (B)$$

The third configuration is a current measurement. We short-circuit points A and B and points C and D. We measure the current I_{24} which enters at point A and we obtain an equation:

$$V_{cc}=\frac{R_2R_4}{R_2+R_4}I_{24} \quad (7)$$

And for the fourth and last configuration, we respectively short-circuit points A and D and points B and C. We measure the current I_{13} which enters at point A. Thus, we obtain:

$$V_{cc}=\frac{R_1R_3}{R_1+R_3}I_{13} \quad (8)$$

$$(7)=(8)\rightarrow\frac{R_1R_3}{R_1+R_3}I_{13}=\frac{R_2R_4}{R_2+R_4}I_{24} \quad (C)$$

From equations (A) and (B) and after simplification, we have:

$$\frac{R_1R_3}{R_1+R_3}=\frac{R_2R_4V_3V_6}{R_2V_3V_5+R_4V_4V_6} \quad (D)$$

The equation (D) in (C), we obtain:

$$\frac{R_2R_4V_3V_6}{R_2V_3V_5+R_4V_4V_6}I_{13}=\frac{R_2R_4}{Re+R_2}I_{24}$$

$$V_3V_6I_{13}(R_2+R_4)=(V_3V_5R_2+V_4V_6R_4)I_{24} \quad (I)$$

We deduce R_2 from (I):

$$R_2=\frac{R_4V_6(V_4I_{24}-V_3I_{13})}{V_3(V_6I_{13}-V_5I_{24})} \quad (II)$$

From Eq. (7), we get:

$$V_{CC}(R_2+R_4)=R_2R_4I_{24} \quad \rightarrow \quad R_4=\frac{V_{CC}R_2}{R_2I_{24}-V_{CC}} \quad (III)$$

Equation (III) in (II), on obtain:

$$R_2I_{24}-Vcc=\frac{V_{cc}V_6(V_4I_{24}-V_3I_{13})}{V_3(V_6I_{13}-V_5I_{24})}$$

Which ultimately gives an expression of R_2 as a function of the measured values:

$$R_2=\frac{V_6Vcc(V_4I_{24}-V_3I_{13})+V_3Vcc(V_6I_{13}-V_5I_{24})}{V_3I_{24}(V_6I_{13}-V_5I_{24})}$$

From Eq. (5), we have then an expression of R_1:

$$R_1=R_2\frac{V_3}{V_4}$$

From equation (10), we will have:

$$R_3=\frac{v_{CC}R_1}{R_1I_{13}-v_{CC}}$$

With Eq. (8), on obtain:

$$R_4=R_3\frac{V_5}{V_6}$$

From these values of the piezoresistors measured as a function of temperature T and pressure P, we can find the fitted expression of their variation as a function of T and P (cf. Fig. 6).

The piezoresistors R1 and R2 decrease while the piezoresistors R3 and R4 increase with the pressure, this increases the sensitivity of the probe with the pressure. The equivalent resistance calculated from the extraction of the piezoresistors (2.88 KΩ at 34°C and 0 mmHg) is in perfect agreement with the direct measurement of the equivalent resistance (2.89 KΩ at 34°C and 0 mmHg).

The measured piezoresistors values will allow us to implement them in the software to simulate the output voltage of the sensor as a function of temperature and pressure in order to correctly compensate its thermal drift.

3.4. Simulation of the sensor

In this study, it is a question of looking for a simulation model which faithfully reproduces the behavior of the probe and the sensor. The interest of modeling the probe lies in the possibility of studying compensation circuits effectively before the experimental study which could be expensive and very long. To our knowledge, no method for modeling the sensor as a function of temperature and pressure is available neither in the electronic simulation software used Cadence/Pspice, nor in the literature. We had to set up our own sensor simulation model and this simulation method must reproduce the function of the sensor as faithfully as possible. However, the Cadence/Pspice software doesn't allow managing two parameters influencing the behavior of an electrical circuit. While in our study we need to consider two parameters, both temperature and pressure. Thus, in our simulation model set-up, the management of the temperature and pressure variation is carried out using two independent blocks. In this sensor simulation model, as shown in Fig. 7, two steps describe the variation of each piezoresistor. The first one describes the effect of temperature (block 1) and the second one describes the effect of pressure (block 2).

The first component (block 1) takes as input a matrix of values ($x_{1,2,3...n}$ and $y_{1,2,3...n}$) at 0 mmHg, with x representing the value of the piezoresistor previously extracted and y representing the corresponding temperature. So, block 1 allows to simulate the variation of each piezoresistor according to the temperature. Block 2 integrates the pressure effect P on the piezoresistor. At the output of this block, we recover the value of the piezoresistor as a function of the temperature and the pressure. The temperature and pressure management are thus carried out in two stages.

The implementation of the piezoresistor model as a function of temperature and pressure in the simulation software is presented in Fig. 8. The two components "ETABLE" and "REFERENCE", defined in the Cadence library, allowed us to reproduce the behavior of the probe. With the "ETABLE" component designated as block 1 above, we can give a table of values corresponding to the variation of the piezoresistor as a function of temperature and the "REFERENCE" component, called block 2 above, takes into account the variation of the piezoresistor as a function of pressure and converts the output into resistance which varies as a function of temperature and pressure. Roff makes it possible to take into account the pressure at the level of the piezoresistor with a slope

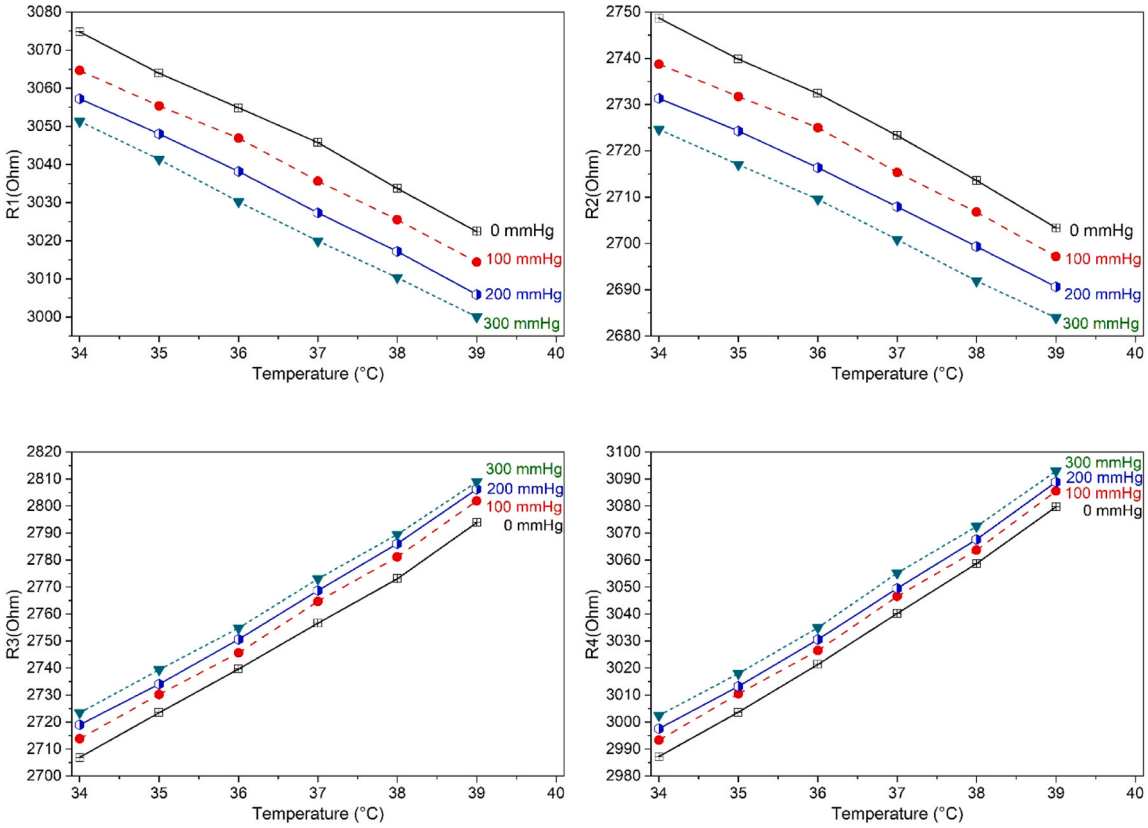

Fig. 6. Measurement of each piezoresistor as a function of temperature for four pressures values (0, 100, 200 and 300 mmHg).

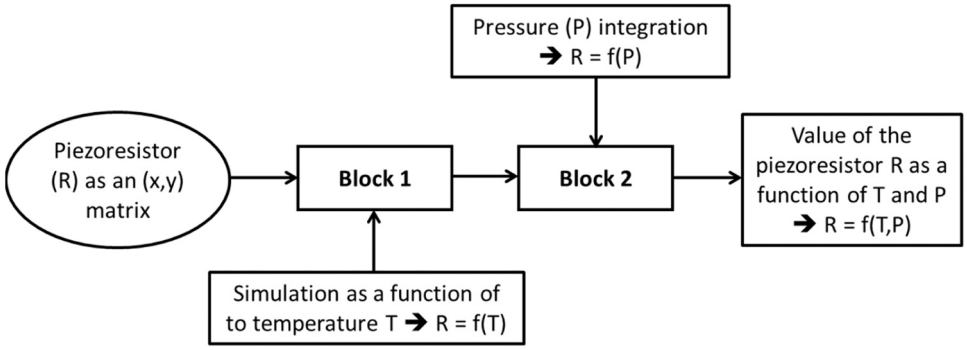

Fig. 7. Synoptic of the simulation model developed in Cadence/Pspice.

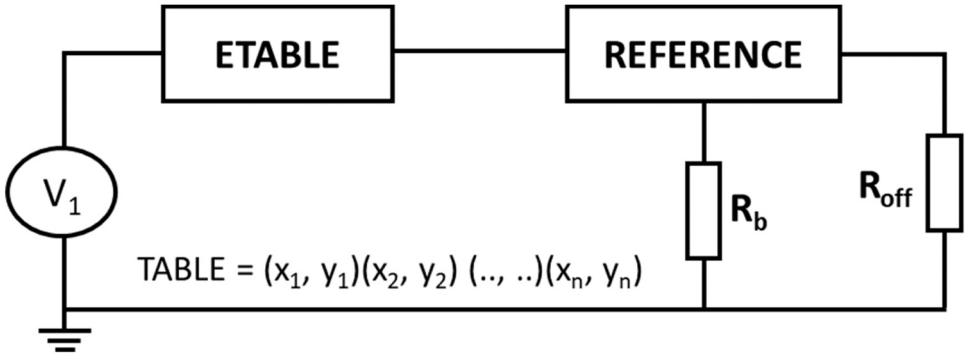

Fig. 8. Simulation model of each piezoresistor as a function of temperature and pressure.

which can be positive or negative according to the variation of each piezoresistor and the resistance Rb, very weak (~1 Ω), enables to have a resistance variation at the output of the system. This whole procedure described above permits to simulate a single piezoresistor as a function of temperature and pressure. It will have to be duplicated four times to simulate the entire probe.

Fig. 9 shows the configuration of the simulation model of the entire sensor, with the instrumentation amplifier, produced with the Cadence/Pspice software, where the piezoresistors R_1, R_2, R_3 and R_4 are formed from the values extracted previously.

Fig. 10 shows that our simulation model faithfully reproduces the behaviour of the sensor as a function of temperature and pressure vs measurement. To better assess the difference between simulated and measured thermal drifts, the deviation Δ is calculated as a percentage as shown in Table 1. This deviation is calculated using the following formula:

$$\Delta\ (\%) = 2^{*}\mathrm{ABS}\ [(R_{ij\_simulated} - R_{ij\_measured}) / (R_{ij\_simulated} + R_{ij\_measured})]$$

As we can see the model obtained in simulation is in good agreement with the measurement results. The maximum difference observed is 1.41 % obtained with a pressure of 300 mmHg and a temperature of 39°C. This difference could be explained by the measurement precision when the pressure and temperature are high.

Table 2 shows the thermal drifts of the sensor in simulation and in measurement. A reliable simulation model makes possible to reproduce the experimental results and allows us to study the different solutions for thermal drift compensation. This constitutes a considerable saving of time and consequently a saving of cost as well.

3.5. Compensation of the thermal drift of the sensor

The modelling of the sensor carried out previously allowed us to

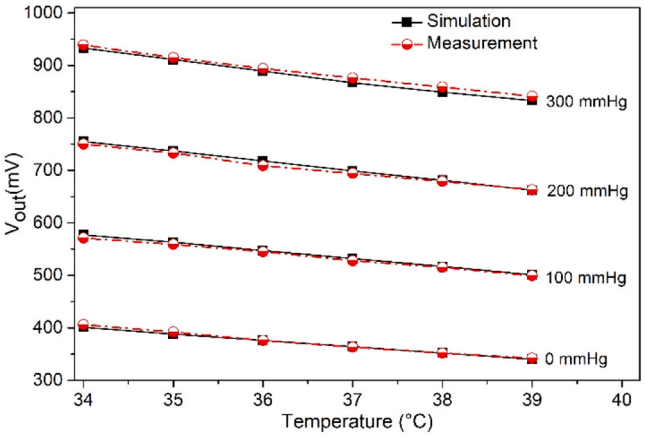

Fig. 10. Simulation and measurement results without compensation of the thermal drift.

Table 1
Relative difference (Δ) between simulation and measurement.

T(°C) P(mmHg)	34	35	36	37	38	39
P(mmHg)						
0	1.09 %	1.02 %	0.00 %	0.27 %	0.00 %	0.58 %
100	1.17 %	0.71 %	0.36 %	0.75 %	0.38 %	0.40 %
200	0.66 %	0.54 %	1.26 %	0.71 %	0.29 %	0.15 %
300	0.64 %	0.43 %	0.56 %	1.03 %	1.24 %	1.41 %

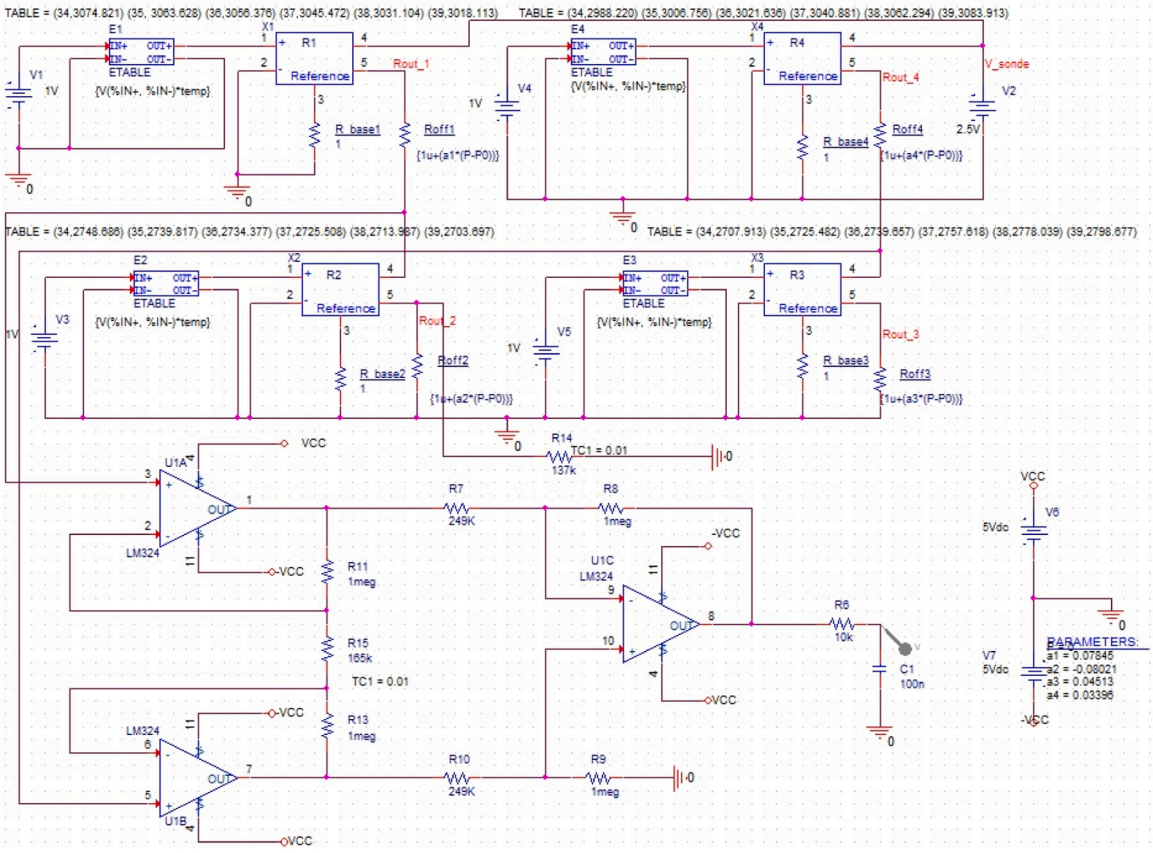

Fig. 9. Sensor simulation model used in Cadence/Pspice software.

Table 2
Comparison of thermal drift in mmHg/°C between simulation and measurement without compensation.

P(mmHg) Drift (mmHg/°C)	0	100	200	300
Simulated	6.25	7.05	8.61	9.81
Measured	6.47	7.27	8.83	9.97

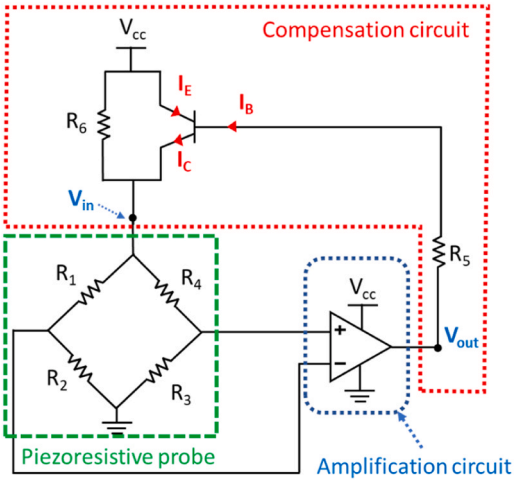

Fig. 11. Compensation circuit optimized to reduce sensor thermal drift.

simulate its behaviour and then to test a compensation circuit based on a PNP transistor and two adjustable potentiometers (cf. Fig. 11).

Indeed, in this circuit, the base current of the PNP transistor is given by the following formula:

$$I_B = I_S\left(e^{\frac{V_{BE}}{U_T}} - 1\right) \text{ with } I_c = \beta I_B$$

Where I_s is the saturation current, $U_T = kT/q$ the thermal voltage (=26 mV at 300 K), k the Boltzmann constant, β current gain and q the elementary charge.

Both currents I_B et I_C depend on the temperature.

Similarly, the voltage V_{EC} is given by the following formula:

$$V_{EC} = \left(\frac{I_C}{\beta I_S \; e^{\frac{V_{BE}}{U_T}}} - 1\right) V_{EA}$$

With V_{EA} the Early voltage

by replacing the current I_C by the previous expression, we obtain:

$$V_{EC} = -\frac{V_{EA}}{e^{\frac{qV_{BE}}{kT}}}$$

This expression allows to have the voltage V_{in} at the input of the Wheatstone bridge (cf. Fig. 11) which increases with temperature as shown in Fig. 12. As the voltage slope is opposite to that of the piezoresistive probe, the circuit can be used to compensate the output voltage of the sensor.

The potentiometer R_6 in parallel with the transistor (cf. Fig. 11) will act on the output voltage of the transistor supplying the piezoresistive probe with Vin. Since the supply voltage of the probe must be at least equal to 1.2 V according to manufacturer's specifications, the potentiometer R_6 must be tuned between 1.5 and 7.5 Ω to make the voltage delivered by the transistor to be high enough to have sensitivity at the output of the sensor. The potentiometer R_5 is used to adjust the output voltage of the sensor between 200 mV and 1200 mV to have the same

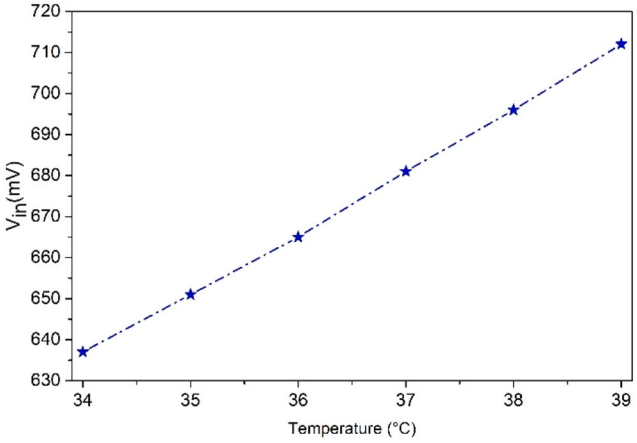

Fig. 12. Output voltage (V_{in}) of the compensation circuit.

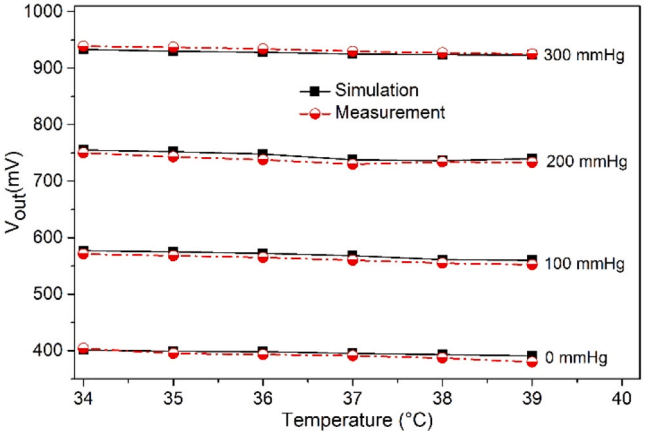

Fig. 13. Simulation and measurement results with compensation of the thermal drift.

range as that of the output voltage without compensation.

Fig. 13 shows the output voltage of the sensor as a function of temperature and pressure obtained by both simulation and measurement after compensation. As can be seen, according to simulation results, thermal drifts are perfectly compensated. However, there is a slight difference between measurement and simulation results. This difference could be due to the potentiometers used in the compensation circuit. The latter shows a drift as a function of the temperature. The difference between the simulation and the measurement of the sensor with the compensation is less than 1.45 % at most, which shows the fidelity of the simulation to the measurement. Table 3 shows the thermal drift of the sensor as a function of temperature and pressure with compensation circuit. For example, the sensor had an experimental thermal drift of 8.83 mmHg/°C at 200 mmHg before compensation (cf. Table 2) and this drift is reduced to 2.04 mmHg/°C after compensation (cf. Table 3). A very good temperature compensation is achieved with the help of the compensation circuit optimized thanks to the developed model in simulation.

Table 3
Comparison of thermal drift in mmHg/°C between simulation and measurement with compensation.

P(mmHg) Drift (mmHg/°C)	0	100	200	300
Simulated	1.85	2.15	1.82	1.75
Measured	2.15	2.29	2.04	2.12

4. Conclusion

In this article, we have presented the study of thermal drift compensation of piezoresistive blood pressure sensors. A detailed characteristic study of the piezoresistive probe used is first performed making it possible to quantify the thermal drift without compensation as baseline of our study. An original method combining calculation and measurement enabling us to extract the value of each piezoresistor without degrading the probe was then developed. Thanks to this new extraction method, we have developed a simulation model, in the Cadence/Pspice electronic simulation software, allowing to determine the output voltage of the probe according to temperature and pressure. After the simulation of the probe, we optimized an analog thermal drift compensation circuit based on a PNP transistor. The measurement results are very promising, thermal drift is reduced for each pressure level. Indeed, we obtained a significant reduction of the thermal drift, by a factor ranging from 3 to 4,7 for pressure ranging from 0–300 mmHg. Therefore, the optimized method makes it possible to reduce the experimental thermal drift of the sensor below 2.3 mmHg/°C whatever the pressure used. This improved thermal stability meets the specifications imposing a drift of less than 3 mmHg/°C.

We are currently working on a wireless data transmission device in order to test our compensation circuit on animals later. This requires developing an antenna that can transmit from biological tissue (animal body), compressed data coding as well as an operating mode compatible with power supply from a small battery. In our current work, we have used commercial pressure probes to save time and reduce the cost. In our future work, we plan to collaborate with researchers in materials and manufacturing technologies to produce probes with less thermal drift. The compensation circuit and the simulation and characterization methods presented in this paper and the wireless data transmission system will be valuable assets for realizing high-performance pressure sensors.

Authors' agreement

We the undersigned declare that the manuscript entitled "A simple and effective method to compensate the thermal drift of implantable blood pressure sensors" is original, has not been full or partly published before, and is not currently being considered for publication elsewhere.

We confirm that the manuscript has been read and approved by all named authors and that there are no other persons who satisfied the criteria for authorship but are not listed. We further confirm that the order of authors listed in the manuscript has been approved by the undersigned.

We understand that the Corresponding Author is the sole contact for the editorial process. The corresponding author "Mohammed El Gibari: mohammed.el-gibari@univ-nantes.fr" is responsible for communicating with the other authors about process, submissions of revisions, and final approval of proofs."

CRediT authorship contribution statement

Hongwu Li: Funding acquisition, Investigation, Methodology, Project administration, Resources, Supervision, Validation, Writing – original draft, Writing – review & editing. **Benjamin Lauzier:** Funding acquisition, Investigation, Validation, Visualization, Writing – review & editing. **Serigne Mbacke:** Conceptualization, Formal analysis, Software, Writing – original draft. **Chantal Gauthier:** Funding acquisition, Project administration, Resources, Supervision. **Mohammed EL GIBARI:** Conceptualization, Formal analysis, Funding acquisition, Investigation, Methodology, Project administration, Supervision, Validation, Writing – original draft, Writing – review & editing.

Declaration of Competing Interest

The authors declare that they have no known competing financial interests or personal relationships that could have appeared to influence the work reported in this paper.

Data Availability

Data will be made available on request.

References

[1] Suresh Neethirajan, Recent advances in wearable sensors for animal health management, Sens. Bio-sens. Res. Vol. 12 (2017) 15–29, https://doi.org/10.1016/j.sbsr.2016.11.004.

[2] Ankur M. Kumar, Kavita Kachhawa. Chapter 14 - Biomedical Applications of Bioelectrochemical Sensors. In: Lakhveer Singh, Durga Mahapatra, Smita Kumar, Editors. Multifaceted Bio-sensing Technology, Academic Press, 2023; vol. 4, p. 239-260. https://doi.org/10.1016/B978-0-323-90807-8.00014-2.

[3] Saleem Khan, Shaukat Ali, Arshad Khan, Amine Bermak, Wearable printed temperature sensors: short review on latest advances for biomedical applications, IEEE Rev. Biomed. Eng. vol. 16 (2023) 152–170, https://doi.org/10.1109/RBME.2021.3121480.

[4] Keaven M. Anderson, Patricia M. Odell, Peter W.F. Wilson, William B. Kannel, Cardiovascular disease risk profiles, Part 2, Am. Heart J. Vol. 121 (Issue 1) (1991) 293–298, https://doi.org/10.1016/0002-8703(91)90861-B.

[5] Suvrajyoti Mishra, Smita Mohanty, Ananthakumar Ramadoss, functionality of flexible pressure sensors in cardiovascular health monitoring: a review, ACS Sens. 7 (9) (2022) 2495–2520, https://doi.org/10.1021/acssensors.2c00942.

[6] Shyamal Patel, Hyung Park, Paolo Bonato, Leighton Chan, Mary Rodgers, A review of wearable probes and systems with application in rehabilitation, J. Neuroeng. Rehabil. vol. 9 (1) (2012) 21, https://doi.org/10.1186/1743-0003-9-21.

[7] Jyh-Jier Ho, The design and fabrication of a micro-thermal/pressure-sensor for medical electro-skin application, Solid-State Electron. Vol. 46 (Issue 8) (2002) 1205–1209, https://doi.org/10.1016/S0038-1101(02)00012-6.

[8] Elena Chan, Dequan Lin, Lei Lu, Deqiang Zhang, Shichao Guo, Yiming Zhang, Kevin Chau, Man Wong, Realization and characterization of a bulk-type all-silicon high pressure sensor, J. Microelectrochem. Syst. Vol. 27 (Issue 2) (2018) 231–238, https://doi.org/10.1109/JMEMS.2017.2786730.

[9] Anh Vang Tran, Xianmin Zhang, Benliang Zhu, Effects of temperature and residual stresses on the output characteristics of a piezoresistive pressure sensor, IEEE Access Vol. 7 (2019) 27668–27676, https://doi.org/10.1109/ACCESS.2019.2901846.

[10] A.S. Fiorillo, C.D. Critello, S.A. Pullano, Theory, technology and applications of piezoresistive sensors: a review, Sens. Actuators A Phys. vol. 281 (2018) 156–175, https://doi.org/10.1016/j.sna.2018.07.006.

[11] Paolo Bruschi, Michele Dei, Massimo Piotto, A method to compensate the pressure sensitivity of integrated thermal flow probes, IEEE Sens. J. vol. 10 (Issue 10) (2010) 1589–1597, https://doi.org/10.1109/JSEN.2010.2046889.

[12] Baohua Tian, Haiping Shang, Weibing Wang, Research on temperature zero drift of SiC piezoresistive pressure sensor based on asymmetric wheatstone bridge, Silicon vol. 14 (2022) 5445–5451, https://doi.org/10.1007/s12633-021-01330-x.

[13] Xueliang Zhao, Ying Chen, Guanghua Wei, Li.Li Pang, Chongxuan Xu, A comprehensive compensation method for piezoresistive pressure sensor based on surface fitting and improved grey wolf algorithm, Measurement Vol. 207 (2023) 112387, https://doi.org/10.1016/j.measurement.2022.112387.

[14] S. Wu, T. Zhang, Z.H. Li, J.W. Jia, Y. Deng, P.L. Xu, Y. Shao, D.Y. Deng, B.W. Hu, Temperature characteristic and compensation algorithm for a marine high accuracy piezoresistive pressure sensor, J. Mar. Eng. Technol. vol. 19 (4) (2020) 207–214, https://doi.org/10.1080/20464177.2019.1633881.

[15] Nina J. Cleven, Jutta A. Muntjes, Holger Fassbender, Ute Urban, Michael Gortz, Holger Vogt, Maik Grafe, Thorsten Gottsche, Tobias Penzkofer, Thomas Schmitz-Rode, Wilfried Mokwa, A novel fully implantable wireless sensor system for monitoring hypertension patients, IEEE Trans. Biomed. Eng. vol. 59 (11) (2012) 3124–3130, https://doi.org/10.1109/TBME.2012.2216262.

[16] Guanwu Zhou, Yulong Zhao, Fangfang Guo, Wenju Xu, A smart high accuracy silicon piezoresistive pressure sensor temperature compensation system, Sensors 14 (7) (2014) 12174–12190, https://doi.org/10.3390/s140712174.

[17] M. Aryafar, M. Hamedi, M. Maghsoudi Ganjeh, A novel temperature compensated piezoresistive pressure sensor, Measurement vol. 63 (2015) 25–29, https://doi.org/10.1016/j.measurement.2014.11.032.

[18] K.M. Tsang, W.L. Chan, Temperature compensated high efficiency inductor current sensor, Sens. Actuators A Phys. vol. 154 (Issue 1) (2009) 16–22, https://doi.org/10.1016/j.sna.2009.06.012.

[19] Jaime Sánchez Moreno, Diego Ramírez Muñoz, Susana Cardoso, Silvia Casans Berga, Asunción Edith Navarro Antón, Paulo Jorge Peixeiro de Freitas, A non-invasive thermal drift compensation technique applied to a spin-valve magnetoresistive current sensor, Sensors 11 (3) (2011) 2447–2458, https://doi.org/10.3390/s110302447.

[20] S.Santosh Kumar, B.D. Pant, Effect of piezoresistor configuration on output characteristics of piezoresistive pressure sensor: an experimental study, Microsyst.

Technol. vol. 22 (4) (2016) 709–719, https://doi.org/10.1007/s00542-015-2451-5.
[21] S.Maflin Shaby, M.S.Godwin Premi, Betty Martin, Enhancing the performance of MEMS piezoresistive pressure sensor using Germanium nanowire, Procedia Mater. Sci. vol. 10 (2015) 254–262, https://doi.org/10.1016/j.mspro.2015.06.048.
[22] Zong Yao, Ting Liang, Pinggang Jia, Yingping Hong, Lei Qi, Cheng Lei, Bin Zhang, Jijun Xiong, A high-temperature piezoresistive pressure sensor with an integrated signal-conditioning circuit, Sensors 16 (6) (2016) 913, https://doi.org/10.3390/s16060913.
[23] Boshan Sun, Jijun Xiong, Zhihong Fang, Lixia Gao, Aodi Xu, Pengyu Jia, Qiyun Feng, Chen Li, High-temperature self-compensating absolute micro-pressure sensor and its testing method (Early Access), IEEE Sens. J. (2023), https://doi.org/10.1109/JSEN.2022.3223981.
[24] Quan Wang, Jianning Ding, Wenxiang Wang, Fabrication and temperature coefficient compensation technology of low-cost high temperature pressure sensor, Sens. Actuators A Phys. vol. 120 (Issue 2) (2005) 468–473, https://doi.org/10.1016/j.sna.2005.01.036.
[25] Mohammed El Gibari, Clément Le Bleis, Guillaume Lirzin, Benjamin Lauzier, Stephane Ginestar, J.érôme Tissier, Mohamed Latrach, Chantal Gauthier, Hongwu Li, Thermal drift compensation of piezoresistive implantable blood pressure sensors with low cost analog solutions, 29th Int. Conf. Microelectron. (ICM) (2017), https://doi.org/10.1109/ICM.2017.8268895. Beirut, Lebanon, 10-13 December.
[26] Serigne Mbacke, Mohammed El Gibari, Chantal Gauthier, Benjamin Lauzier, Hongwu Li, Analog, compact and economical solution for the compensation of implantable piezoresistive blood pressure sensors for wireless medical monitoring, 28th Telecommun. Forum (TELFOR) (2020), https://doi.org/10.1109/TELFOR51502.2020.9306571. Serbia, Belgrade, 24-25 November.

Dr. Mohammed El Gibari received his PhD from Nantes University in 2009. From 2011, he is an Associate Professor at Nantes University. His current research interests at Institut d'Electronique et des Technologies du numéRique (IETR) include biomedical sensors, broad bandwidth microwave photonic devices on electro-optic polymers and Band-pass filters based on thin film polymers. he was the leader and scientific manager of the Interdisciplinarity (2017–2022) Engineering-Health project entitled "Implantable wireless blood pressure sensors with high precision and autonomy". He has also participated in several research projects with the National Research Agency, French Ministry of Industry and Region of Pays de la Loire. He is author and co-author of over 70 articles and conferences (ORCID: 0009–0004–3451–4314).

Dr. Serigne Mbacke received his PhD from Nantes University in 2022 on the study of thermal drifts of implantable piezoresistive sensors for medical applications. From 2023, he is an engineer in a company that works on thermal problems in electronic systems.

Pr. Chantal Gauthier, is Professor of Physiology at Nantes University, France. Education/training: PhD of the University of Poitiers, Mention Life sciences - "Biomembranes" option "Electrophysiology and Pharmacology Cellular" in 1991. Main administrative activities: Member at the Scientific Committees of "Fondation pour la Recherche Medicale" (2016–2019). Member elected at the Scientific Committees of INSERM (1999–2002). Expert for AERES, British Heart foundation, Chinese University of Hong Kong. Peer-reviewed publications: Number of publications: 1) total: 48, 2) 10 as 1st author and 3) 24 as last author. H index: 20; n citations: 2150.

Pr. Benjamin LAUZIER, is the scientific coordinator of pathophysiological axis of the team II, a 15 member-group at l'institut du thorax (INSERM UMR 1087 /CNRS UMR 6291). He is recognized for his skills and knowledge on cardiac function evaluation (particularly that of isolated heart) and O-GlcNAc. In 2019, he obtained an ASTRID program Grant, Specific Support for Defense Research Projects and Innovation implemented by ANR, to conduct a project on the link between cardiac function and O-GlcNAcylation. He has also an excellent track record (ORCID: 0000–0002–1370–6155). He has been working for many years on the role of O-GlcNAc in the regulation of cardiac function and has published recently several article on the precise regulation of O-GlcNAc level during cardiac post-natal development.

Pr. Hongwu LI worked at the University of Angers as Assistant (1987–1990). He worked on semi-conductor optical devices for telecommunications as Associate Prof. at National Engineering School of Brest (1990–2001). Then, he worked on RF signal generation and optical switches as Prof. at Institute of Electronics, Microelectronics and Nanotechnology (Lille, 2001–2005). Since 2005, he is Prof. at Nantes University. His research interests at Institut d'Electronique et des Technologies du numéRique (IETR) include microwave photonic devices based on polymers and biomedical sensors. He has led research projects with ANR, Orange, Thales and ESA. He has published over 100 scientific and technical papers.